The Influence of Hail on Wind Turbine Blade Leading Edge Erosion and Damage

PhD Thesis

Hamish Macdonald

Wind Energy Systems Centre for Doctoral Training
Department of Electronic & Electrical Engineering
University of Strathclyde, Glasgow, Scotland

October 24, 2017

Abstract

Wind turbine blade damage, particularly leading edge erosion, is a significant problem faced by the renewable energy industry. Wind turbines are subject to a wide range of environmental factors during a 20+ year lifespan, with hailstones often touted as a key contributor to the deterioration of blade profile. The consequences of blade damage are exhibited in terms of cost of component repair but, perhaps more seriously, in the reduced performance and thus annual energy production (AEP) of the turbine.

This thesis firstly presents the likelihood of hail events with respect to wind turbine locations, from an investigation of UK meteorological data. Three datasets were obtained: surface observations from UK-wide MIDAS stations, detailing back to 1949; as well as precipitation individual measurements from instruments located at CFARR and NERC facilities, also located in the UK. The prevalence of hail incidents is related to both onshore and offshore wind turbine operation. Particular attention was paid to the rotational speed of the wind turbine blades, which was determined to be a fundamental component of the energy associated with hail impact.

From these impressions, an experimental campaign was carried out to investigate the effects on of repeated impact of simulated hail ice (SHI) on composite materials. Hailstones at four different diameters (5 mm, 10 mm, 15 mm and 20 mm) were fired at a range of velocities and for different numbers of impacts. Samples used for experimentation were manufactured from triaxial stitched glass fibre ($0°$, $-45°$, $+45°$) and epoxy resin. Damage was analysed qualitatively using scanning electron microscopy.

A computational model was developed to compare the simulated damage of a singular hailstone impact to that of the experimental findings and examine other parameters not available in a practical setting. A survey of calculation methods was undertaken, to determine the elastic properties of the composite required prior to simulation. Threshold velocities were obtained for the onset of damage caused by singular impact of the different diameters of SHI.

Contents

Acknowledgements **xvii**

1 Introduction **1**

2 Literature Review **6**

2.1 Summary of Blade and Rotor Design 6
2.1.1 History of Blade Technology 6
2.1.2 Blade Design Considerations 9
2.1.3 Rotor and Control Strategy Design Considerations 11
2.1.4 Contemporary Blade Structure 12
2.2 Wind Turbine Blade Material Technology and Manufacturing 14
2.2.1 Polymer Matrix Composites 14
2.2.2 Manufacturing Processes 17
2.2.3 Sandwich Core 18
2.2.4 Structural Adhesive 19
2.2.5 Surface Coatings and Protections 20
2.3 Blade Damage 21
2.3.1 Damage Characteristics and Repercussions 22
2.3.2 Erosion Mechanisms and Factors 27
2.4 Hail 30
2.4.1 Hail Formation 32
2.4.2 Hailfall 35
2.4.3 Sensing/Forecasting 39
2.4.4 Hail Impact in the Literature 39
2.4.5 Ice Impact - Experimental Work 41
2.4.6 Ice Impact - Computational Modelling 49
2.5 Other Environmental Factors of Blade Damage 54
2.5.1 Liquid Impact 54
2.5.2 Ultraviolet Light 57

2.5.3 Lightning . . . 57
2.5.4 Accretion . . . 58
2.5.5 Other Abrasive Air Particles . . . 59
2.6 Maintenance and Standards . . . 60

3 Hail Impact Scenarios from Meteorological Data 63
3.1 Considerations . . . 64
3.1.1 Hail Impact Factors . . . 64
3.1.2 Meteorological Data . . . 64
3.1.3 Prevalence of Hail in The UK . . . 68
3.1.4 Durations and Rates of Hail . . . 71
3.1.5 Velocity Components . . . 73
3.1.6 Case Studies . . . 86
3.1.7 Hailstorms . . . 89
3.2 Discussion . . . 92
3.3 Conclusion . . . 97

4 Experimental Simulations of Hail Impact on Composites 100
4.1 Introduction . . . 101
4.2 Simulated Hail Ice Manufacture . . . 102
4.3 Hail Rig Data Collection . . . 107
4.4 Composites . . . 112
4.4.1 Composite Manufacture . . . 112
4.4.2 Composite Properties . . . 117
4.4.3 Samples . . . 119
4.5 Experimental Protocol and Calibration . . . 121
4.5.1 High Speed Video . . . 140
4.6 Experimental Forces and Velocities . . . 144
4.7 Damage evaluation . . . 151
4.8 Discussion . . . 169
4.9 Conclusion . . . 172

5 Computational Modelling 174
5.1 Methods of Determining Composite Characteristics . . . 175
5.1.1 Rule of Mixtures . . . 176
5.1.2 Hart-Smith Rule (10%) . . . 177
5.1.3 Classical Laminate Analysis . . . 178
5.1.4 Engineering Sciences Data Unit (ESDU) . . . 178

5.1.5 Autodesk Helius Composite Simulation Design 179
5.2 Comparison of Elastic Properties 179
5.3 Computational Model Geometry and Material Characteristics 184
5.3.1 Composite 184
5.3.2 Metals 186
5.3.3 Ice 188
5.4 Control and Additional LS-DYNA Considerations 189
5.4.1 Termination and Timestep 189
5.4.2 Damping 189
5.4.3 Contact 189
5.4.4 Hourglass 190
5.4.5 Gravity 193
5.4.6 Mesh Refinement 194
5.5 Model Calibration 196
5.6 Damage Analysis 202
5.7 Discussion 210
5.8 Conclusion 213

6 Overall Discussion and Future Work 214
6.1 Meteorological 214
6.2 Experimental and Computational 215

7 Summary of Conclusions 219

List of Figures

1.1 Worldwide capacity [1] 2
1.2 Top 10 countries for wind generation (markets bigger than 200 MW) [1]. 2
1.3 Worldwide categorised climates [2]. 3
1.4 Global wind resource [3]. 4

2.1 Transportation of a steel blade from the Smith-Putnam wind turbine to site at Grandpa's Knob [4]. 6
2.2 Specific stiffness vs. specific strength of various Materials [5]. 8
2.3 Blade structural design process [6]. 10
2.4 Wind turbine structural concepts: structural shell with one Shear Web (l) and box spar with shell fairings (r) [6]). 13
2.5 Composite material comprising of unidirectional fibres aligned within a matrix. 14
2.6 Stacking of plies of different fibre orientations to form a laminate. 16
2.7 Wind turbine blade attributes [7]. 19
2.8 Observed damage types for a wind turbine blade subjected to a compressive load (*note "chanal" should be "channel"*) [7]. 24
2.9 Damage footprint of a typical blade - locations [8]. 25
2.10 Damage footprint of a typical blade - types [8]. 25
2.11 Progression of leading edge erosion. 1 - coating removal, 2 - damage of the matrix 3 - delamination and fibre damage [9]. 26
2.12 Impingement angle of Particle. 29
2.13 Possible mechanisms of erosion; abrasion at low impact angles; b) surface fatigue during low speed, high impingement angle, c) brittle fracture or multiple plastic deformation during medium speed, larger impingement angle impact, d) surface melting at high impact speeds and e)macroscopic erosion with secondary effects [10]. 31
2.14 Major growth stages of hail in a cloud of supercooled droplets [11]. . . . 32
2.15 Cross-sections of hailstones [12]. 34

2.16 Experimentally determined densities for graupel and hail [13]. 34
2.17 Global map of hail days experienced annually [13]. 36
2.18 Radar scan through a hail storm [14]. 38
2.19 Schematic stress-strain curves. I, II, and III denote low, intermediate and high-strain rates. The arrows indicate either ductile (horizontal) or brittle (vertical) behavior [15]. 40
2.20 Comparison of Split Hopkinson Pressure Bar data with strength reported in existing literature [16]. 41
2.21 Nitrogen gas cannon used in [17, 18]. 42
2.22 High speed video of ice impact on force measurement bar [19] 44
2.23 Failure modes observed experimentally for high-velocity ice impacts [17]. 44
2.24 Different response types during impact on plates [20]. 45
2.25 Comparison between delamination velocity from FE and experiments with analytical upper and lower bounds [21]. 46
2.26 Experimental and simulated hail ice composition [17]. 48
2.27 DYNA3D model pan15b contour plot of τ_{xz} at time t = 12 θs, maximum $\tau_{xz} = 83.9\,\text{MPa}$ [17]. 50
2.28 Peak force versus kinetic energy relationship showing simulation and experimental results [19]. 50
2.29 Hail impact at t=0.150 $\times 10^{-3}$ s and numerical-experimental correlation. (a) FE; (b) ALE; and (c) SPH models [22] 51
2.30 Simulation of SHI impact using a smooth particle hydrodynamics model [21]. 53
2.31 Solid to fluid transition of the Carney model using an Eulerian formulation [23]. 53
2.32 Schematic of 3-D water erosion impact [24]. 55
2.33 Damage modes related to droplet impingement. 56
2.34 Effects of combined UV-A exposure and liquid droplet impact on polyurethane tape compared with a control [25] 57
2.35 Still image taken from a video showing upside down lightning effecting a wind turbine [26] 58
2.36 Examples of accretion. 59
2.37 Technicians inspecting a turbine blade via rope access [27]. 61

3.1 Impact velocity components during wind turbine blade revolution: horizontal wind speed (green), hailstone terminal velocity (blue) and wind turbine tip speed (red). 65
3.2 UK MIDAS stations. 66
3.3 Percentage of UK MIDAS stations reporting a "hail day" (1949-2013). . 68

3.4 Number of hail observational stations over the period of data. 69
3.5 Total number of hail incidents at UK MIDAS stations (1949-2013). . . . 70
3.6 Average number of days per year of hail at UK MIDAS stations including position of wind farms. 71
3.7 Number of UK MIDAS stations that experience a range of hail days on average, segregated into groups of those a certain distance from the coast. 72
3.8 Hail rate vs time at NERC MST for separate instances of continuous hail. 74
3.9 Velocity comparisons for varying diameter between fall-speed relations and CFARR data. 76
3.10 Relationship of power and mean wind speed for a variable speed, pitch regulated turbine. 77
3.11 Nominal tip speeds and diameters for wind turbines $\geq$ 1MW. Empty markers represent turbines still in the prototype stage or awaiting certification (as of July 2014). 77
3.12 Example Weibull distributions of different shape parameters, scale parameter, $C = 8.463$. 78
3.13 Probability of being within the "below cut-in" speed region ($u_1 = 0$, $u_2 = cis$) for different values of shape parameter and V_{ave}. 80
3.14 Probability of being within the "cut-in to rated" speed region ($u_1 = cis, u_2 = rs$) for different values of shape parameter and V_{ave}. 80
3.15 Probability of being within the "rated to cut-out" speed region ($u_1 = rs, u_2 = cos$) for different values of shape parameter and V_{ave}. 81
3.16 Probability of being within the "above cut-out" speed region ($u_1 = cos, u_2 = 50$) for different values of shape parameter and V_{ave}. 82
3.17 Probability of being within design wind speed regions by an example 2.3 MW class IIa onshore turbine for different values of shape parameter. . 83
3.18 Probability of being within design wind speed regions by an example 6 MW class Ia offshore turbine for different values of shape parameter. . . 83
3.19 Average and Standard Deviation of daily mean wind speed at MIDAS stations subject to a discrete range of hail days on average per year. . . 84
3.20 Distribution 85
3.21 Distribution of daily mean wind speed at MIDAS stations subject to a discrete range of hail days on average per year. 85
3.22 Mean wind speeds at the NERC facility for instances of hail and no hail. 85
3.23 Incidents per year for different categories of hail in the UK. 87
3.24 Kinetic energy of different diameters of hailstone for impact at certain radial positions of a wind turbine blade. 88

3.25 Hail rate and rainfall rate for an example hailstorm at CFARR - 26th Novemember 2009 90
3.26 Hail rate and rainfall rate for an example hailstorm at CFARR - 13th May 2014 91
3.27 Mean rainfall rate for separate incidents of hail at CFARR. 91
3.28 Mean and standard deviation of days of thunder at MIDAS stations subject to a discrete range of hail days on average per year. 92
3.29 Probability of maximum hail diameter for four regions in China [28]. . . 93
3.30 Relative frequency distribution of hailstone size (taken from 1972 NHRE data) [29] 94
3.31 Example SHI impact velocities and diameters (M & S - Mahinfalah & Skordal, K & K - Kim & Kedward, K *et al.* - Kim *et al.*, * - estimated, J & O - Juntikka and Olsson, P & K - Park & Kim, T *et al.* - Tippmann *et al.*). Line plots indicate diameter range. 95
3.32 Change in failure threshold impact with glancing angle [18]. 97

4.1 Schematic of hailstone impact experimental rig. 101
4.2 Detachable barrel with light gates affixed for measurement of velocity. . 102
4.3 CAD drawing of 10 mm mould. 103
4.4 Estimated freezing times from Heisler chart equations for a sphere. . . . 105
4.5 Original range of mass of 10 mm SHI. 106
4.6 Improved range of mass of 10 mm SHI. 106
4.7 Range of mass of 5 mm SHI. 107
4.8 Range of mass of 15 mm SHI. 107
4.9 Range of mass of 20 mm SHI. 108
4.10 Example velocity measurement of a ceramic projectile. 110
4.11 Example resting noise for 5 separate measurements. 111
4.12 Dynamic force transducer and clamping arrangement. 111
4.13 Hail rig barrel and plastic sabot used to hold the projectile. 112
4.14 Glass fibre reinforcement used in vacuum infusion. 113
4.15 Vacuum infusion composite layup sequence. 113
4.16 Infusion process set-up. 116
4.17 A composite sample in the clamping arrangement. 117
4.18 SEM image of poorly-wetted composite sample. 120
4.19 SEM image of a slightly improved composite sample. 120
4.20 SEM image of an example composite sample selected for experimentation. 121
4.21 Surface melting times from Heisler equation for $T_i = -2.5\,^{\circ}\mathrm{C}$. 123

4.22 Radial melting times for different diameters of hail from Heisler equation for $T_i = -2.5\,°\text{C}$ and $T_i = -5\,°\text{C}$. 124
4.23 Surface melting times from Heisler equation for $T_i = -5\,°\text{C}$. 125
4.24 Average velocities vs. pressure for cannons of different projectile diameter. 126
4.25 Experimental and fitted trend for 5mm SHI projectile. 127
4.26 Experimental and fitted trend for 10mm SHI projectile. 127
4.27 Experimental and fitted trend for 15mm SHI projectile. 128
4.28 Experimental and fitted trend for 20mm SHI projectile. 128
4.29 Force transducer impact profiles for 5 mm SHI fired at 0.6 bar. 129
4.30 Force transducer impact profiles for 10 mm SHI fired at 0.6 bar. 129
4.31 Force transducer impact profiles for 15 mm SHI fired at 0.6 bar. 130
4.32 Force transducer impact profiles for 20 mm SHI fired at 0.6 bar. 130
4.33 Mean force transducer impact profiles for 5 mm SHI fired at 0.6 bar compared to most similar individual example. 131
4.34 Mean force transducer impact profiles for 10 mm SHI fired at 0.6 bar compared to most similar individual example. 132
4.35 Mean force transducer impact profiles for 15 mm SHI fired at 0.6 bar compared to most similar individual example. 132
4.36 Mean force transducer impact profiles for 20 mm SHI fired at 0.6 bar compared to most similar individual example. 133
4.37 Force transducer impact profiles for 5 mm SHI fired at 3 bar. 134
4.38 Force transducer impact profiles for 10 mm SHI fired at 2.4 bar. 134
4.39 Force transducer impact profiles for 15 mm SHI fired at 2.8 bar. 135
4.40 Force transducer impact profiles for 20 mm SHI fired at 3.4 bar. 135
4.41 Mean force transducer impact profiles for 5 mm SHI fired at 3 bar compared to most similar individual example. 136
4.42 Mean force transducer impact profiles for 10 mm SHI fired at 2.4 bar compared to most similar individual example. 136
4.43 Mean force transducer impact profiles for 15 mm SHI fired at 2.8 bar compared to most similar individual example. 137
4.44 Mean force transducer impact profiles for 20 mm SHI fired at 3.4 bar compared to most similar individual example. 137
4.45 Peak force versus kinetic energy relationship (all diameters) compared with Tippmann *et al.* [19] data. 138
4.46 Peak force versus kinetic energy relationship (individual diameters) compared with data from Tippmann *et al.* [19]. 139

4.47 Peak force vs. selected pressure compared with estimated values from Roisman & Tropea [30]. 139
4.48 High speed video footage of 5 mm SHI impact. 141
4.49 High speed video footage of 10 mm SHI impact. 142
4.50 High speed video footage of 15 mm SHI impact. 143
4.51 High speed video footage of 20 mm SHI impact. 144
4.52 Average velocities for samples impacted by 5 mm SHI for a selected firing pressure and number of impacts. 145
4.53 Average velocities for samples impacted by 10 mm SHI for a selected firing pressure and number of impacts. 145
4.54 Average velocities for samples impacted by 15 mm SHI for a selected firing pressure and number of impacts. 146
4.55 Average velocities for samples impacted by 20 mm SHI for a selected firing pressure and number of impacts. 146
4.56 Average peak force for each set of 5 mm impacts at a certain mean velocity. 147
4.57 Average peak force for each set of 10 mm impacts at a certain mean velocity. 147
4.58 Average peak force for each set of 15 mm impacts at a certain mean velocity. 148
4.59 Average peak force for each set of 20 mm impacts at a certain mean velocity. 148
4.60 Legend for Figures 4.61, 4.62, 4.63, 4.64, 4.65 and 4.66. 149
4.61 Total *measured* force subjected to each sample. 149
4.62 Total *measured* force subjected to each sample (reduced force range). . . 150
4.63 Total *projected* force subjected to each sample. 150
4.64 Total *projected* force subjected to each sample (reduced force range). . . 151
4.65 Cumulative kinetic energy subjected to each sample. 152
4.66 Cumulative kinetic energy subjected to each sample (reduced KE range). 152
4.67 Mass loss for each sample subject to 5 mm impacts 153
4.68 Mass loss for each sample subject to 10 mm impacts 154
4.69 Mass loss for each sample subject to 15 mm impacts 154
4.70 Mass loss for each sample subject to 20 mm impacts 155
4.71 Visual surface quality of sample M5-V4. 155
4.72 Visual surface quality of sample M10-V3. 156
4.73 Visual surface quality of sample M15-V3. 156
4.74 Visual surface quality of sample M20-V4. 157
4.75 Overview SEM image for sample M15-V3. 157

4.76 Close-up SEM images for sample M15-V3. 158
4.77 Overview SEM image for sample M20-V4. 159
4.78 Close-up SEM images for sample M20-V4. 160
4.79 Overview SEM image for sample M20-V1. 161
4.80 Close-up SEM images for sample M20-V1. 161
4.81 Overview SEM image for sample M15-V4. 162
4.82 Close-up SEM images for sample M15-V4. 162
4.83 Overview SEM image for sample S15-V4. 163
4.84 Close-up SEM images for sample S15-V4. 163
4.85 Overview SEM image for sample S20-V3. 164
4.86 S20-V3. 165
4.87 Overview SEM image for sample M15-V1. 165
4.88 Close-up SEM images for sample M15-V1. 166
4.89 Overview SEM image for sample M10-V3. 167
4.90 M10-V3. 167
4.91 Overview SEM image for sample M10-V4. 168
4.92 Close-up SEM images for sample M10-V4. 168
4.93 Overview SEM image for sample M5-V4. 169
4.94 Close-up SEM images for sample M5-V4. 169
4.95 Overview SEM image for sample S10-V1. 170
4.96 Close-up SEM images for sample S10-V1. 170

5.1 Experimentally determined modulus properties of a six ply unidirectional glass/epoxy composite by Samborsky *et al.* compared with various estimation methods. 180
5.2 Experimentally determined Poisson's ratios of a six ply unidirectional glass/epoxy composite by Samborsky *et al.* compared with various estimation methods (see Figure 5.1 for full legend). 181
5.3 Strength properties of the 'Samborsky *et al.* composite' compared with estimations by Autodesk Helius Composite. 181
5.4 Ultimate strain properties of the 'Samborsky *et al.*' composite compared with estimations by Autodesk Helius Composite. 182
5.5 Various estimated modulus properties for the 5-ply triaxial glass/epoxy composite used for hailstone impact. 183
5.6 Various estimated Poisson's ratios properties for the 5-ply triaxial glass/epoxy composite used for hailstone impact (see Figure 5.5 for full legend). . . . 183
5.7 Dynamic force transducer and clamping arrangement. 187

5.8 System internal energy, hourglass energy and the respective ratios for viscous hourglass algorithms (IHQ=2, IHQ=3). 192
5.9 Part internal energy/hourglass energy ratios for viscous hourglass algorithms (IHQ=2, IHQ=3). 192
5.10 System internal energy, hourglass energy and the respective ratios for stiffness hourglass algorithms (IHQ=4, IHQ=5, IHQ=6). 193
5.11 Part internal energy/hourglass energy ratios for stiffness hourglass algorithms (IHQ=4, IHQ=5, IHQ=6). 194
5.12 Distortional kinetic energy and convergence factor during dynamic relaxation phase. 195
5.13 Contact force between composite and hailstone shown for coarser mesh generations (Selections 1 and 2) the converged profile (Selection 5). . . . 196
5.14 Contact force between composite and hailstone shown for finer mesh generations (Selections 3 and 4) the converged profile (Selection 5). . . . 197
5.15 Simulated force profile for a 5 mm hailstone at 49.6 $\mathrm{m\,s^{-1}}$ and experimental counterparts. 198
5.16 Simulated force profile for a 10 mm hailstone at 50.7 $\mathrm{m\,s^{-1}}$ and experimental counterparts. 198
5.17 Simulated force profile for a 15 mm hailstone at 53.0 $\mathrm{m\,s^{-1}}$ and experimental counterparts. 199
5.18 Simulated force profile for a 20 mm hailstone at 49.3 $\mathrm{m\,s^{-1}}$ and experimental counterparts. 199
5.19 Simulated force profile for a 5 mm hailstone at 90.2 $\mathrm{m\,s^{-1}}$ and experimental counterparts. 200
5.20 Simulated force profile for a 10 mm hailstone at 96.4 $\mathrm{m\,s^{-1}}$ and experimental counterparts. 201
5.21 Simulated force profile for a 15 mm hailstone at 98.6 $\mathrm{m\,s^{-1}}$ and experimental counterparts. 201
5.22 Simulated force profile for a 20 mm hailstone at 87.2 $\mathrm{m\,s^{-1}}$ and experimental counterparts. 202
5.23 Visualisation of 5 mm, 10 mm, 15 mmand 20 mm simulated impact on a composite disc at the highest mean experimental velocities. 203
5.24 Velocities of individual SPH nodes upon contact of 20 mm hailstone with the composite disc (legend units in $\mathrm{m\,s^{-1}}$). 204
5.25 Stress contours in the form of a shockwave during simulated impact of 20 mm hailstone with an initial velocity of 87.2 $\mathrm{m\,s^{-1}}$ (legend units in Pa). 205

5.26 Von-Mises histories for the element of the composite experiencing the maximum stress for the lowest respective mean velocities for each diameter. 205
5.27 Von-Mises histories for the element of the composite experiencing the maximum stress for the highest respective mean velocities for each diameter. 206
5.28 Failure flags for 20 mm composite impact at 49.3 $\mathrm{m\,s^{-1}}$ viewed from top, bottom and isometric perspectives (top row - fibre tensile failure, 2nd row - matrix tensile failure, 3rd row - matrix compressive failure, bottom row - delamination). 207
5.29 Failure flags for 15 mm composite impact at 98.6 $\mathrm{m\,s^{-1}}$ viewed from top, bottom and isometric perspectives (top row - fibre tensile failure, 2nd row - matrix tensile failure, 3rd row - matrix compressive failure, bottom row - delamination). 208
5.30 Failure flags for 20 mm composite impact at 87.2 $\mathrm{m\,s^{-1}}$ viewed from top, bottom and isometric perspectives (top row - fibre tensile failure, 2nd row - matrix tensile failure, 3rd row - matrix compressive failure, bottom row - delamination). 209
5.31 Bottom surfaces of experimental discs for 15mm and 20mm SHI impacts (1st Row L-R) S15-V1, S15-V4, M15-V4; (2nd Row L-R) S20-V1, S20-V4, M20-V4 (Note that the velocity description on each sample label in the images are 10 $\mathrm{m\,s^{-1}}$ less than the subjected velocity, for all samples). 211
5.32 Simulated damage threshold velocities and energies for each diameter of hail. 212

6.1 Levels of computer simulated damage on GFRP samples obtained from single impact of hailstones of different diameters, fired at different speeds. 217

List of Tables

1.1 Wind turbine environmental parameters - IEC 61400-1 [31]. 5

2.1 Effect of leading edge erosion on wind turbine blade performance as estimated by PROPID [32]. 27
2.2 Revised TORRO international hailstorm intensity scale [33]. 37
2.3 Reported Youngs modulus and failure strain of freshwater ice and sea ice [34]. 42
2.4 Experimental velocities from the literature. 45
2.5 Delamination and strength reduction of CFRP specimens to mutiple ice impacts [35]. 47
2.6 Experimental diameters from the literature. 48

3.1 World meteorological code 6001 - NCM table 23 [36]. 67
3.2 Duration of hailstorms at CFARR and NERC observatory stations. . . . 73
3.3 Summary of fall-speed relations for a range of hail ($_H$) and graupel ($_G$) diameters (D), adapted from Dawson *et al.* [37]. C_d represents the co-efficent of drag, ρ_G and ρ_H particle densities and g the gravitational constant. 74
3.4 Example worst case terminal velocities (m/s) for different categories of hail 75
3.5 Basic parameters for wind turbine classes 79
3.6 Impact Energy for different categories of hail. 89

4.1 SHI Volumes. 103
4.2 Diameters and velocities associated with samples used for single impacts. 122
4.3 Diameters and velocities associated with samples impacted 5 times. . . . 122
4.4 Diameters and velocities associated with samples impacted 10 times. . . 122
4.5 Diameters and velocities associated with samples impacted 25 times. . . 122
4.6 Diameters and velocities associated with samples impacted 50 times. . . 122

5.1 Properties of reinforcement and matrix materials 176
5.2 Mechanical properties of the *MAT 022 COMPOSITE DAMAGE model. 186
5.3 Metal material properties. 187
5.4 Ice material properties. 188
5.5 Mesh computational times. 195

6.1 Damage observed under SEM of different diameters of SHI, fired at low and high velocities, for different numbers of impacts. 218

Acknowledgements

Firstly I would like to acknowledge my supervisors Professor Margaret Stack and Professor David Nash for their tutelage. Their expertise and guidance, both inside and outside the focus of the PhD, was invaluable throughout my studentship. I would also like to thank everyone associated with the Wind Energy Systems Centre for Doctoral Training for hosting and administering such an important area of research. A special shout-out to Drew Smith for all his support and being the glue that holds the centre together. All my friends and colleagues in the centre make it a thriving and stimulating place to be immersed in and although we may be involved with different disciplines, working alongside each other and the sharing of knowledge ensure that PhD life is not as solitary.

As part of my practical work, I relied upon the assistance of many technical members of staff, including Chris Cameron, Drew Irvine, James Gillespie and Gerald Johnstone. I would also like to thank all the members of the Tribology Research group and those within the Advanced Composites group that provided guidance on the manufacture of materials and experimental analysis.

The British Atmospheric Data Centre were also instrumental in the provision of all three meteorological datasets, that allowed the early insight possible.

I would like to thank the UK Engineering and Physical Sciences Research Council (EPSRC), Doctoral Training Centre grant number EP/G037728/1, for providing the financial support that made this PhD conceivable.

Finally I would like to thank the love and support of my partner, family and friends. Throughout the years of challenges, their belief in me never faltered. Without them I would not be where I am today.

Chapter 1

Introduction

The European 2020 climate and energy package aims to, along with other key objectives, raise the share of EU energy consumption produced by renewable resources. As part of this binding legislation [38], introduced in 2009, member states are required to meet mandatory national renewable energy targets by 2020. The variability in targets for each country represent different starting points and potential for increasing renewable energy production. Both onshore and offshore wind technologies are expected to account for a considerable share of the generation deployment up to this deadline. In 2011 the European Wind Energy Association (EWEA) devised two 2020 projections for wind energy: a "baseline" scenario and a "high" scenario [39]. The conservative approach for the "baseline" scenario estimated that the installed capacity would be 230 GW, around $15\% - 17\%$ of EU electricity. The high scenario acknowledges that due to the affordability of wind energy in comparison to other renewable technologies a higher capacity of 265 GW would be met. According to 2013 European statistics published by EWEA [40], there are now currently 117.3 GW of installed wind energy capacity in the EU. Although many projects will still be going through construction or planning phases of development, this would indicate that a considerable amount of installation still has to take place in order to meet even the baseline projection for 2020.

Although not beholden to the same deadline as the European Union countries, there is an obligation for the majority of United Nations member states to reduce greenhouse gas emissions as part of the Kyoto Protocol [41]. Along with other national prerogatives and motivations, this has lead to a continual increase in total wind energy installed capacity worldwide, as described in Figure 1.1a. Figure 1.1b describes for the same time frame, the trend for *new* capacity, which shows diminishing returns from 2009 onwards. Although there are many factors connected with this decreasing trend, one predominant cause is the suitability of wind farm locations that are constrained by a number of parameters. Most notable restrictions include: the availability of the wind resource,

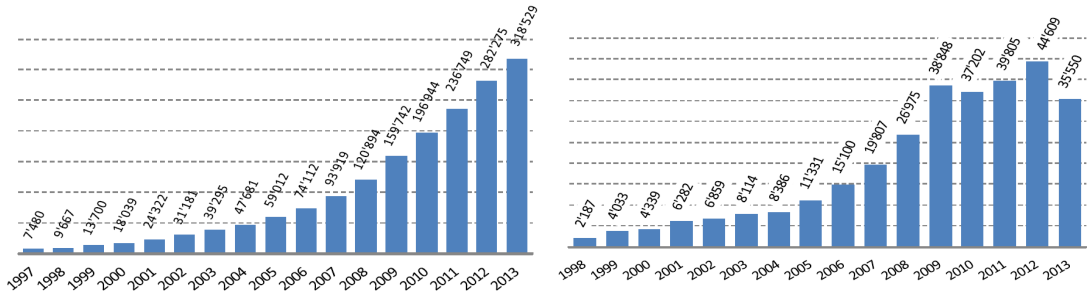

(a) Total installed [MW]

(b) Newly installed [MW]

Figure 1.1: Worldwide capacity [1]

economic viability and planning restrictions. All are identified by the International Energy Agency as barriers to development as part of the wind energy roadmap [3]. As installed capacity of wind energy increases, the availability of conventional onshore sites will decrease.

Figure 1.2a details the ten countries around the world that have the greatest installed capacity. Here, China and the USA dominate proceedings, with European countries making up the majority of the remainder along with India and Canada. The top ten countries with the highest percentage growth rate are shown in Figure 1.2b, where contributions from South America (Chile, Argentina, Brazil) and Africa (Morocco), Mexico and a smattering of other European countries are also present.

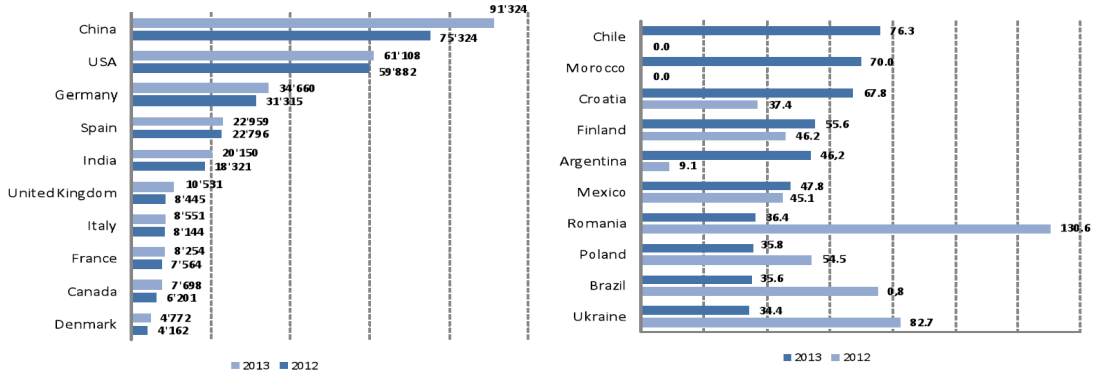

(a) Total capacity [MW].

(b) Growth rate [MW] [%].

Figure 1.2: Top 10 countries for wind generation (markets bigger than 200 MW) [1].

One of the first modern Danish-concept wind turbines (three-bladed, fixed rotor) was designed in 1956 by Gedser and installed in a temperate region in southern Denmark [42]. Re-examining the countries detailed in Figures 1.1a and 1.1b it is apparent there are contributions from each the four main continents. With respect to Figure 1.3, the various climates associated with these constituent countries are noticeably wide

ranging. China, USA and India particularly experience a multitude of weather conditions, within the geographical area that they encompass. The emerging countries are also subject to polar, arid, equatorial and snow atmospheres. This demonstrates that wind turbines are present in the full spectrum of categorised climates.

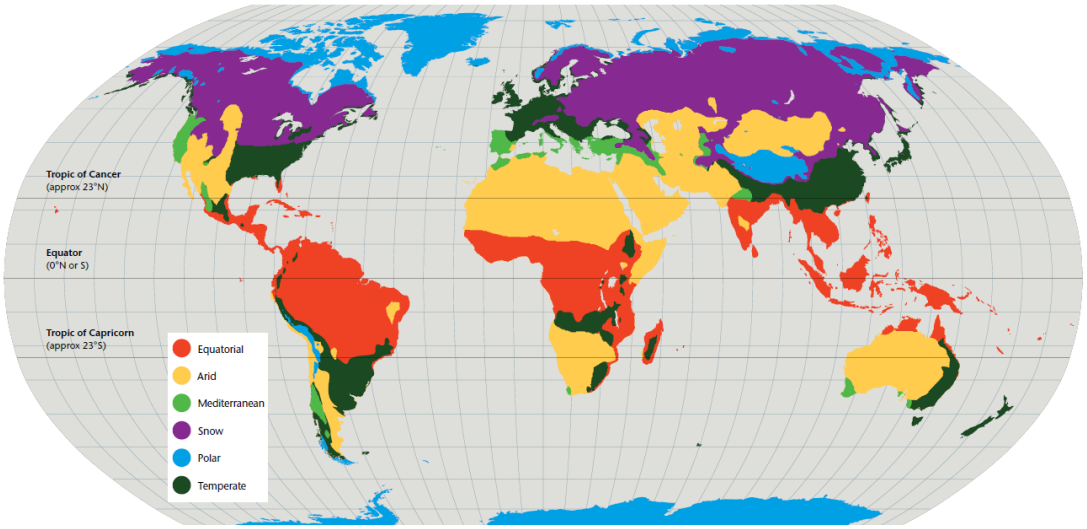

Figure 1.3: Worldwide categorised climates [2].

Comparing the global wind resource in Figure 1.4 to the generalised climates, there appears to be a clear deficit in mean wind speed around the equatorial regions. High wind speeds are found in many of the other climate types, including substantial speeds in arid and polar areas. Extreme areas within these climates discourage human habituation and as such are typically a greater distance from population centres. However, it is for these very reasons that wind turbines situated in harsher environments could be more commonplace. The VTT Technical Research Centre of Finland forecasts that between 45 and 50 gigawatts of wind energy will be built in icy regions by 2017 [43]. The centre claims that "cold climates represent encouraging potential for wind energy companies because of their sparse population and favourable wind conditions.

Of the 117.3 GW installed in the EU, 110.7 GW is situated onshore and 6.6 GW offshore. According to EWEA, offshore wind power installations in 2013 represent over 14% of the annual EU wind energy market, up from 10% in 2012 [40]. The European installations represents the vast majority of the 7.4 GW global offshore generation, as stated by the WWEA [1]. Once completed, 12 offshore projects currently under construction will increase installed capacity by a further 3 GW, bringing cumulative capacity in Europe to 9.4 GW. There are notable differences between offshore and onshore turbine installation that have to be addressed for design [44] and certification [45],

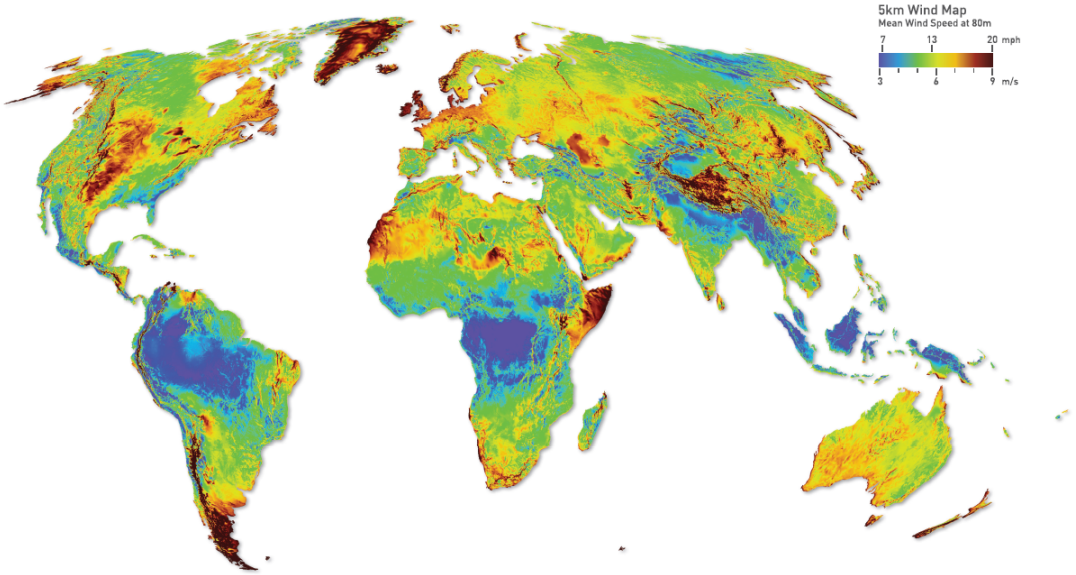

Figure 1.4: Global wind resource [3].

due to the nature of the surroundings.

Accompanying such a diverse range of environmental and geotechnical conditions of wind turbine locations, are the associated challenges of each of these respective environments. The International Electrotechnical Commission (IEC) recognise key parameters that need to be determined as part of the designation of wind turbine 'classes' in IEC 61400-1. [31]. These include reference wind speed, annual average wind speed, wind speed probability distribution, wind direction distribution, turbulence intensity and wind shear. The IEC also recognises other environmental considerations, as displayed in Table 1.1, of which hail is included. These oceanographic, meteorological and electrical conditions may affect the loading, durability and operation of these machines which are expected to operate for 20 years or more in service. For wind energy to continue as a competitive technology source, advances in turbine efficiency most also be coupled with reduced costs. In the NREL cost of energy review [46], the total levelised cost of energy (LCOE) was summarised for both a land-based and an offshore project. In each cases, maintenance costs consist of 55% and 59% of the overall operational expenditure. However, the estimated cost for maintenance increases from 28 \$/kW/yr to 81 \$/kW/yr when going from onshore to offshore.

Of all the different components of a wind turbine, the most frequently reported damage is to the blades [47]. It is also the most expensive form of damage in terms of repair cost; and the rotor the greatest contributor to wind turbine unavailability. The consequences of blade damage take multiple forms (as discussed in Section 2.3.1)

Table 1.1: Wind turbine environmental parameters - IEC 61400-1 [31].

Marine Considerations	Other Considerations
• Waves • Currents • Sea level, bathymetry • Extreme wind direction change • Sea ice • Marine growth	• Normal and extreme temperature ranges • Humidity • Air density • Solar radiation • Rain, hail, snow and ice formation • Chemically active particles • Mechanically active particles • Lightning • Earthquakes • Sand dune movements (sea bed variation) • Water density (offshore) • Salinity of water (offshore) • Scour • Corrosion

but the major issues involve the loss of aerodynamic profile [32] and the requirement for maintenance or blade replacement that would otherwise result in blade failure. For the various stakeholders in a wind turbine or farm, the repercussions of aerodynamic shape degradation are recognised in terms of a reduction in energy capture and hence revenue received. Similarly any requirement for corrective maintenance or full-on blade replacement may likely result in a loss in turbine availability, a key performance indicator that the IEC defines as 'the fraction of a given operating period in which a wind turbine generating system is performing its intended services within the design specification'. Any period where an turbine experiences downtime where generation was possible again corresponds to financial income. Availability issues could also be compounded in harsh or offshore environments due to required conditions associated with safe and practical maintenance access. Both loss of annual energy production (AEP) and availability reduction become even more significant considering the aforementioned lifetime of a turbine.

Chapter 2

Literature Review

2.1 Summary of Blade and Rotor Design

2.1.1 History of Blade Technology

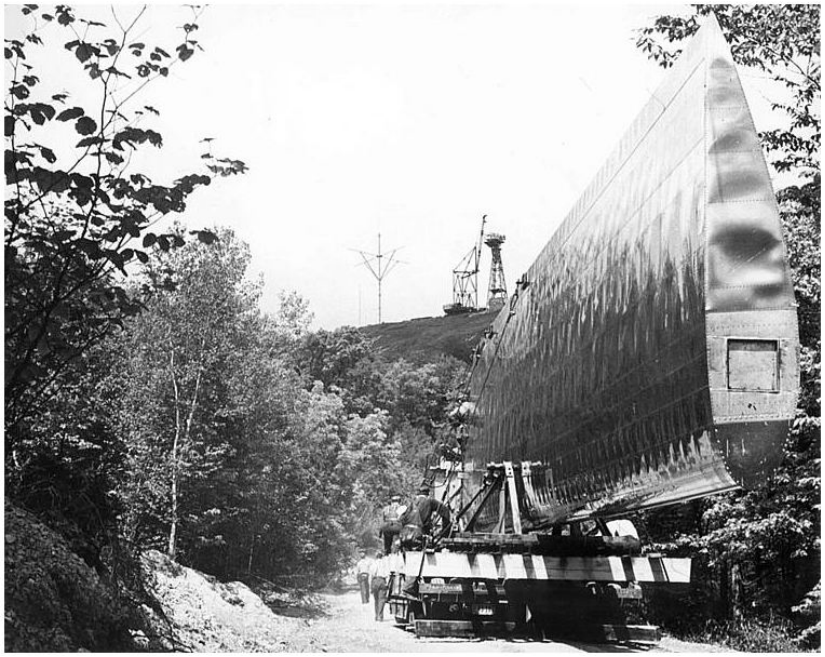

Figure 2.1: Transportation of a steel blade from the Smith-Putnam wind turbine to site at Grandpa's Knob [4].

Wind turbine design has seen considerable refinement since James Blyth first managed to generate electricity at his holiday home in Marykirk, Scotland in 1887. He described his invention as "being of a tripod design, with a 33 foot windshaft, four arms of 13 feet with canvas sails, and a Burgin dynamo driven from the flywheel using

a rope" [48]. Despite the work by other early pioneers such as Charles Brush in the USA and Poul La Cour in Denmark, the role of wind in energy generation lay relatively dormant for much of the twentieth century. One historic anomaly, was the construction of the world's first megawatt-size wind turbine, designed by Palmer Cosslett Putnam and manufactured by the S. Morgan Smith Company at Grandpa's Knob in Castleton, Vermont. The turbine was constructed in 1941, with a steel rotor 53m in diameter, complete with full span pitch control and flapping blades to reduce loads [42], as seen in Figure 2.1. The turbine ran at a fixed speed and as such was able to tie-in directly to the grid. However, the turbine suffered failure due to severe fatigue damage of the blade after only a few hundred hours of intermittent operation, eventually resulting in the abandonment of the whole project. Rated at 1.25 MW, it still remained the largest wind turbine installation for approximately 40 years, highlighting that the capability of wind turbine technology of that time could not match the ambition of the venture. It also demonstrated the importance in appropriate selection of materials and the inherent limitations of metals for wind turbine blades, especially on such a grand scale.

One of the important milestones in wind energy is often tracked back to the construction of the Gedser wind turbine by Johannes Juul in 1957 in the south of the Danish island of Falster. Consisting of a three bladed rotor 24m in diameter, the particular blade design allowed aerodynamic stall to be used as a means to regulate power. Along with the use of an induction generator, it was one of the main concepts that stimulated Danish wind turbine development over the 1980's and formed the basis of the 'Danish' wind turbine concept' [49]. Although stall has been displaced by more sophisticated control methods, the three bladed horizontal-axis configuration still represents the industry standard in use today.

The industry was given an injection of interest due to ongoing oil shortages during the 1970's along with growing concern of the environmental practices associated with traditional fossil fuel generation. The US government funded a number of prototype wind turbine projects in the wake of rising oil prices. The support mechanisms eventually led to the 'California Wind Rush' in the early 1980's, where a huge number of turbines were installed, typically in a group ('wind farm') and grid-connected. The majority of these prototype turbines struggled in terms of reliability and durability, mainly due to underestimation of the harsh wind climate [42]. Despite the fact the size of these machines lent themselves to fairly straight forward maintenance and modification, it is remembered a tumultuous period for wind energy.

The early 1980's did however, provide the opportunity to evaluate and disregard certain rotor blade technologies [50]. In the aftermath of the Smith-Putnam wind turbine, steel rotors were rejected primarily because of their weight. Aluminium was

also overlooked as concerns were raised over fatigue endurance, particularly due to increasing requirement of a high strength to weight ratio. Wood was an early naturally sourced alternative, with initial problems of moisture stabilisation overcome thanks to a wood-epoxy system developed by the Geougeon Brothers in the US. This technology was developed further by the UK but began to lose favour due to the increasing use of fibreglass that was originally adopted from the boat-building industry and gradually evolved to more sophisticated glass fibre reinforced polymers (GFRP). Further advances to wind turbine composites included the use of higher quality fibres in carbon fibre reinforced polymers (CFRP). Both GFRP and CFRP versions of composites dominate today's turbine blade industry thanks to superior stiffness to weight ratios. The selection of fibre is often a trade off between performance and the manufacturing cost.

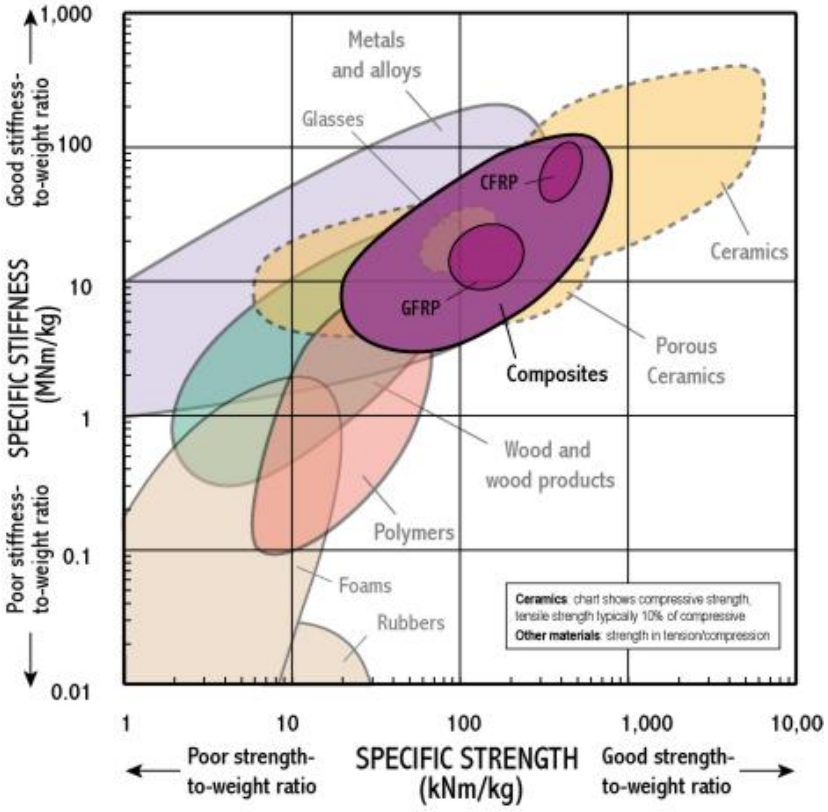

Figure 2.2: Specific stiffness vs. specific strength of various Materials [5].

Along with the advancement in blade materials and technology since the 1980, there has also been considerable progression in the sizes of wind turbine rotors and subsequently the blades involved. The trend in increased turbine diameter is primarily driven by the desire to exploit sites with a high wind resource and thus capture as much

energy from the wind field as possible. This can be achieved by building turbines with longer blades, as demonstrated by the following established equation

$$P_{wind} = \frac{1}{2}\rho A v^3. \tag{2.1}$$

Where ρ = air density, A = cross sectional area of the rotor disc (which relates to the rotor diameter) and v = wind velocity [51].

2.1.2 Blade Design Considerations

The design of discrete wind turbine components is difficult to attain in isolation, as certain design decisions in one area can impact on those in another. The various design options all have associated advantages and disadvantages and these all have to be weighed up by the manufacturer. However, in order for the design process to progress, certain variables will have to be initially chosen. The majority of these will be informed by the blades that make up the rotor composition.

Through interaction with the wind field, the wind turbine rotor extracts kinetic energy for conversion into electrical energy. In order to extract as much energy as possible, the design of the rotor is chiefly driven by the aerodynamic influences and will be key to determining the shape of the blade. Blade length will inform the total 'swept area' of the rotor and hence the quantity of air that can be used to capture energy from the wind. The blade's aerodynamic profile, planform shape, aerofoil thickness and twist angle are all important attributes of individual blade construction and will also play a crucial role in optimising energy acquisition.

There are other important factors involved in the overall blade design that result in a trade-off in aerodynamic performance. One major consideration is the structural attributes of the design. It is vital for a wind turbine blade to be able to handle the structural loads connected with its operation. For example, the bending moment on the blade, due to the wind load, increases towards the root of the blade and as such the thickness at the root is typically designed to be greater. The consequences of rotational sampling of the wind field are manifested through a variety of structural modes, felt not just in the blades but most notably in the drive train and tower. There are also fatigue and extreme loads associated with the full operative life cycle of the turbine. As discussed previously, the environmental hazards that the turbine is exposed to can result in the degradation of the blade through erosion. The trade-off between aerodynamic and load considerations throughout the design process is demonstrated in Figure 2.3.

Material selection and composition will have a bearing on all these considerations, with material weight and stiffness key to decision making. Of particular concern are tip

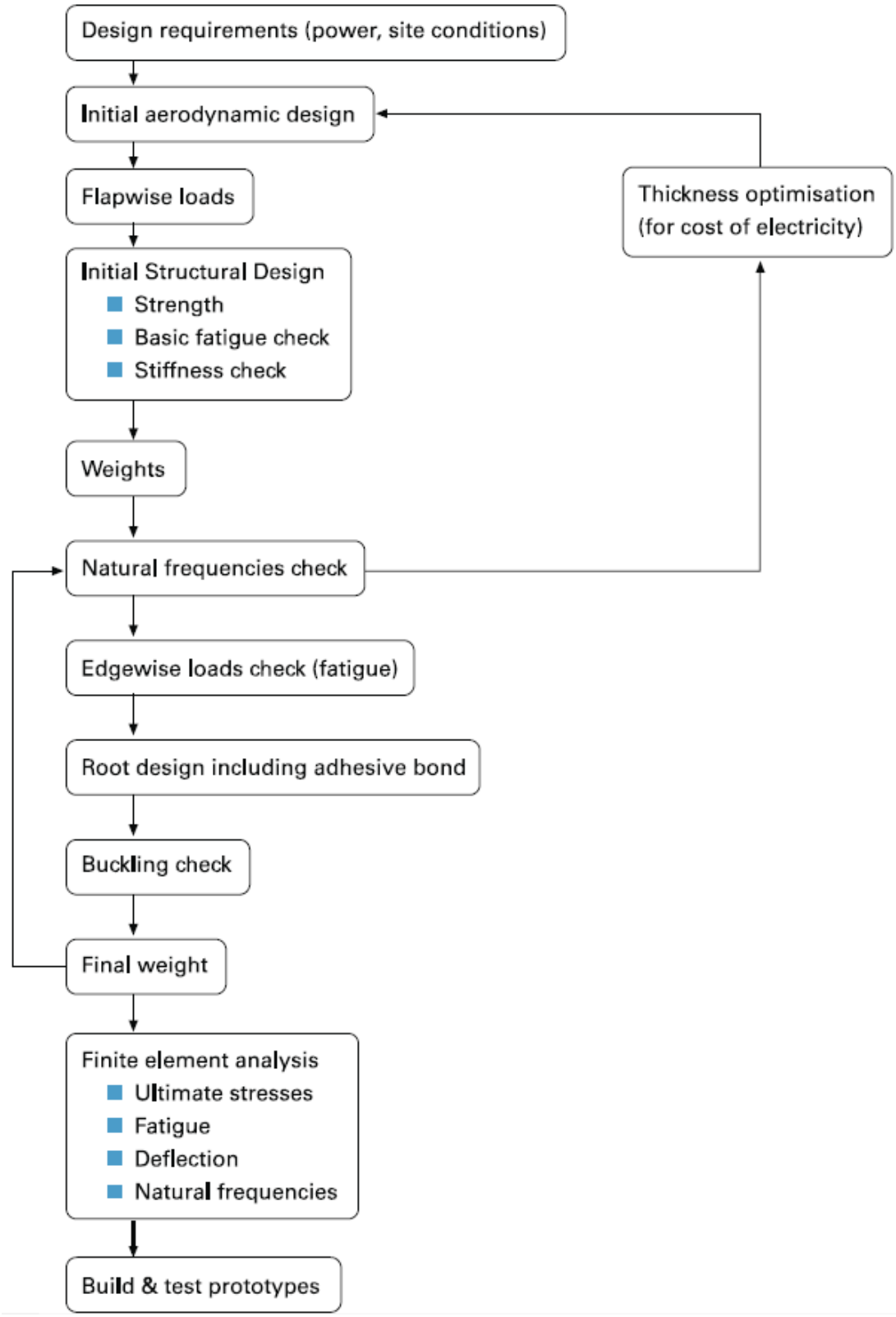

Figure 2.3: Blade structural design process [6].

deflections, due to blade flexibility that could result in blade/tower collision. They will also influence the subsequent transportation, installation and final decommissioning following the construction of the blade components.

Lastly, all these factors of blade design have to be optimised or traded-off with regards to financial cost, a vital design element to the wind turbine constructor and any future stakeholders. For instance, the economics of scale may favour turbines of larger rotor diameters but there are also implications of the square-cube law [50], whereby the mass of a blade (and therefore the cost) increases with the cube of the diameter. Overall cost is primarily accounted by the material capital costs, of which the rotor will typically contribute around 15% -22% [52, 53] depending on the model and installation. However, loss of annual energy production (and hence revenue) due to damage should be considered, along with the future maintenance costs involved in repair and what is often overlooked, decommissioning.

2.1.3 Rotor and Control Strategy Design Considerations

As the rotor is the aggregation of the number of blades in a wind turbine, many of the material design considerations will be inferred from individual blade design, which is discussed in Section 2.1.2. However, there are aspects of rotor design that can be treated holistically as they will have a significant bearing on blade design and durability.

One key aspect of wind turbine design is the operational strategy it employs and the effect that has on the rotational speed. The relationship between rotational speed and the power performance of the turbine is typically described in terms of a non-dimensional $C_p - \lambda$ curve (and similarly a $C_Q - \lambda$ for torque considerations). C_p is numerically the fraction of the total wind kinetic energy that is captured from the swept area fo the rotor. λ is defined as the ratio between the tangential speed of the tip of a blade and the actual velocity of the wind. On this curve there exists a maximum value of C_p that represents the maximum energy capture for a given tip speed ratio. However, the speed of the wind is not held constant and in fact varies stochastically. This implies differing performance characteristics depending on whether the wind turbine operates at constant or variable speed. For many years, grid-connected wind turbines were operated at a constant speed to ensure the frequency of the AC output matched that of the electrical network. Advancements in semiconductors enabled the rotor speed to vary freely through the use of a power converter, so that an optimum tip speed ratio could theoretically be continuously achieved [54]. Despite some notable drawbacks, variable-speed topologies have been widely adopted, ostensibly due to the attractiveness of increased energy capture and electrical power quality. Typically, the rotational speed experienced by the generator in the turbine is required to be of higher rpm than that

of the rotor and is accomplished through the use a gearbox. A recent development in drive-train topologies is to remove the dependency on a gearbox completely and instead install a larger, permanent magnet, multi-pole generator to form a "direct-drive" wind turbine.

Regardless of the applied configuration, a turbine will typically have a nominal rotational speed that the rotor - and through extension the generator - will adhere to in the "above-rated" wind speed operational regime. The choice of nominal speed that a turbine experiences is a major factor, not just in terms of performance but also in cost. If the rotor radius and power rating have already been determined the rotor torque will be informed by the reciprocal of the rotational speed. The adoption of a high rotational speed would appear to help decrease the drive-train cost and thus that of the supporting structures. However, such an increase has a detrimental effect on the blade out-of-plane fatigue loads [42]. Therefore, a trade-off has to be made between increasing the costs of the rotor or that of the drive-train, nacelle and tower.

Another operational feature is the method used for limiting the power produced to a machine's specific power rating. This is achieved by active and passive variants of stall or pitch control. Passive power control usually takes the simple form of a fixed-blade pitch, such that the resulting reduction in lift coefficient and increase in drag coefficient from post-stall places a ceiling on turbine generation at a desired wind speed. Passive pitch can also achieved by allowing the blades and/or the hub to twist under large wind loads, reducing the angle of attack and hence the lift coefficient and power production. This is less common in grid-connected turbines. Active versions require actuators, bearings for individual or collective pitch regulation. As a consequence, these control approaches are accompanied by additional power consumption, maintenance demands and costs. 'Active-pitch' is by far the most prevalent in modern turbines, once again due to the appeal of increased energy capture. A blade can be pitched to reduce the angle of attack - a process known as blade feathering. Pitching the blade in the other direction ('to stall') is also an option but the unpredictability of aerodynamic behaviour in stall is a major concern.

Although not a key performance or financial motivation, the motion of blades through the air provides an aerodynamic source of noise and can be undesirable depending on the installation site. If necessary, the performance of the turbine may have to sacrificed in order to mitigate such noise.

2.1.4 Contemporary Blade Structure

The typical horizontal-axis wind turbine blade has a fairly standardised structure, mainly comprised of composite materials. In order to cope with the bending moments

caused by the lift force, a blade is designed to be thicker at the root and thinner at the tip. Fortunately this tapering of the blade planform still supports the aerodynamic profile, both in terms of lift force production and drag force reduction. The blade is also twisted along the length to compensate for the change in apparent angle of attack due to the velocity variation along the length of the blade. The root of the blade is usually made circular for ease of connection to the rotor hub and typically separately produced and bonded to the rest of the blade, for ease of manufacturing.

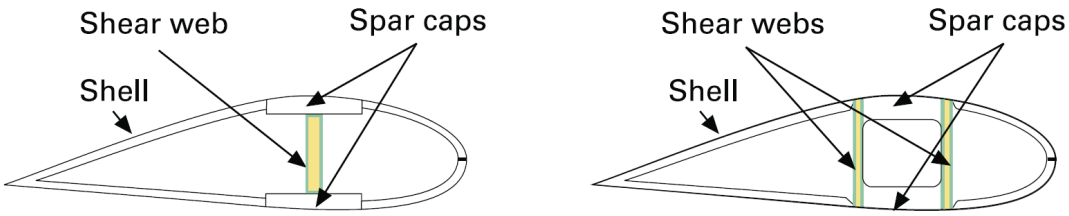

Figure 2.4: Wind turbine structural concepts: structural shell with one Shear Web (l) and box spar with shell fairings (r) [6]).

In order to reduce weight and material costs, the majority of the blade's internal section is made hollow, resulting in a shell-like structure. The blade still requires sufficient strength to cope with the forces associated with wind turbine operation. Shear strength is imperative in ensuring the upper and lower surfaces of the blade do not slide relative to each other and thus retaining the aerofoil shape and associated bending strength. This is achieved by implementing one or more shear webs between the two surfaces (or skins), connected by spar caps, to contribute to the bending strength of the blade. Spar caps consist mostly of unidirectional fibres and are built typically either as part of the shell, with the shear web(s) bonded between them; or shear webs and spar caps are built as part of a structural box to be later joined to the blade shell (see Figure 2.4). Shear webs should be constructed of diagonal fibres to provide shear stiffness. The stiffness requirements of the blade shell are important for maintaining aerodynamic shape and buckling resistance. With weight reduction again a key motivation, shell thickness is provided by a 'sandwich' of a low density core between the composite skins.

2.2 Wind Turbine Blade Material Technology and Manufacturing

The manufacturing process has become paramount with the increasing scale and complexity of blade design. There is also a motivation to streamline and reduce the cost of the process, without sacrificing the performance of the blades. Composites have been the material of choice for wind turbine blade construction for several decades, partly due to their superior fatigue performance compared to other materials. Similarly the aviation industry has shown increasing adoption of composite materials in aircraft structures. Although the practical application of wind turbines and aircraft are dissimilar, the concerns of loading and climatic conditions are shared [55, 56] and will be discussed in future sections. Although wind turbine manufacturers are keen not to disclose the exact specifications of wind turbine blades, details on the manufacturing process can be obtained through providers of material solutions e.g. Gurit [6].

2.2.1 Polymer Matrix Composites

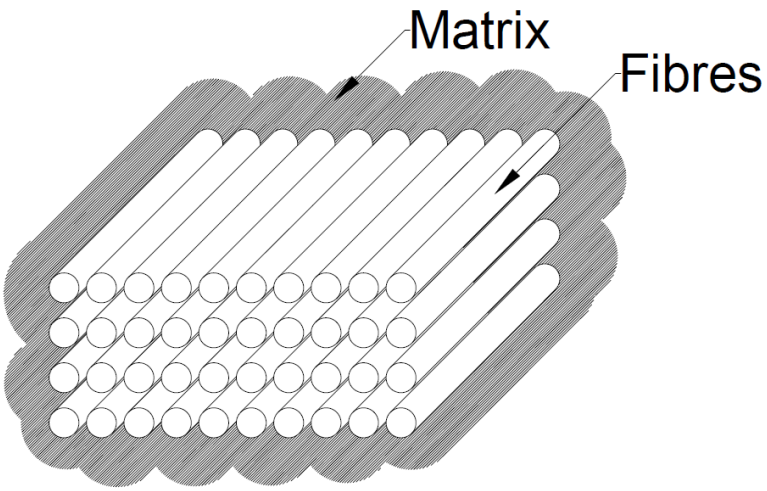

Figure 2.5: Composite material comprising of unidirectional fibres aligned within a matrix.

A composite is defined as a structural material that consists of two or more constituents that are combined at a macroscopic level and are not soluble in each other. These constituents are defined as either a *reinforcing phase* or a *matrix phase*. Composites are customarily classified by the geometry of the reinforcement or by the type of matrix. For the case of wind turbines, polymer matrix composites (PMCs) are the most

commonly used, where reinforcements take the form of small diameter fibres combined with a polymer matrix (typically a resin). Composite fibre selection is a key issue, as the choice will directly influence the mechanical performance of composites, which are required to have high elastic moduli and strength. Factors such as length, shape, diameter and orientation of fibre are also highly influential in the performance of the composite. Conventional fibres for wind turbines are confined to mainly traditional glass-fibre (GFRP) or carbon-fibre (CFRP). Carbon offers a greater specific stiffness and strength than glass-fibre but suffers from a more stringent and sensitive manufacturing process, accompanied by a higher cost. These issues of contention become more apparent with increasing blade length. Carbon "nanofibres" also offer an attractive prospect as they can reinforce polymer resins at low mass percentages but concerns have been raised regarding their energy-intensive production methods [57].

The properties of the composite are greatly informed by the direction in which the reinforcing fibres are orientated. Often, unidirectional fibres are arranged within a matrix that result in a single flat ply or lamina. These can be stacked in various orientations and consist of different material types. The maximum stiffness and strength of the lamina will be found in the direction parallel to fibres and so these should be positioned with respect to the loading axis. Fibres can also arranged in multiple directions, to suit situations of complex loading and reduce the directional load sensitivity of the material. This is achieved by either layering the fibres on top of one another or assembling them in a fabric weave. A range of configurations are possible but biaxial and triaxial are more commonly exploited. Another alternative is to randomly orientate and distribute the fibre, such as in chopped strand mat (or "veils"), allowing close to isotropic material behaviour. The composite will exhibit greater strength and stiffness in the in-plane direction at the expense of reduced performance in the out-of-plane direction.

The task of the matrix/resin is to bind the fibres together, distributing the load whilst simultaneously protecting them from possible outside damage. The resin also contributes somewhat to the mechanical properties, providing transverse and shear modulus and strength. Composite resins used for blade construction are highly represented by thermosetting variants, due to their low viscosity and temperature requirements for curing. Epoxy, polyester and vinyl-ester are the most commonly used resins, with epoxy currently the most popular due to increased tensile and flexural strength characteristics. Thermoplastic processes are more complex and have been largely overlooked as a result. However, their ability to reshape upon melting could lead to recycling advantages in the decommissioning phase.

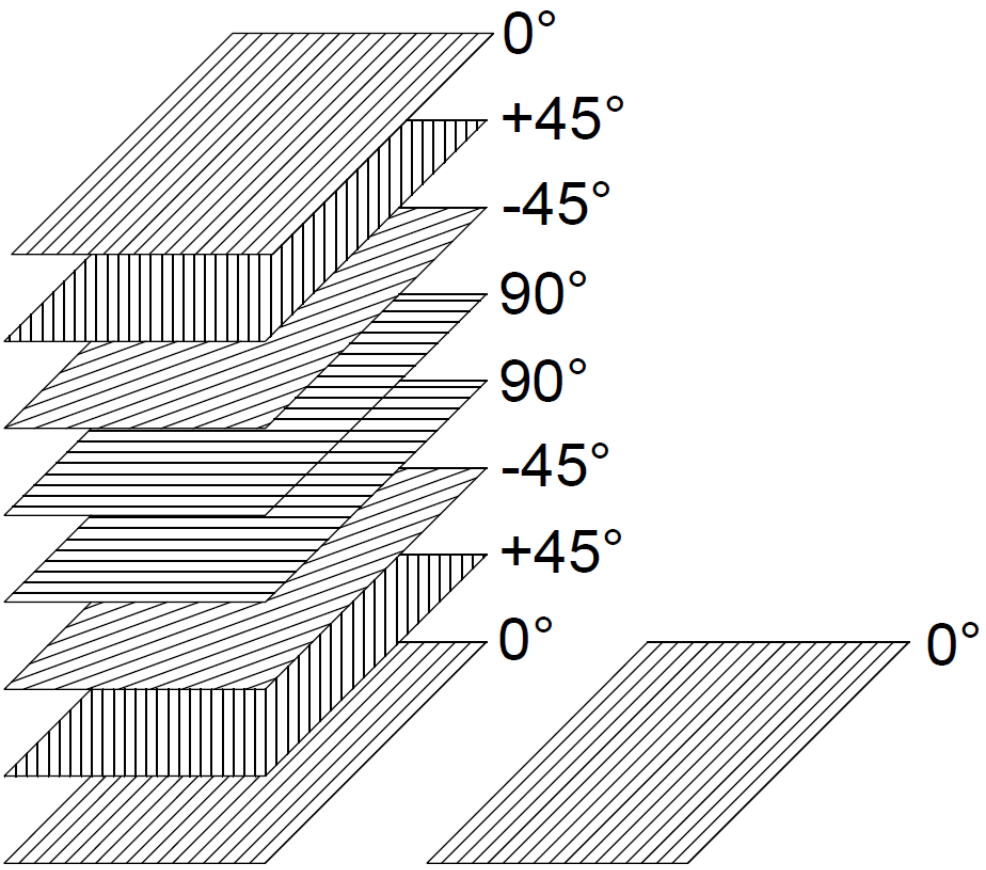

Figure 2.6: Stacking of plies of different fibre orientations to form a laminate.

2.2.2 Manufacturing Processes

The overall composition of the blade and associated bill of materials depends largely on the manufacturing process employed. The two most common approaches are infusion and pre-impregnation ("prepreg"). Wet lamination - where the bonding agent is still in a liquid state when the webs are joined together - is also an option but the ever increasing sizes of blades, coupled with health and safety requirements make it a less attractive option. Although either of the main manufacturing methods can be utilised for the two common structural designs described in Figure 2.4, prepreg is almost entirely used for construction of the box spar, as the load bearing laminate needs to precisely aligned and ideally free from air.

Infusion represents a closed mould manufacturing process with the general objective to allow the resin to permeate the fabric through suction. This is achieved under heat and vacuum, reducing the pressure at one end of the fabric which forces the resin through the fibres. It is by no means a straightforward or predictable process, with one of the major challenges being the complete and sufficient wetting of all the fibres. With timing being crucial to the process, hardeners are typically used to catalyse the change of state of the matrix from a liquid to a solid. Following infusion the laminate is allowed to cure. Heat is often applied with a slow ramp rate, to reduce the duration of the process but so as not to exceed the thermal resistance of the resin and distort the material. Mould utilisation and cycle time are key factors for reducing cost and increasing productivity. The speed at which a fabric stack can be infused and the distance the resin can travel are dependent on: viscosity of the resin, the permeability of the fabric and the pressure gradient acting on the infused resin. A low resin viscosity is desirable and this is determined by the chemical composition. Viscosity can be decreased further by increasing the temperature of the resin and it may seem beneficial to use a heated resin. However, care must be taken to not accelerate the start of the curing procedure. The permeability is in turn affected by the diameter and sizing of the fibre, in addition to the fabric material selection. The pressure gradient is limited by the atmospheric pressure of the surroundings and the capacity of the vacuum pump employed.

Prepregs are pre-manufactured layers of fibres that have been pre-impregnated with resin. They can be assembled in various orientations to form a composite structure. Typically the resins involved are of higher viscosities, so that the prepregs are semi-solid at room temperatures and have to stored in colder environments to prevent premature curing. Once arranged in a wind turbine blade mould, final curing takes place under vacuum at higher temperatures than that of infusion. For ease of transportation and assembly, the prepregs are often supplied in a roll format. Hand lay-up is often exercised

but the advantages of automated gantry delivery are clear for increased productivity and reliability.

The selection of either infusion or prepreg once again comes down to a cost versus performance debate. Infusion is perceived to be a cheaper manufacturing process due to the overall lower cost of the materials. Prepreg lay-ups are thought to experience higher manufacturing costs due to the requirement for high-cost materials, higher temperature tooling, as well as demanding environmental control and storage constraints. However, where there is a motivation to improve the automation of the process, prepreg may be more advantageous. The method can be theoretically repeatable without sacrificing process reliability and carbon utilisation. When considering performance aspects, using prepreg can result in the production of a lighter blade. This advantage will become even more apparent with the design of blades of greater length.

Regardless of the method employed, there are several key challenges associated with the manufacturing of wind turbine blades that are being addressed to help improve the overall wind turbine cost of energy. Cure cycle times and material depositions are areas that are targeted for increased productivity. There are also a number of different manufacturing defects that can be detrimental to the lifetime of a wind turbine once it has been deployed. These can include:

- wrinkles,
- de-laminations,
- dry-spots,
- under cure,
- fibre misalignment and
- sandwich core-skin de-bonding.

2.2.3 Sandwich Core

As mentioned previously, a low density core is often used to increase the thickness of a blade material panel without drastically adding to the weight. Such a feature is typically composed of two composite skins separated by the core material that results in a sandwich like structure. The core has been compared to the separator that is observed in a traditional 'I-beam'. For resin infusion methods, the core can be infused simultaneously with the skins of the laminate. Avoiding absorption of the resin is important and pre-sealing can help reduce this, albeit adding to the overall weight. Shear strength and stiffness are a priority for core material selection but it must also be capable of

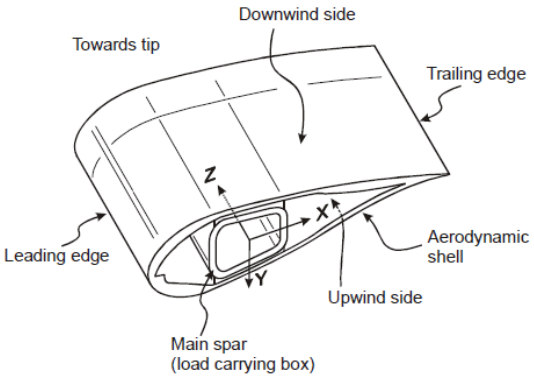

(a) Aerofoil features.

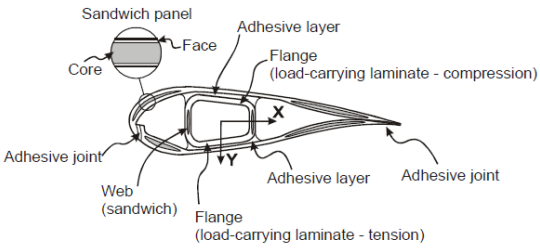

(b) Internal composition (spar box).

Figure 2.7: Wind turbine blade attributes [7].

withstanding a compressive loading without failing prematurely. Such materials can range from balsa wood to honeycombs (e.g. aluminium and thermoplastics). The most common are foam cores made from synthetic polymers. These can be supplied in a variety of densities and thicknesses.

2.2.4 Structural Adhesive

In order to bond the two aerofoil shells to each other and the structural spar, an adhesive is required. The demands placed upon adhesive bonds through cyclic loading and exposure to operational climates are considerable. For infused blades, the shear webs are first bonded to the bottom spar cap before the upper shell is lowered into position. Reheating the mould both accelerates the adhesive bonding and enables the blade to be removed from the mould. The shells are held together by both a leading and trailing edge bond. The adhesive connection between the spar cap and shear web is over laminated to assist in load transfer and strength at the joint. There are an assortment of joint designs that will perform differently under operational loading and as such the appropriate selection will be pivotal. The loads in the adhesive for box-spar configurations associated with prepreg blades are less severe and the bonding process is overall less complex than the shear web design.

A significant modern development to the infusion process is the advent of Siemens' patented Integral Blade technology [58]. A special moulding arrangement, with a closed outer mould and an expanding inner mould, allows for a single-piece blade to be produced without the need for adhesively bonded joints.

2.2.5 Surface Coatings and Protections

One of the final steps before the blade is complete is to apply a surface coating to protect the composite shells from the environmental threats that a wind turbine may be exposed to. The primary objective of the coating is to act as a boundary to the outside elements. Moisture ingress is a major concern, as this can cause deterioration of the matrix resin. In colder climates the water can also freeze and provoke cracking of the composite through expansion, resulting in the eventual failure of the composite. The degradation of the coating by ultraviolet (UV) radiation is also an important issue, as is the erosion due to various airborne particles. There are other more specific coating threats that become apparent based on the location that the wind turbine is placed. Several different coating technologies are available but the main methods are either applied in-mould as the first gelcoat layer or as flexible coatings ("paints"). that are applied after the blade has been extracted from the mould. Tapes are typically administered post-manufacture to mitigate or prevent further damage to the blade.

Similar to the shell material, both gelcoats and paints can be made from various polymer types but thermosetting matrices such as unsaturated polyester, epoxy, acrylate and polyurethane are mainly used. Selection of a softer coating may provide superior resistance to wear by absorbing hard particles but this would need to be of reasonable thickness. The thickness of the coating will have considerable implications to the resistance of the layer. However, thinner layers can offer better chemical and mechanical resistance. Thicker coatings will have a bearing on the weight of the blade, especially for longer blades. There are also enhanced UV risks compared with that of a harder surface. The selection of a particular material to minimize a particular type of damage from the environment has been suggested [59]. Adhesion of the surface layer is a concern for both types. Gelcoats should be selected to be compatible with the main laminate and painted coatings are required to sufficiently wet the applied surface. Tapes often represent a low cost and fast curing solution, especially for those turbines already in a operational capacity. Sareen *et al.* [32] recently carried out an investigation to examine how turbine blade performance would be effected by the implementation of tape. Although, there was an associated increase in drag due to the presence of the tape, it was found to be far less detrimental than if there was no protection method employed. Keegan [60] has also performed studies to computationally assess the behaviour of protection methods with respect to hailstone and rain droplet impact.

2.3 Blade Damage

The blades of a wind turbine can be damaged by factors from a multitude of sources. Design loads hold great influence, with aerodynamic, gravitational, inertial (including centrifugal and gyroscopic effects) and actuation/control loads all contributing to the loading on the turbine. The sheer size of wind turbine blades have seen the increasing influence of inertia and gravity loads over aerodynamic loads. Although not often taken into account, accidental sources of harm can cause damage. This can occur from defects and flaws in manufacturing and unintentional damage right through from transportation to installation and maintenance.

In terms of frequency of occurrence, the separate groups of *extreme loads* and *fatigue loads* are instrumental in assessing the strength and integrity of the structural design. *Extreme loads* are seen as ultimate in nature, with the potential to reach the largest permissible value that the turbine can withstand. These types of loads can be either due to very high wind speeds or machine fault states. Assuming a 20 year or more lifespan, a typical turbine is subject to $> 2^{10}$ cycles throughout its installation [42]. Individually these load cycles do not significantly contribute to material damage but over such a duration of loadings, the cumulative effect is profound. As the load magnitude and frequency is dependant on the wind characteristics at a local site, the predictability of fatigue loads becomes a particular challenge. Fatigue is now a major consideration in wind turbine design due to the lifespan of these machines and drives a considerable portion of composite design.

Similar to fatigue are the mechanisms that contribute to erosion and wear caused by environmental exposure. These are predominately experienced at the leading edge of the turbine. As discussed previously (see Section 1), wind turbines can be subject to various adverse conditions. Those that can be detrimental to the rotor blades in the form of erosion have been identified by Kjærside Storm [59] as:

- extreme temperature (from $-50\,^{\circ}\mathrm{C}$ to $70\,^{\circ}\mathrm{C}$),
- UV radiation from sunlight,
- chemical attack (from various chemicals as well as insect blood and bird droppings),
- lightning and other mechanical attack,
- ice,
- water attack,

- hailstorms,
- rain erosion,
- salinity in the air and
- wear from sand and other small particles.

Erosive wear from hailstorms will form most of the further research investigation and will be discussed later in Section 2.3.2. It is still important to understand the other detrimental sources as each one can contribute to the damage of a wind turbine blade and in most cases they cannot be treated as separate processes.

2.3.1 Damage Characteristics and Repercussions

The damage to wind turbine blades is a sensitive and contentious issue for the wind energy industry and the various stakeholders involved. Manufacturers are protective of the performance details of the materials or production practices they employ. As a result many are disinclined to publish detailed information or statistics reporting the extent of damage to wind turbine blades. There are however, examples of studies and reports that reflect upon damage characteristics and the resulting impact that has on a wind turbine.

Typical impact damage to composites is apparent from transverse cracks (or matrix cracking) and separation of plies in the form of delamination, with fibre fracture also possibility. It is quite possible for a composite structure to suffer fibre damage and massive delamination between plies, but to recover after the impact with very little evidence of the event. Barely visible impact damage (BVID) is a hidden menace and the residual strength in compression may be only 30% of the undamaged value [61]. Sorensen *et al.* [7] remarked on the several types of damage observed when a 25m wind turbine blade was tested to failure under static and cyclic loadings. Those examined in the study were categorised as follows:

- Type 1: Damage formation and growth in the adhesive layer joining skin and main spar flanges (skin/adhesive debonding and/or main spar/adhesive layer debonding);
- Type 2: Damage formation and growth in the adhesive layer joining the up- and downwind skins along leading and/or trailing edges (adhesive joint failure between skins);

- Type 3: Damage formation and growth at the interface between face and core in sandwich panels in skins and main spar web (sandwich panel face/core debonding);
- Type 4: Internal damage formation and growth in laminates in skin and/or main spar flanges, under a tensile or compression load (delamination driven by a tensional or a buckling load);
- Type 5: Splitting and fracture of separate fibres in laminates of the skin and main spar (fibre failure in tension; laminate failure in compression);
- Type 6: Buckling of the skin due to damage formation and growth in the bond between skin and main spar under compressive load (skin/adhesive debonding induced by buckling, a specific type 1 case);
- Type 7: Formation and growth of cracks in the gel-coat; debonding of the gel-coat from the skin (gel-coat cracking and gel-coat/skin debonding).

A number of these different types of damage can be viewed in Figure 2.8, which shows an example wind turbine blade that was loaded compressively. This demonstrates the wide range of distinct damage modes involved in wind turbine blades which are not mutually exclusive.

One of the key outlets for improving blade integrity management practices across the wind energy industry is the annual Blade Inspection Damage And Repair Forum [62]. As well as the main turbine figureheads, such as developers and original equipment manufacturers (OEMs), assisting repair, inspection and preventative companies are also significant contributors. From events such as these, greater insight can be gained into the issues and manifestations associated with wind turbine blade erosion and damage. The percentage breakdown of damage location and types taken from a database of 1013 blade cases can be viewed in Figures 2.9 and 2.10 respectively. Damage to the surface coatings, adhesive bonding and external portions of the blade are most apparent[1]. Erosion counts for 8% of the cases, with transverse cracks, spalling, cavities, surface cracks and fracture other more prevalent types[2].

Observations from wind farm sites have provided noticeable cases of the degradation and erosion due to environmental conditions, of which the condition of the blade can vary from limited to extremely noticeable damage. This will certainly differ from site to

[1] "Other" locations include: flange, adhesion bonding, sandwich, inner configuration, receptor block and sandwich & main belt

[2] "Other" types include: 3-D turbulator, adhesive defect, pores and cavities, receptor defect, vortex defect, trailing edge flaps, fibre reinforcement, pores, pollution, lightning protection system, corrosion, lack resin, defective drainage

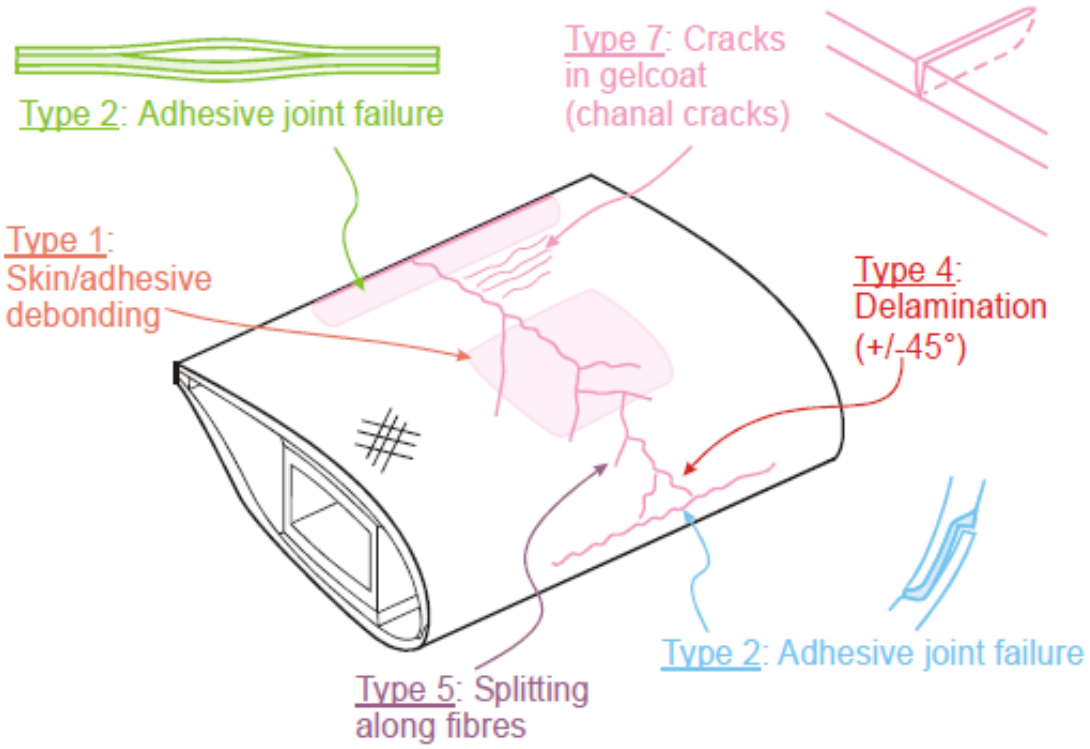

Figure 2.8: Observed damage types for a wind turbine blade subjected to a compressive load (*note "chanal" should be "channel"*) [7].

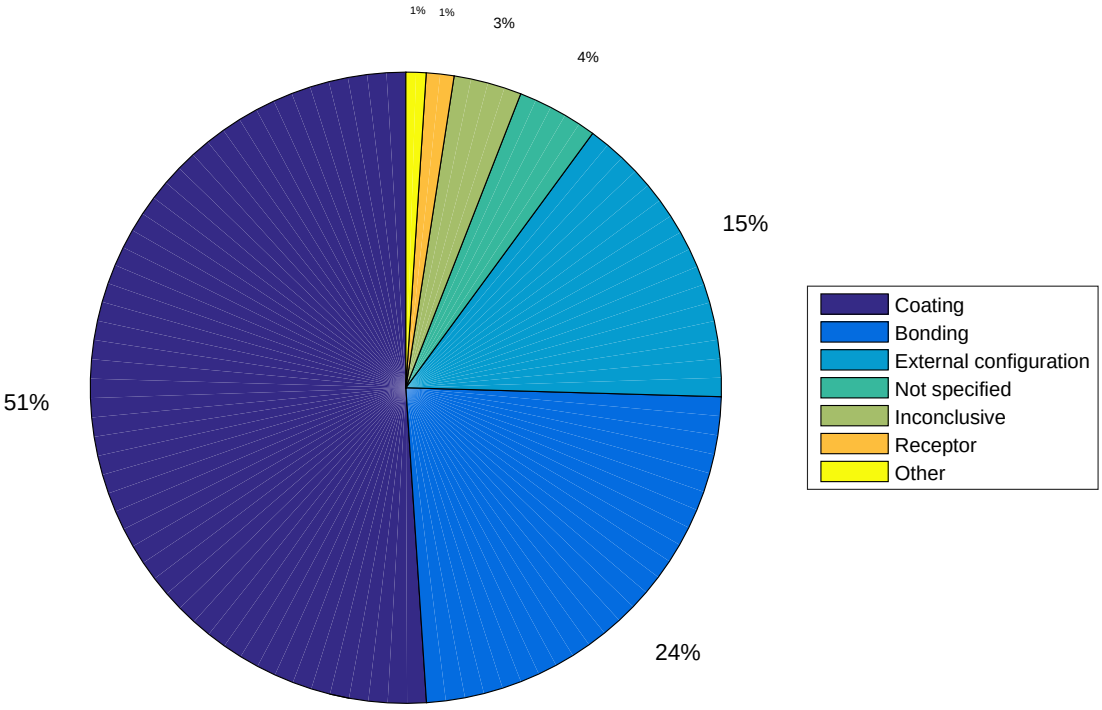

Figure 2.9: Damage footprint of a typical blade - locations [8].

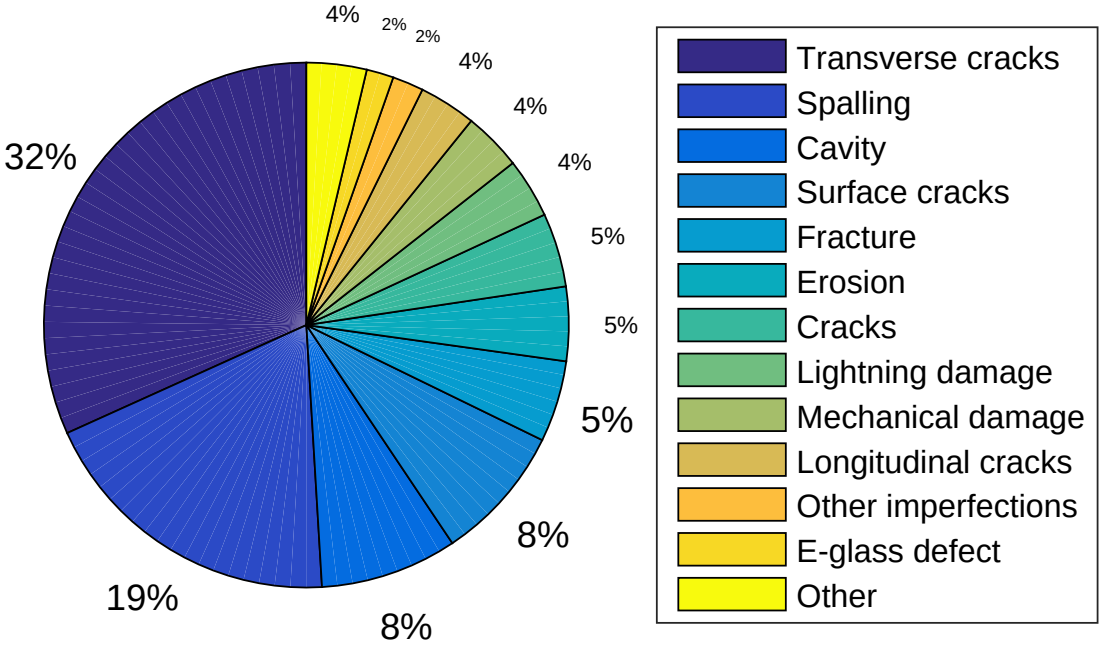

Figure 2.10: Damage footprint of a typical blade - types [8].

site and turbine to turbine. Consensus is reached on the fact that if left untreated, the condition of the blade will worsen over time. The progression of erosion damage can be clearly seen in Figure 2.11. Visual signs of erosion usually start near the leading edge in the region of the blade tip, where damage to paints and coatings are first noticed. Erosion then propagates towards the blade root and the upper and lower surfaces of the aerofoil spreading to the leading edge in the tip area until whole coatings are blasted away. Under extreme degradation exposure of the structural matrix resins and fibres is evident.

Figure 2.11: Progression of leading edge erosion. 1 - coating removal, 2 - damage of the matrix 3 - delamination and fibre damage [9].

A prominent investigation into the effect of leading edge erosion on a DU 96-W-180 wind turbine aerofoil was carried out by Sareen *et al.* [32]. Assorted degrees of damage in the form of: pits (Type A), pits and gouges (Type B) and pits, gouges and leading edge delamination (Type C) were assessed. A substantial increase in the coefficient of drag and a slight decrease in lift production was found as the aerofoil condition worsened, shown in more detail in Table 2.1. This was predominately due to the modification of the roughness characteristics and overall profile of the aerofoil. These repercussions are clearly presented to the wind turbine/farm owner by a significant decrease in annual energy production (AEP) and thus revenue.

Water ingress and absorption of moisture will also pose problems for those areas of the blade where the surface coating protecting the substrate has been removed, particularly in a marine environment. The permeated water can induce deterioration of epoxy resin matrices [6] and can potentially freeze in colder climes, causing expansion cracking and failure of the composite. If the extent of erosion and water ingress is not uniform among the wind turbine blades, the rotor could become unbalanced. This

Table 2.1: Effect of leading edge erosion on wind turbine blade performance as estimated by PROPID [32].

Condition	ΔC_d	ΔC_l	Wind speed (Average) [$\mathrm{m\,s^{-1}}$]	AEP loss [MWh/yr]	AEP loss [%]
A1	+6%	-0.07	- 7.05	- 383	- 4.85
A2	+80%	-0.12	7.93 8.81	392 392	4.10 3.49
A3	+150%	-0.15	-	-	-
B2	+150%	-0.16	- 7.05	- 902	- 11.42
B3	+200%	-0.14	7.93 8.81	930 917	9.73 8.33
B4	+400%	-0.15	-	-	-
C3	+150%	-0.16	- 7.05	- 1858	- 23.53
C4	+400%	-0.15	7.93 8.81	1948 1947	20.38 17.68
C5	+500%	-0.17	-	-	-

could have undesired ramifications in terms of vibrations and harmonics experienced by other turbine components, such as the gearbox and yaw system, reducing efficiency and provoking additional maintenance requirements. These issues will be especially realised for longer blades.

Any maintenance or mitigatory work carried out will have an associated downtime of the turbine, again reducing the annual energy production. Full blade replacement is an understandably expensive and complicated task and therefore would be favourable to avoid if possible. Maintenance work is compounded for larger offshore turbines where any undertaking will be more extensive and difficult. The window of opportunity will also be restricted by the conditions of the sea.

2.3.2 Erosion Mechanisms and Factors

Erosive wear is caused by the impact of particles of solid or liquid against the surface of an object. It can be categorised into the following forms:

- solid particle erosion or solid impingement,
- slurry erosion (hard particles carried by a liquid) and
- liquid erosion

Solid and liquid particle erosion is the most applicable for wind turbine blades, due to surrounding medium being composed of air. Similar to other wear processes,

mechanical strength does not necessarily guarantee erosive wear resistance. Erosion involves several factors that contribute to wear, with noteworthy examples including: the material properties of the particle and surface, the angle of impingement, impact velocity and particle size [10].

One of key parameters involved in erosion that will influence the rate of wear is the hardness, typically determined from a Vickers hardness test. Particles that exhibit lower hardness (H_a) than that of the surface (H_s) produce a great deal less wear than that of harder particles. By definition, conditions where $\frac{H_a}{H_s} < 2$ is often referred to as *soft abrasion* and conversely as *hard abrasion* when $\frac{H_a}{H_s} > 2$. For hard particles with solid characteristics the process will take a form similar to abrasion. Whereas if liquid particles are involved, abrasion is absent and repetitive stresses due to impact are what drives the wear on the material. According to tests carried out on three polymer resins by Kumosa *et al.* [63], neat and with glass fibres, the Vickers hardness number ranged from 13.9 Hv to 22.4 Hv. It is difficult to directly compare the hardness of hailstone ice as it varies with temperature but a field study by Giammanco and Brown [64, 65] found that the mean compressive stress to failure was typically no more than a few MPa which would translate to less than 1 Hv. Therefore we would expect soft abrasion for hailstone impact.

Another important consideration is the respective resilience of the particle and surface. Resilience is the the capacity of an elastic body in storing elastic energy [66] during loading and which is subsequently released when this loading is removed. When examining the stress/strain curve of a material, the modulus of elasticity E_r is the area underneath the elastic portion of the curve. In terms of erosion, a high resilient material tends to imply high erosion resistance [67].

The angle in impingement is defined as the angle between the eroded surface and the trajectory of the particle at the moment just before impact. These angles range from 0° to 90°. A low angle will tend to favour the process of abrasive wear, mainly because the particles will tend to continue their movement across the subjected surface. High angles will most likely result in erosive wear mechanisms. For cases where maximum erosion is experienced at low impingement angles it is assumed that the mode of ductile erosive wear is prevailing. Conversely, a brittle mode is assumed for cases of maximum erosive wear at high impingement angles.

The speed of the particle is very influential in the wear process, informing the mechanism of erosion. Figure 2.13 describes the different mechanisms of erosion for different ranges of velocity, combined with impingement angle. A threshold velocity is often evident, below which wear is of a negligible degree. If the speed is found to be very low, particle impact will cause fatigue at the material surface (a). If the

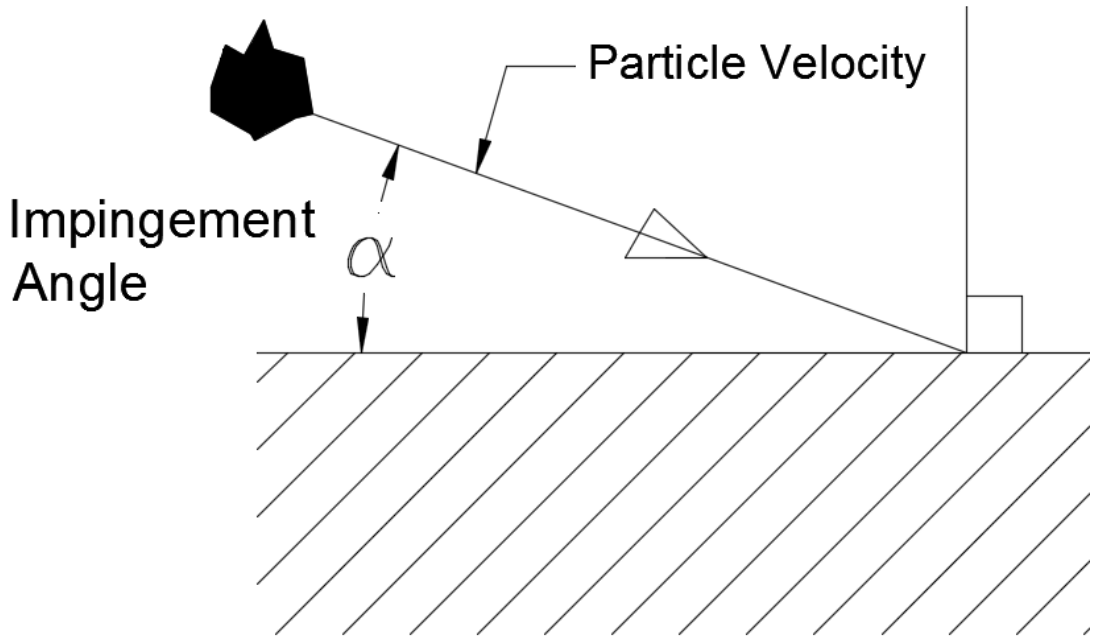

Figure 2.12: Impingement angle of Particle.

speed of the eroding particle is increased to a sufficient degree then the surface undergo either plastic or brittle deformation (b or c), depending on its inherent plasticity, with brittle wear influenced by repeated impact of this kind. For mechanisms of extreme plastic deformation, thin plates or flakes of worn material can form on the surface if the particles are blunt or spherical. Cutting or brittle fragmentation is often due to sharp particles. The damage caused by brittle materials is often manifested as subsurface cracking. In cases of extremely high speed, the impacted surface may be subject to melting (d or e). For medium to high speeds, wear rate can be determined by the following expression

$$\frac{dm}{dt} = kv^n. \tag{2.2}$$

Where: m is the mass of the worn specimen, t is the duration of the process, k is an empirical constant, v is the impact velocity and n is a velocity exponent (usually in the range of 2 and 3 for solid particles). Due to the lack of analytical data for the parameters that infer the value of 'k' (such as particle density and shape), Equation 2.2 is not extensively used. However it does highlight the importance of velocity in wear rate.

The

Particles responsible for abrasive erosive wear typically fall into dimensions of 5 µm - 500 µm but are by no means limited to this range. Variations in particle size can result in fundamental changes to the erosion mechanism and the ranking of materials in terms of their wear resistance. Solid particle erosion is typically measured in terms of mass loss but with the different forms of damage possible, visual inspection is also important. With smaller projectiles this may be carried out at a microscopic scale [68, 69].

2.4 Hail

As mentioned previously (Section 1), hail is one of the many environmental parameters considered by the IEC. In addition, providers of protection measures and repair solutions regularly include hail under an umbrella of factors that cause wind turbine blade erosion. In this section the phenomenon of hail is described, including its formation and material properties. The various examples of experimental and computational literature involving ice impact on composite materials are also discussed. The aspects of hail incidence and size in relation to wind turbine locations are only covered lightly, as they will be investigated and discussed later in Chapter.

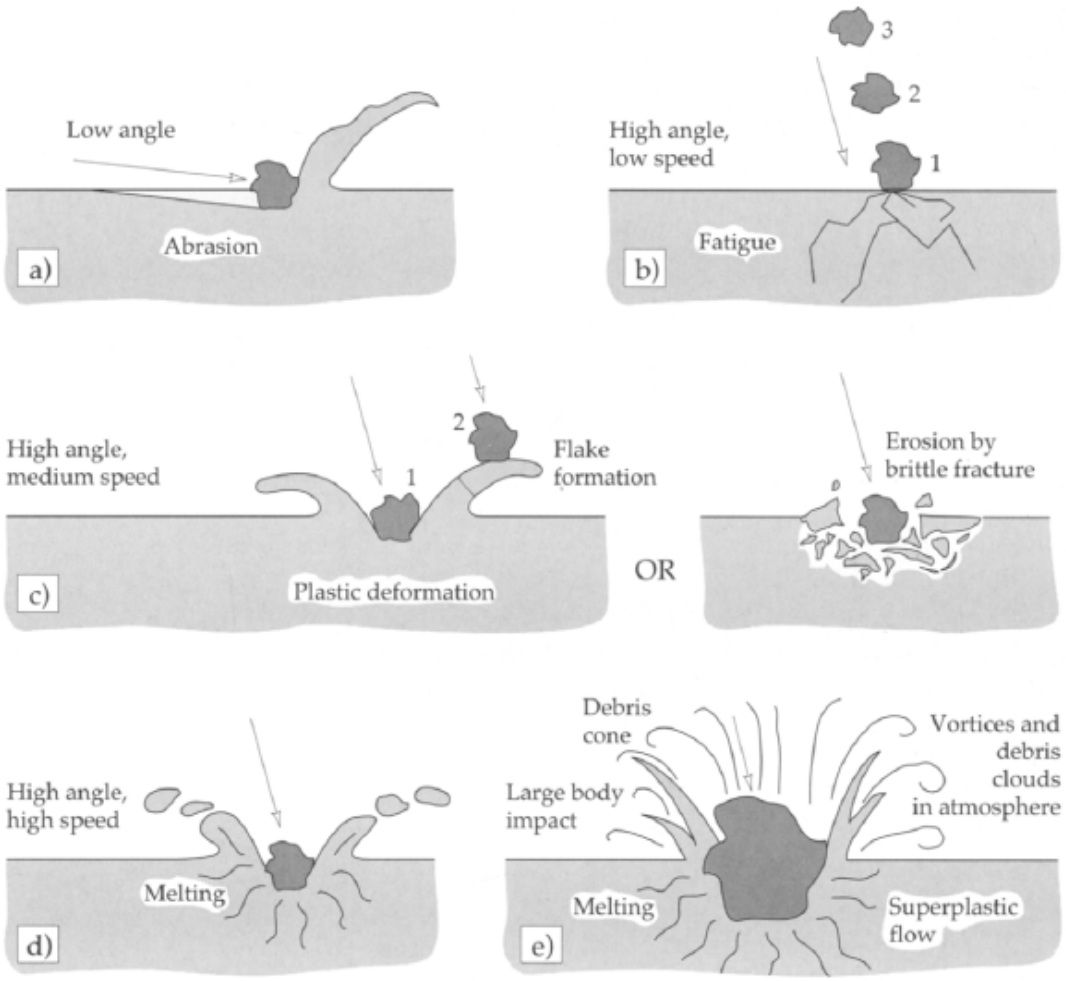

Figure 2.13: Possible mechanisms of erosion; abrasion at low impact angles; b) surface fatigue during low speed, high impingement angle, c) brittle fracture or multiple plastic deformation during medium speed, larger impingement angle impact, d) surface melting at high impact speeds and e)macroscopic erosion with secondary effects [10].

2.4.1 Hail Formation

The general classification of "hail" covers a range of different categories. The major types of ice particles that fall under this banner include graupel, small hail, ice pellets and hailstones. Also considered by the World Meteorological Organisation in the classification of a "hail day" are snow grains and diamond dust [70].

The hail formation process takes place inside clouds containing regions of temperature below 0° and supercooled water droplets that originate from condensation and updrafts. Hail growth stems from the accretion and freezing of these droplets onto cloud condensation nuclei, which are typically of the order of $0.1 - 1\mu m$ in diameter. Other small media such as dust and salt can also serve as hailstone embryos. The different types and sizes of precipitation that fall to the earth is dependent on the state of progression through the different stages of development the hail is before the cloud can no longer provide support [11]. The evolution of hail can be seen in Figure 2.14.

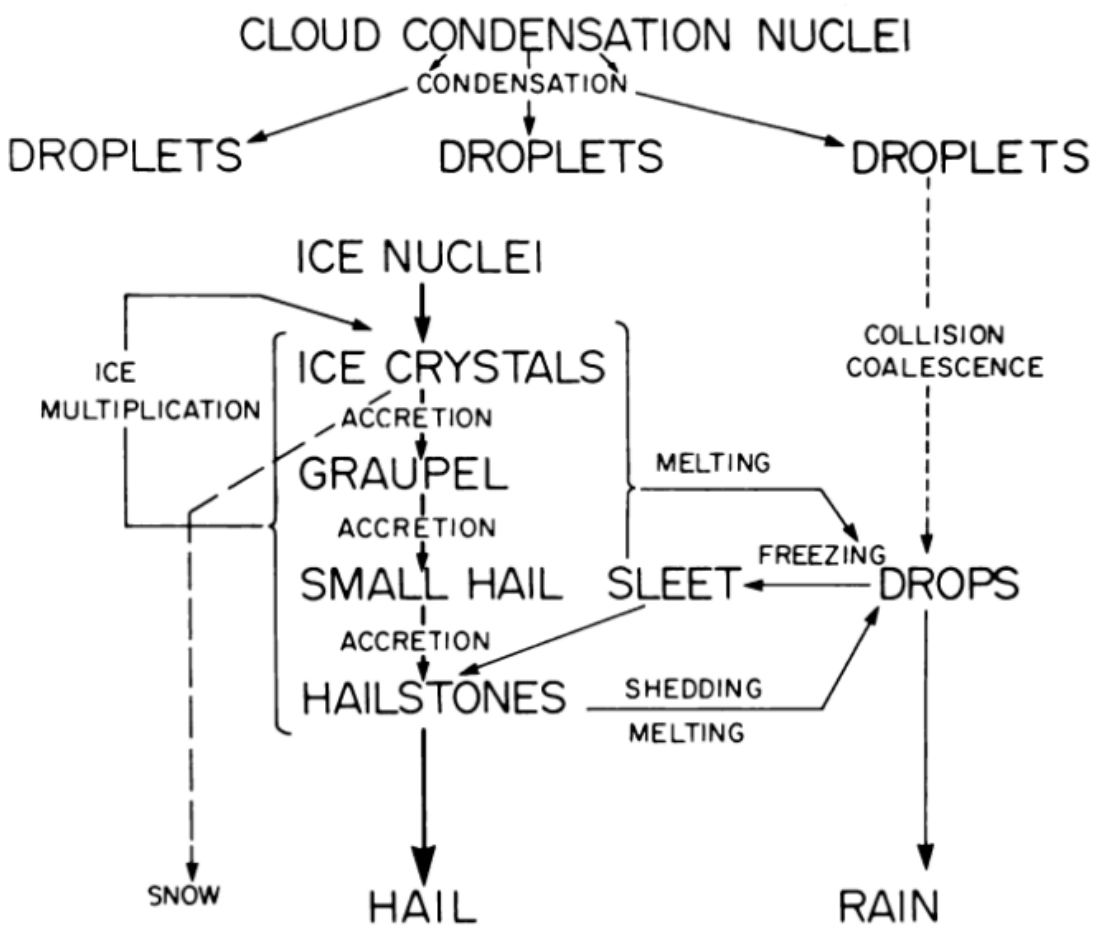

Figure 2.14: Major growth stages of hail in a cloud of supercooled droplets [11].

Various ice nucleation mechanisms are recognised that lead to the growth of ice crystals from this nucleus state but all involve the deposition of water at the expense of omnipresent cloud droplets. Once the diameter of these ice crystals reaches $0.3 - 1$mm or more, the fall velocity allows the collision with and subsequent collection of quasi-stationary cloud droplets. These droplets freeze very quickly, marking the initiation of graupel formation.

Graupel are white, opaque, conical pellets (but sometimes take on a irregular, round dentritic structure) with a rimed exterior and diameters up to 5 mm. It is often referred to as soft hail and incorrectly as snow pellets, with the key distinction being the incorporation of ice crystals in the composition.

As the particle size and thus fall velocity is increased, the graupel is exposed to warmer parts of the cloud. In these regions, the accumulation of droplets increases and the freezing process becomes slower. Droplets are allowed to travel through the air capillaries of the graupel, increasing the density of the particle. Semi-transparent and rounded particles released at this transitory stage would be classed as small hail. Hail defined as small is differentiated from graupel by their greater densities and slightly glazed appearance.

Once the densification stage is complete, volumetric growth is re-established that takes the form of a hailstone. Hailstones are distinguished from small hail by possessing diameters greater than 5 mm. There are two main routes to the formation of hailstones. One, defined as "wet growth", occurs when latent heat is released faster than it can be diffused away from the particle. Liquid water will then exist on the surface, allowing air to escape and ice to build up without the inclusion of many air bubbles. "Dry growth", on the other hand, is the result of the growing particle losing heat to the atmosphere faster through diffusion. Latent heat is then released from the droplet, freezing the surface. The layers that build up will contain many air bubbles. The alternation of different growth modes can give rise to a layered shell structure. A range of unusual hailstone shapes have been observed but will usually take roughly spherical or conical forms.

Ice pellets are manifested by the freezing of raindrops or refreezing of partially melted snowflakes. Diameters are less than 5 mm and densities fall just below $1\,\mathrm{gcm}^{-3}$, indicating a high water content. In Figure 2.14, hard ice pellets are labelled sleet but in Commonwealth countries sleet refers to a snow that partially melts as it falls.

Classifying the density of hail is a complicated issue due to the range of forms throughout the different methods of growth, of which a translational densification process is a key stage. As a result of trapped air within layers, the density of hailstones is typically less than pure ice ($0.917\,\mathrm{gcm}^{-3}$). From measurements taken from an early

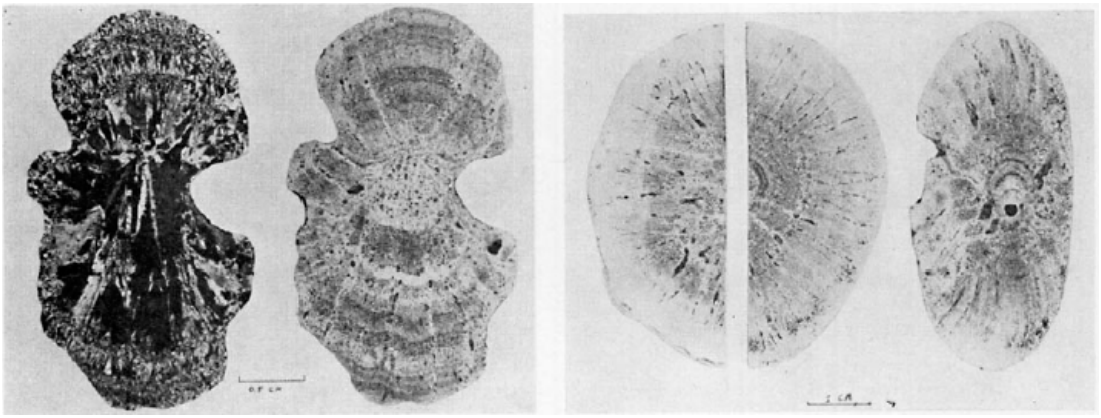

Figure 2.15: Cross-sections of hailstones [12].

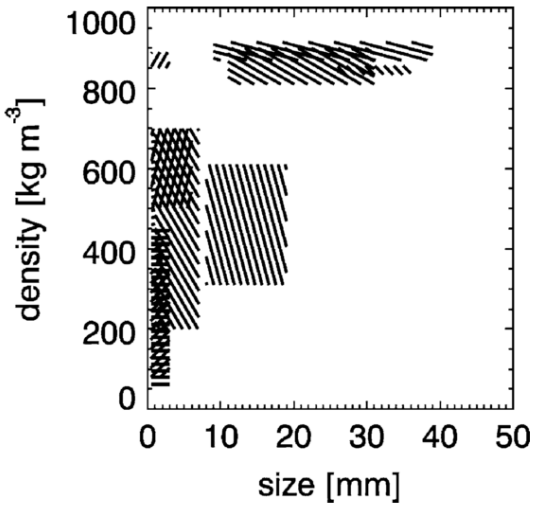

Figure 2.16: Experimentally determined densities for graupel and hail [13].

spring hailstorm in Colorado, Knight *et al.* [71] found particularly low hailstone densities ranging from 0.31 to 0.61 gcm^{-3} for equivalent spherical diameters of 0.63 to 1.54 cm. Many bulk parametrisation schemes have been proposed for density [72–74], described along with terminal velocity and temperature, which are often valid only for certain ranges. Worst case densities (i.e. larger) are usually assumed for safety applications and analysis. It is suggested that the growth rate of a hailstone can be expressed as a combination of "wet growth" and "dry growth" to form the overall growth relationship, described in Equation 2.3 [75]

$$\frac{dD}{dt} = \frac{C_e f f V_t r_l \rho_a}{2\rho_w} \tag{2.3}$$

where: ρ_a and ρ_w are the respective densities of air and water, V_t is the vertical speed of the hailstone with respect to the air, r_l is the liquid water mixing ratio and C_{eff} is the efficiency of the accretion (which usually lies between 0 and 1).

The length of time that a hailstone can spend elevated in a convective cloud will have considerable bearing on the eventual size and form that hail will obtain before descending to the ground. Larger hailstones are plausible in storms with:

- large updraft speeds and wide updraft areas,
- high liquid water content above the freezing level and
- long lifetime [76].

Large updraft speeds can be found in storms that develop in environments of large convective available potential energy or in supercell storms. Strong wind shear is a considerable influence in both supercell occurrence and storm duration. Additionally, when the dew points and mixing ratios of air entering a storm from low altitudes are high, greater liquid water content above the freezing level can also be expected.

2.4.2 Hailfall

As discussed in the previous section, there is a requirement for the temperature in the upper atmosphere to be sufficiently low to develop ice formation but warm enough on the surface in order to encourage thunderstorm development. These climactic stipulations mean that in many places a severe hailstorm is a singular and memorable event. There are however, several regions across the world where hail is a much more frequent occurrence, particularly in mid-latitudes during spring and summer. In the northern hemisphere, the two largest contiguous areas are located in the upper Great Plains of North America and over parts of the USSR and Europe, as described in Figure 2.17.

There is a significant localised prevalence over the mountain landforms of Asia. In the southern hemisphere high profile areas include the western coastal regions of South America and north-eastern South Africa. Towards the poles, hail frequency is less common [11].

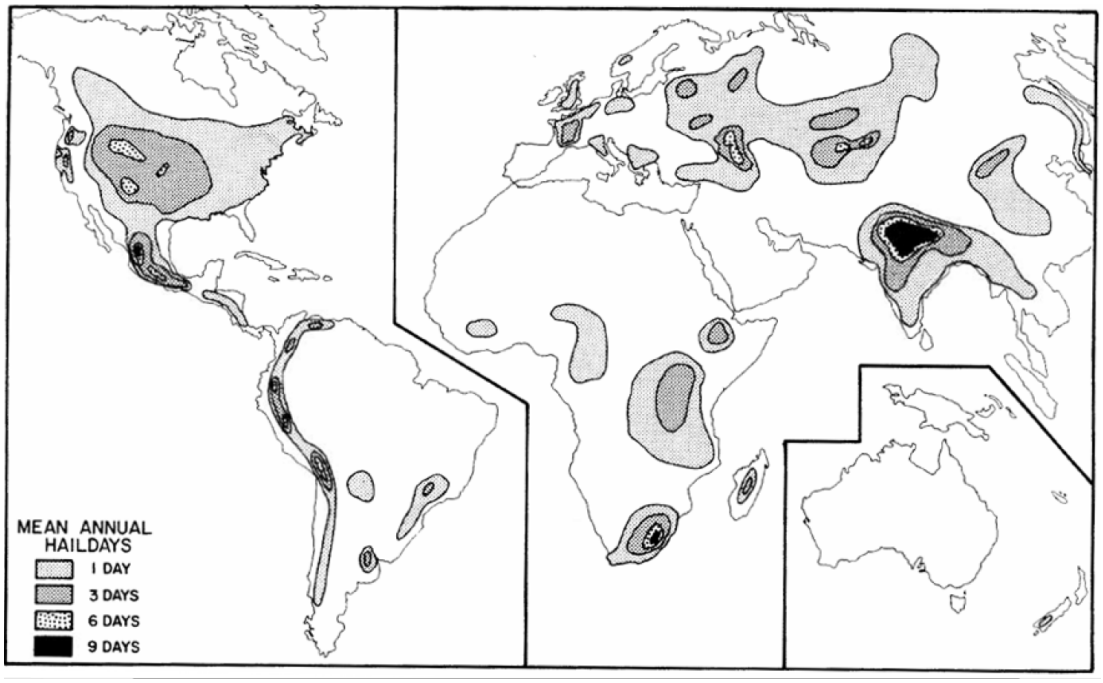

Figure 2.17: Global map of hail days experienced annually [13].

Hail is thought to be much more common along and near mountain ranges because mountains force horizontal winds upwards (through a process known as orographic lifting), thereby intensifying the updraughts within thunderstorms and making hail more likely. Records of large and frequent hail in mountainous regions, such as in the North West of China can also be found in the literature [77]. The documentation of instances of hail occurrences offshore is sparse, mainly due to the lack of observation stations located in marine and oceanic settings. Notable exceptions include an 1895 article by Harries [78] and an extensive summation of accounts regarding Hail Incidence in the Tropics by Frisby and Sansom [79], whereby the consistent topography of the sea compared to mountainous regions would lend itself to less severe and frequent hail.

Similar to the frequency, the size distribution of hailstones will vary depending on the country or region of assessment. Durations of hailstorms will be different if discussed in either a continuous or non-continuous sense. Hail often comes in short, intense bursts with intervening lulls or even gaps. In Canada continuous hail was found to last from a few seconds up to an hour [11]. Longer total durations were more likely

to be interrupted. To assess the intensity of hailstones, a scale was introduced by the Tornado and Storm Research Organisation in 1986 based on diameter ranges. A minor revised version has been used since 2005 and can be seen in Table 2.2.

Table 2.2: Revised TORRO international hailstorm intensity scale [33].

Scale	Intensity Category	Typical Hail Diameter [mm][3]	Probable Kinetic Energy [$J\,m^{-2}$]	Typical Damage
H0	True (hard) Hail	5 - **9**	0 - 20	No noticeable damage.
H1	Potentially Damaging	10 - **15**	> 20	Slight general damage to plants, crops.
H2	Significant	16 - **20**	> 100	Significant damage to fruit, crops, vegetation.
H3	Severe	21 - **30**	> 300	Severe damage to fruit and crops, damage to glass and plastic structures, paint and wood scored.
H4	Severe	31 - **40**	> 500	Widespread glass damage, vehicle bodywork damage.
H5	Destructive	41 - **50**	> 800	Wholesale destruction of glass, damage to tiled roofs, significant risk of injuries.
H6	Destructive	51 - **60**		Bodywork of grounded aircraft dented, brick walls pitted.
H7	Destructive	61 - **75**		Severe roof damage, risk of serious injuries.
H8	Destructive	76 - **90**		Severe damage to aircraft bodywork (Severest recorded in the British Isles).
H9	Super Hailstorms	91 - **110**		Extensive structural damage, risk of severe or even fatal injuries to persons caught in the open.
H10	Super Hailstorms	> 110		Extensive structural damage, risk of severe or even fatal injuries to persons caught in the open.

Due to the complex nature of the thunderstorms and supercells that harbour hailstones, hailfall will not be the only form of precipitation or weather associated with a hailstorm. Hail-producing storms are known to produce rain as well as lightning. In

[3] Approximate range (typical maximum size in bold), since other factors (e.g. number and density of hailstones, hail fall speed and surface wind speeds) affect severity. For non-spheroidal hailstones, the diameter refers to the mean of the co-ordinates

terms of mass output, hail is a very minor product of a hailstorm. The different forms of hail will also not be mutually exclusive during this period. Often bulk characteristics are applied to the range of sizes and densities produced during hailfall. Figure 2.18 shows a radar scan of intense hail storm that occured on the afternoon of July the 10th 1995 at Chilbolton Observatory, with the first view illustrating the strength of echoes and the second, the polarisation properties of these echoes.

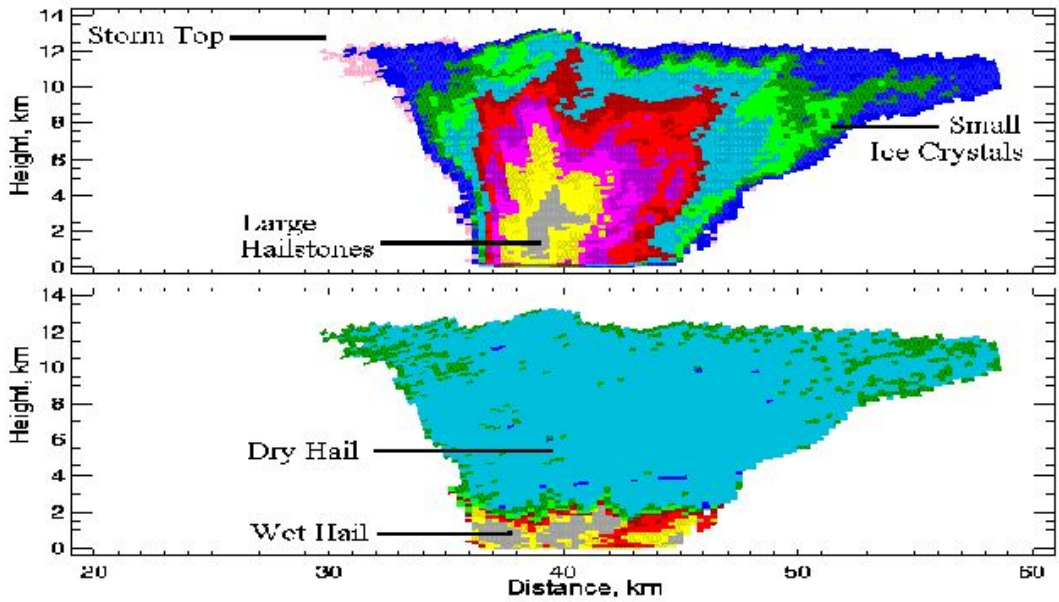

Figure 2.18: Radar scan through a hail storm [14].

The characteristics of hailfall patterns and motions of storms are key to the eventual subjected area that will be effected by hail. As a single hailstorm moves along, the hail produced on the ground can be correlated spatial and temporally into a path, otherwise known as a "hailswath". In some prevalent parts of the world these swaths can stretch as long as several hundred kilometres, with widths up to 10 kilometres. The patchiness and subareas of hailfall are described further by continuous "hailstreaks" and hail cores/hail spikes that are smaller in length and width. On a large or national scale coherence can also be observed. Hail does not always fall with strong winds but the wind will greatly inform the angle of incidence of the blades, as well as the operational parameters of wind turbines.

2.4.3 Sensing/Forecasting

As demonstrated by the TORRO hail intensity scale 2.2, the threat of hail is not just an issue for wind turbines but also for crops and other infrastructure. These concerns have driven research into the detection and prediction of hail, not just in terms of probability but also in terms of size and characteristics. The prediction of hail precipitation is a difficult task as impacts on the ground do not spread over a wide area and irregular space-time evolution of a hailstorm.

A common device for obtaining data on the size and mass of hailstones is the hailpad. This usually consists of a plastic foam panel covered by aluminium foil or white latex paint and set in a frame that is hammered into the ground. Any hail that impinges on the panel leaves an imprint and the dimensions of the dent will infer the size and mass of the hailstone. The number of dents will inform the frequency. A number of hailpad networks have been set up and are operating continuously in different countries [80]. There will obviously be a location bias related to the distribution of the hailpad network. Hailpads only provide information on hail that has already happened but can also used in the calibration or validation of prediction approaches.

Forecasting methods often take the form of Numerical Weather Prediction (NWP) models, which use complex computer programs to simulate the atmosphere. Due to the level of computational capacity required, the models do not lend themselves to short-term prediction and other methods have also been developed. Some of the difficulty lies in distinguishing storm cells that produce hail from those only generating liquid precipitation.

Sánchez *et al.* utilised radar to determine the kinetic energy of hail, paying particular attention to hail of TORRO Scale H1 and greater [81]. The model found great uncertainty using C-band radar, whereas the S-Band radar performed a lot better, with the Probability of Detection (POD) of 85.7%, a False Alarm Ratio (FAR) of 14.3% and an explained variance of 61.2%. Due to high operating costs and coverage, weather radar data may not always be available. For this reason Melcón developed a hail detection tool based on satellite remote sensing [82]. After refinements a POD of 69.3% was achieved with a FAR of 15.4%. A prototype algorithm using microwave imagers and radiometers has also been developed [83] but early evaluations show a POD of around 40% and a high FAR of 70%.

2.4.4 Hail Impact in the Literature

There is a plethora of hail experiments involving hail impact analysis in the literature. A recent paper by Olsson *et al.* [34] reviewed modelling and experimental testing of high

velocity hail impact on composite laminates. The work of Kim involving composite materials is also of particular note, with several papers in the subject area [16–19, 84, 85]. In 2008, the EASA published a research project report entitled Hail Threat Standardisation [13], which covered a review the existing literature of global hail threat data and how it pertains to aircraft. In fact, the vast majority of the literature applies to aviation considerations. The Insurance Institute for Business & Home Safety (IBHS) in the USA also began a long-term hail field research program in 2012 in an effort to characterize damaging hail [64, 65].

Material Properties of Hail Ice

The complexity and highly variable nature of the formation of hailstones has meant the understanding of the material properties of hail ice is limited and as such are usually represented by the category of polycrystalline ice (sometimes referred to as ordinary or terrestrial ice) [34]. Polycrystalline freshwater ice (clear ice) is obtained by freezing water under ambient temperature and pressure, and has a hexagonal crystal structure with a density of around 0.9 gcm^{-3}. For randomly oriented polycrystals, typical values of Young's modulus range from 6 GPa to 12 GPa and Poisson's ratio approximately 0.33.

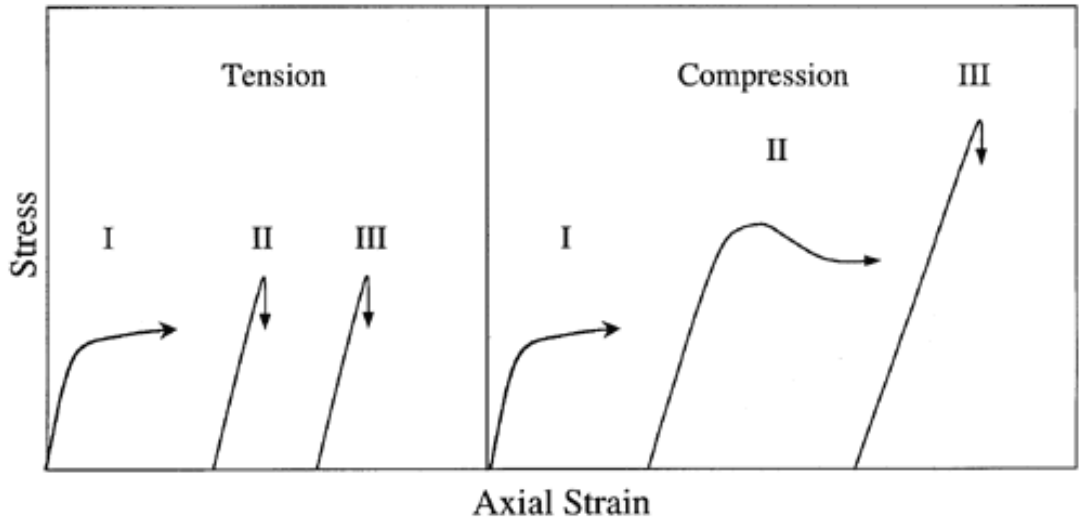

Figure 2.19: Schematic stress-strain curves. I, II, and III denote low, intermediate and high-strain rates. The arrows indicate either ductile (horizontal) or brittle (vertical) behavior [15].

Ice is viscoelastic rather than elastic and the properties of ice strongly depend on temperature and loading rate. A key feature of ice is the separate types of inelastic

behaviour exhibited when under compressional and tensile stress, as described in Figure 2.19. For tensional stress and at low rates of strain, ductile behaviour is observed and at intermediate and high rates of strain brittle behaviour is evident. Whereas for compressional stress, low and intermediate strain rates give rise to ductile behaviour and high rates result in brittle behaviour. Schulson investigated this behaviour under compression over a range of strain rates ($10^{-7} - 10^{-1} s^{-1}$). The transitional change was found to occur around $-10^{-3} s^{-1}$ for polycrystals of ice Ih of $\sim$ 1 mm grain sizes at $\sim$ $-10\,^{\circ}$C [86]. Kim and Keune also examined the compressive strength of ice at high strain rates [16] to fill this gap in the literature. In general the strength in tension is found to be less sensitive to strain rate and temperature compared to that in compression. Further details on the engineering properties of ice can be obtained from review papers by Sculson [86] and Petrovic [87].

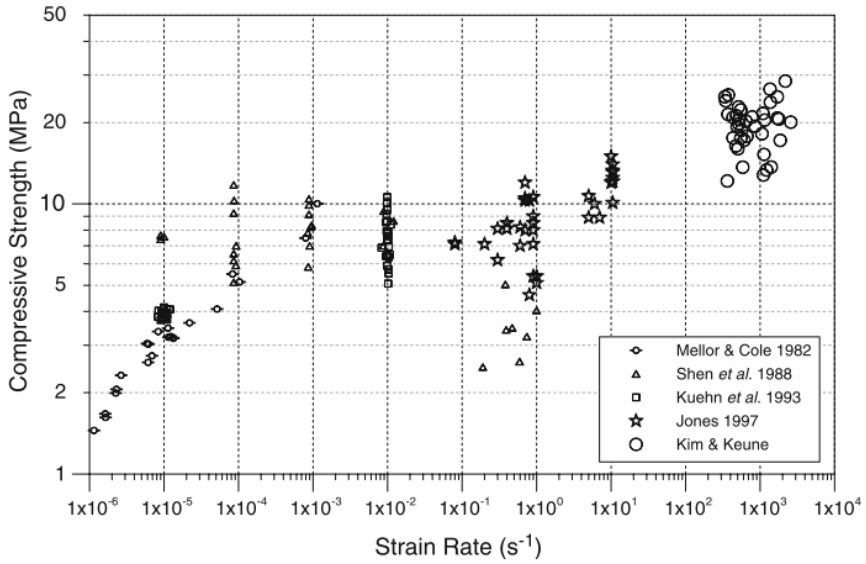

Figure 2.20: Comparison of Split Hopkinson Pressure Bar data with strength reported in existing literature [16].

Little has been published on the formation and subsequent falling of hail over sea. As such, the properties of "sea hail" are difficult to establish. Some details may be inferred from the comparative properties of freshwater and sea water ice, as displayed in Table 2.3.

2.4.5 Ice Impact - Experimental Work

One of the earliest investigations into hail impact on composite materials was carried out by Mahinfalah and Skordahl [88]. Here the fatigue life of 2 mm carbon/epoxy

Table 2.3: Reported Youngs modulus and failure strain of freshwater ice and sea ice [34].

Property	Freshwater ice	Sea ice
Density, ρ [kgm^{-3}]	~900	865
Tensile Young's modulus [GPa]		6.6 {-5°C;10^{-3}s^{-1}} 7.3 {-20°C;10^{-3}s^{-1}}
Compressive Young's modulus [GPa]	1.6 {-10°C;4.10^{-4}s^{-1}} 2.8 {-33°C;4.10^{-4}s^{-1}}	6.2 {-5°C;1.10^{-2}s^{-1}} 7.5 {-20°C;1.10^{-2}s^{-1}}
Compressive failure strain [%]	0.5 {-10°C;4.10^{-4}s^{-1}} 0.64 {-33°C;4.10^{-4}s^{-1}}	0.07 {-5°C;1.10^{-2}s^{-1}} 0.12 {-20°C;1.10^{-2}s^{-1}}

laminates was tested by allowing 25.4 and 38.2 mm ice projectiles to fall at a terminal velocity of approximately 45 ms^{-1} and comparing the inflicted damage to 12.7 mm aluminium balls. The latter was impacted at higher velocity to show equivalent kinetic energy and was found to cause noticeable reductions in the fatigue life, whereas the ice balls caused no delaminations and no reductions in fatigue life of the laminates. The reason was firstly attributed to the increased rigidity of the aluminium but on reflection the higher velocity appeared to be the root cause.

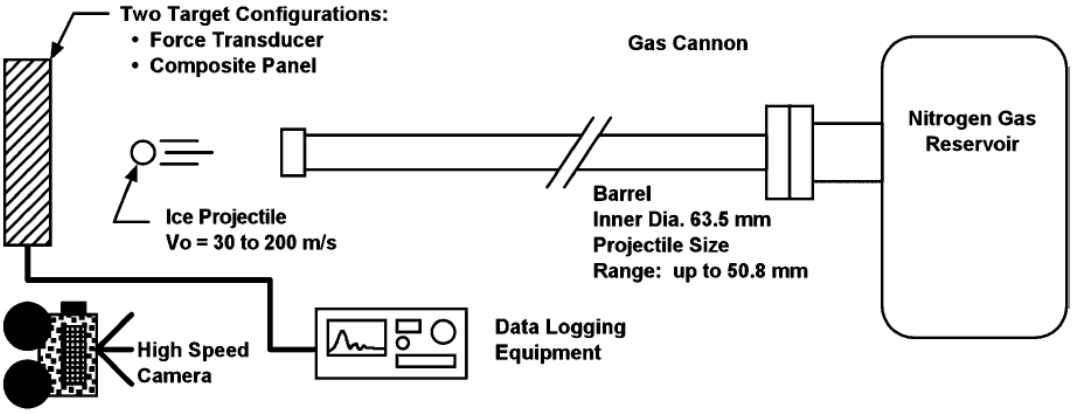

Figure 2.21: Nitrogen gas cannon used in [17, 18].

Early ground was also trod by Kim and associates, with extensive experimental and computational studies on the impact response and resulting damage by artificial or simulated hail ice (SHI). For many of the experiments in the literature the apparatus described in Figure 2.21 or similar was utilised. Kim and Kedward [17] investigated the discharge of different diameter SHI on composite panel targets and a force measurement transducer system. High speed photography was used to examine the nature and progression of collision. Images showed that the ice spheres crushed immediately on impact with the transducer face and micro-cracking throughout the sphere evident during this process.

Further analysis of the fracture modes under high velocity impact using a fast hydraulic jack, as well as standard material characterization under compression, was presented by Combescure *et al.* [89]. Measurements of force history showed a peak force occurring at 98 µs, when only disintegration of a small portion of the volume had occurred. In later investigations, the peak force was found to vary linearly with projectile kinetic energy [18]. A sequence of impressively distinct photographs from a recent series of experiences by Tippmann *et al.* [19] provides a much greater insight into the progression of impact. Here the initial contact, crack formation and local crushing of the front face, propagation of longitudinal cracks, travelling at approximately $2000\,\mathrm{m\,s^{-1}}$ oriented along the direction of travel and final transition to small fragments and powder spray are all clearly visible in Figure 2.22. The instance where the cracks reach the rear face sphere and break down into smaller fragments was determined to coincide with the peak value of the impact force. It was then postulated that this peak marked a change in phase of the forces involved from

(i) elastic-dominated structural response during early time following first contact, in which cracks develop and the impact force is increasing, to

(ii) fragmentation and cracking which imparts mainly a momentum based loading that corresponds with the decreasing force trend following the peak force.

Kim and Kedward were also one of the first researchers to determine the contrasting types of failure modes associated with high velocity ice impact, displayed in Figure 2.23. The categories were further classified by those causing barely visible and visible damage, as well as penetration and non-penetration of the composite material. The more discernible categories were found to transpire with increasing energy/velocity.

The importance of velocity in determining impact severity is a prevailing theme throughout several pieces of literature. For cases of small hard mass impact (excluding hail), Olsson [90] dismissed the influence of impactor mass and thus impact energy on impact severity to the point of negligibility. Later work by Olsson *et al.* [20] remarked that the onset of delamination occurs at a specific load that is essentially linearly proportional to the impact velocity. Similarly Kim and Kedward [17] reported that *"a smaller diameter projectile is more severe than one of larger diameter when impacting an identical panel target at the same level of projectile kinetic energy"*. Experimental velocities from ice impact in the literature can be viewed in Table 2.4, ranging from $30\,\mathrm{ms^{-1}}$ to approximately $213\,\mathrm{ms^{-1}}$. This range does fall within impact velocities theoretical possible for wind turbines, although several high velocity cases do exceed these limits.

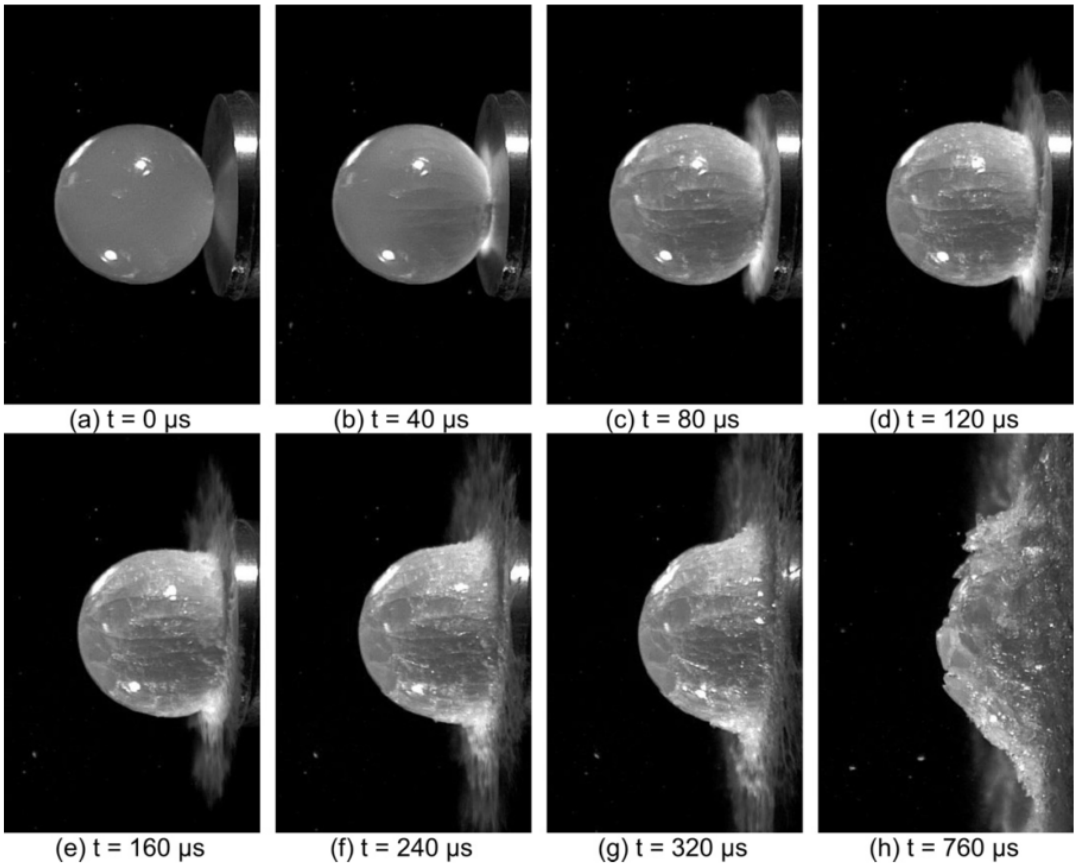

Figure 2.22: High speed video of ice impact on force measurement bar [19]

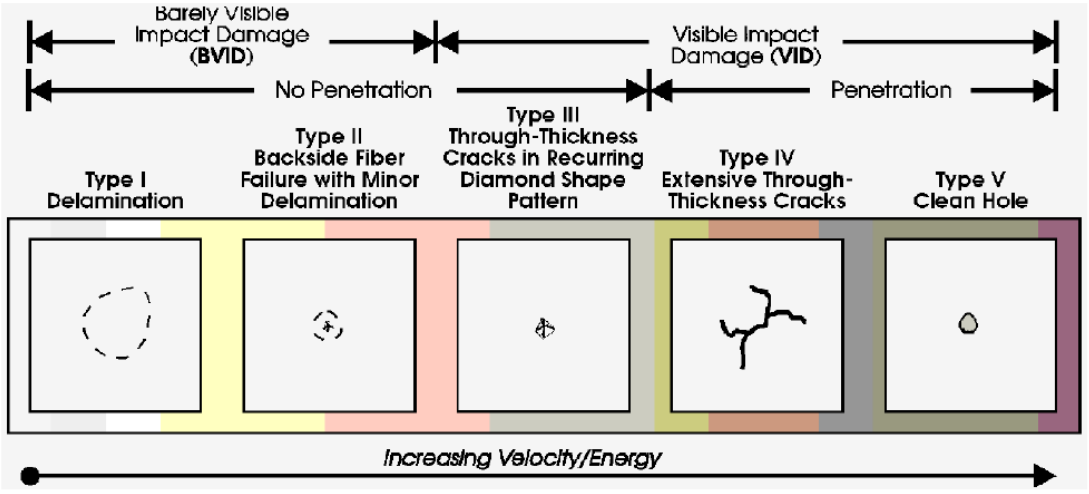

Figure 2.23: Failure modes observed experimentally for high-velocity ice impacts [17].

Table 2.4: Experimental velocities from the literature.

Paper	Year	Velocities Tested [$\mathrm{m\,s^{-1}}$]
Mahinfalah & Skordahl	1998	43.0, 45.9
Kim & Kedward	2000	30-200
Kim et al.	2003	30-200
Carney et al. (Pereria)	2006	91.44, 152.4, 213.36
Kim & Keune	2007	-
Juntikka & Olsson	2009	77, 126
Park & Kim	2010	82.3, 116.7 136.6
Appleby-Thomas et al.	2011	81-268
Tippmann et al.	2013	19-194

The types of response to different impact durations can be viewed in Figure 2.24. In *a*, very light impactors will not have time to deflect and the response of the impacted surface will be dominated by through-thickness waves. For most small impactors intermediate impact times are a consequence, where the response involves transient shear waves and flexural waves as in *b*. For the quasi-static response for large mass impactors in *c* the deflection shape and amplitude is equivalent to a static loading case. It should be noted that for sufficiently high velocities the mass ratio of the impactor and target material is irrelevant for the response type, as penetration occurs prior to any deflection similar to the failure modes presented in Figure 2.23.

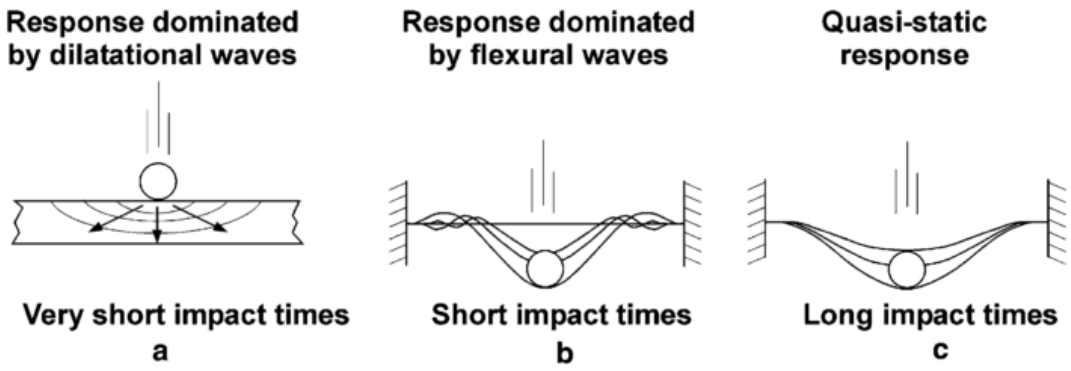

Figure 2.24: Different response types during impact on plates [20].

The topic of failure threshold energy (FTE) with respect to ice impact has been explored in many of the experimental research papers. Kim *et al.* [18] first made it a focus of investigation and found that a linear relationship between the kinetic energy at which failure initiates and the thickness of the panel. Smaller diameter SHI were found to exhibit lower FTE than larger diameters, due to the impact force being more localised

on the specimen for a smaller sized projectile. The measurements for glancing impacts were also found to follow a trigonometric scaling relationship. Park and Kim [84] found that the FTE for single lap adhesive composite joints was 210 J, with no damage observed for impacts at energies below this value. Between 210 J and 250 J, the damage was localised to mainly delamination of the plies adjacent to the adhesive layer. Beyond this threshold, the damage area versus kinetic energy increased dramatically and the damage observed was catastrophic. The delamination threshold velocity (DTV) for different diameter was inspected by Juntikka and Olsson [21]. A comparison between the experiments and finite element analysis can be seen in Figure 2.25. For T800/3900-2 carbon/epoxy tape material Rhymer *et al.* [85] noted that the initiation of delaminations was dominated by the matrix interlaminar fracture and strength properties, rather than the properties of the fibres and the associated architecture.

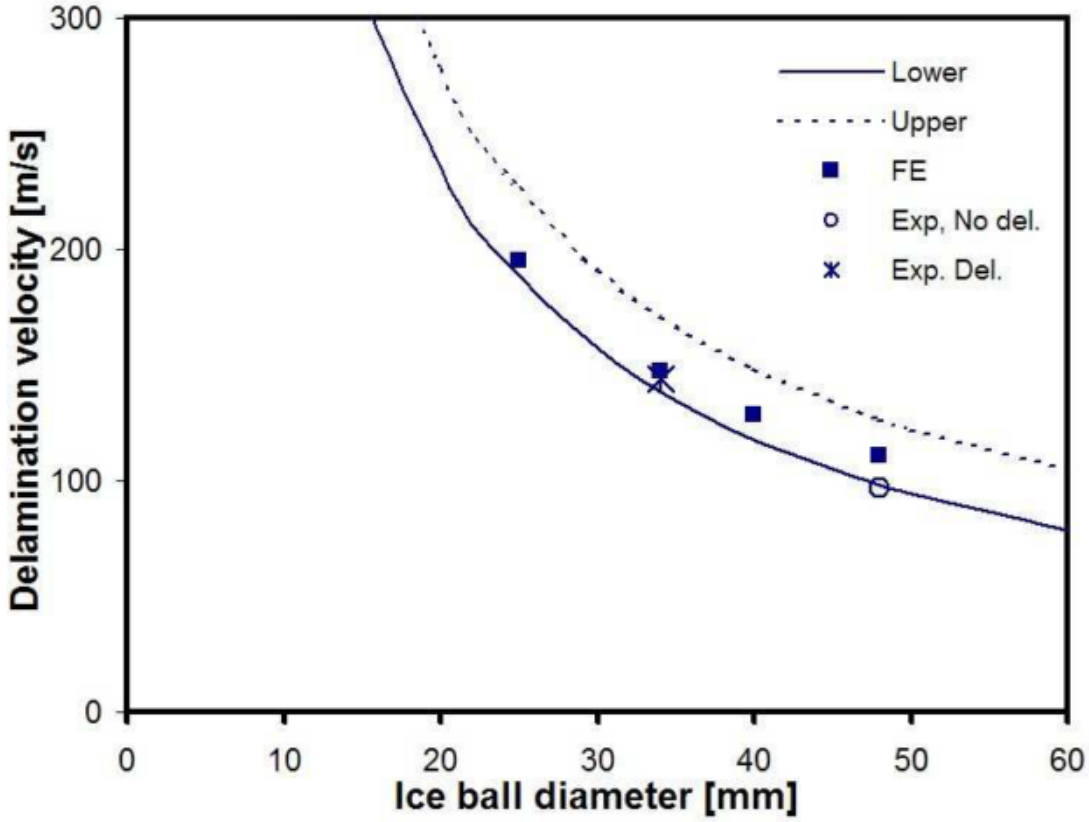

Figure 2.25: Comparison between delamination velocity from FE and experiments with analytical upper and lower bounds [21].

The work by Appleby-Thomas et al [35] represents one of the few examples of investigation into the cumulative damage as a result of *repeated* SHI impact. The

results of the experiments for both woven (CFRP-1) and uni-directional (CFRP-2) specimens can be seen in Table 2.5. The damage categories in the right hand column are comparable with the classifications in Figure 2.5, with category 6 showing extensive through thickness cracking plus penetration.

Table 2.5: Delamination and strength reduction of CFRP specimens to mutiple ice impacts [35].

Experiment number	No. of Impacts	Cumulative Impact Energy [J]	Delamination area [mm^2]	CAI Strength (MPa)	Strength reduction (%)	Damage
CFRP-1						
1	1	72.2	0	175.0	0.0	0
2	3	237.8	476	134.7	23.0	1
3	5	400.0	2592	140.7	19.6	1
4	1	83.7	-	143.9	17.8	0
5	2	261.5	5398	128.1	26.8	2
6	3	317.9	3327	123.0	29.7	2
7	5	629.7	10795	121.0	30.9	3
8	1	140.0	4969	152.4	12.9	2
9	3	431.3	9870	118.4	32.4	3
10	5	721.7	11951	67.8	61.2	4
12	7	1146.4	18117	35.6	79.7	5
CFRP-2						
1	2	72.2	7862	69.9	30.7	2
2	3	72.2	9760	34.4	66.2	2
3	5	72.2	13,433	21.5	78.9	3
4	7	72.2	19,796	17.8	82.5	4
5	1	72.2	7989	58.0	43.1	1
6	3	72.2	15859	49.3	51.6	3
7	5	72.2	16926	30.3	70.3	3
8	7	72.2	20500[4]	94.0	0.0	4
9	1	72.2	7943	75.6	25.7	1
10	3	72.2	16042	25.7	74.8	3
11	5	72.2	18907	25.3	75.2	4
12	7	72.2	21500[4]	96.9	0.0	6

Manufacture of Artificial Hail

The creation of simulated hail ice in a laboratory setting to match real life instances is a complicated task, mainly due to the complexity of the formation process. Replication of the spherically layered "onion-like" is a particular challenge and one that is yet to be achieved and tested. In early experiments, Kim and Kedward [17] were able to produce both 'monolithic' and 'flat-wise layered' ice spheres, as shown in Figure 2.26.

Spherically layered ice is thought to be significantly tougher and although not exactly comparable, the flat-layered ice would be a more representative projectile. The

[4]C-Scan analysis not possible due to excessive target disruption; damage estimated based on a visual target inspection.

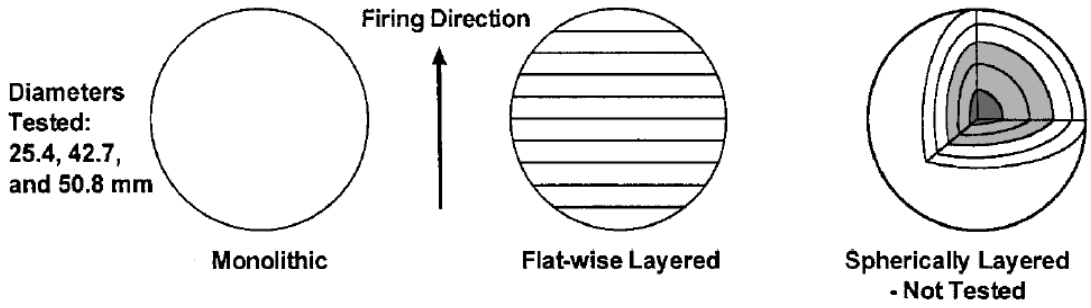

Figure 2.26: Experimental and simulated hail ice composition [17].

monolithic ice spheres were cast in a split spherical mold over 1 filling session, and the flatwise layered spheres were constructed by casting over 10 to 11 filling sessions. The layers were aligned normal to the impact surface and the moulds were modified slightly to have a filling hole for a later investigation. Cast spheres were kept frozen at a temperature of $-27\,^{\circ}\mathrm{C}$. This method utilised by Kim and collaborators has remained largely unchanged [19, 84, 85] for more recent experiments. To create similar mono-crystalline ice cylinders, Combescure *et al.* [89] froze a water cylinder very slowly. Water was added everyday, at a growth rate of 1 cm a day until a desired thickness as achieved. Juntikka and Olsson [21] used squash balls and plastic balls to act as moulds, filling in water and allowing air to escape during a period of 1 week. Afterwards the water was frozen at a temperature of $-2\,^{\circ}\mathrm{C}$ and then lowered to a storage temperature of $-10\,^{\circ}\mathrm{C}$. Creation of SHI using deionised water is prevalent through the majority of the aforementioned literature. The diameter ranges of SHI used in experimental investigations can be seen in Figure 2.6. These would correlate to a intensity category range of H2 (significant) to H7 (destructive).

Table 2.6: Experimental diameters from the literature.

Paper	Year	Diameters Tested [mm]
Mahinfalah & Skordahl	1998	25.4, 38.2
Kim, H & Kedward	2000	25.4, 42.7 and 50.8
Kim et al.	2003	25.4, 42.7 and 50.8
Carney et al (Pereria).[5]	2006	17.5
Kim & Keune	2007	12.7
Juntikka & Olsson	2013	34.0 and 48.0
Park & Kim	2010	50.8
Appleby-Thomas et al.[5]	2011	22.0
Tippmann et al.	2013	38.1, 50.8 and 61.0

[5]Not SHI ice: Carney et al. (Pereria) - cylindrical Ice; Appleby-Thomas et al - hemispeherically-fronted ice projectiles

2.4.6 Ice Impact - Computational Modelling

As in the case of experimental breakthroughs, Kim and Kedward [17] were one of the first to computationally simulate hail ice impacts on a composite structure. Using the explicit finite element code DYNA-3D, which later went on to become the software package LS-DYNA in commercial use today, a quarter-model mesh of an ice sphere impacting a force measurement transducer was created. The material model chosen in the initial studies included hardening plastic behaviour that adequately accounts for the micro-crack evolution, as viewed in high-speed imagery, just prior to crushing. When the plastic failure strain is reached in the material model, all shear stress components reduce to zero. Similarly, when the tensile failure pressure is reached, the material is restricted to only carry hydrostatic compressive stress, to replicate fluid behaviour. These early developments demonstrated that numerical simulation of ice impact models could successfully represent the experimental equivalent. Park and Kim [84] later migrated the ice impact model to ABAQUS/Explicit to compare simulations with the aforementioned experimental transverse impacts on composite joints.

Tippmann *et al.* [19] updated the Lagrangian method to include strain rate-dependant material parameters in Abaqus. In previous versions, the yield strength had to be tuned in relation to the size and velocity of the projectile. By modifying the yield strength to be strain rate dependent, different regions of the SHI sphere could possess different values of yield strength based on the local strain rate of the individual elements. Peak forces for a range of SHI kinetic energies were compared to experimental results obtained from both Kim et al. [17] (DS1) and Tippmann et al. [19] (DS2), as described in Figure 2.28a. Due to the scatter of the experimental data, three bounds (upper, lower and average) were created to represent the scatter in measured ice compressive strength. Good correlation was found across the full range, with the lower bounding curve showing better agreement for the majority of the experimental data that involved kinetic energies of 400 J or less. The model was also able to exhibit the initial onset of length-wise cracks in the early uploading response up until the development of peak force. However, the model was declared to be unsuitable for prediction of the lateral spreading and flow of crushed ice debris after this threshold.

Anghileri *et al.* [22] compared three numerical hailstone models using LSTC LS-DYNA:

(a) lagrangian finite element (FE),

(b) arbitrary lagrangian eulerian (ALE) and

(c) smooth particle hydrodynamics (SPH).

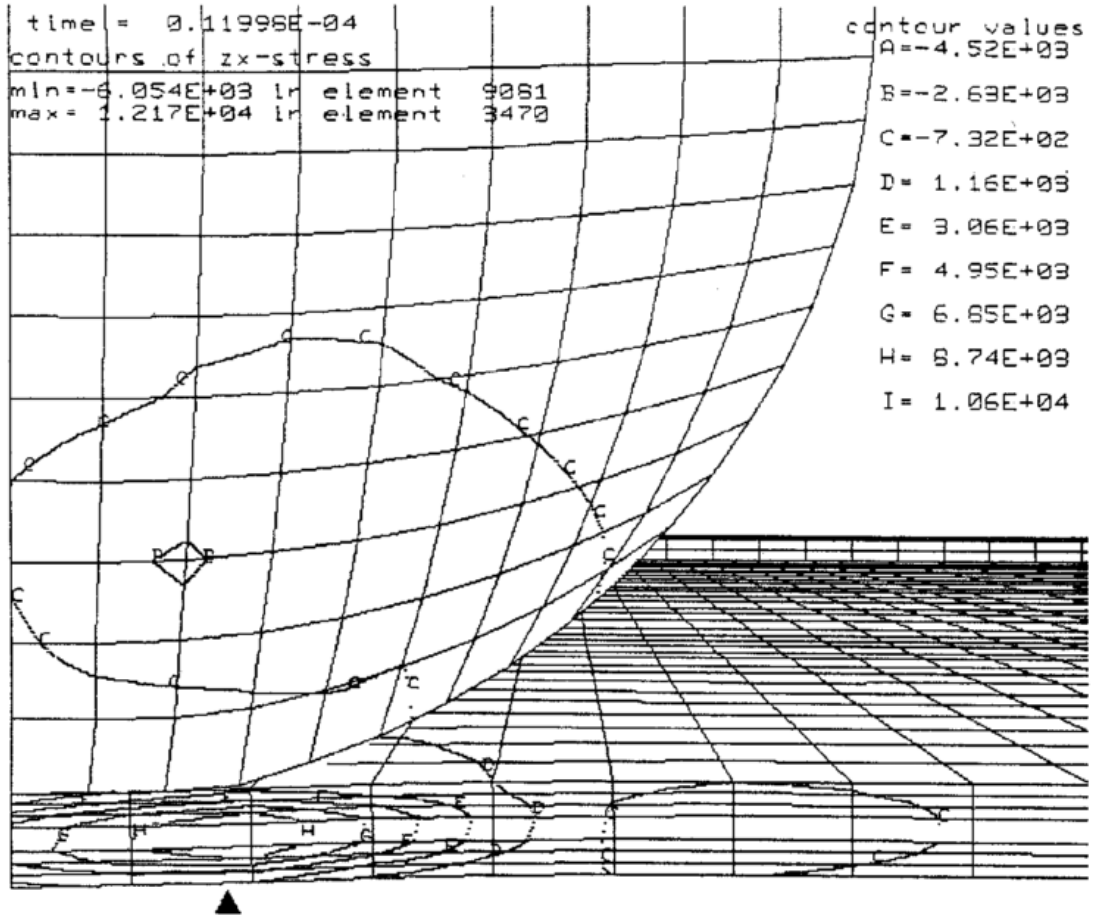

Figure 2.27: DYNA3D model pan15b contour plot of τ_{xz} at time t = 12 θs, maximum τ_{xz} = 83.9 MPa [17].

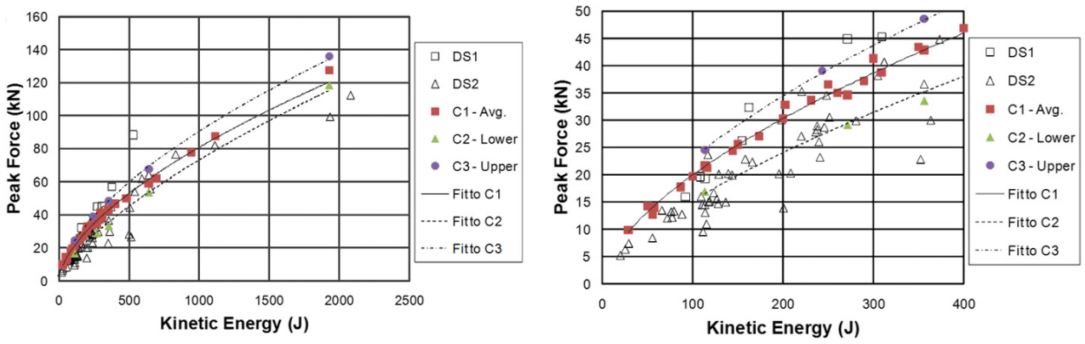

(a) Full kinetic energy range.

(b) For kinetic energy < 400 J.

Figure 2.28: Peak force versus kinetic energy relationship showing simulation and experimental results [19].

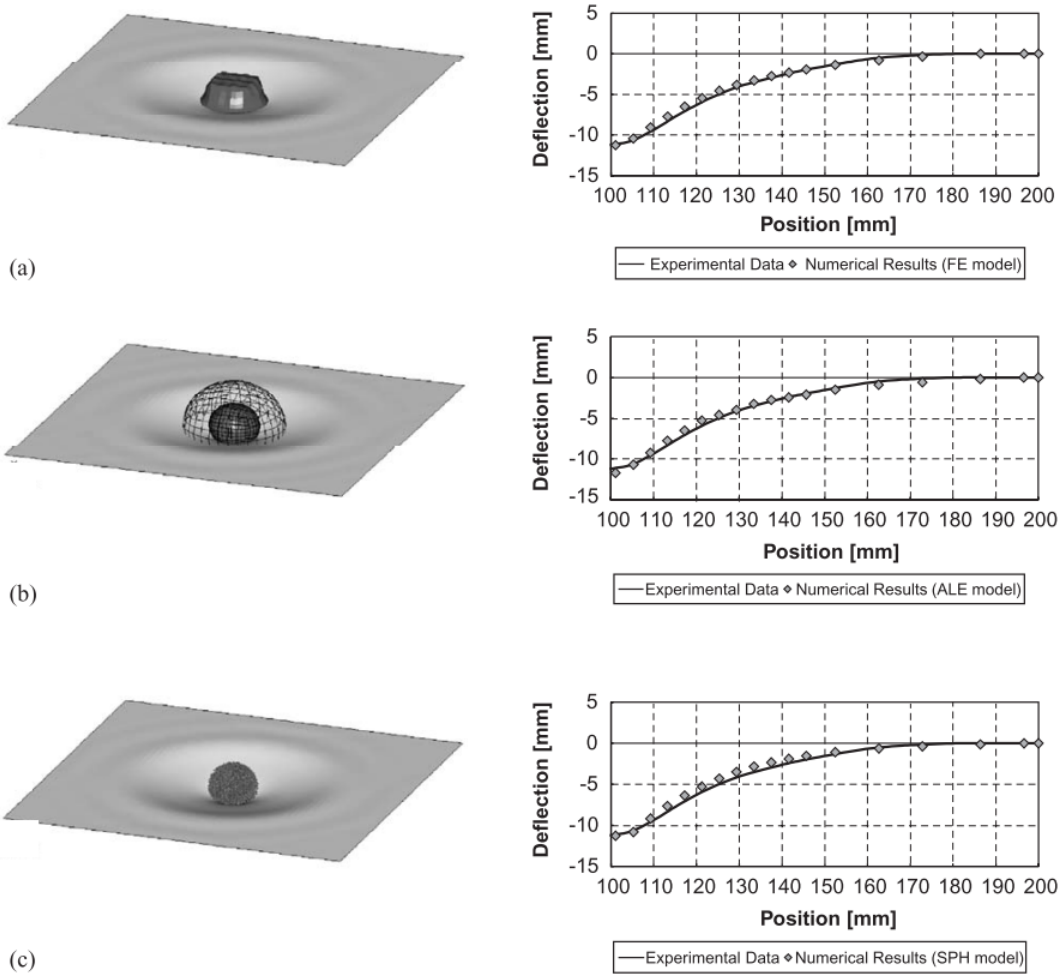

Figure 2.29: Hail impact at t=0.150 $\times 10^{-3}$ s and numerical-experimental correlation. (a) FE; (b) ALE; and (c) SPH models [22]

The customary FE approach, as adopted by Kim and Kedward [17], is typical for continuum mechanics as it is efficient for non-linear problems. Concerns have been raised regarding the excessive mesh distortions that are more characteristic of soft bodies or fluid-like media. A hybrid of both Langrangian and Eulerian practices, the aim of the ALE method is to obtain the advantages from both constituents. The mesh can move arbitrarily and thus independently of the motion of the material. SPH is a completely meshless method and originates from astrophysics research. The mesh is replaced with a set of particles that are endowed with a mass and not directly connected. The material model used for the first two methods was not developed for SPH interaction and a different model had to be implemented. The three approaches were validated against the impact of a 25.4 mm diameter hailstone against an aluminium alloy 2014-T4 plate at $192\,\mathrm{m\,s^{-1}}$, as carried out by the British Royal Aircraft Establishment. The numerical comparisons can be seen in Figure 2.29, where all three match the experimental data quite well. Visually, the SPH model reproduced physical hailstone behaviour the closest. The methods were then prescribed to replicate the impact on the intake of an engine. Concluding remarks decreed that the SPH model was the most effective. The FE model was only suitable for early stages of impact and the ALE model could not imitate collapsing of the nacelle, common for coupling of solvers based on different approaches. In terms of processing durations, SPH also performed the best, with a CPU time of ∼1h compared with 14.5h and ∼39h for that of ALE and FE respectively. For experimental comparison of impact events on composite materials Juntikka and Olsson [21] used a SPH approach for the SHI sphere in LS-DYNA®. The model is able to capture both the stress wave in the sphere and the subsequent microcracking, as evident in Figure 2.30.

Motivated by the Columbia space shuttle tragedy, Carney *et al.* [23] developed a phenomenological ice model for ballistic impact. A key incentive was to build upon the work by Kim and associates by better representing the rate sensitive nature of ice. No reference was made to SPH models or the preceding evaluation. The analytical ice model was validated against a internal NASA technical report that included a short series of impact tests inside of a vacuum chamber. The model performed both quantitatively and qualitatively better than other ice models [17, 18] for cylindrical projectiles. Other critical merits of this model are the independent failure stress in tension and compression, the strain rate sensitivity of the flow stress, the ability of the failed ice to continue to carry hydrostatic stress and the use of the Eulerian mesh. Sain and Narasimhan [91] used this model as a basis for further constitutive analysis in the high strain rate regime.

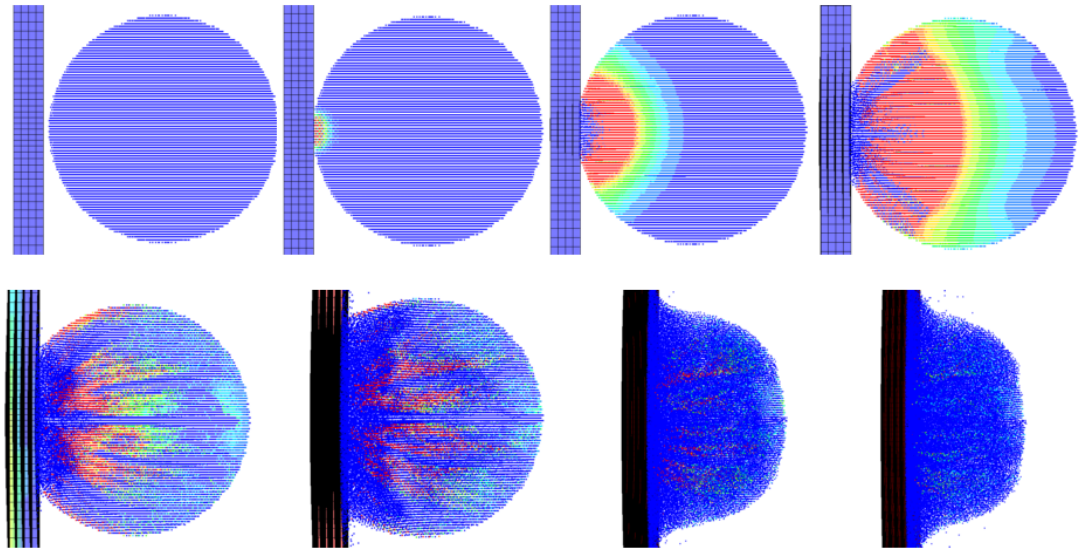

Figure 2.30: Simulation of SHI impact using a smooth particle hydrodynamics model [21].

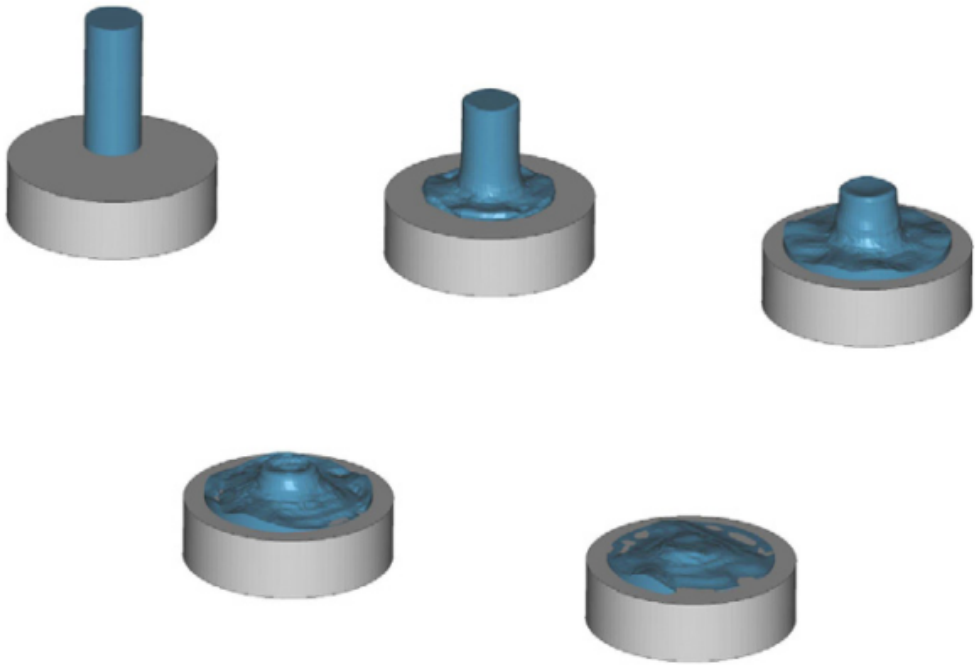

Figure 2.31: Solid to fluid transition of the Carney model using an Eulerian formulation [23].

2.5 Other Environmental Factors of Blade Damage

The scope of this PhD research is to investigate the physical effects of hail on wind turbine blade damage. However, it would be remiss not to at least mention the other environmental factors as part of this literature review. Depending on the location of the turbine, a number of these environmental factors may occur concurrently and the subsequent degradation imparted on blades should be included when developing a comprehensive strategy for addressing wind turbine damage. The influence of oxygen, humidity and chemical attack on blade damage is not examined but as polymers react with water and oxygen, there is potential for structural change that could lead to damage. These effects could be especially apparent combined with other factors or with already exposed layers of matrices and fibres.

2.5.1 Liquid Impact

Droplet impact is included by Keegan [60], with a considerable portion of the thesis dedicated to a review of experimental and modelling techniques as well as a dedicated section discussing his own computational rain droplet impact modelling.

Rainfall is arguably a more contentious and persistent issue compared to hailfall and other forms of precipitation, relative to the climate of contention. Particularly in the UK, the number of days of occurrence are considerably more substantially than that of hail. For rainfall $\geq 0.2\,\text{mm}$, $\geq 1\,\text{mm}$ and $\geq 10\,\text{mm}$ the number of days of rain can exceed 260, 220 and 70 days respectively [70] for some parts of the country. The rainfall can range from $< 600\,\text{mm}$ to $> 3000\,\text{mm}$ at various land observation stations, with copious amounts visible in Scotland and the south and south-west of England. The continuous duration of rainfall is also known to greater than that of hail. Typical droplet diameters can range from 0.5 to 5 mm, with smaller sizes more common for moderate rain rates and vice versa [60].

The phenomena of liquid impact with a solid surface can be viewed in Figure 2.32, where the progression consists of two main aspects. Initially, the liquid will behave in a compressible manner, generating "water-hammer" pressures that are responsible for most of the damage. The second aspect is a result of the edge of the contact area, between the impacting liquid and the solid, moving supersonically with respect to the shock speed [92]. This is often referred to as guided acoustic shock theory (or GAS) [93]. A compressional wave is firstly generated in the solid material, which propagates outwards from the source of impact. Shortly after, the surface contact area is increased and shear waves are created in the target material, again moving outward from the impact zone and causing possible, complex interaction with the compressional

waves. A Rayleigh wave also disperses radially along the surface of the material. The shock wave formed in the water drop breaks away from the body of the drop with lateral jetting commencing after this specific moment. Impact pressures are released as energy transforms to the kinetic energy of lateral jet [24].

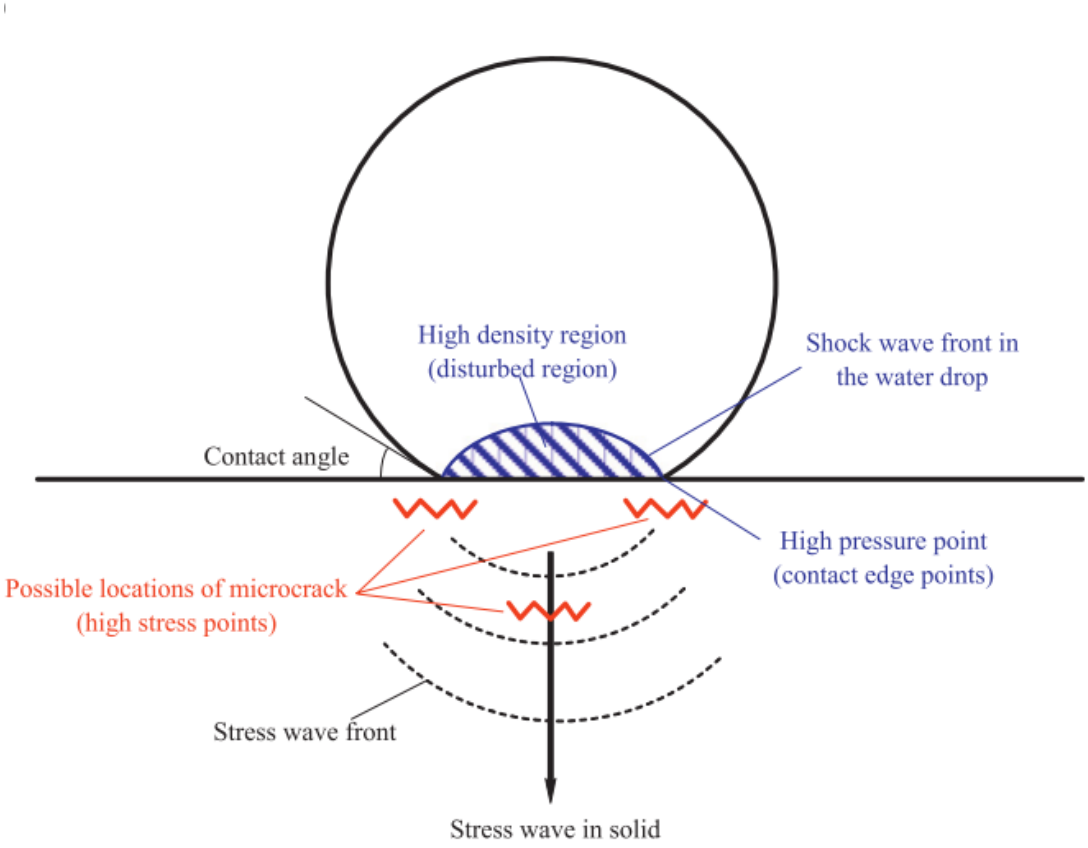

Figure 2.32: Schematic of 3-D water erosion impact [24].

Although Keegan [60, 94] represents the primary investigation of droplet impact with respect to wind turbines, other relevant composite research has been carried out. Gohardani [95] performed a comprehensive review of liquid erosion for current and future flight conditions. Here the importance of the damage threshold velocity (DTV) and damage modes related to droplet impingement (adapted from Adler and Hookers' investigation of brittle glass materials) were discussed. The rain progression of these damage modes can be seen in Figure 2.33. This summarises a brief overview of what is a complicated mechanism with many governing factors influencing damage and erosion.

Although the issue has not been properly explored, the effects of sea spray may become apparent for turbines in marine environments. The impact scenarios may very well be similar to that of rain droplet impact but there are several aspects that will

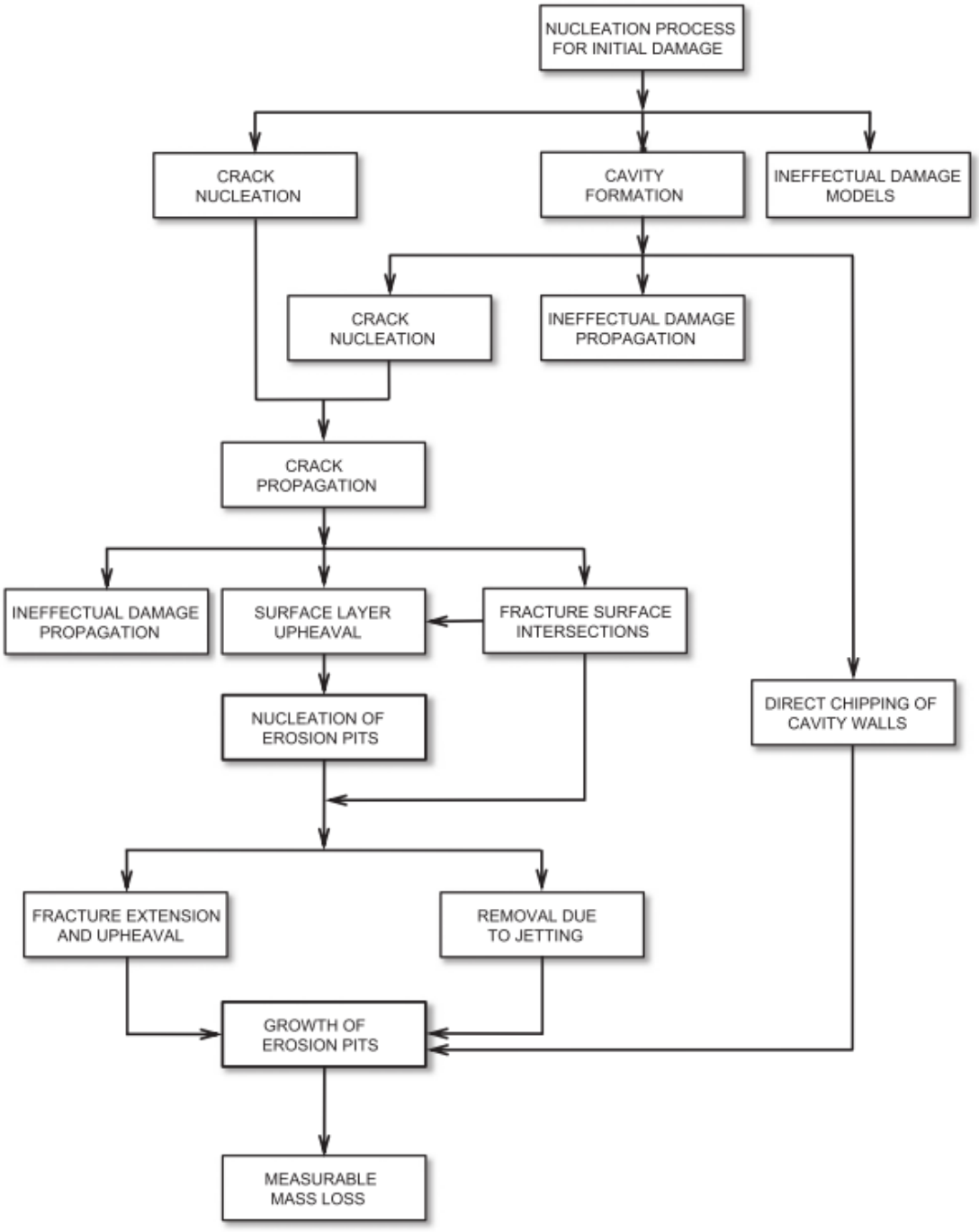

Figure 2.33: Damage modes related to droplet impingement.

be different, for instance droplet size and frequency of occurrence. Seawater is also a saline solution and an ionic conducting electrolyte, which may present the development of tribocorrosion related concerns, if the salt content is of a sufficient degree.

2.5.2 Ultraviolet Light

Ultraviolet light exposure, particular the high energy content of UV-A, can result in a dramatic reduction in the erosion resistance of wind turbine blade coatings and protection measures. Further damage can take the form of shrinkage, cracking and blistering [59]. The effects of exposure to non UV stable tapes, in conjunction with liquid droplet impact, can be seen in Figure 2.34. Both images show the aftermath of 6 hours of rain testing at 125-150 $\mathrm{m\,s^{-1}}$ (greater than fastest wind turbine tip speed) and 30-35 $\mathrm{mm\,h^{-1}}$ [60]

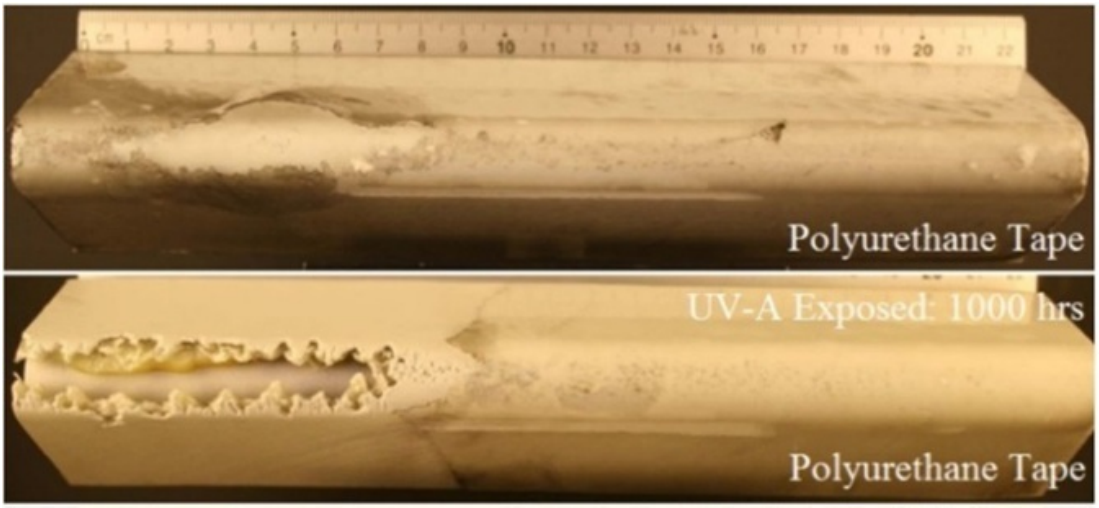

Figure 2.34: Effects of combined UV-A exposure and liquid droplet impact on polyurethane tape compared with a control [25]

Areas of the world will differ in ultraviolet radiation, with those countries around and south of the equator the recipient of higher intensities than of those in the Northern Hemisphere.

2.5.3 Lightning

Lightning poses a threat to a number of wind turbine components, especially to electrical equipment housed within the turbine. There are also numerous cases of localised damage to the blades, as demonstrated in Figure 2.10, in Section 2.3. As part of IEC design recommendations [31] (in particular IEC61400-124), a local earth electrode system is required for correct operation of the electrical installation and for lightning

Figure 2.35: Still image taken from a video showing upside down lightning effecting a wind turbine [26]

protection. There are different forms of lightning protection systems, all of which have a down conductor with the receptor often placed at the tip [59].

An observational study recorded several instances of lightning attaching to wind turbines at a wind farm in Kansas [96], with all lightning attachments taking place at the blades. Upward leading flashes, as displayed in Figure 2.35, are more difficult for lightning detection networks to discern. However, the study found that blade damage was more likely to occur *"as result of a direct downward negative cloud-to-ground flash*".

2.5.4 Accretion

Similar to the consequences of erosion, wind turbines can experience substantial reductions in power output due to the effects of accretion of certain substances on the blades [97]. Accretion takes many forms but the example that is often discussed is blade icing. Not surprisingly, this is a problem for areas of particular cold climates. Depending on the icing conditions, ice shapes that develop on rotating blades can be categorised into three groups: glaze ice, rime ice and mixed ice. Glaze ice is formed as impacting water droplets freeze as they travel along the blade surface, resulting in protruding, feathery features. The water droplets that form rime ice, freeze immediately upon impingement and the ice localises around the leading edge. Mixed ice is a blend of both rime and glaze ice and as such exhibits the characteristics of both types. Temperatures, angle of attack, liquid water content and icing times all play a

role in the culmination of the different types and ice thickness [98]. In some instances ice can even be "thrown" from the turbine, potentially hitting and causing damage to personnel, vehicles and residencies [99]. For non-accessible locations, both active and passive methods for the prevention of icing of blade surfaces have been proposed, predominately hydrophobic foils and heating [59].

(a) Build-up of ice on a wind turbine [100].

(b) Extreme blade contamination due to insects [101].

Figure 2.36: Examples of accretion.

In some countries the accretion issue can be the result of the the contamination of dead insects on the leading edge, as evident in Figure 2.36b. For levels of extreme contamination, the change in annual energy production can be profound, particularly for high winds [101]. The deposition of salt and pollution on a wind turbine blade has also been noted in the literature [102].

2.5.5 Other Abrasive Air Particles

Possibly due to the current lack of installed capacity in arid and equatorial regions compared with others, the specific case erosion of wind turbine blades due to sand and dust has been proclaimed but not heavily investigated. High growth rates in Morocco, Brazil and Mexico, as shown in Figure 1.1b, could result in the stimulation of further research. The threat may also encompass near-shear locations. A recent evaluation of carbon nanofibre (CNF) based nanopaper coatings against sand-blasting of silica sand (SiO_2) was carried out by Zhang *et al.* [77], with reference to wind turbine blades. For a non-specific application, a series of experiments by Tewari *et al.* [103] examined the erosion behaviour of unidirectional carbon and glass fibre reinforced composites, for a range of test conditions and erodents. Silica and natural sea sand were used among other traditional laboratory solid particle erodents.

2.6 Maintenance and Standards

Although there is a paucity of published research surrounding wind turbine erosion and damage, the industry is certainly not oblivious to the issue. Companies such as LM and 3M are noteworthy developers, attempting to provide advancements in leading edge protection measures. The types of different material technologies and their effectiveness are discussed in more detail by Keegan [60]. There are also a considerable number of organisations that attempt to address an already manifesting problem in-situ through maintenance and mitigatory means.

Blade maintenance, repair and operations procedural steps are as follows:

- Survey and mapping of damages ,
- coating overhaul (e.g. leading-edge erosion),
- structural repair (e.g. bond-lines) and
- blade substitution (heavy repair).

Regardless of the severity of damage, it will first need to be discovered and inspected before any mitigatory measures can be carried out. Accurate non-destructive inspection is a challenge due to the extensive size of modern blades, turbine location and the various damage modes that are presented. The method most currently employed is manual and visual inspection by skilled technicians. This obviously requires extensive training, with a enormous emphasis on Health & Safety. Specialists access the blades via synthetic ropes (rappelling) and are required to painstakingly examine the surface with the naked eye [104]. Other manual maintenance methods used in practice include cherry-pickers (depending on hub heights) and descending modules/platforms that provide greater support.

Internal damage cannot be assessed using external means and therefore other techniques must be employed. Ultrasonic testing is one such method which can detect different defects such as delamination, voids or disbonding and how deep that defect is. Currently the technology and cost does not make it ideal for in-situ inspection. Other techniques such as digital shearography and passive/active thermography are also being developed [105]. The surge of interest in remotely operated air vehicles (or "drones") has seen developments in mounting cameras and attaching other imaging techniques in order to improve upon the current set-up [106]

Condition monitoring is also a prevalent theme throughout various wind turbine components and the installation of sensors, strain gauges and accelerometers has been

Figure 2.37: Technicians inspecting a turbine blade via rope access [27].

discussed as part of an "intelligent" blade design. Li *et al.* discusses the disadvantages and advantages of deploying different sensors in comprehensive review [107].

Any challenges for inspection seem trivial when compared to implementing any required repair. Also, weather conditions have to be mild enough in order for the appropriate curing/drying of repair composites. Despite these difficulties, maintenance service providers claim to able to carry out small surface repairs to medium structural repairs. As a technician has either to take everything required for a job with him (or her), or have it hoisted up or lowered down to the working position, repair procedures have to be carefully pre-planned and managed, with adequate back-up from other team members. To accelerate the repair strong hand-held ultraviolet lamps are an attractive tool. The unwieldiness and cost implications of full turbine blade replacement, especially for the large multi-megawatt designs, mean that full on blade substitution should only be considered as a last resort [108]. The implications to access posed by remote and offshore turbines are pronounced. Not only does the duration of travel to and from site become significant but the repair can only take place during certain windows of time where the weather and/or sea conditions are suitable. Regions of localised damage can be repaired by patches of different configurations. Moisture absorption by either the parent materials or repair materials prior to curing is also a concern as it introduce

considerable defects in the patch and bondlines [105].

There are currently no general standards for the testing of surface protection of rotor blades. There are an assortment of related standards that can be used as guidelines, including those involving helicopters, offshore structures and miscellaneous paints and varnishes. A standardised test, taken from the Norsok petroleum industry Standard M-501, exposes the material to a cycle of different atmospheres and weathering at an attempt to compare the specimen degradation of rotor blades to that of a marine atmosphere. However, the Norsok test does not examine wear resistance (including erosion due to rain and hailstorms) and chemical attack [59].

Chapter 3

Hail Impact Scenarios from Meteorological Data

List of Symbols

Symbol	Definition	Units
$\varnothing$	diameter	m
ρ_a	air density	$\mathrm{kg\,m^{-1}}$
γ	density correction factor	
$_G$	graupel (subscript)	
$_H$	hail (subscript)	
C	scale parameter	
C_d	coefficient of drag	m
D	hail/graupel diameter	m
I_{ref}	turbulence intensity	
T	kinetic energy	J
U	wind speed	$\mathrm{m\,s^{-1}}$
V_1	'cut-in' wind speed	m
V_2	'rated' wind speed	m
V_3	'cut-out' wind speed	m
V_{ave}	average annual wind speed	$\mathrm{m\,s^{-1}}$
V_{ref}	reference wind speed	$\mathrm{m\,s^{-1}}$
g	gravitational constant	$\mathrm{m\,s^{-2}}$
k	shape parameter	
m	mass	kg
$p(U)$	probability of wind speed	
u_0	initial impact velocity	

Prior to modelling the currently undefined role of hail on wind turbine blade erosion, it is important to recognise the likelihood of hailstone erosion events occurring. An understanding of realistic impact scenarios experienced by wind turbines is imperative in order for representative damage to be relevant to actual wind turbine installations. This chapter will evaluate various hail impact considerations, paying particular attention to meteorological data. Certain pieces of this investigation were published as part of a Wind Energy short communication [109].

3.1 Considerations

3.1.1 Hail Impact Factors

The extent of solid particle erosive wear is influenced by key factors including: the number and mass of individual particles, the velocity of impact and impingement angle [110]. Although there are several other factors to consider when examining material erosion resistance; these directly relate to the erodent and the motion of the blade.

The number of particles is influenced by the number of hail events, the rate of particles within those events and the duration of the hailstorm. It should also be noted that the conditions required for hail will mean that instances will show some seasonal trends. The assortment of categories and the fact that hail specimens possess varying densities and sizes, results in a significant range of different particle masses. The overall impact velocity can be characterised by a combination of velocity components. Keegan *et al.* [25, 111] determined these to be: the terminal velocity of the hailstone, the mean wind speed and the wind turbine tip speed, as evident in Figure 3.1. One example in this study used a 15 mm or 30 mm diameter hailstone entrained in a $20\,\mathrm{ms}^{-1}$ horizontal wind striking a blade tip, with $90\,\mathrm{ms}^{-1}$ tip speed. The interaction of these different components implicate that variety of impact angles could be possible and should also be examined.

3.1.2 Meteorological Data

Meteorological data were provided by the British Atmospheric Data Centre (BADC), consisting of three separate datasets: Met Office Integrated Data Archive System (MIDAS) land and marine surface stations [70], the Chilbolton Facility for Atmospheric and Radio Research (CFARR) [112] and the Natural Environment Research Council (NERC) Mesosphere - Stratosphere - Troposphere (MST) Radar Facility at Aberystwyth [14].

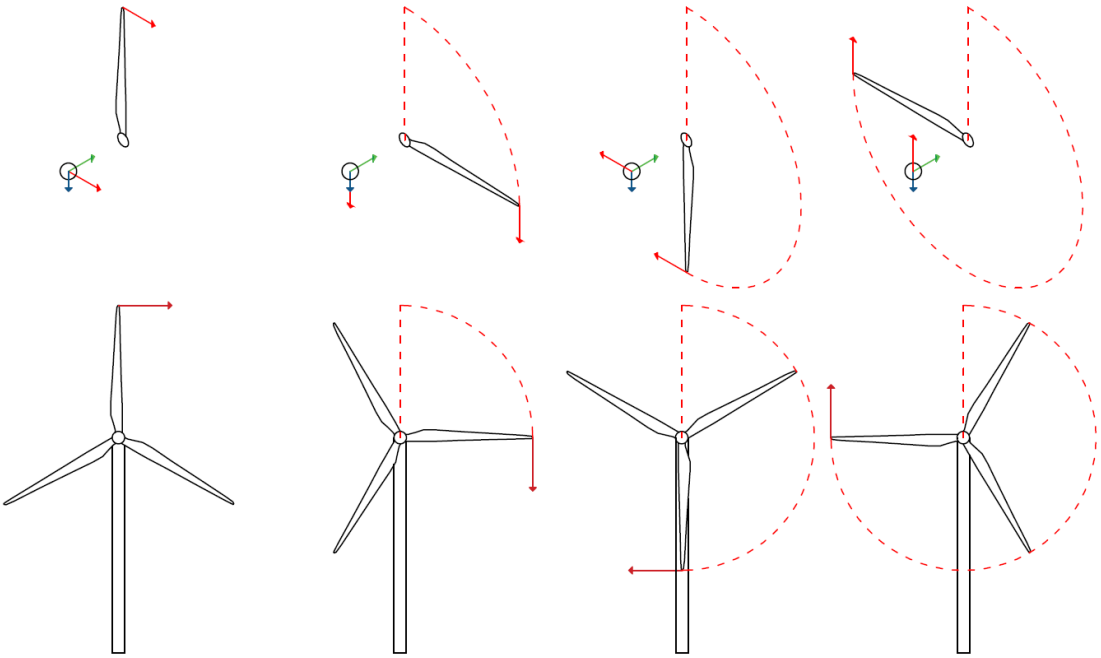

Figure 3.1: Impact velocity components during wind turbine blade revolution: horizontal wind speed (green), hailstone terminal velocity (blue) and wind turbine tip speed (red).

MIDAS Station Data

A surface station contains a collection of instruments and observing systems to meet a variety of applications. Stations are organised into networks, designed to meet particular user requirements. It should be noted that MIDAS does not contain any remote sensing data such as radar estimates of precipitation, thunderstorm locations or satellite imagery. The number of stations available from the overall dataset totals close to 17400 and the spread across UK can be seen in Figure 3.2a However, the vast majority of stations do not include hail observations within their remit. Therefore the data available for analysis was restricted to around 1000 stations Figure 3.2b.

The MIDAS dataset contains surface observations over land areas of the UK as far back as the digital record extends. Daily, hourly and sub-hourly measurements of historical UK weather conditions are available depending on the weather data type. A selection of global surface and marine observations from UK and non-UK stations is also included. For this particular examination, the data was restricted to the subsets of UK Daily Weather (where hail observations are contained) and UK Mean Wind. Available UK Daily weather can be found as far back as 1875 but hail information is restricted to 1949 onwards. The data interval was therefore taken from the start of 1949 to the

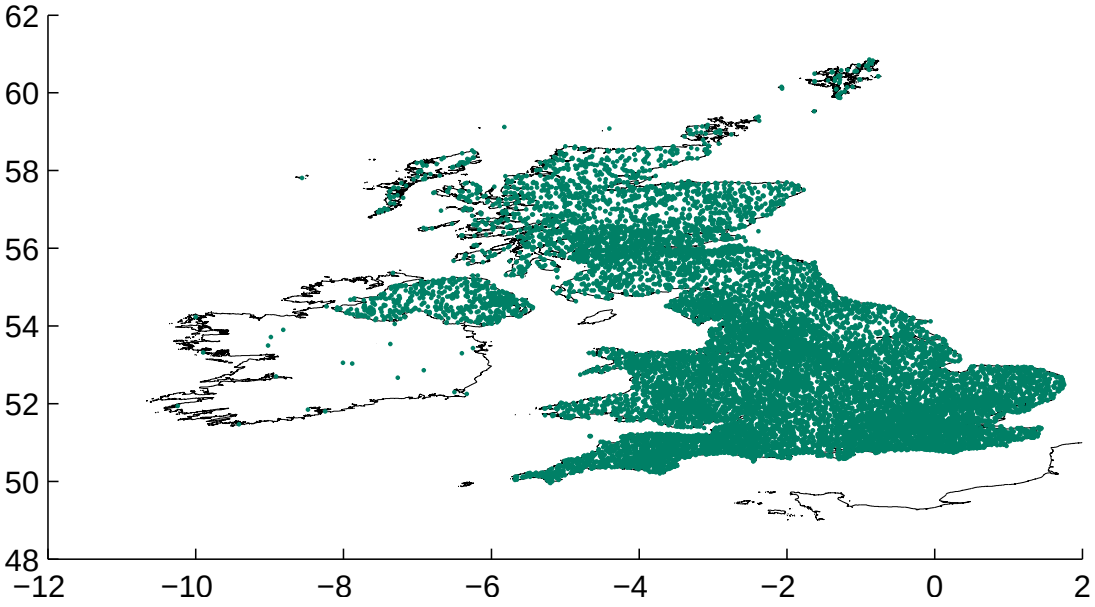

(a) All MIDAS stations.

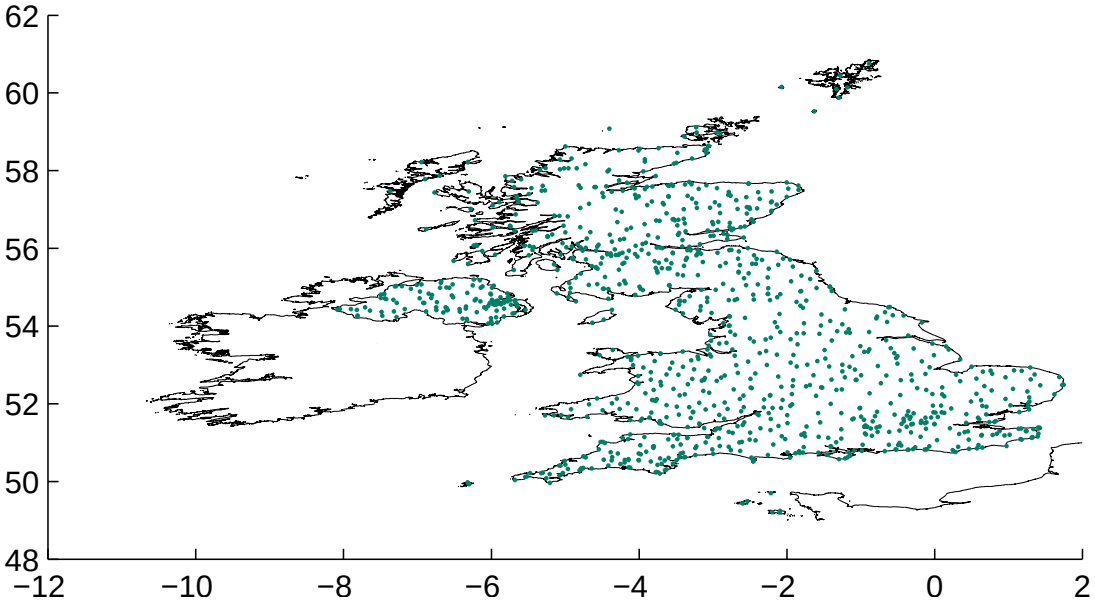

(b) MIDAS stations that record hail observations.

Figure 3.2: UK MIDAS stations.

end of 2013. A description of a "hail day" is recorded at a capable MIDAS station and categorised by World Meteorological Organisation (WMO) codes that can be seen in Table 3.1. Days of hail codes are recorded either in the form of National Climate Messages (NCM), produced from all Met office and many auxiliary stations, or daily observations from climate stations. It is not stated whether stations utilise hailpads or

manual observing practices for recording hail days. In the case where an observer logs the state of the ground, the recorded hail size would its minimum diameter.

Table 3.1: World meteorological code 6001 - NCM table 23 [36].

0 - no hail, ice,etc (0000-2400gmt)
1 - diamond dust
2 - snow grains
3 - snow pellets
4 - ice pellets or small hail (less than 5 mm)
5 - hail (diameter 5-9mm)
6 - hail (diameter 10-19mm)
7 - hail (diameter 5-9mm)
8 - hail (diameter 20mm or more)
9 - no hail, ice etc restricted period

The codes from 1 to 8 show a general increase in particle size. Diamond dust is defined by the WMO as "precipitation which falls from a clear sky in very small ice crystals, often so tiny that they appear to be suspended in the air" [36]. Snow grains are similarly described as "precipitation of very small opaque white particles of ice which fall from a cloud and which are fairly flat or elongated with diameters generally less than 1 mm". Snow pellets, often referred to as soft hail or graupel, are generally conical or rounded and white or opaque ice particles with diameters attaining as much as 5 mm. Ice pellets (small hail) differ in that they can be spherical or irregular transparent particles of ice, which have a diameter of 5 mm or less. A hailstone is reported when the diameter of the largest hailstone observed is 5 mm or more. These are classified further by the appropriate diameter ranges categorised by codes 5-8.

Wind information is reported as an average direction from which the wind is blowing and speed. Speed at UK stations is measured in knots ($0.515\,\mathrm{m\,s^{-1}}$), to the nearest knot. The wind dataset takes measurements that are from the synoptic network (NSYNOP) and climatological wind network.

CFARR Station Data

The facility at Chilbolton has a variety of instruments used to measure precipitation. On the 12th of December 2011, a Campbell Scientific PWS100 weather sensor was installed at the site [113]. This laser based instrument is capable of determining different varieties of precipitation by analysing size and velocity measurement signals. Included in the distinct classifications are hail and graupel (snow pellets). The measurements were taken at intervals of one minute up to the 31st October 2014.

NERC Station Data

The NERC MST dataset utilises a Vaisala Weather Transmitter WXT510 which measures a variety of surface meteorological parameters in three independent measurement cycles. Precipitation is measured by a piezoelectric sensor which has an area of 60 cm^2. Hail accumulation and rate are measured at 10 second intervals. Internal signal processing is used to differentiate between the signals generated by rain, hail and undesired sources. Ultrasound is used to determine horizontal wind speed and direction. Datasets were available from the 21st of December 2007 to the 31st of October 2014, however between 2007 to 2013, the measurements for each year restricted to periods October and December.

3.1.3 Prevalence of Hail in The UK

Seasonality

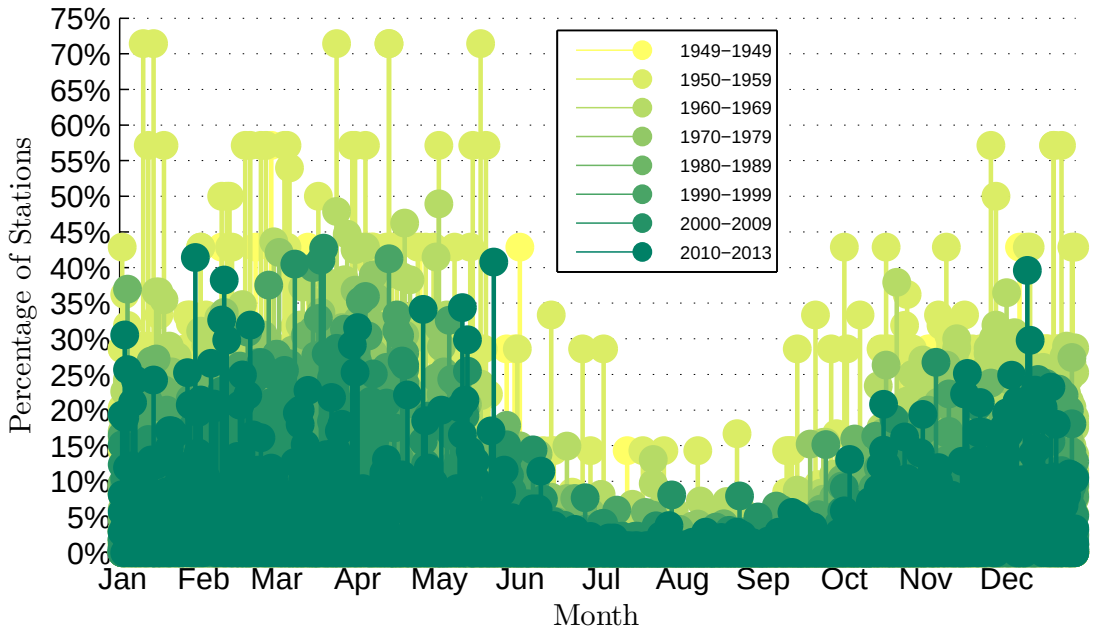

Figure 3.3: Percentage of UK MIDAS stations reporting a "hail day" (1949-2013).

In order for hailstones to form in convective storms, the temperature has to be close to water freezing levels [75]. Consequently, hailstone occurrences at MIDAS stations in the UK are highly seasonal, as demonstrated in Figure 3.3. The percentage of stations reporting a "hail day" is severely diminished over the Summer months for all the years of data. The Winter and Spring periods see increased hail activity, when the temperature in the upper atmosphere is sufficiently cool to develop ice formation but warm enough

on the surface to encourage thunderstorm development. This demonstrates that the NERC facility measurement period (October - December) is likely to miss a large number of hail events.

Figure 3.3 also appears to show a change in reported hail days over the years, indicating a possible change in weather patterns. Alternatively the apparent difference could be a result of the change in the number of operating hail recording stations. Figure 3.4 shows how from decade to decade, the number of observational stations has developed. Notable increases were recorded in 1959, 1971 and 1994. Since 1994 the number of these stations has been in steady decline.

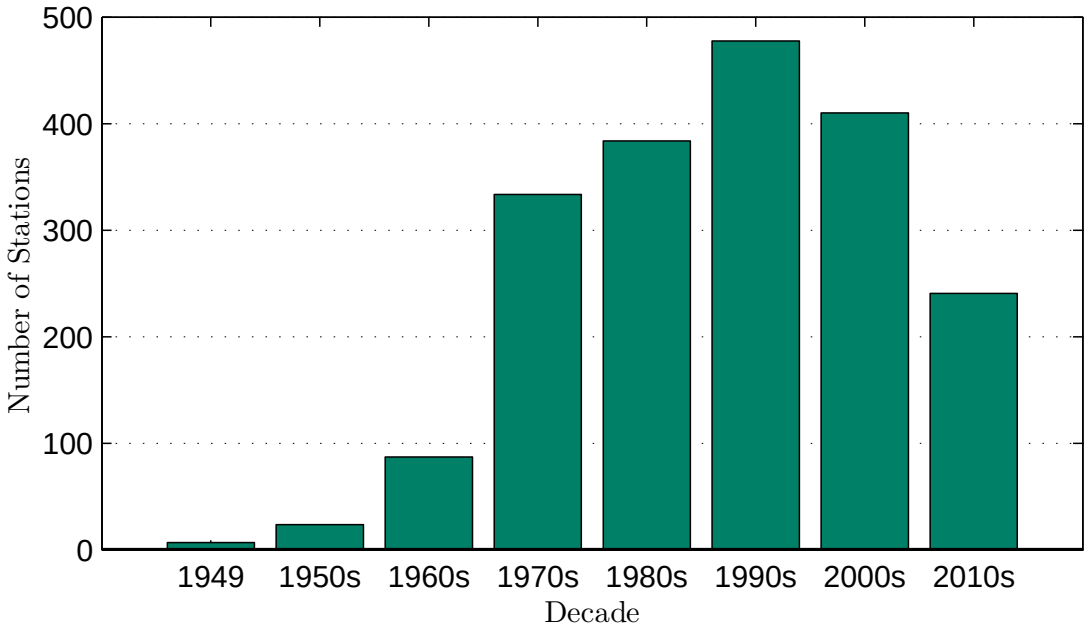

Figure 3.4: Number of hail observational stations over the period of data.

Size Distribution

By analysing the number and type of "hail days" across the United Kingdom from MIDAS meteorological data, an impression of hail occurrence was formulated. Firstly, a distribution of the different hail types was created for the time frame studied, as displayed in Figure 3.5. Inspection of the distribution shows that ice pellets/small hail ($\varnothing < 5\,\text{mm}$) is definitely the most frequent category, with hail ($5\,\text{mm} \leq \varnothing \leq 9\,\text{mm}$) the next ranked. Conversely, the largest hail category, Hail ($\varnothing \geq 20\,\text{mm}$), has the lowest frequency of all the classifications, with only 102 recorded incidents over the entire 65 year period. Hail ($10\,\text{mm} \leq \varnothing \leq 19\,\text{mm}$) is also considerably low in occurrence and Snow pellets/graupel, snow grains and diamond dust make up the remaining rankings

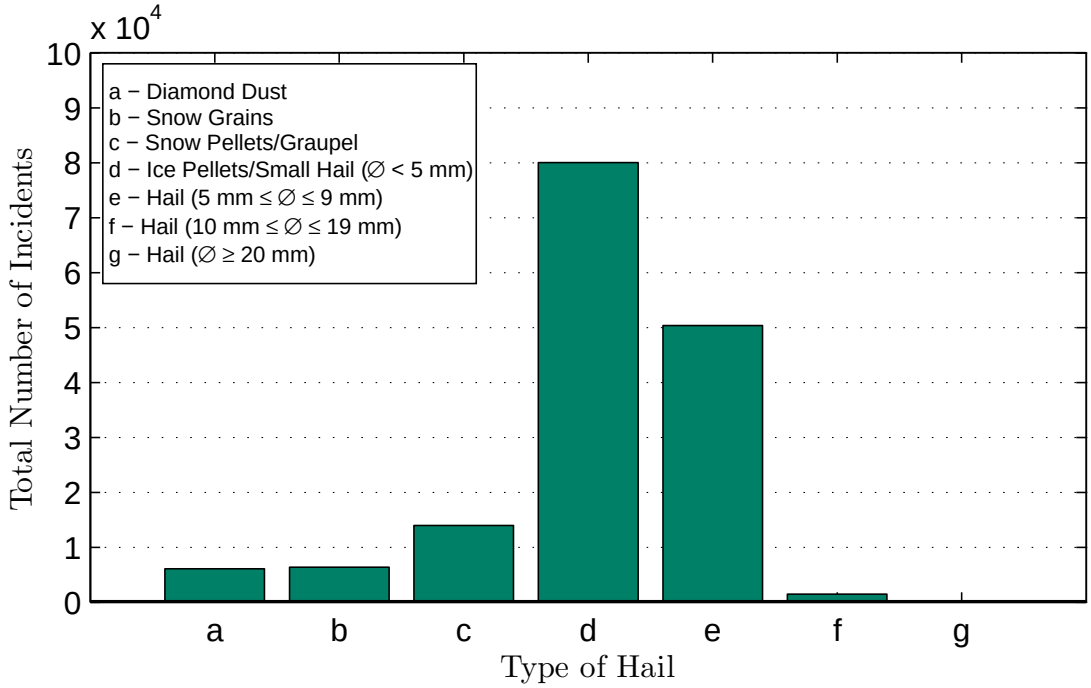

Figure 3.5: Total number of hail incidents at UK MIDAS stations (1949-2013).

of 3rd, 4th and 5th respectively.

Hail Days

The annual number of hail days at each MIDAS station per year were categorised into ranges, with the upper limit defined as stations that experience greater than 30 days of hail" a year on average. These are displayed geographically in Figure 3.6. Wind farm locations across the UK are also presented and scaled according to total wind farm capacity. These were obtained through the renewable energy planning database extract published by the Department of Energy and Climate Change (DECC). It was possible to determine and filter those wind farm locations in operation, as well as those awaiting or under construction [114]. This information was detailed up to September 2014 and was limited to only include farms greater than 1 MW capacity.

The stations that endure the most hail annually are found mainly in the west and north of Scotland, as well as Orkney and Shetland. Noticeably these stations are typically situated near the coast or on islands. There are also clusters of higher frequency stations located in the south west of England and Wales. Locations experiencing little or no hail are evident right across the UK, although there are more cases of hail than not. Areas of high wind farm density are clear, particularly in Northern Ireland, the

central belt of Scotland and north east of Scotland. These do not coincide with regions of frequent hail but there are individual examples where this occurs.

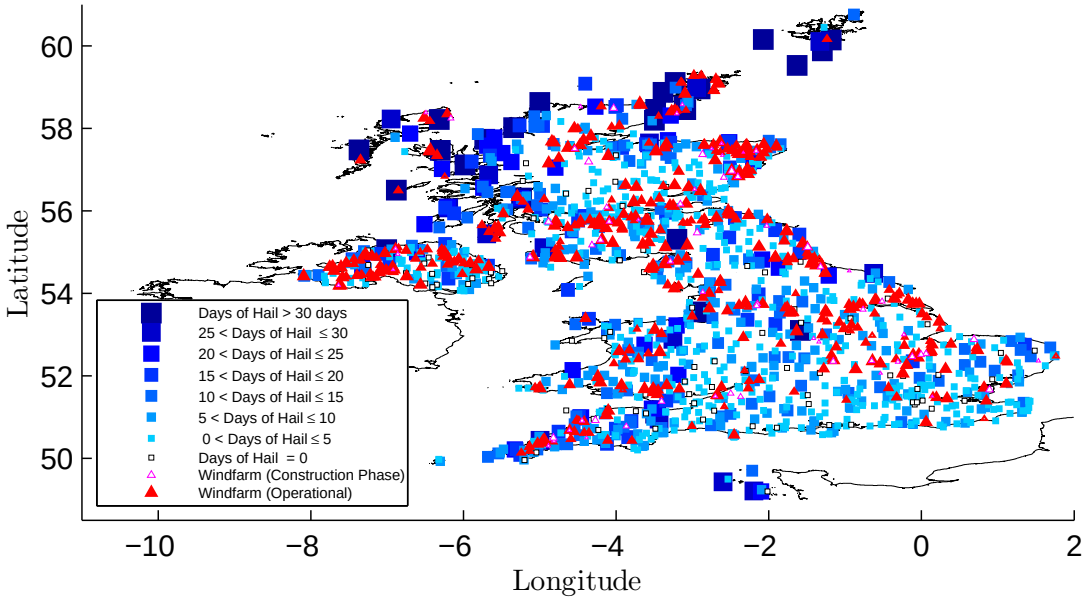

Figure 3.6: Average number of days per year of hail at UK MIDAS stations including position of wind farms.

Coastal Considerations

The coastal observations from Figure 3.6 were investigated and quantified further. Figure 3.7a displays the breakdown of hail experienced at those MIDAS stations separated by a 1 km distance from the coastline. Many of the stations which receive the greatest amount of hail (hail days > 30) are situated closer to the coast. The mean number of hail days per year for these coastal stations is ~ 10.5 compared with ~ 6.5 for those more inland. By increasing the threshold to 5 km, a greater portion of the frequent stations are captured, as shown in Figure 3.7b. Approximately 2.26% of all MIDAS stations receive more than 30 days of hail per year on average. However, the trend for all cases indicate lower occurrences are more commonplace, with the majority of stations subject to five or fewer hail days per annum.

3.1.4 Durations and Rates of Hail

Due to the insufficient resolution provided by the number of days of hail obtained from MIDAS, data from the CFARR and NERC stations was also analysed. Table 3.2 describes the duration of both continuous and non-continuous hailstorms (the former

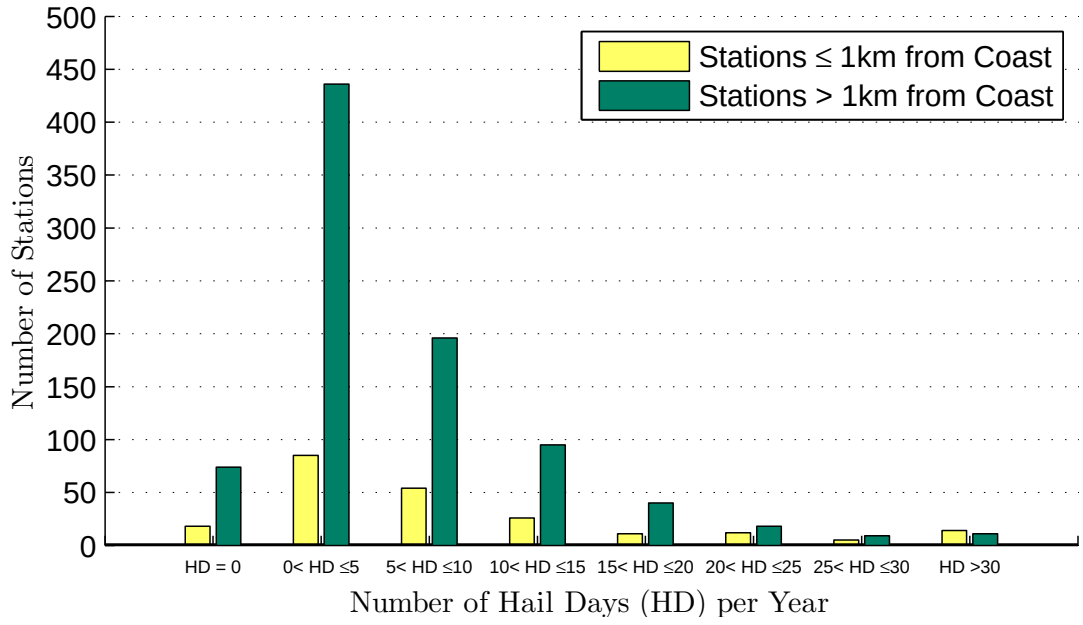

(a) For a 1 km boundary.

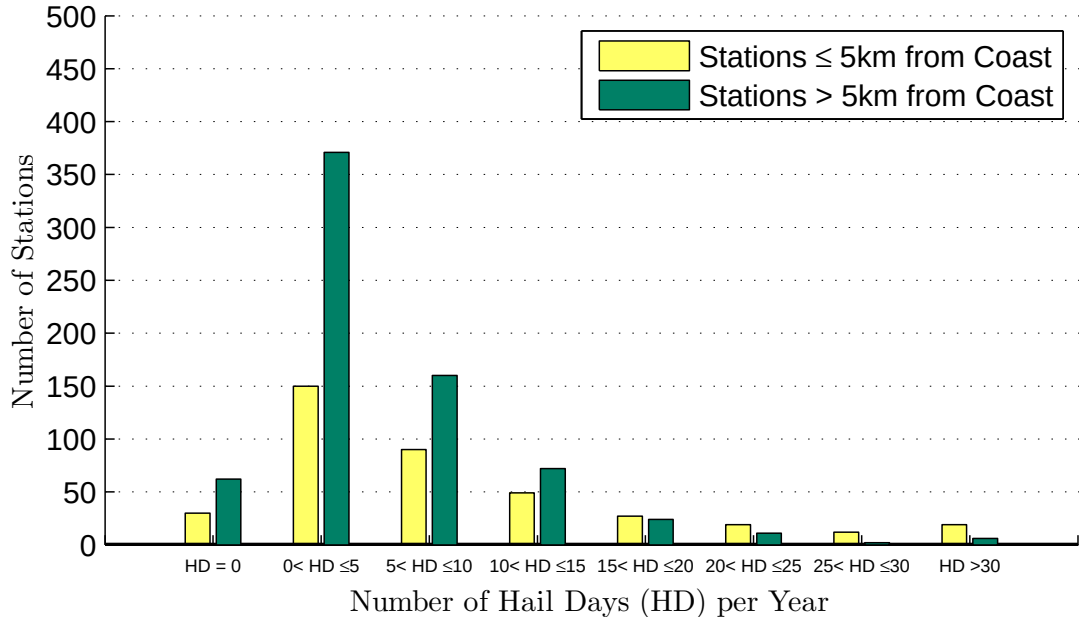

(b) For a 5 km boundary.

Figure 3.7: Number of UK MIDAS stations that experience a range of hail days on average, segregated into groups of those a certain distance from the coast.

defined as interrupted periods within 24 hours of a hail event). Continuous hail is found to last a matter of minutes at both stations, whereas non-continuous instances of hail can last significantly longer with examples of several occurrences on the same

day. Different types of hail are not mutually exclusive, with incidents of graupel and hail occurring during the same intervals at the CFARR observatory. It should be noted that the number of hail days at both facilities is greater than their nearest MIDAS station counterparts. The CFARR station on average experiences 11.66 days of hail (and 4.66 of graupel), with the NERC facility encountering 12 days of combined hail and graupel. The nearest respective MIDAS equivalent records less than a day of hail a year. This observation is magnified at the NERC station where measurements are only taken between October and December and hence likely to miss some periods of peak hail, as demonstrated in Figure 3.3. Unfortunately, the information obtained from these datasets is primarily limited due to the location of these observatory instruments at less prevalent sites.

Table 3.2: Duration of hailstorms at CFARR and NERC observatory stations.

Station	Resolution	Continuous		Non-Continuous	
		Mean	Maximum	Mean	Maximum
CFARR (Hail)	1 minute	1.79 min	10 min	3.49 hr	13.23 hr
CFARR (Graupel)		2.2 min	10 min	3.82 hr	6.55 hr
NERC MST	10 seconds	1.19 min	3.33 min	3.07 hr	17.19 hr

The history of mean hail rate (over the preceding 60 seconds) over time for different hail events can be seen in Figure 3.8. The mean rate of hail measured at the NERC facility ranges from 1 to 21 hits cm^{-2} $hour^{-1}$, with lower rates occurring far more regularly. Those incidents that exhibit high rates of hail still begin at low values and reach a peak rate before decreasing to a diminished intensity and stopping. The start and end hail rates do not exceed more than 4 hits cm^{-2} $hour^{-1}$, with 1 hits cm^{-2} $hour^{-1}$ the most common. Those incidents which last longer than 1 minute, typically involve higher rates in the lifetime of the incident. The total hail accumulation measured by the instrument (accumulation since the last non-zero measurement) over the entire data interval was 3.1 hits cm^{-2}.

3.1.5 Velocity Components

In this section, the likelihoods of the component impact velocities are evaluated. These include the terminal velocity of the hailstone, mean wind speed and the rotational speed of the wind turbine, as previously described in Figure 3.1.

Terminal Velocity

The velocity of both small hail and graupel, measured by the Campbell Scientific PWS100 weather sensor at the CFARR facility is displayed in Figures 3.9a and 3.9b.

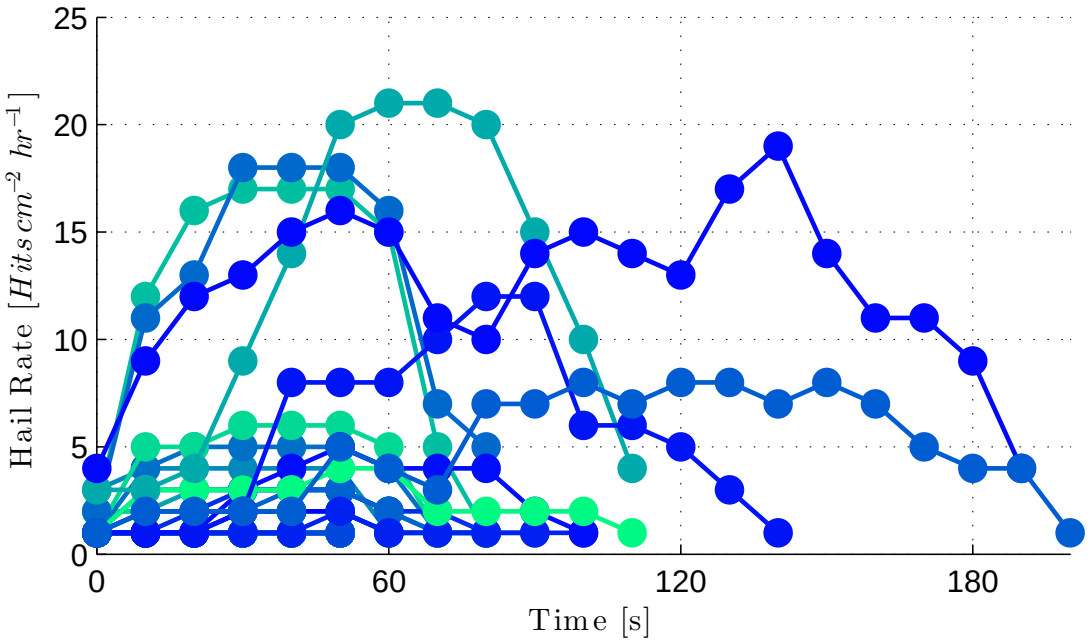

Figure 3.8: Hail rate vs time at NERC MST for separate instances of continuous hail.

Exponential least squares approximations of the trends for both hail types are also exhibited, along with the fall-speed relations from Wisner *et al.* [73] and Ferrier [115], displayed in Table 3.3.

Table 3.3: Summary of fall-speed relations for a range of hail ($_H$) and graupel ($_G$) diameters (D), adapted from Dawson *et al.* [37]. C_d represents the coefficent of drag, ρ_G and ρ_H particle densities and g the gravitational constant.

Author	Category	Fall-Speed Relation	$\mathbf{a_H}$ or $\mathbf{a_G}$	$\mathbf{b_H}$ or $\mathbf{b_G}$
Wisner *et al.*	Hail	$v_{tH} = \gamma \boldsymbol{a_H} D_H^{\boldsymbol{b_H}}$	$\frac{4\rho_H g}{3C_d\rho_a}, C_d = 0.8$	0.5
	Graupel	$v_{tG} = \gamma \boldsymbol{a_G} D_G^{\boldsymbol{b_G}}$	$\frac{4\rho_G g}{3C_d\rho_a}, C_d = 0.45$	
Ferrier	Hail	$v_{tH} = \gamma \boldsymbol{a_H} D_H^{\boldsymbol{b_H}}$	19.3	0.37
	Graupel	$v_{tG} = \gamma \boldsymbol{a_G} D_G^{\boldsymbol{b_G}}$	206.984	0.6384

The Wisner relation represents the method for terminal velocity calculation utilised by Keegan *et al.* [25,111]. Both sets of formulae depend on: the density correction factor $\gamma = (\frac{\rho_0}{\rho_a})^{0.5}$ (where $\rho_0 = 1.204\,\mathrm{kgm}^{-3}$ and ρ_a is the air density), the particle diameter (D), a further parameter $\boldsymbol{a}$ and an exponent $\boldsymbol{b}$. For small hail, the Ferrier relation tends to overestimate the velocity for varying diameters. However, the relation compares considerably better for graupel. The Wisner calculation only shows similarities with the CFARR data at uncharacteristically low densities, for both small hail and graupel.

Both hail types appear to feature higher than expected velocities for lower diam-

eter ranges, resulting in poor least squares approximation trends. This phenomenon was not accounted for by the recent PWS100 optical present weather sensor evaluation conducted by Agnew and Brettle [113]. The average graupel and hail diameters measured at the facility were 2.232 mm and 2.037 mm respectively. This is equivalent to the closest MIDAS station, which primarily encountered hail (diameter 5 - 9 mm) and ice pellets (diameter < 5 mm).

The terminal velocities for a larger diameters of hail and graupel are calculated for each fall-speed relation and displayed in Table 3.4. For Wisner *et al.*, worst case densities are assumed i.e. $500\,\mathrm{kg\,m^{-3}}$ for graupel and $900\,\mathrm{kg\,m^{-3}}$ for hail.

Table 3.4: Example worst case terminal velocities (m/s) for different categories of hail

Author	Graupel ($500\,\mathrm{kg\,m^{-3}}$)	Hail ($900\,\mathrm{kg\,m^{-3}}$)			
	5 mm	5 mm	10 mm	15 mm	20 mm
Wisner *et al.*	6.9429	9.3148	13.1732	16.1338	18.6297
Ferrier	2.5692	6.6464	10.3459	13.4024	16.1044

Wind Turbine Rotational Speed/Tip Speed

The variation of wind turbine power output with wind speed can be seen in Figure 3.10. Modern horizontal-axis designs will start to rotate and generate power at a designated cut-in speed, V_1. The rotor speed is varied with wind speed to maintain peak aerodynamic efficiency. At a certain speed, V_2, the power output is kept at a rated value in order to conform to the limit of the electrical generator. For most models this is achieved by pitching the blades. In order to protect the turbine from excessive mechanical loading, a shut down procedure is initiated at cut-out wind speed, V_3. From this diagram, four distinct wind speed regions are visible: 'below cut-in', 'cut-in to rated', 'above rated' and 'above cut-out'. The variation in rotational speed of the wind turbine depends on both the wind speed distribution at a particular site and the design speeds (V_1,V_2 and V_3) of the turbine.

The choice of nominal rotational speed at rated wind speed that is selected is a major factor, not just in terms of performance but cost. If the rotor radius and power rating have already been determined the rotor torque will be informed by the reciprocal of the rotational speed. The adoption of a high rotational speed would appear to help decrease the drive-train cost and thus that of the supporting structures. However, such an increase has a detrimental effect on the blade out-of-plane fatigue loads.

The tip speed is the tangential speed of the turbine at the tip of the blade. The nominal tip speeds of a variety of different wind turbines greater than 1 MW are displayed in Figure 3.11. Despite the range of design choices between different manufactures, a

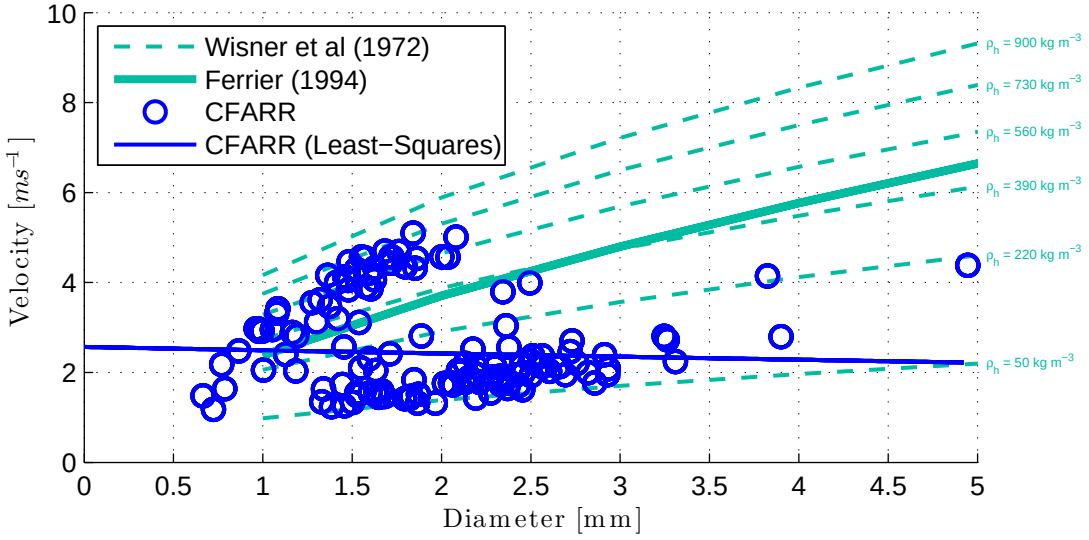

(a) Small Hail

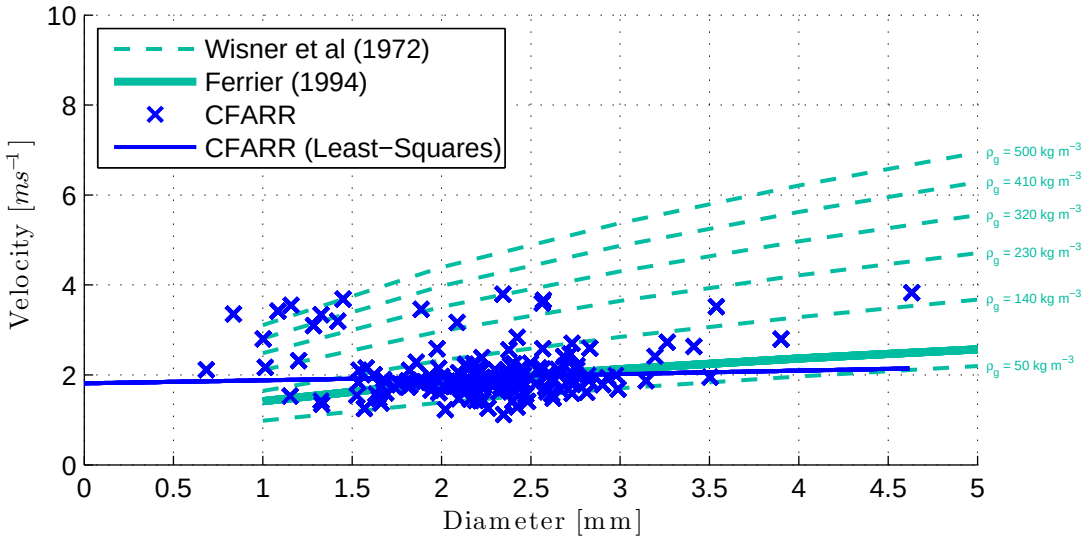

(b) Graupel

Figure 3.9: Velocity comparisons for varying diameter between fall-speed relations and CFARR data.

general trend is observed whereby the greater the size of the turbine, the higher the tip speed will be. Assuming the majority of wind turbines have a cut out wind speed of around 25 m s^{-1}, it is clear that despite the range of design preferences, the rotational speed is the most important factor in defining the severity of the impact velocity. Re-examining the example of Keegan discussed in Section 3.1.1 for a 5 mm hailstone, the tip speed component constitutes between 88.8% and 95.2% of the overall resultant

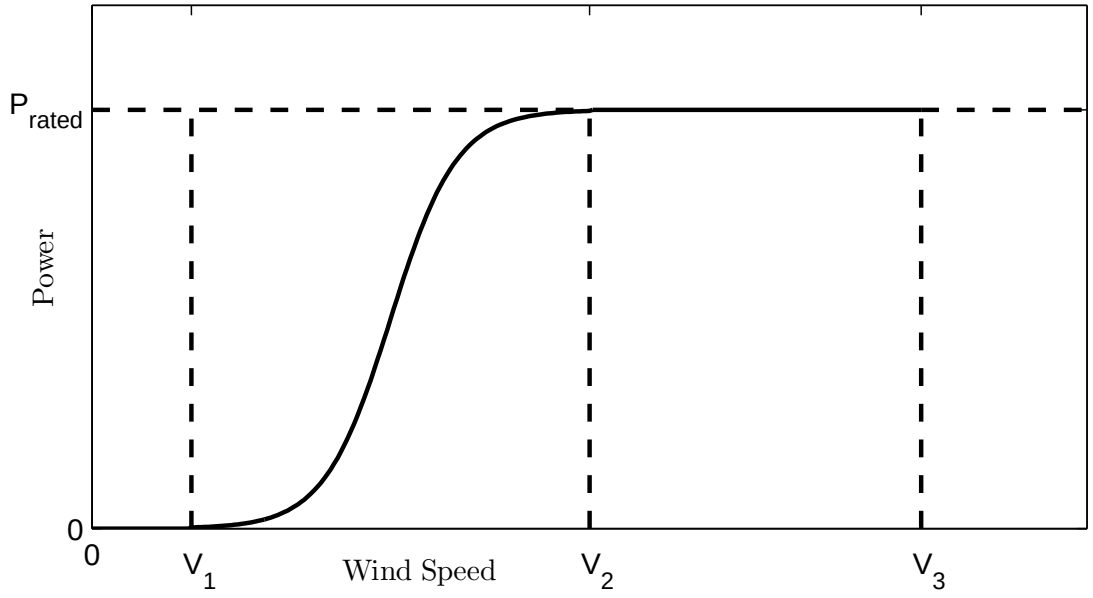

Figure 3.10: Relationship of power and mean wind speed for a variable speed, pitch regulated turbine.

impact velocity in a typical rated range.

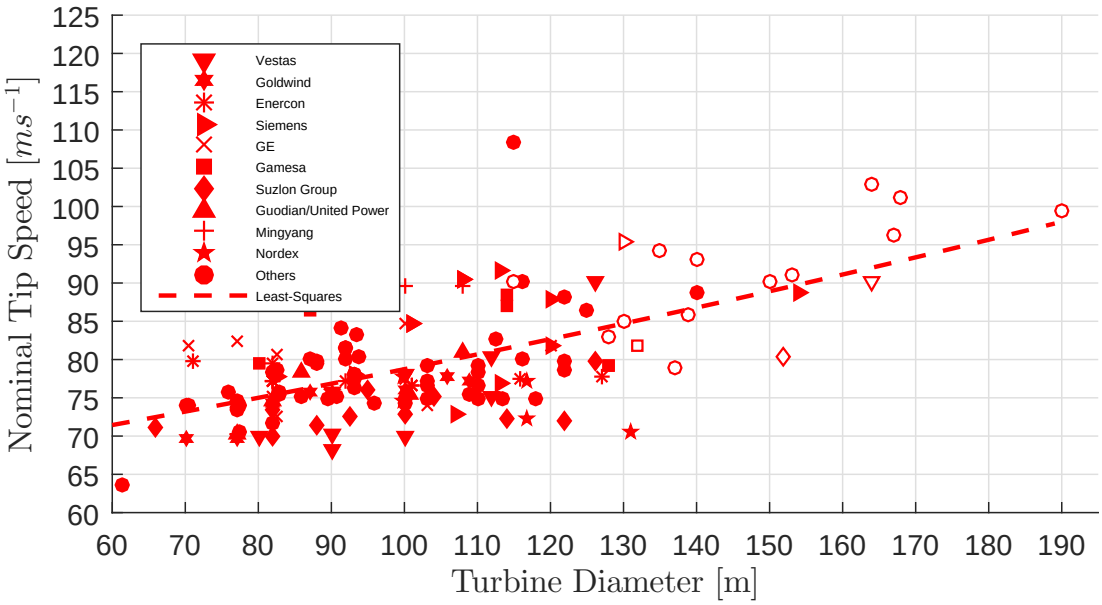

Figure 3.11: Nominal tip speeds and diameters for wind turbines $\geq$ 1MW. Empty markers represent turbines still in the prototype stage or awaiting certification (as of July 2014).

Wind Speed

The Weibull probability density function (Equation 3.1) is often used to represent the variation in mean wind speed for potential wind farm installation sites. Here the probability of the wind speed , $p(U)$, is characterised by two important parameters: a scale parameter, C and a 'shape parameter', k.

$$p(U) = \frac{k}{C}(\frac{U}{C})^{k-1} exp(-(\frac{U}{C})^{k}) \tag{3.1}$$

The shape parameter is related to the annual wind speed and the scale parameter accounts for the variability about the mean. Higher values of k describe a site where the variation of wind speed about the annual mean is small and lower values indicate greater variability, as evident in Figure 3.12. The Weibull distribution is reduced to a Raleigh distribution when the shape parameter takes the value of 2, a fairly typical value for many prospective wind farm locations. The scale parameter can actually be shown to be constant multiple of the average wind velocity $\tilde{U}$, provided that the shape parameter lies between 1.6 and 3 [116].

$$C \approx \frac{2\tilde{U}}{\pi^{1/2}} \quad \text{for} \quad (1.6 \leq k \leq 3.0) \tag{3.2}$$

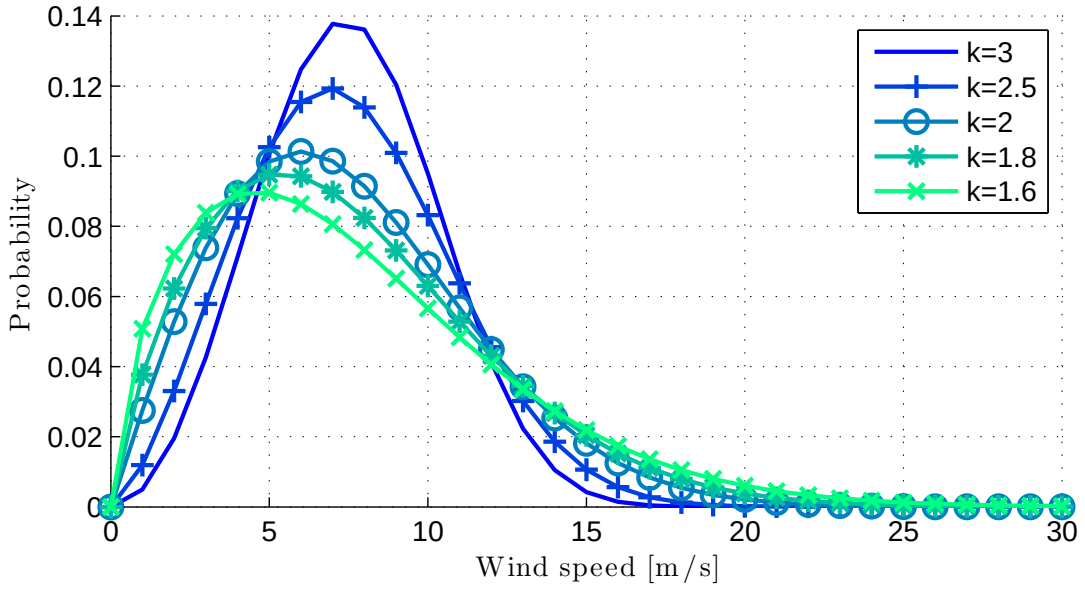

Figure 3.12: Example Weibull distributions of different shape parameters, scale parameter, $C = 8.463$.

Wind turbines are classified in terms of wind speed and turbulence parameters, as shown in Table 3.5, with a view to cover most applications. Although the external

conditions for classes I, II and III are not intended to cover offshore conditions, wind speed and turbulence parameter values remain appropriate as a basis of design of an offshore wind turbine and several commercial machines have classified in this manner.

Table 3.5: Basic parameters for wind turbine classes

Wind Turbine Class	I	II	III	S
V_{ref} (m/s)	50	42.5	37.5	Values
A I_{ref} (-)	0.16			specified
B I_{ref} (-)	0.14			by the
C I_{ref} (-)	0.12			designer

The reference wind speed, V_{ref}, is used to derive other climatic and basic wind turbine class parameters. A turbine of a particular class is designed to withstand climates for which the extreme 10 minute average wind speed with a recurrence period of 50 years at turbine height is *lower* or *equal to* the V_{ref} of that class. The respective annual average wind speed, V_{ave}, is chosen as $V_{ave} = 0.2V_{ref}$. I_{ref} is the expected value of the turbulence intensity, the ratio of wind speed standard deviation to the mean wind speed, at 15 m/s.

Utilising the respective values of V_{ave} in place of the mean wind speed a variety of scale parameters can be calculated using Equation 3.2. Along with a range of shape parameters, an impression of the time spent in each of the regions is identified in Figure 3.10 is formulated. Contrasting cut-in, rated and cut-out speeds from industry turbines are also employed to demonstrate how these design choices can effect the probability of being within a certain wind speed range ($u_1 - u_2$). These speeds often represent the extreme ends of design options, with many modern turbines specifications falling within the range. The probabilities are calculated in the following manner:

$$p(u_1 - u_2) = exp((-(u_1/C))^k) - exp((-(u_2/C))^k) \tag{3.3}$$

For Figure 3.13, u_1 is selected to be 0 m/s and u_2 the choice of cut-in speed (cis). Here the influence of the shape parameter can be seen along the x-axis, with the value of 2 that informs the Rayleigh distribution highlighted. The probability decreases for increasing values of k. For $k = 2$, the probability can range from 0.068 ($V_{ave} = 10\,\mathrm{m\,s^{-1}}$, $cis = 3$) to 0.295 ($V_{ave} = 7.5\,\mathrm{m\,s^{-1}}$, $cis = 5$). The difference in probability for specific values of V_{ave} is more notable for a cut-in speed of 5 m/s, compared with 3 m/s.

Figure 3.14 describes the same arrangement for the region of 'cut-in to rated' speed ($u_1 = cis$, $u_2 = rs$. The probability of being in this region increases with increasing parameter, with diminishing returns. For $k = 2$, the probability ranges from 0.435 ($V_{ave} = 10\,\mathrm{m\,s^{-1}}, cis = 5, rs = 11$) to 0.8387 ($V_{ave} = 7.5\,\mathrm{m\,s^{-1}}, cis = 3, rs = 15$),

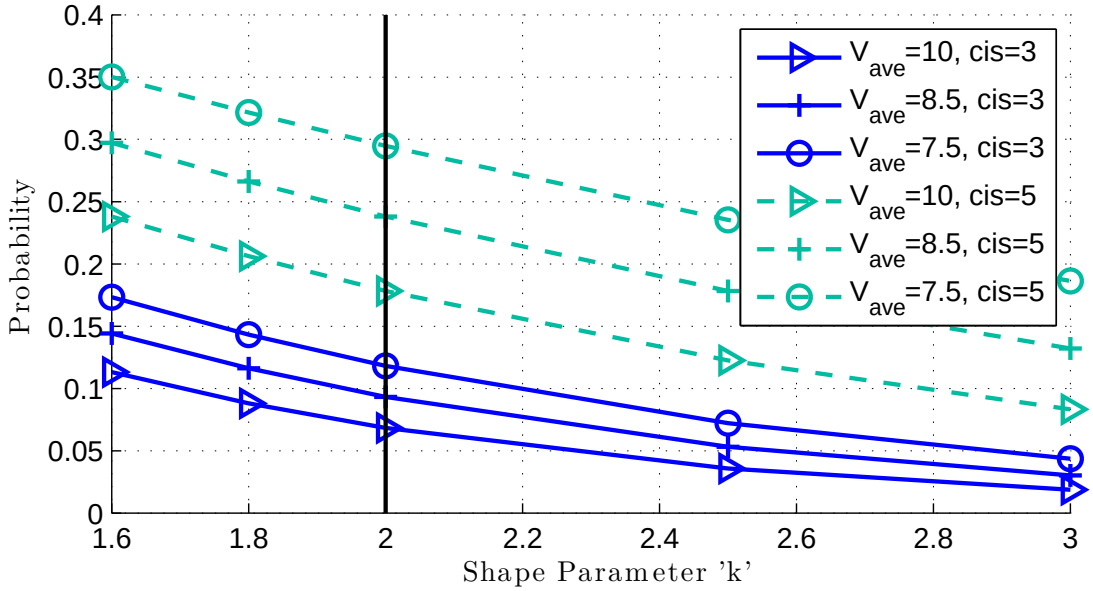

Figure 3.13: Probability of being within the "below cut-in" speed region ($u_1 = 0$, $u_2 = cis$) for different values of shape parameter and V_{ave}.

a considerable difference compared with Figure 3.13. It also appears that the design selection of both the turbine cut-in and rated speed has more of a bearing on the probability than the annual mean wind speed, defined here as V_{ave}.

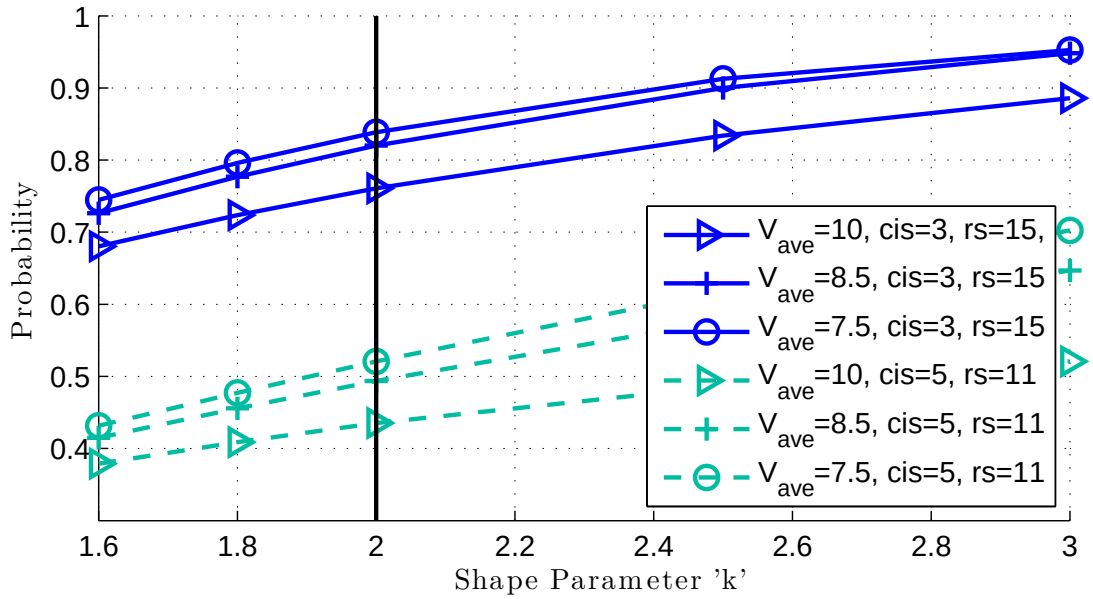

Figure 3.14: Probability of being within the "cut-in to rated" speed region ($u_1 = cis, u_2 = rs$) for different values of shape parameter and V_{ave}.

The range of probabilities for the rated to cut-out region, Figure 3.15, is similar to the below cut-in region. The maximum at $k = 2$ is 0.356 ($V_{ave} = 10\,\mathrm{m\,s^{-1}}, rs = 11, cos = 30$) and the minimum, 0.039 ($V_{ave} = 7.5\,\mathrm{m\,s^{-1}}, rs = 15, rs = 20$). Again the selection of design speeds is key to the probability of being in this region. The influence of the annual mean wind speed is particularly notable for the lower cut-in speed/higher cut-out speed specification. Whereas the shape parameter has less of an impact.

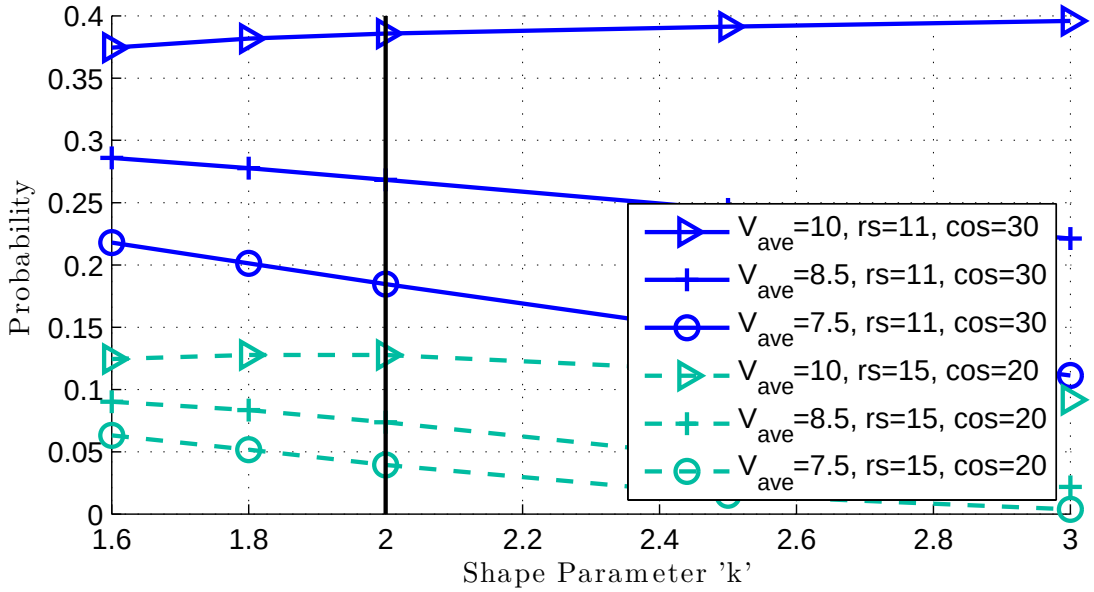

Figure 3.15: Probability of being within the "rated to cut-out" speed region ($u_1 = rs, u_2 = cos$) for different values of shape parameter and V_{ave}.

The probability of wind speed being above the cut-out speed is much lower, as evident in Figure 3.16. At $k = 2$, the probability ranges from 0.0000035 ($V_{ave} = 7.5\,\mathrm{m\,s^{-1}}$, $cos = 30$) to 0.043 ($V_{ave} = 10\,\mathrm{m\,s^{-1}}$, $cos = 20$). Even for a combination of low shape parameter, high annual wind speed and low cut-out speed, the expected time spent in this region would be minimal.

The probabilities in Figures 3.13, 3.14, 3.15 and 3.16 demonstrate the range of likelihoods for standard classes of turbines and plausible wind farm sites. It is evident that regardless of site location a significant portion of the time will be spent between cut-in and rated speeds, where the rotational speed of the turbine will be varied. The expected proportion of time spent 'below cut-in' and 'between rated and cut-out' are comparable, with 'above rated' by far the least likely region.

These wind speed divisions can be evaluated further for example wind turbines. Figure 3.17 describes the breakdown for each section for an onshore class IIa 2.3 MW machine, for different values of k. The proportion of time for each region matches up

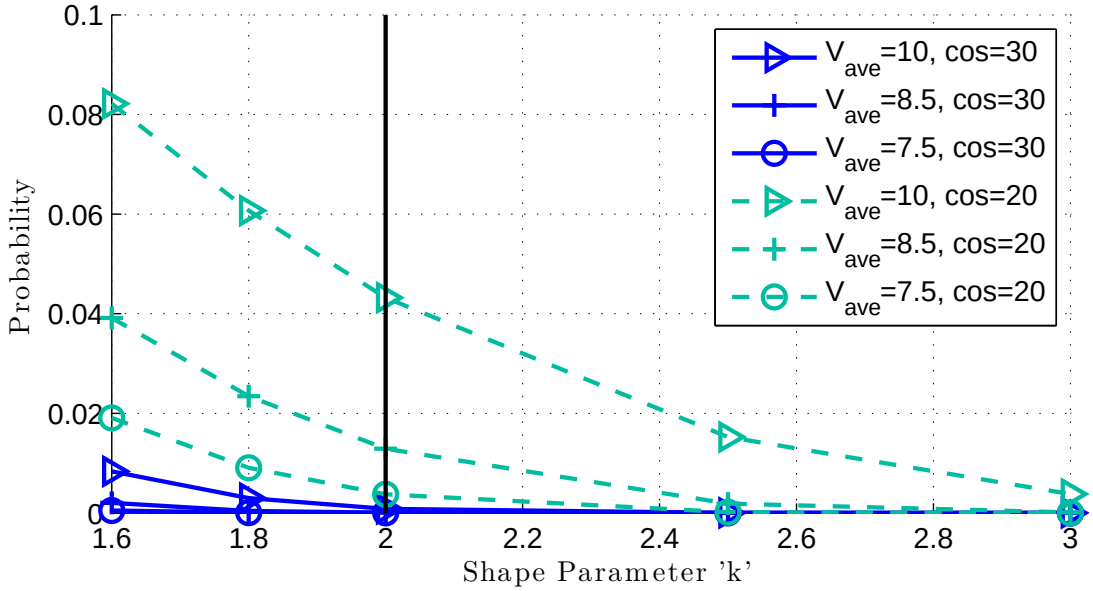

Figure 3.16: Probability of being within the "above cut-out" speed region ($u_1 = cos, u_2 = 50$) for different values of shape parameter and V_{ave}.

with the representation of the previous figures. The fraction of time spent 'above cut-out' speed is barely noticeable. 'Below cut-in' and between $V_1 - V_2$ are similar and both decrease with an increase in shape parameter, whereas, the region of $V_2 - V_3$ increases with greater values of k.

Figure 3.18 shows the same breakdown for a class Ia 6 MW offshore. Again the 'above cut-out' region represents a tiny, albeit slightly increased, fraction of the total. The time spent below cut-in is noticeably less but decreases with increasing k in a similar fashion. The probability for the cut-in to rated speed region is overall slightly less and does not increase as much for higher values of k. However the percentage of time spent between rated and cut-out is considerably more and does not appear to diminish for higher values of shape parameter. In fact the range of probabilities for this region stayed consistently around 0.3 (0.304, 0.312, 0.315, 0.311 and 0.300 for the corresponding k value).

Wind Speed During Hail

The observations made in the previous section apply to general conditions for turbines and wind farm sites. However, these must be extended to particular instances of hail to provide a more detailed representation of impact scenarios. Figure 3.19 describes the average mean wind speeds taken from stations that experience a certain range of hail days per year, with Figure 3.20 describing daily mean speed distributions at those

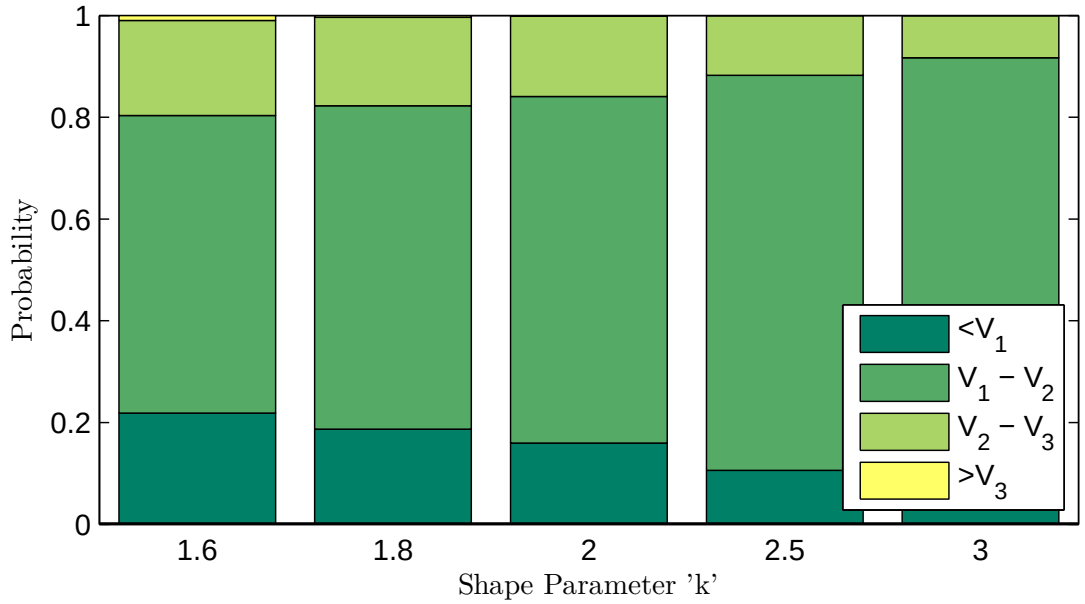

Figure 3.17: Probability of being within design wind speed regions by an example 2.3 MW class IIa onshore turbine for different values of shape parameter.

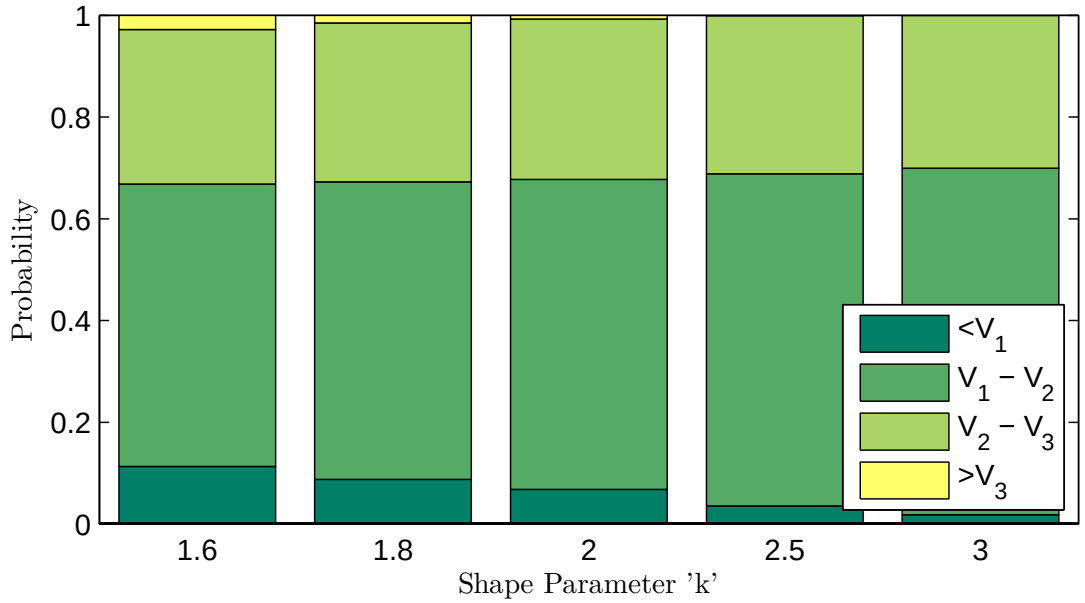

Figure 3.18: Probability of being within design wind speed regions by an example 6 MW class Ia offshore turbine for different values of shape parameter.

stations.

In Figure 3.19, categories 'a' (zero annual days of hail) to 'd' (10 < annual days of hail < 15) do not differ considerably, ranging from 4.68 m/s ('d') to 4.84 m/s ('c').

However, there is a steady increasing trend from categories 'e' (15 < annual days of hail < 20) to 'h' (annual days of hail > 20), with values of 5.09 m/s and 6.46 m/s respectively.

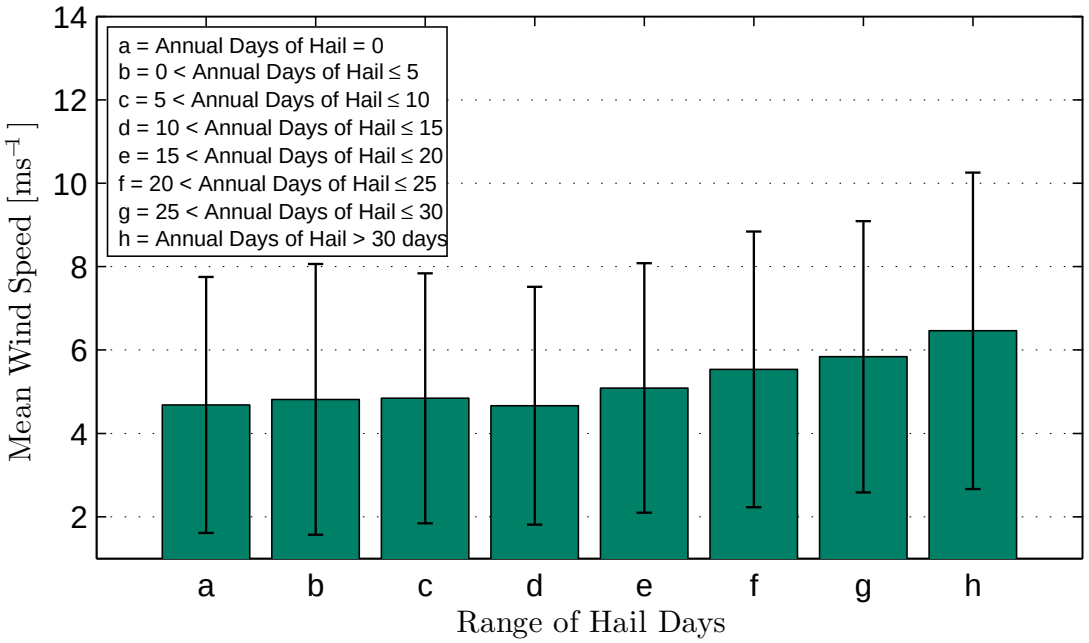

Figure 3.19: Average and Standard Deviation of daily mean wind speed at MIDAS stations subject to a discrete range of hail days on average per year.

Figure 3.20 also shows that those stations which are subject to more hail days show a broader wind portfolio and overall higher mean wind speeds. Increased probability of wind speed around the rated wind speed range (11-15 m/s) is evident for the higher hail contingent, especially for those stations enduring 20 days or more.

Given the continuous durations shown in Table 3.2, it is clear that the resolution of a hail day is not sufficient enough to gain an appreciation of the wind speed during hail events. The instrument installed at the NERC facility can also determine wind speed for the same time periods as the hail measurements at 10 second intervals, enabling the wind speed for instances and absences of hail to be determined. Figure 3.22 shows the mean wind speed for both scenarios. Periods of no hail during the period of measurement show a mean wind speed of 2.18 m/s , whereas for times of hail, the overall mean wind speed was found to be slightly greater at 3.15 m/s. The standard deviation for each case was similar, at 1.8 m/s and 2 m/s respectively. As can be seen from the figure, the wind speed measurements at this site are particularly low. This could be either due to improper placement of the device or simply that the site itself is relatively calm compared with other locations. Consequently in this example wind

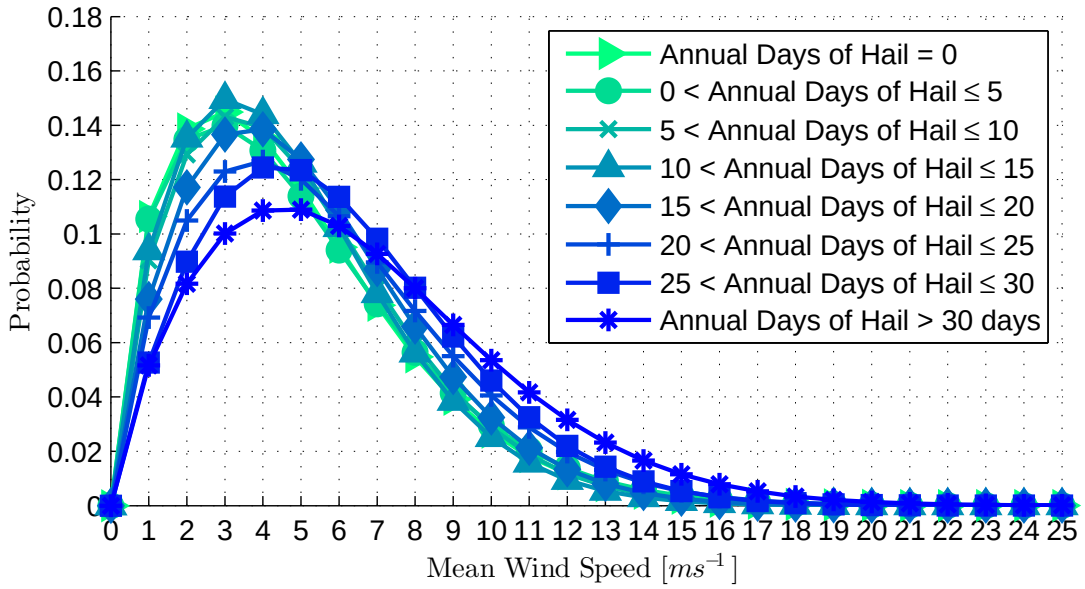

Figure 3.20: Distribution

Figure 3.21: Distribution of daily mean wind speed at MIDAS stations subject to a discrete range of hail days on average per year.

speed distribution did not provide sensible profiles for comparison and discussion.

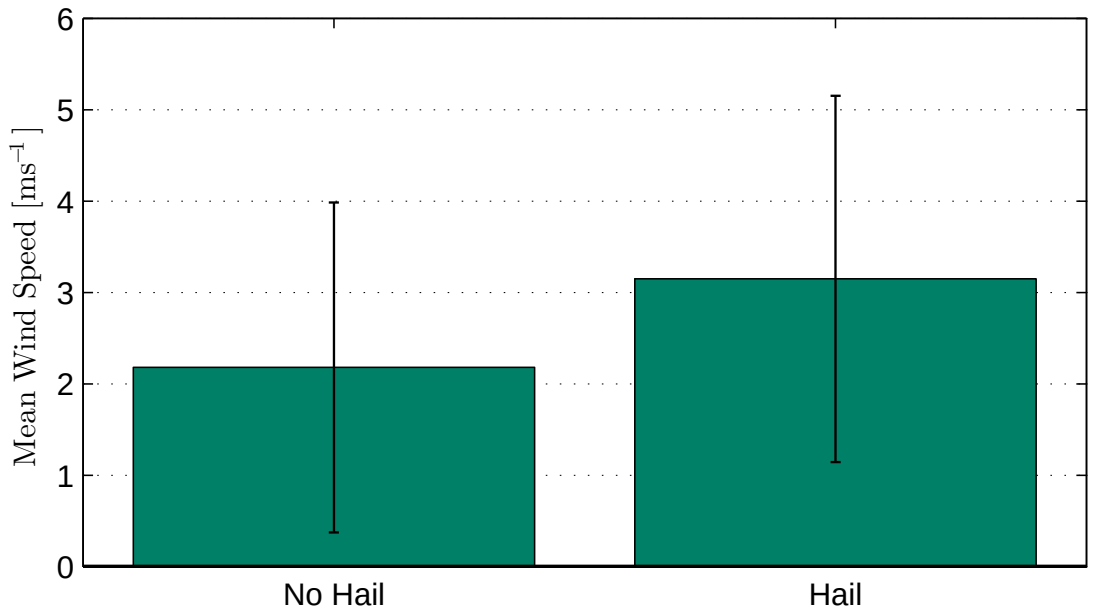

Figure 3.22: Mean wind speeds at the NERC facility for instances of hail and no hail.

3.1.6 Case Studies

Collating all the distributions from the MIDAS stations, an average impact profile for each category of hail was produced, as shown in Figure 3.23a. Standard deviations for each category are included. The profile follows a similar rank to that of Figure 3.5, with categories 'd' and 'e' shown to have the greatest mean number hail days per year: 3.91 and 2.5 respectively. Category 'c' was found to have less than a day of hail a year on average but this would obviously increase over the number of years of operation of the turbine. Categories 'a' and 'b' experience even fewer days of hail and are unlikely to be considered for damage modelling due to their size and composition. The mean occurrence for the larger sizes of hail would represent a one-off unique event in the lifetime of a wind turbine for such a profile in the UK.

To offer a higher frequency case study, the distribution profile of MIDAS station that experienced the highest average number of annual hail days can be used to simulate the upper range number of incidents, as displayed in Figure 3.23b. The number of incidents per year at this station for the three middle categories are considerably more than those shown in Figure 3.23a. Category 'c' is shown to experience approximately 17 more hail days than the national average. Category 'd' is subject to 11 times as much hail, up to 43 days and category 'e' has also increased to around 8 days.

Energy

Combining all the analyses of prevalence, duration and the velocity components of hail impact in the UK, the likelihood of annual hail damage through erosion can be estimated for the case studies discussed in the previous section. As was highlighted in earlier, the possible velocity components can be quite wide-ranging. Hence, for the purpose of analysis and discussion, the worst-case scenario will be employed. Assuming nominal operation of the wind turbine and utilising the high density ($900\,\mathrm{kgm}^{-3}$ for hail and $500\,\mathrm{kgm}^{-3}$ for graupel) Wisner *et al.* fall-speed relations and associated parameters, the kinetic energy for different sizes of hail can be calculated. These are obtained using the formula $T = \frac{1}{2}mu_0^2$, where m is the mass of the hail particle and u_0 the initial impact velocity. Different values of kinetic energy just before impact can be observed for discrete locations along a 2.3 MW blade in Figure 3.24a. Comparable values for a 6 MW blade can also be seen in Figure 3.24b. The kinetic energy for hail of 5 mm diameter is observed to be low for both turbines, with neither exceeding 0.25 J at the blade tip. The contrast between the 2.3 MW and 6 MW turbines becomes greater for increasing diameter, with the impact of 10 mm diameter hail resulting in 1.511 J and 1.928 J of kinetic energy respectively. The difference in kinetic energy along sections of the blade for greater diameters of hail is more prominent. For 20 mm hail impacting a

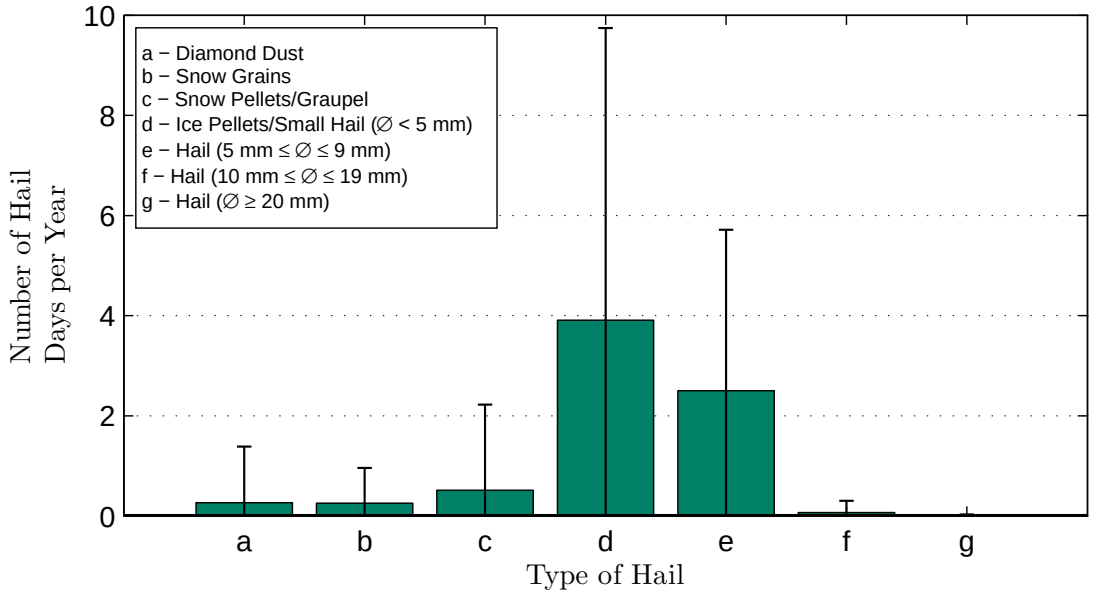

(a) Average and standard deviation from all MIDAS stations.

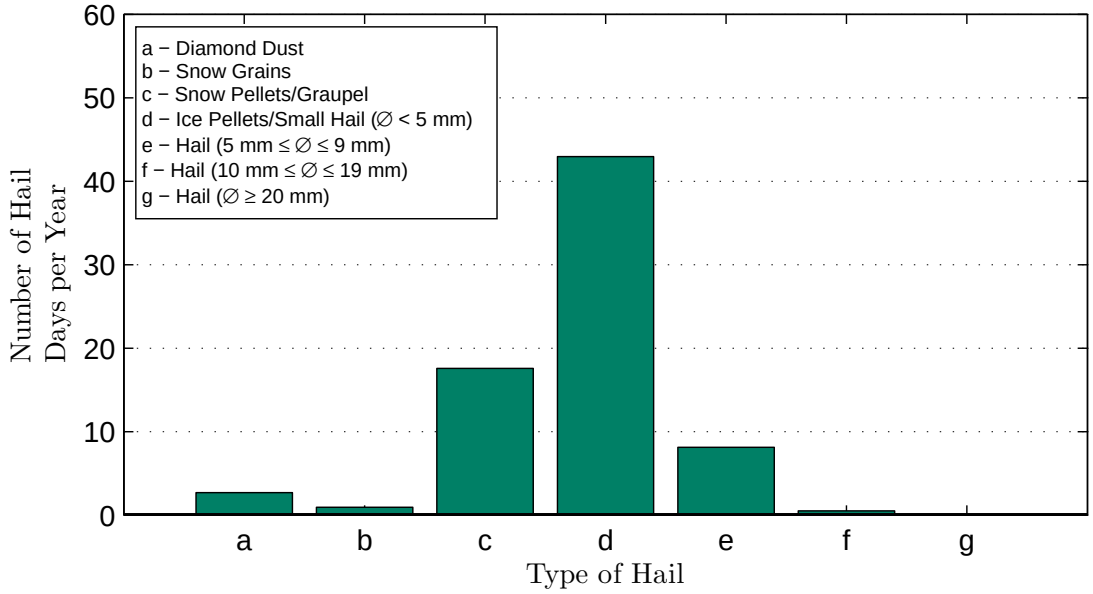

(b) At the MIDAS station with the greatest number of hail days.

Figure 3.23: Incidents per year for different categories of hail in the UK.

2.3 MW, there is an approximate 92% reduction in kinetic energy from the blade tip (12.41 J) to the furthest inboard section (1.087 J). Similarly, the 2.3 MW shows a 93% reduction from 15.76 J to 1.074 J.

For both the mean profile in Figure 3.23a and the high frequency case in Figure 3.23b, the annual average cumulative energies for blade tip impacts by each hail

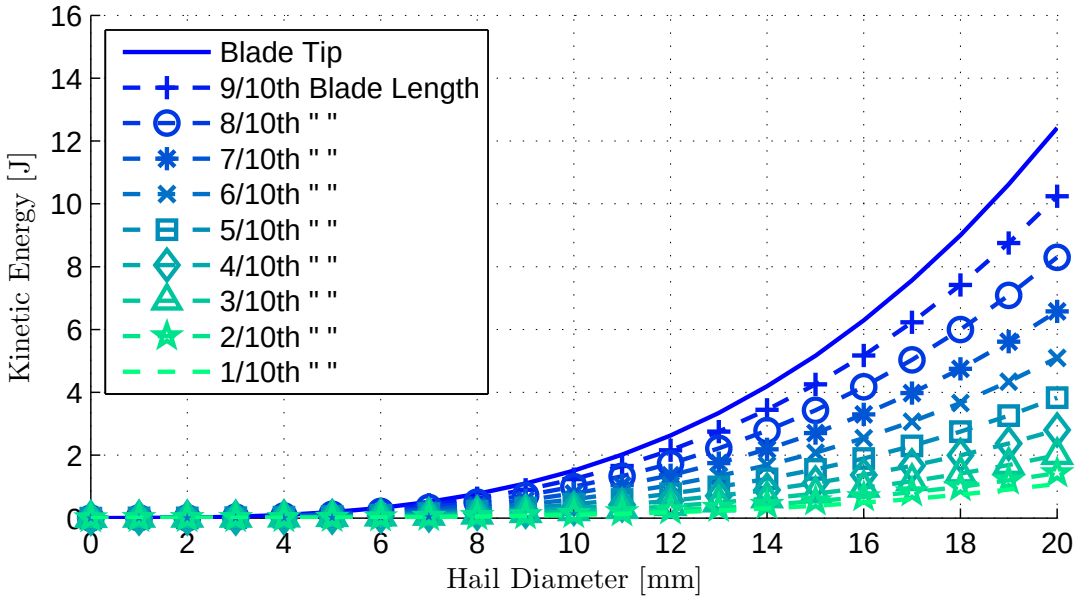

(a) 2.3 MW Onshore turbine

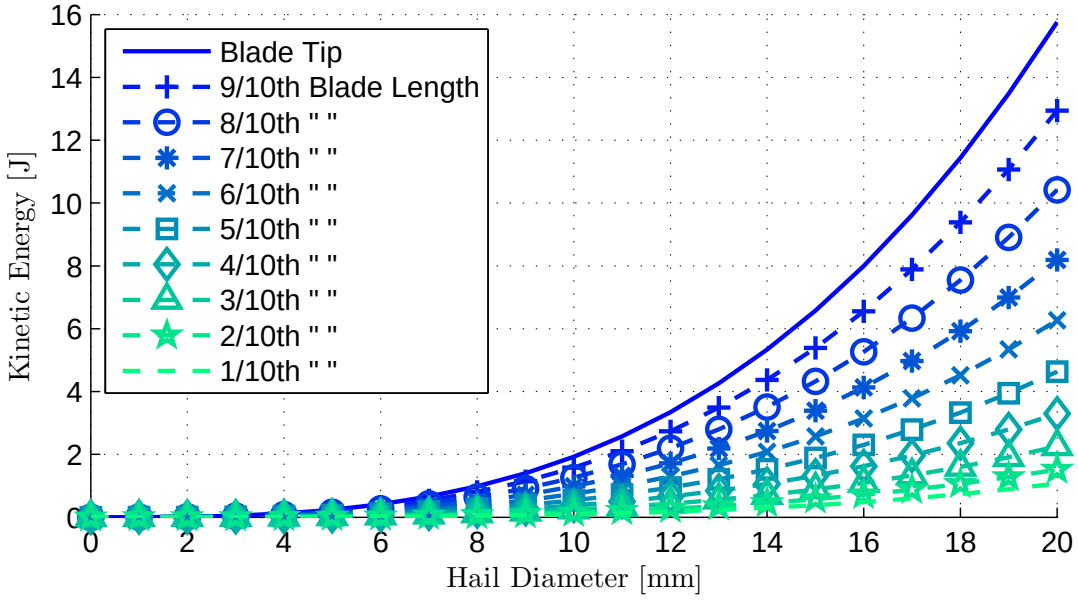

(b) 6MW offshore turbine

Figure 3.24: Kinetic energy of different diameters of hailstone for impact at certain radial positions of a wind turbine blade.

category were calculated. This was performed for impacts of the 2.3 MW and 6 MW and displayed in Table 3.6. Diamond dust and snow grains were excluded from considerations. One impact per hail event and the upper diameter threshold were assumed for each category. Despite being associated fewer number of days of hail compared to

other sizes, 'hail (5 mm $\leq \varnothing \leq$ 9 mm)' contributed the most to the overall cumulative energy for all profiles and turbines, with roughly 65% of the total energy for mean profiles and 39% for the extreme profiles. Lower density 'snow pellets/graupel' contributed the least to the cumulative impact energy with only 0.9% for the mean and 6% for the extreme case. With the most number of days, especially for the extreme profile, the contribution of 'Ice pellets/small hail ($\varnothing <$ 5 mm)' to the total cumulative energy was 12% (average) and 26% (extreme). Conversely, with such a small incidence 'hail 10 mm $\leq \varnothing \leq$ 19 mm' still contributed 29% and 21% respectively. The contrast between the cumulative totals for the average profile and the station with the greatest number of hail days is considerable, with a difference of 12.88 J for the 2.3 MW turbine and 16.44 J for the larger 6 MW example. The comparison between the two turbines is only noteworthy for the extreme case, where a difference of 4.38 J was estimated.

Table 3.6: Impact Energy for different categories of hail.

	Category				Total
	c	*d*	*e*	*f*	
2.3 MW Class IIa Onshore Turbine					
Mean Profile	0.027 J ± 0.090 J	0.372 J ± 0.555 J	1.92 J ± 2.47 J	0.631 J ± 2.11 J	2.95 J
Extreme Profile	0.930 J	4.08 J	6.25 J	4.57 J	15.8 J
6 MW Class Ia Offshore Turbine					
Mean Profile	0.035 J ± 0.116 J	0.477 J ± 0.711 J	2.46 J ± 3.16 J	0.801 J ± 2.68 J	3.77 J
Extreme Profile	1.19 J	5.23 J	7.98 J	5.81 J	20.2 J

3.1.7 Hailstorms

Due to the complex nature of the thunderstorms and supercells that harbour hailstones, hailfall will not be the only form of precipitation or weather phenomenon associated with a hailstorm. Hail-producing storms are also known to release rain and lightning concurrently. Figures 3.25 and 3.26 gives an example of variation in rainfall rate compared to hail measured at the CFARR observatory for the same periods of time.

Figure 3.25 represents the occasion where the highest hail rate was experienced. The trends of the graphs follow each other quite well, with the peaks occurring at roughly the same time. The incident displayed in Figure 3.26 is the longest period of hail at the facility. Although the hail rate seems to vary more over the occurrence, again the overall trend is quite similar. Both exhibit extremely high maximum rainfall rates over these periods of 114.8 mm h^{-1} and 153.3 mm h^{-1}, with the mean rainfall rate equating to 54.59 mm h^{-1} and 94.41 mm h^{-1}.

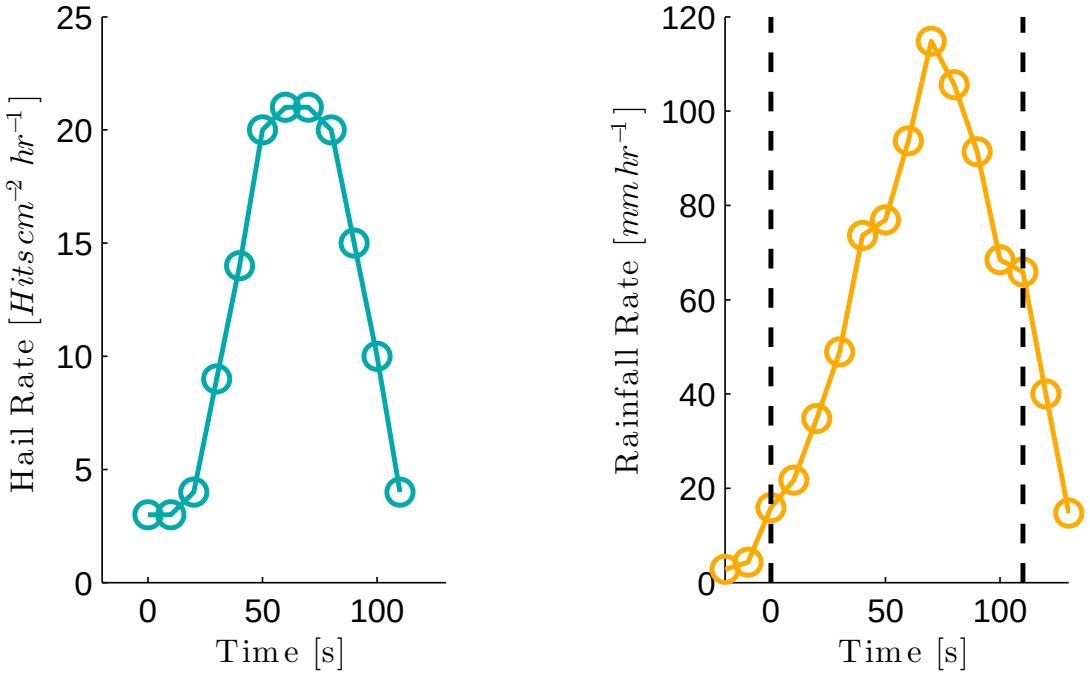

Figure 3.25: Hail rate and rainfall rate for an example hailstorm at CFARR - 26th Novemember 2009

The mean rainfall rate for all the incidents of hail at the CFARR observatory are displayed in Figure 3.27. For synoptic purposes, rain showers are classified as slight, moderate, heavy, or violent for rates of accumulation of about 0 to 2 $\mathrm{mm\,h^{-1}}$, 2 to 10 $\mathrm{mm\,h^{-1}}$, 10 to 50 $\mathrm{mm\,h^{-1}}$, or greater than 50 $\mathrm{mm\,h^{-1}}$, respectively. Only 2.5% of occurrences could be classified as slight and 10% as moderate rain showers, whereas the majority of incidents (57.5%) would fall into the category of heavy and a substantial portion (24%) would be treated as violent rainfall.

Thunder is another form of weather associated with storms that can be analysed with respect to hail using MIDAS weather data. Similar to Figure 3.19, Figure 3.28 displays instead the average number of days of thunder at stations where the number of days per year falls within a certain range. Although not entirely visible in the graph, the mean number of days of thunder at stations where hail does not occur, equates to approximately 0.4 days. This increases to around 3.7 days of thunder for '0 $<$ Annual Days of Hail $\leq$ 5'. No overall trend is apparent, as the remaining categories generally experience between six and seven days of thunder, with the maximum (7.4 days) experienced by those subject to 10 $<$ Annual Days $\leq$ 15 of hail. With the exception of the first category, the deviation is fairly high across the stations.

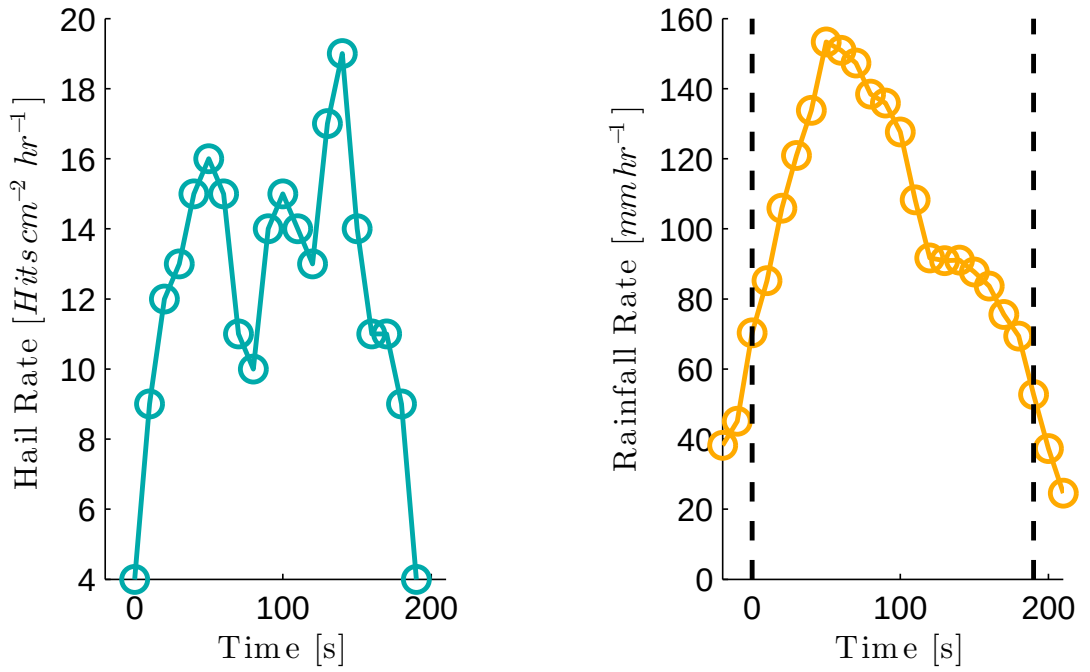

Figure 3.26: Hail rate and rainfall rate for an example hailstorm at CFARR - 13th May 2014

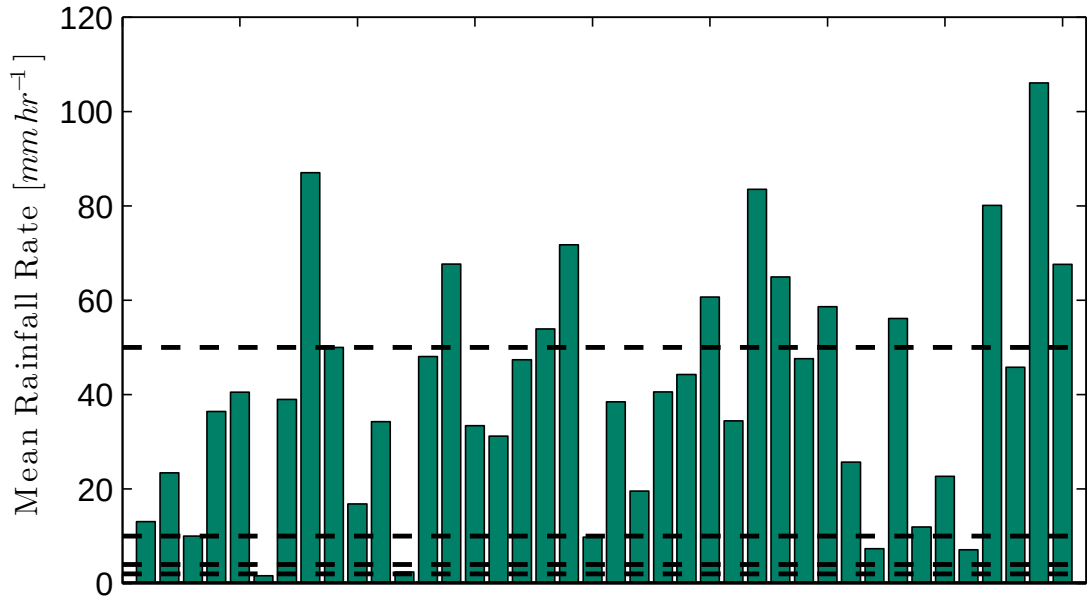

Figure 3.27: Mean rainfall rate for separate incidents of hail at CFARR.

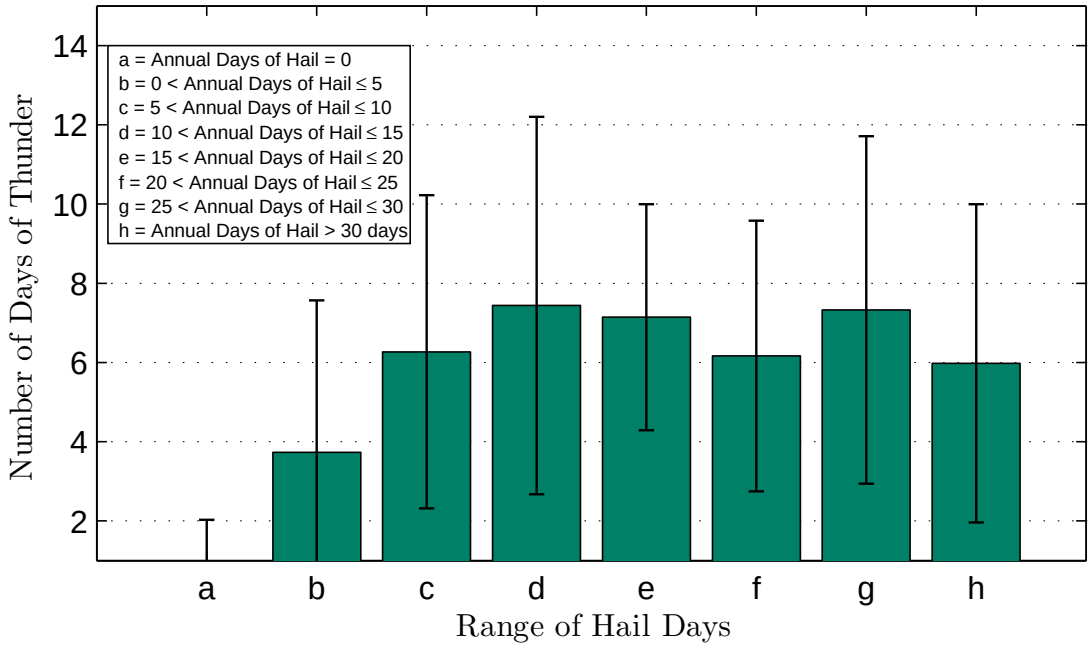

Figure 3.28: Mean and standard deviation of days of thunder at MIDAS stations subject to a discrete range of hail days on average per year.

3.2 Discussion

The combination of conditions required for hailstorms mean that the hail is particularly prone to seasonal variation. It also means that this form of precipitation is far less frequent than rain. Most locations in the UK experience less than 5 days of hail per year on average with those stations receiving high degrees of hail being few in number and noticeably localised. The overlap between these locations and areas of high wind farm density is not highly correlated.

Although hailstorms and extreme hail sizes are not as prevalent in the UK as they are in other countries around the world, similarities can be observed between UK data and other areas. China and the USA provide useful points of comparison, being the top two countries for wind generation and notorious for experiencing a greater quantity of extreme hailstorms. Figure 3.29 describes the maximum hail diameter distribution in four regions of China in a study by Xie *et al.* [28]. Similarly to Figure 3.5 by far the most common categories of hail are the '$\varnothing < 5\,\text{mm}$' and '$5\,\text{mm} < \varnothing < 10\,\text{mm}$', with the latter being the most prevalent in this case. As expected, occurrences of hail '$\varnothing > 10\,\text{mm}$' are more noticeable, with examples of hail '$\varnothing > 40\,\text{mm}$' apparent.

Colorado data gathered in the National Hail Research Experiment can be viewed in Figure 3.30. Cox and Armstrong [29] note that "*the frequency of occurrence of hail*

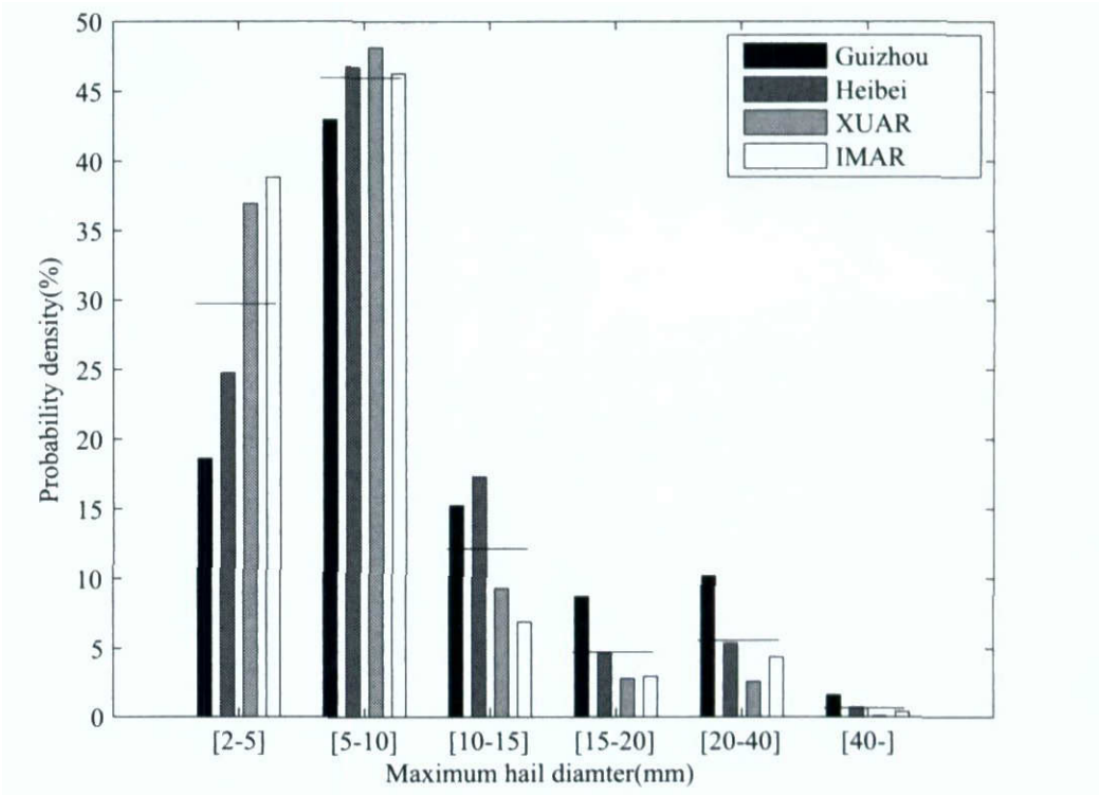

Figure 3.29: Probability of maximum hail diameter for four regions in China [28].

of hailstones larger than 2.5 cm is quite low". In more recent research by Gianmmanco and Brown [64,65], characteristics of severe hail were analysed in separate field studies conducted in 2012 and 2013 for the Insurance Institute for Business & Home Safety (IBHS). Long range numerical weather prediction (NWP) models were used to determine thunderstorms that could potential harbour large hailstones for collection and analysis of compressive stress. Although the aim of the study was to collect hail of substantial size, the diameters collected were particularly large. The average of the mean stone dimensions from the 2012 and 2013 deployments were 23.82 mm and 18.79 mm respectively, with the largest individual hailstones from each year measuring 77.5 mm and 48 mm. These were taken from states in central USA, close to the great plains, that have a history of costly and deadly hailstorms such as Kansas, Oklahoma, Colorado, Nebraska and Wyoming.

The vast majority of hail impact literature has focussed on the risks posed to the aviation industry. The diameters of simulated hail ice and associated impact velocities of prominent experiments in the literature can be seen in Figure 3.31. The velocities investigated often range up to the subsonic cruising speeds of commercial jets (150 m/s to 250 m/s). The tumbling motions of hail mean that centrifugal forces can cause

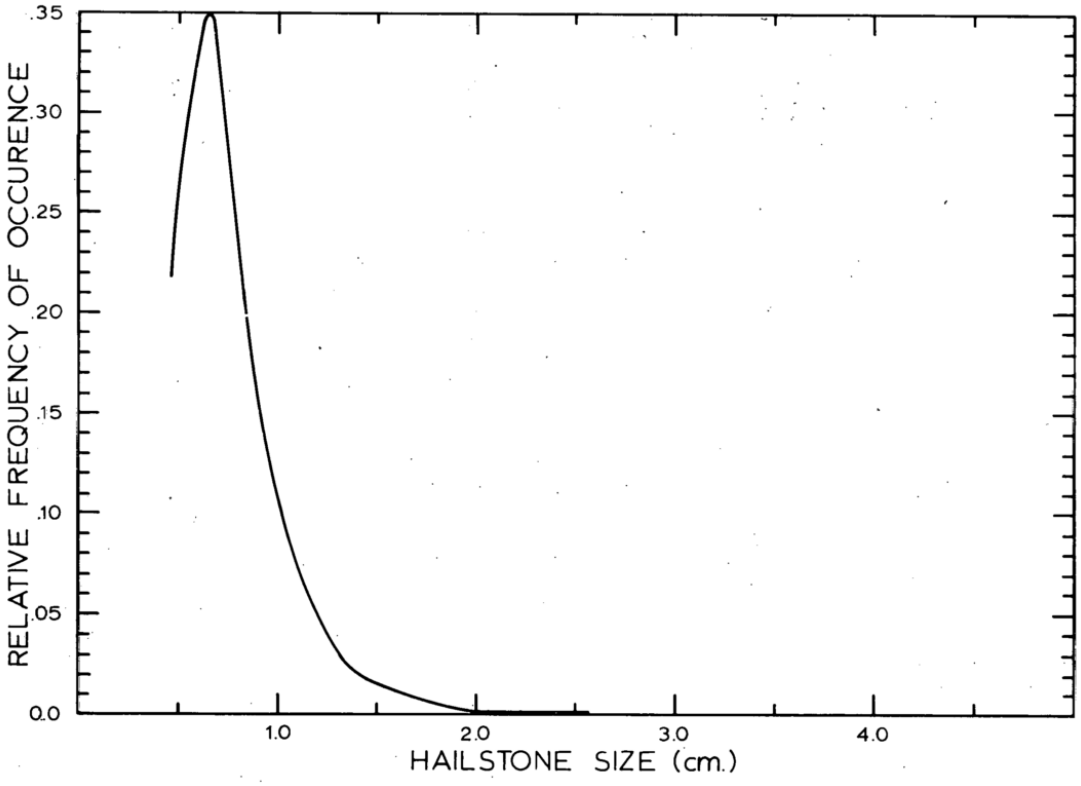

Figure 3.30: Relative frequency distribution of hailstone size (taken from 1972 NHRE data) [29]

shedding of water from growing hail [12]. Thus the hailstones encountered by aircraft is most likely to be of a larger nature than on the ground. Regardless of motivations, the diameters of manufactured hail in the literature have been selected to represent extreme sizes. In the key papers chosen, the diameters can range from 25.4 mm all the way up to 61 mm.

There is a considerable dearth of data in the diameter-velocity range that would be applicable to frequent wind turbine hail impact, as indicated by the red region in Figure 3.31, that would provide a realistic representation of persistent annual impact for the lifetime of many wind turbines.

The translation of the hail data observations to the offshore environment is difficult. as the availability of dedicated hail measuring stations out in the ocean is rare/non-existent. One of the few examples of reference to the phenomenon at sea is an excerpt from a correspondence in 1895 [78]. The evidence from Figures 3.7a & 3.7b suggests that locations of higher frequency of hail in the UK can be found close to the coast. For hail incidence in the tropics [79] there is allusion that hailstorms occur far more regularly over hilly and mountainous terrain, where convective and orographic effects

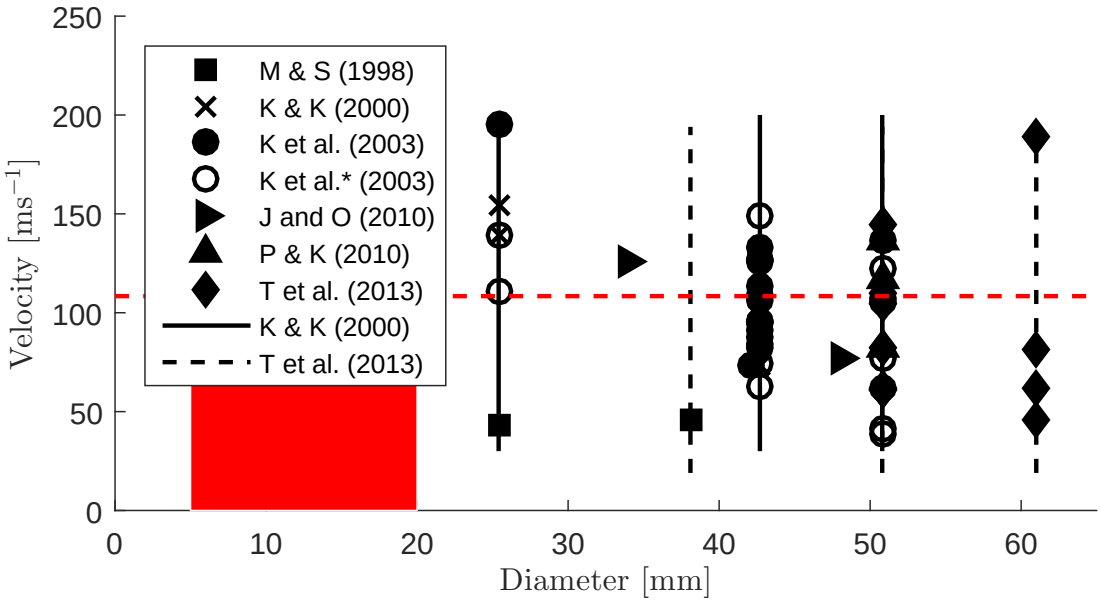

Figure 3.31: Example SHI impact velocities and diameters (M & S - Mahinfalah & Skordal, K & K - Kim & Kedward, K *et al.* - Kim *et al.*, * - estimated, J & O - Juntikka and Olsson, P & K - Park & Kim, T *et al.* - Tippmann *et al.*). Line plots indicate diameter range.

play a major role in the origin, than at sea level. However, the study found that there are some localities where hail evidently occurs fairly frequently at low elevations, whereas there are others in higher elevations in the same general meteorological regime where hail is apparently rare.

The durations of hailstorms are quite short compared to other forms of precipitation, lasting no more than a few minutes continuously. The typical rates of hail combined with the durations imply that the same 1 cm location on the blade is unlikely to be hit more than once during a singular event of hail. Although the units do not make for a direct comparison, the rain accumulation measured by the same instrument for the same interval was 2113 mm. Due to the restricted measuring period, this would be equivalent to 1343 mm annually. This is considerably greater than the hail accumulation of 3.1 hits cm^{-2} over the entire measurement period. The rates of rain from this dataset were on average 1.792 mmhr^{-1} but maximum rates can be well in excess of 100 mmhr^{-1}.

The difference between the CFARR experimental data and terminal fall speed relations is disconcerting. Without a greater quantity of measurements, especially at higher diameters, it is difficult to ascertain if the instruments used are at fault or whether the fall relations are indeed overestimating the terminal velocity. However, it is not unreasonable to suggest that the actual terminal velocities for a range of diameters are in

indeed less those observed in Table 3.4.

From both the MIDAS dataset and the data retrieved from the Vaisala Weather Transmitter WXT510 at the NERC facility, a greater understanding for the wind speed during hail events is formed. Although the hail day does not provide adequate precision for the length of hailstorms, the wind speed distributions at the categories of MIDAS station do provide an impression of the likelihood. The wind speeds collected at the NERC facility are more interpretable due to the resolution of measurement. They indicate that the wind speed is higher during hail events, although the average wind speeds measured are notably low. The contribution of the wind speed component to the overall impact velocity is perhaps less consequential compared to the influence it has on the rotational speed of the turbine.

The weather profiles presented provide a range of possible impact scenarios. The contrast between the number of days for the mean and maximum prevalence case studies for ice-pellets/small hail $\varnothing < 5\,\text{mm}$ is quite profound and the difference suggests these extreme prevalences are actually quite rare. The number of days of larger sizes of hail is more similar for both mean and maximum profiles alike. The annual impact energies derived from these profiles provide an interesting prognosis as to the likely damage experienced by such case studies by comparing them to Failure Threshold Energies (FTE) provided in the literature. Although this also depends on the composite make-up, lay up orientation and thickness, it still serves as an indicator. Interestingly enough Kim *et al.* [18] found that impacts by smaller diameter SHI were more severe than larger SHI for a given composite thickness and show lower FTE values. Appebly-Thomas *et al.* [35] found this to be in the region of 72-140J for carbon fibre reinforced polymers of nominal thickness of 3 mm and 4 mm. For carbon fibre pre-preg of thickness ranging from 1.42 mm and 2.62 mm, Kim *et al.* [18] found that for glancing impact the values of FTE were even higher (see Figure 3.32), which may apply to a number of impact conditions.

The main purpose of this ancillary investigation is to highlight the possibility that other, indirect forms of damage will be enhanced during times of hailstorms. The subject of wind turbine rain erosion is perhaps a more involved topic in itself, as evident in the research by Keegan *et al.* [94] and will not be discussed in detail here. However, the average rainfall rates associated with such incidents are significantly high and such locations with high occurrences of hail could be at risk to the effects of considerable rain erosion. It appears that sites of very low or no hail may experience less thunder and thus less possible lightning damage. However, the trend does not seem to worsen for those with higher or extreme prevalence.

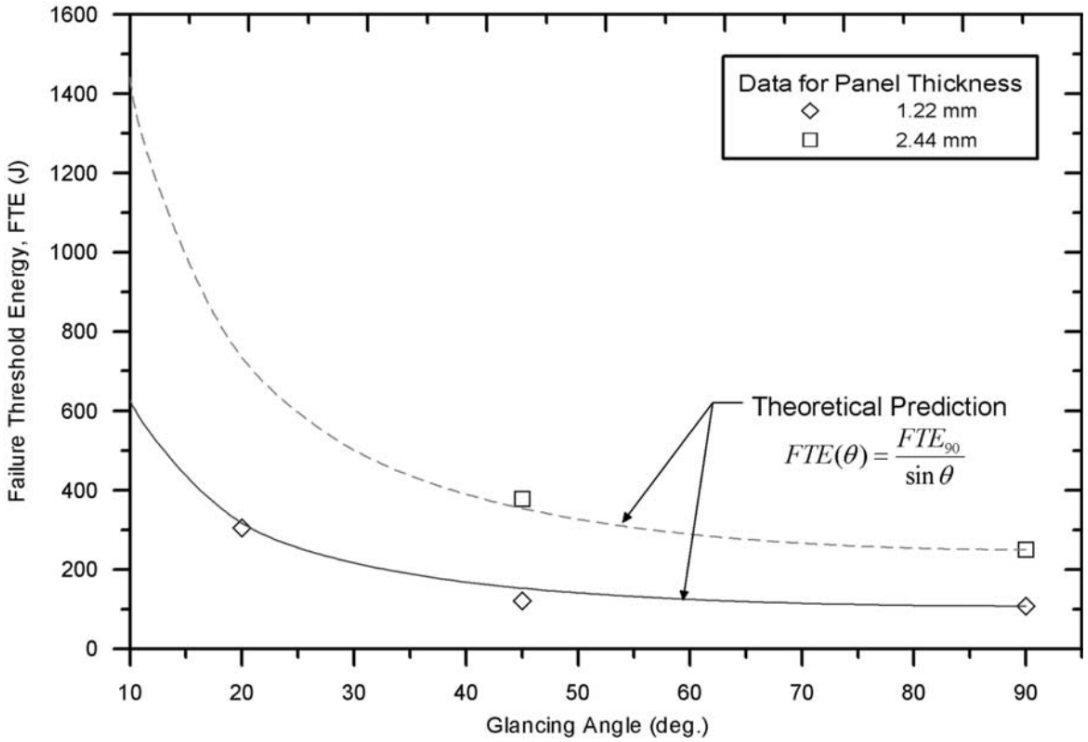

Figure 3.32: Change in failure threshold impact with glancing angle [18].

3.3 Conclusion

The analysis of weather data provides an important link between hail impacts occurring on practical, industrial wind turbines and those analysed in a laboratory setting or using computer simulations. Accurate data on hailfall is difficult to obtain because of the infrequent and short duration of precipitation. What data is available is limited by seasonality and location of measurement. This chapter describes the analysis, not previously undertaken, of a combination of UK weather datasets (MIDAS, CFARR and NERC stations) that provide different hail characteristics to provide a more complete understanding of hailstone impact relating to wind turbine operation. The potential for other forms of damage such as lightning and high-rates of rain during hailstorm events are also highlighted.

From the meteorological data investigated, ice pellets/small hail (diameter < 5 mm) is the most frequent category of hail experienced by MIDAS stations. Incidents involving diameters of hailstones greater than 20 mm are very rare events, with only 102 incidents recorded over the entire 65 year period. The majority of stations experience fewer than 5 days of hail a year, with both an average and a maximum incident profile per year developed. The stations that endure more hail are found mainly in the north

and west of Scotland. These stations do not correlate with the areas where wind farms are most prominent but there are individual examples throughout.

The contribution of the tip speed to the overall impact velocity is underlined, as is the percentage of time spent at rated operation. The difference between an example onshore and a larger offshore is also noted. The wind speed is found to be greater at stations experiencing more frequent hail days, which indicates that rated operation of wind turbines will be more likely at these stations. As well as directly influencing the rotational speed, the wind speed will also inform the pitching of the blades. As impact angle is an important variable in erosion of materials, a range of impact angles on the turbine blade should be considered.

For a study with a high frequency of hail, the average annual cumulative impact energy was calculated to be approximately 16 J and 20 J at the blade tip for two different turbines. For this exceptional case, the early signs of damage would not be expected until a wind turbine blade, composed of carbon fibre-reinforced polymer, has experienced multiple years of impact. There is a gap in the literature regarding the implications for blades constructed using glass fibre, which subsequent chapters will attempt to address.

Chapter 4

Experimental Simulations of Hail Impact on Composites

List of Symbols

Symbol	Definition	Units
$_M$	measured (subscript)	
$_T$	theoretical (subscript)	
$_c$	composite (subscript)	
$_f$	fibre (subscript)	
$_m$	matrix (subscript)	
ρ	mass density	$\mathrm{kg\,m^{-3}}$
α	thermal diffusivity	$\mathrm{m^2\,s^{-1}}$
A_w	fibre area weight	$\mathrm{kg\,m^{-2}}$
F	Force	N
L	characteristic length	m
T_i	initial temperature	°C
T_0	target/final temperature	°C
T_{inf}	environmental temperature	°C
V_f	volume fraction	
V_w	weight fraction	
V_v	void content	
c_p	specific heat capacity	$\mathrm{J\,kg^{-1}\,K^{-1}}$
h_c	heat transfer coefficient	$\mathrm{W\,m^{-2}\,K^{-1}}$
k_c	thermal conductivity	$\mathrm{W\,m^{-1}\,K^{-1}}$
m	mass	kg
n	number of layers	
p	pressure	bar
r	radial position	m
r_0	radius	m
t	thickness	m
u_0	velocity	$\mathrm{m\,s^{-1}}$

4.1 Introduction

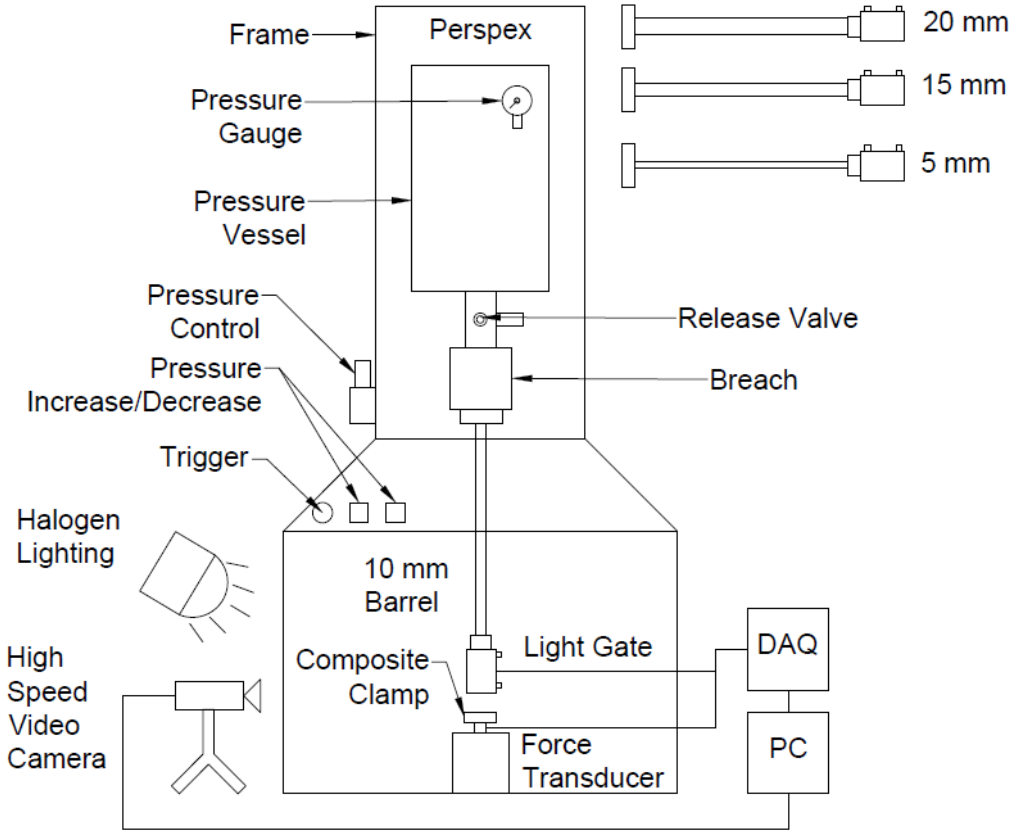

Figure 4.1: Schematic of hailstone impact experimental rig.

After creating an impression of hail impact scenarios through the investigation of UK meteorological datasets, incidences of hail on composite materials were examined experimentally. Hailstones were fired at the composite samples using a vertically-orientated experimental rig, as displayed in Figure 4.1. Variable speeds were achieved by altering the pressure level in the vessel/chamber. Hailstones of different sizes could be fired through the use of detachable barrels of differing diameters, shown in Figure 4.2. In order to execute the experimental research, the implementation of key requisite tasks had to be undertaken:

1. Manufacture of hailstones.
2. Assembly of hail rig measurement equipment.
3. Requisition of appropriate composite samples.

4. Creation of a realistic and consistent experimental protocol (including hail rig calibration and examination of impacts using high-speed video).

This sections are detailed extensively below, before the main methodology and the effects of damage are analysed.

Figure 4.2: Detachable barrel with light gates affixed for measurement of velocity.

4.2 Simulated Hail Ice Manufacture

The manufacture of simulated hail ice (SHI) requires the careful and stringent following of procedures in order to ensure the quality and consistency of the projectile. With environmental temperature being a particular concern, time management becomes even more imperative to the process. Simulated hail ice of different diameters was created using two PTFE polymer mould-halves. Four different diameters of SHI were possible: 5 mm, 10 mm, 15 mm and 20 mm. The 10 mm diameter mould had the capacity to create 10 spheres. The calculated volume of each individual particle can be seen in Table 4.1. This provides a rough prediction of the volume of liquid required for insertion and freezing.

Table 4.1: SHI Volumes.

Diameter	Volume
5 mm	0.0655 ml
10 mm	0.524 ml
15 mm	1.767 ml
20 mm	4.189 ml

After the two halves had been fixed together using guiding pins, they were then fastened together using two clamping plates with fixing bolts and nuts. The bolts were screwed tightly to ensure a secure seal between the two halves and prevent leakage. Washers were also used between the nuts to protect the clamping plate from constant use.

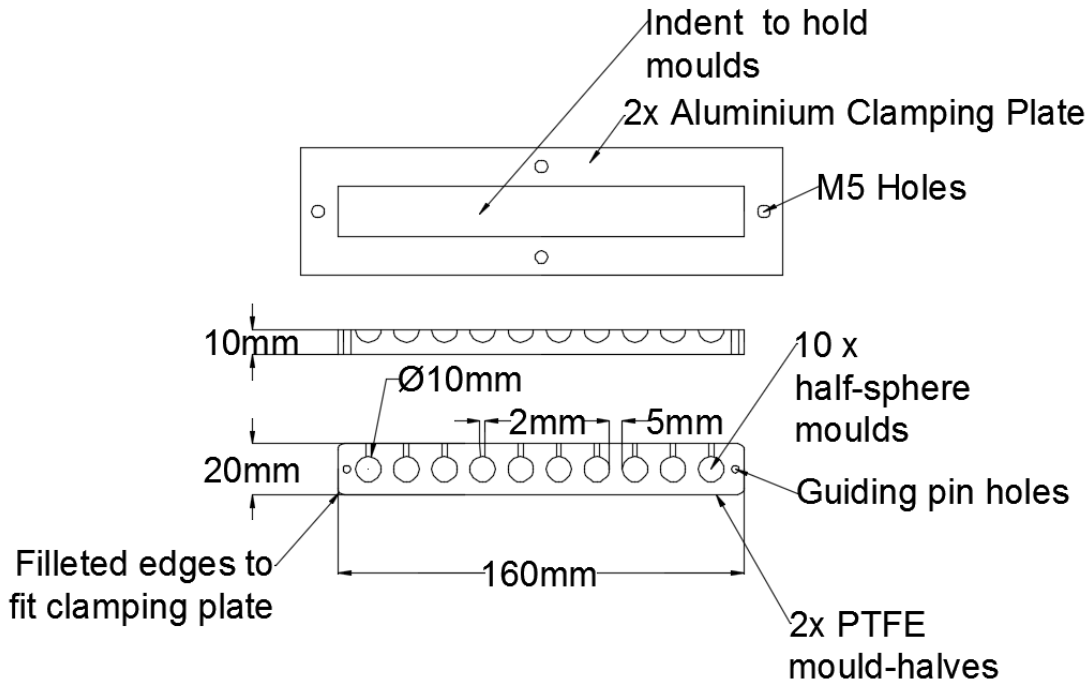

Figure 4.3: CAD drawing of 10 mm mould.

Each sphere had a small diameter aperture up at the top of the mould that allowed the insertion of a hypodermic needle. Distilled water at room temperature ∼22.8 °C was used as the solution. The determination of particle velocity, explained later in Section 4.3, was difficult when using a projectile that can transmit light. To assist in accurate velocity measurement, a small amount of black dye was also added to the water until the mixture became opaque. The needle had to be inserted to the bottom

of the sphere and pressed slowly and steadily, as the strength of the surface tension could prevent water filling the cavity. As the addition of air to the mould might result in poor production of SHI and a large density variance in the ice spheres, the needle had to be tapped to push air bubbles upwards and care was taken to ensure that these bubbles were not emptied into the mould. Although the presence of the needle would account for a portion of the volume during this process, the expansion of water during freezing would ensure a full sphere was produced. Filling of the moulds was an individual event, creating a monolithic sphere. The creation of a flat-wise layered SHI projectiles [17] would require particular precise control of the hypodermic needle, which would be difficult at the contrasting volumes of 10 mm or even 5 mm. Before filling the cavities were sprayed with PTFE mould release, to ease in the safe removal of the particles. The mould was then placed in a chest freezer at a temperature of $-24\,^{\circ}\mathrm{C}\ \pm 2\,^{\circ}\mathrm{C}$.

To assist in the timely production of the hail ice, the freezing time was estimated using empirical heat transfer relations. Utilising the dimensionless heat transfer coefficient, the Biot number ($Bi = \frac{h_c L}{k_c}$) and dimensionless time parameter, an estimation of the surface temperature after 3 minutes could be made. Once the Biot number is known the constants A_1 and λ_1 are found from interpolation of values from Heisler charts [117]. Assuming an initial temperature (T_i) of 25 °C, a temperature at the centre of geometry 0 °C the Fourier number (τ) is determined using Equation 4.1 for different specified environment temperatures (T_∞).

$$\theta(r,t) = \frac{T_0 - T_\infty}{T_i - T_\infty} = A_1 e^{-\lambda_1^2 \tau}, \quad \tau > 0.2 \tag{4.1}$$

$$t = \frac{\tau L^2}{\alpha} \tag{4.2}$$

The freezing times can then be calculated using Equation 4.2, where the characteristic length (L) for a sphere is the outer radius r_0, giving the results displayed in 4.4.

The above calculations, although simplistic, give an impression of the minimum time required for freezing simulated hail ice (SHI) of certain diameters. The 5 mm SHI takes around 10/15 minutes to freeze, whereas but the 10 mm, 15 mm and 20 mm diameters are more affected by freezer temperature, with the 20 mm requiring a number of hours. Upon removal from the freezer, the assembly was allowed to thaw for a short period of time, which was dependent on the SHI diameter. Attempts to separate the two PTFE moulds immediately, resulted in the fracture of the specimens into two hemispherical halves. The 5 mm and 10 mm projectiles were then removed carefully with plastic tweezers and placed in Polyproplylene storage boxes and returned to the freezer.

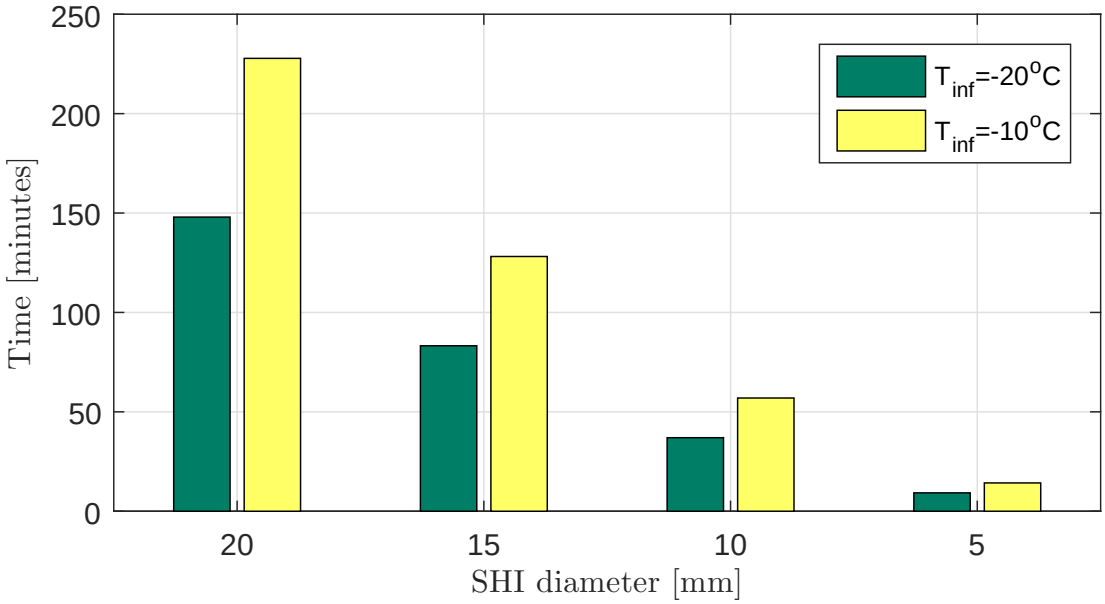

Figure 4.4: Estimated freezing times from Heisler chart equations for a sphere.

The wells inside the boxes meant that the projectiles would not adhere to each other during storage. Unfortunately the box divisions could not accommodate the larger 15 mm and 20 mm sizes of hail. Instead they were kept inside sealed polythene bags in the freezer.

It was important to aim for a consistent mass for each diameter of SHI as a large spread of masses could mean a large deviation in kinetic energy. Individual 10 mm samples were weighed, using a scale with a precision of 0.001 mg, in order to determine the range of masses produced from the hail manufacturing process. The weights of 26 SHI particles can be seen in Figure 4.5. The spread was higher than expected, with a mean of mass of 0.4728 g and a standard deviation of 0.0587 g. The density of distilled water is 1 g cm^{-3} and assuming a perfect spherical volume, this should result in a mass of 0.5382 g. The density of the black dye, although higher than the water, was used in such small quantities that the effect upon the overall density of mixture would be negligible. On examination, the shape of some of the SHI spheres were not perfectly round due to the marginal misalignment of the hemi-spherical half moulds. In addition, there was often a small protrusion or "nib" due to overfilling and the subsequent expansion of ice up the aperture as it freezes. This could account for the additional mass in many of the examples. Those few cases that fell below the expected mass could be either due to additional air entering the inlet or melting of the ice during weight either during the measurement or the release of the particles from the moulds. To ensure the consistency of manufactured SHI it was proposed to include a brief inspection and "nib" removal

stage (using a scalpel) in the manufacturing procedure. The difference in spread of mass in the 10 mm ice spheres after implementing the modified procedure can be seen in Figure 4.6

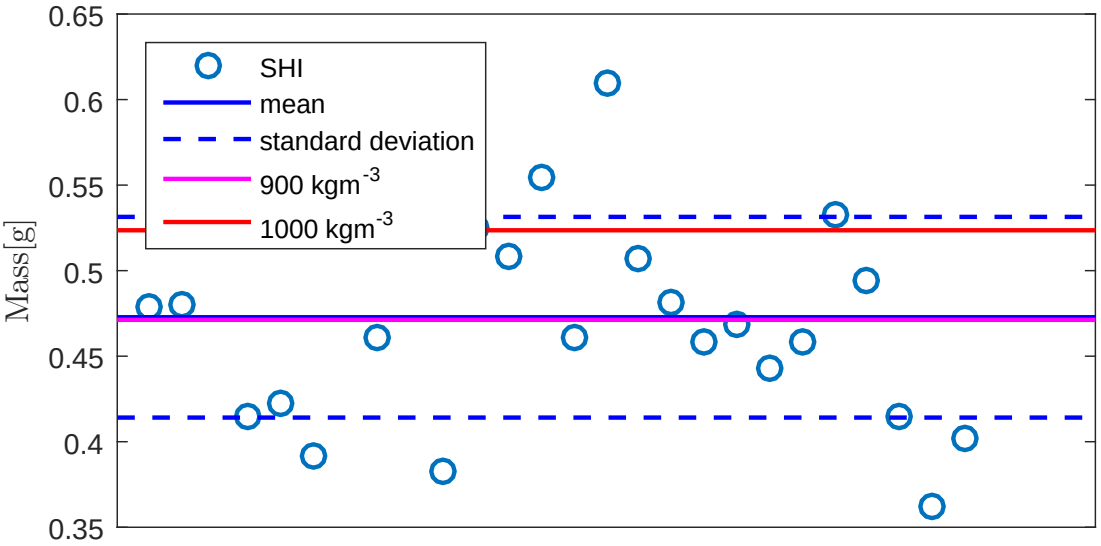

Figure 4.5: Original range of mass of 10 mm SHI.

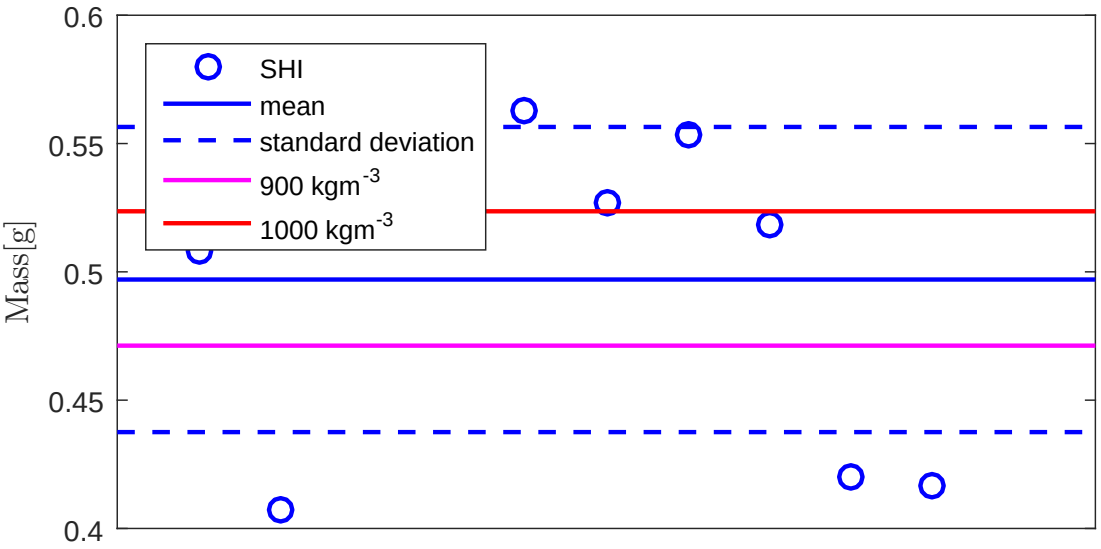

Figure 4.6: Improved range of mass of 10 mm SHI.

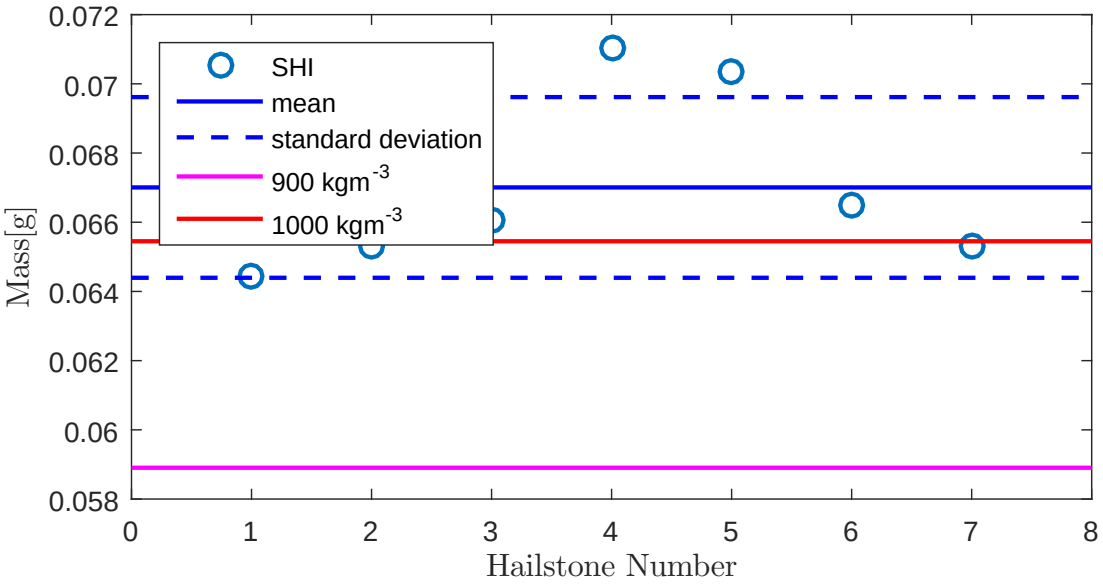

Figure 4.7: Range of mass of 5 mm SHI.

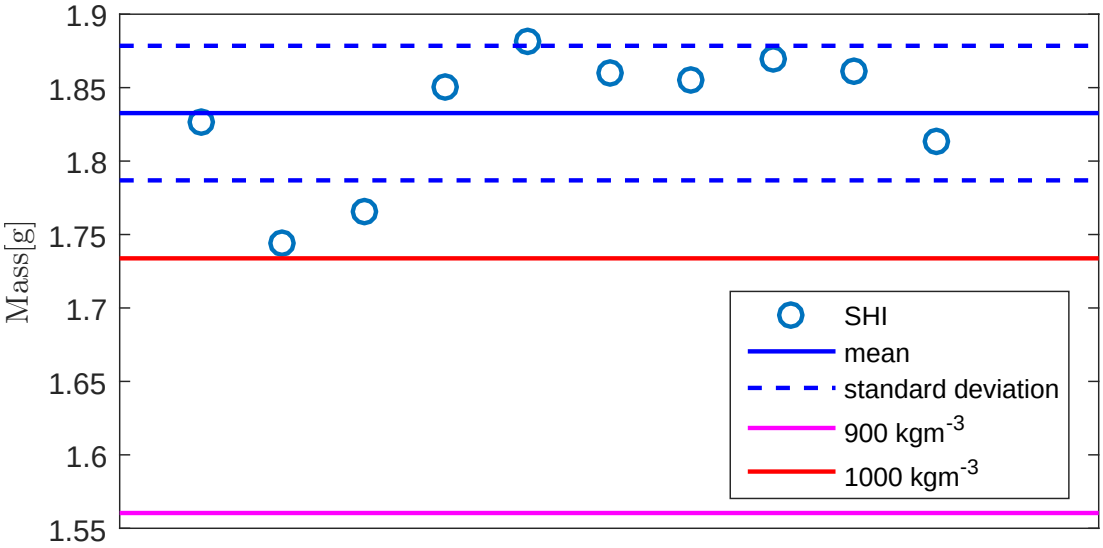

Figure 4.8: Range of mass of 15 mm SHI.

4.3 Hail Rig Data Collection

Information on both velocity and force of a fired particle was extracted using a National Instruments USB DAQ device so that it could be analysed in National Instruments Labview. Originally a USB-6008 DAQ was used to for this purpose. However, the data acquisition for this model could only achieve a maximum sampling rate of 10 kS/s for one channel. In total two channels are needed for velocity measurement (one channel

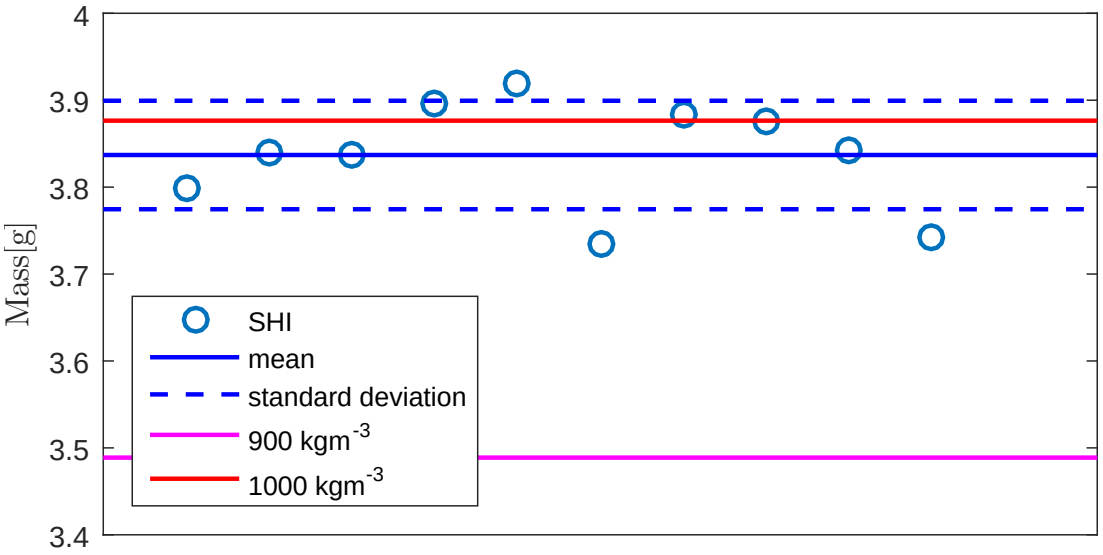

Figure 4.9: Range of mass of 20 mm SHI.

for each light gate) and one for force measurement. By having 3 channels operational within the one "Virtual Instrument" the maximum sampling rate was further reduced to 3.33 kS/s.

The limitations of using this piece of equipment become apparent when examining the time periods associated with high velocity impact. If three channels are used, the maximum sampling rate would result in a sample being taken every 0.0003 seconds. For comparison, the sampling rate achieved by Kim and Kedward [17] for force measurement was 200 kS/s. The distance between the individual light sensors is 100 mm. If an example tip speed of 100 ms^{-1} is proposed, the time taken to pass the two sensors would be approximately 0.001 s. That means that 3 data points could be plotted in this time. A different DAQ device (USB-6210) was sourced with a maximum sampling rate of 250 kS/s for one channel and thus 83.33 kS/s for the three required.

Figure 4.10a represents an example of a velocity measurement of a ceramic particle taken over 2 seconds. The voltage signal fed through the light gates to the DAQ device is 5V. When the light from the source to the sensor was unobstructed, the voltage should remain constant. From the graph, the voltage level from the 2nd light gate is very close to the expected level (around 4.966 V), whereas for the 1st light gate it is slightly less (around 4.737 V) and there appears to be a small amount of variance around this voltage level. The difference is most likely attributable to the marginal misalignment of the light source and the sensor. When the light path is blocked, the voltage drops close to zero (0.0229 V for the 1st gate and 0.0131 V for the 2nd). A closer inspection of the two signals is displayed in Figure 4.10b. The decrease for 2nd

light gate is fairly smooth and uniform. Whereas for 1st light gate there appears to be a small "nick" in the profile when it starts to decrease from the maximum value and again when the voltage starts to increase. The time difference between these signals was taken from their respective minimum levels. For this case the difference was found to be 0.002 192 s, which works out to be 45.6204 ms^{-1}. Although the light gate sensors were capable of measuring time to a low resolution, the distance between the sensors could not be known to the same number of units. Therefore for the purpose of this chapter, the measurement will only be to three significant figures i.e 45.6 ms^{-1}.

Force measurement was originally carried out using a 7kg rated TEDEA 1042 load cell. It was determined in early tests that this type of equipment was unsuitable for the highly dynamic impact associated with the firing of high velocity projectiles. Instead a new dynamic force transducer was sourced that could better deal with these type of loads. A Brüel & Kjaer 8230-002 DeltaTron Force Transducer with a sensitivity of 2.2 mVN^{-1} was selected. A type 1704-A-002 CCLD conditioning amplifier was used to provide power to the transducer instrument and also to provide analogue gain and filtering. The polarity of the electrical signal is positive for compression. The transducer was screwed to a support at the bottom and the top attached to the clamp. This arrangement can be seen in Figure 4.12a. The clamp which holds the circular specimen of roughly 57 mm diameter in place by a screwed cap. The transducer works through the principle of the piezoelectric effect of quartz, which when stressed, gives an electrical charge proportional to the compressing force. Figure 4.12b shows a perspex specimen held securely by the clamp that still allows a significant area of the specimen to be impacted. As the transducer measures "change in force", it could not be calibrated with dead weights. The transducer was supplied with an individual calibration of its sensitivity by the manufacturer. Sophisticated methods for testing this calibration require external equipment and services that were not possible for the scope of this project.

The signal from the force transducer was fed through to a Type 1704-A-001 CCLD conditioner of the same manufacturer. The conditioner also provided analogue gain and filtering. Gain could be used before the analogue to digital conversion to improve the system's noise floor. Either a linear (no filtering), an acoustic band-pass or an 'A-weighting' type 0 filter were selectable. The low pass feature removes high frequency components, whereas the A-weighting filter roughly corresponds to the equal-loudness curve for the human ear, making it less sensitive to the very high and very low frequencies. It was decided that implementing any gain would not be appropriate due to the +-10V limit of the DAQ. Residual noise from the force transducer was specified as 0.031 N in the calibration certificate. Even with the complete experimental set-up, the

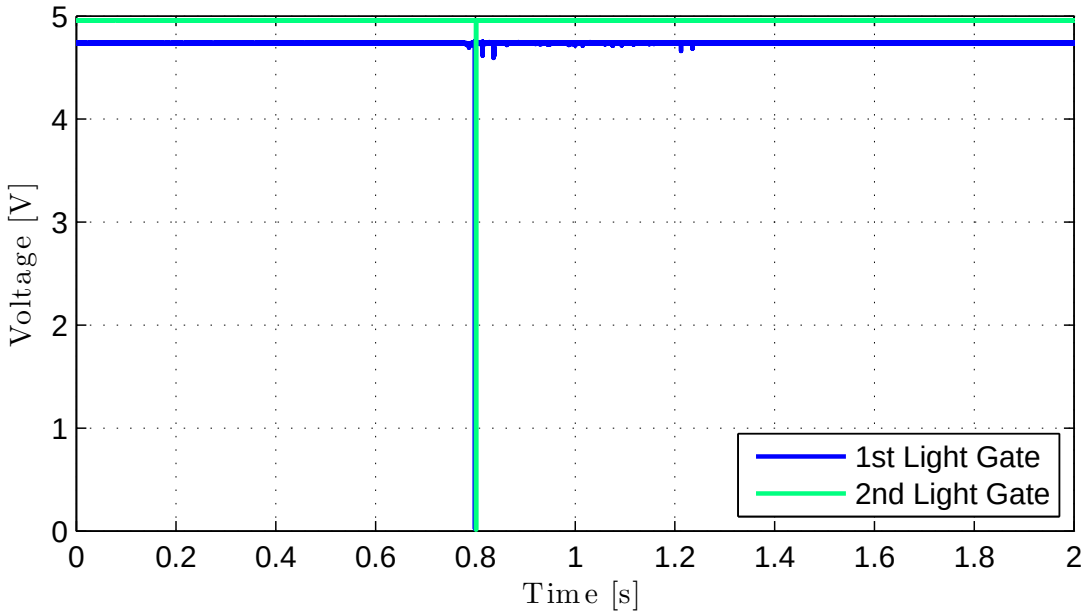

(a) Over the length of Measurement.

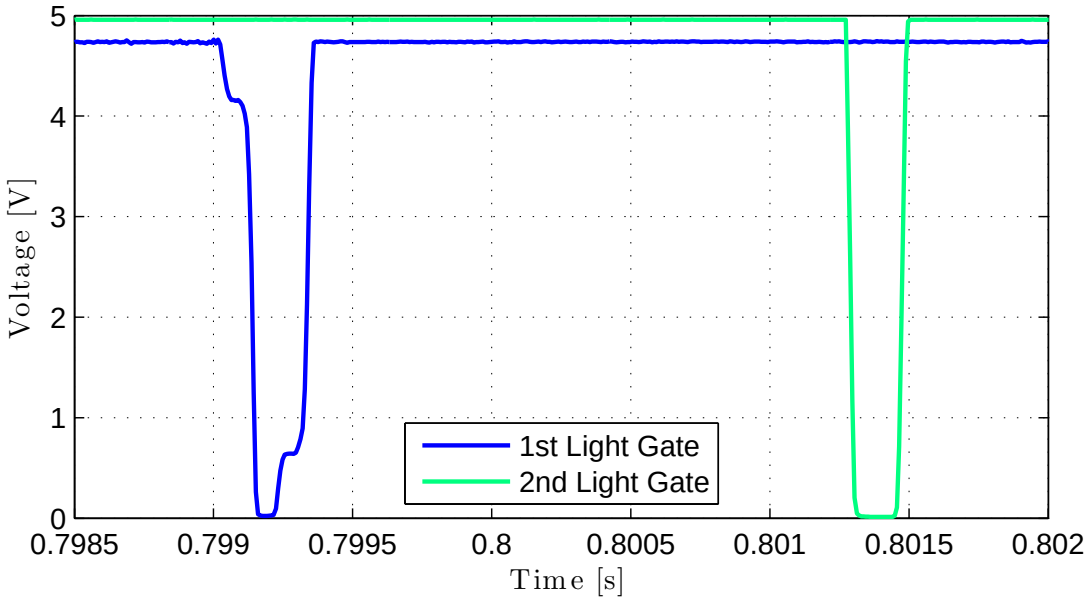

(b) Close-up of Signal Drop.

Figure 4.10: Example velocity measurement of a ceramic projectile.

noise profile was minimal, as shown in Figure. The acoustic band-pass filter was found to remove some undesired noise without affecting the profile of the force measurement. For the majority of the measurement, the noise sits less than $\pm$ 0.25 N, with maximum spikes of $\sim$0.7 N, which should not significantly affect the force measurement, even for

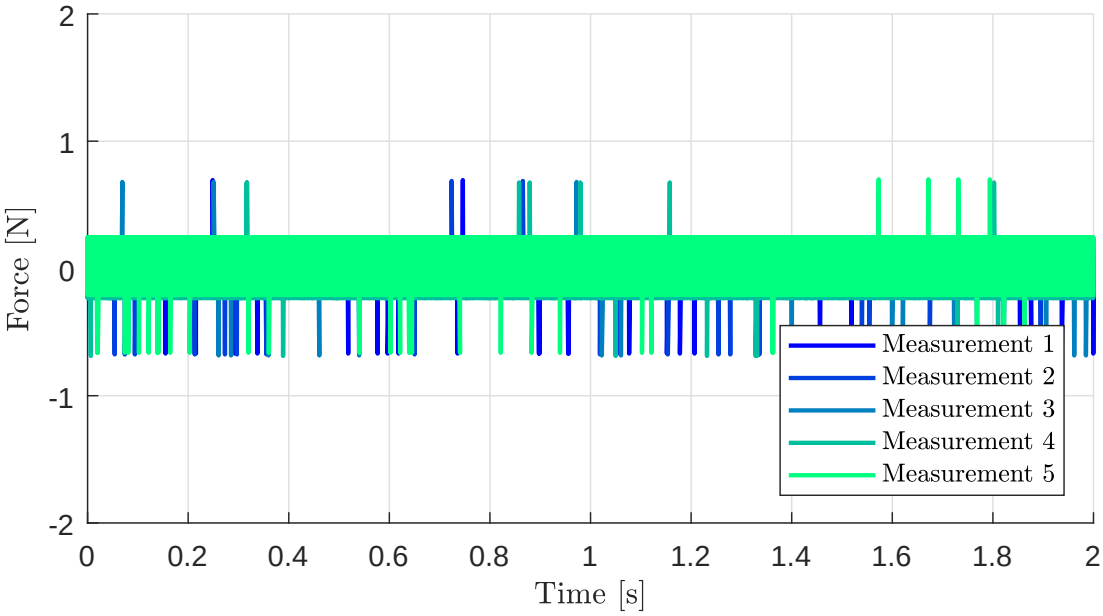

Figure 4.11: Example resting noise for 5 separate measurements.

the smallest diameter 5 mm SHI impacts.

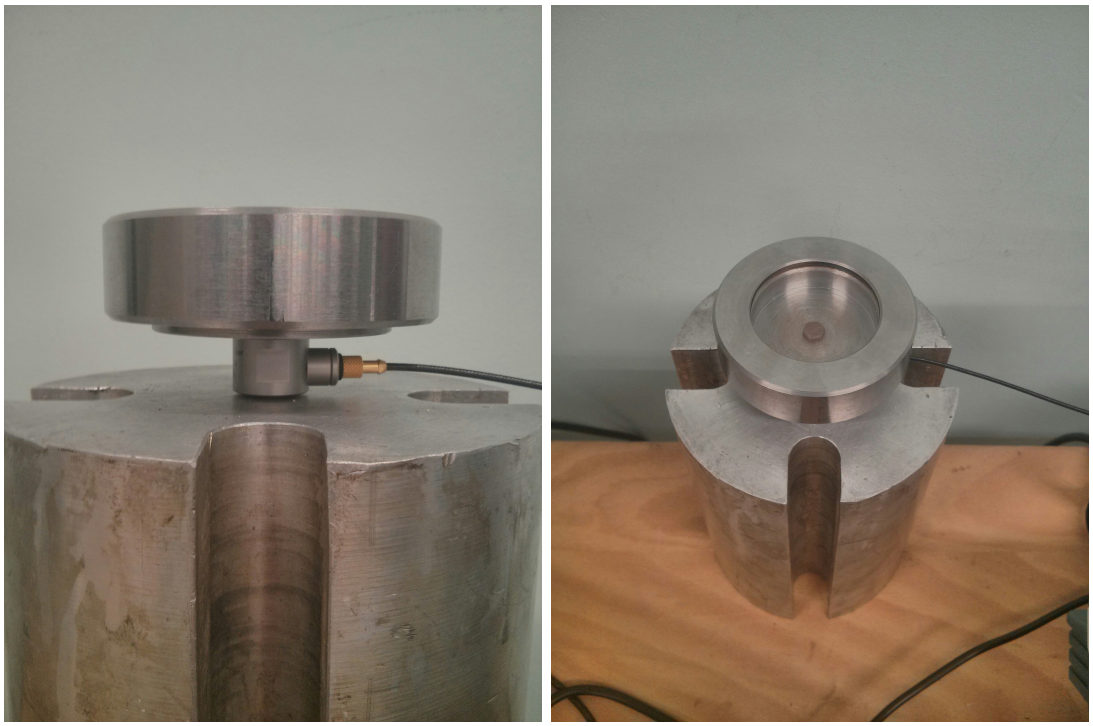

(a) Side view. (b) Elevated view.

Figure 4.12: Dynamic force transducer and clamping arrangement.

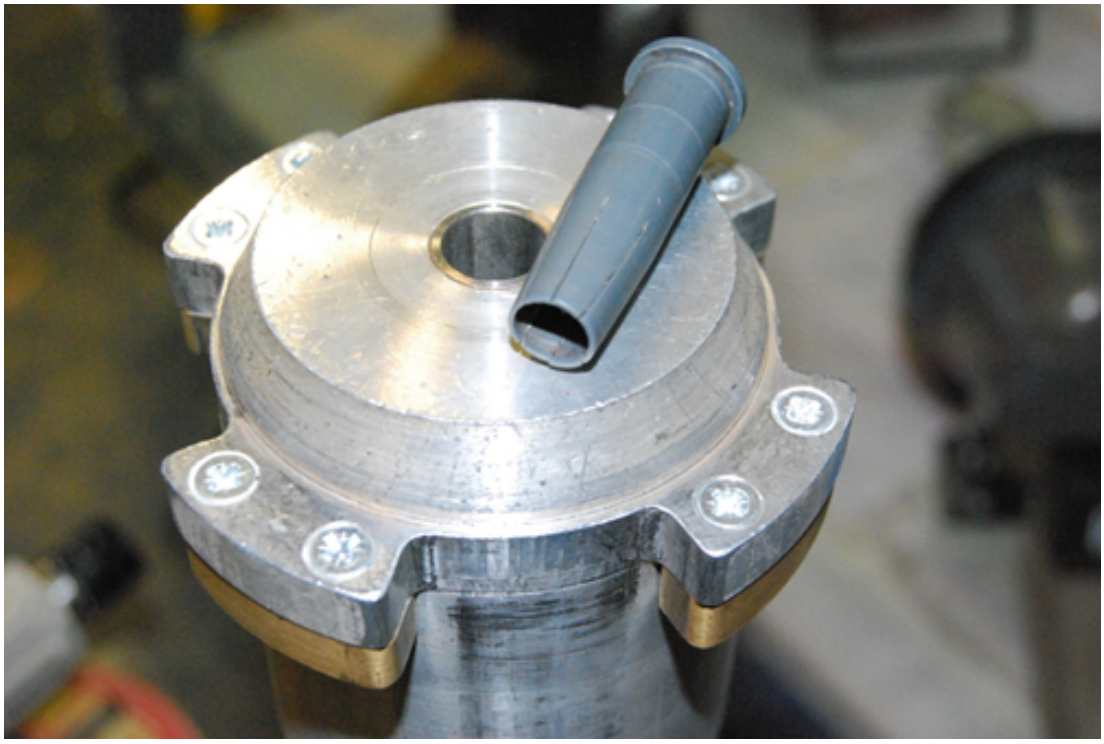

Figure 4.13: Hail rig barrel and plastic sabot used to hold the projectile.

4.4 Composites

4.4.1 Composite Manufacture

The material constituents required to create the composite for use in experimental testing were chosen to be an epoxy based resin and a glass fibre based reinforcement, similar to industry equivalent components used in wind turbine blade skins. Triaxial stitched E-glass with a 0/-45/+45 orientation was selected. This was supplied in a 1 m wide roll and layers were cut to the appropriate dimensions. Epoxy resin was used together with an extra slow hardener in vacuum infusion.

In undertaking the vacuum infusion, fibre reinforcement was laid out dry and then enclosed in a stack of bagging materials in a specific order, as detailed in Figure 4.15. The prepared stack was then vacuum-bagged and once any possible air leaks from the bag were eliminated, resin was drawn through the laminate, wetting the fabric from above. Stitched materials are well suited to this process as the gaps allow fast transport of the resin.

Vacuum resin infusion, like many other processing routes, has both advantages and disadvantages. The main positives are that high fibre volume laminates are possible with low void contents at a relatively low tooling cost. The major issue for the process

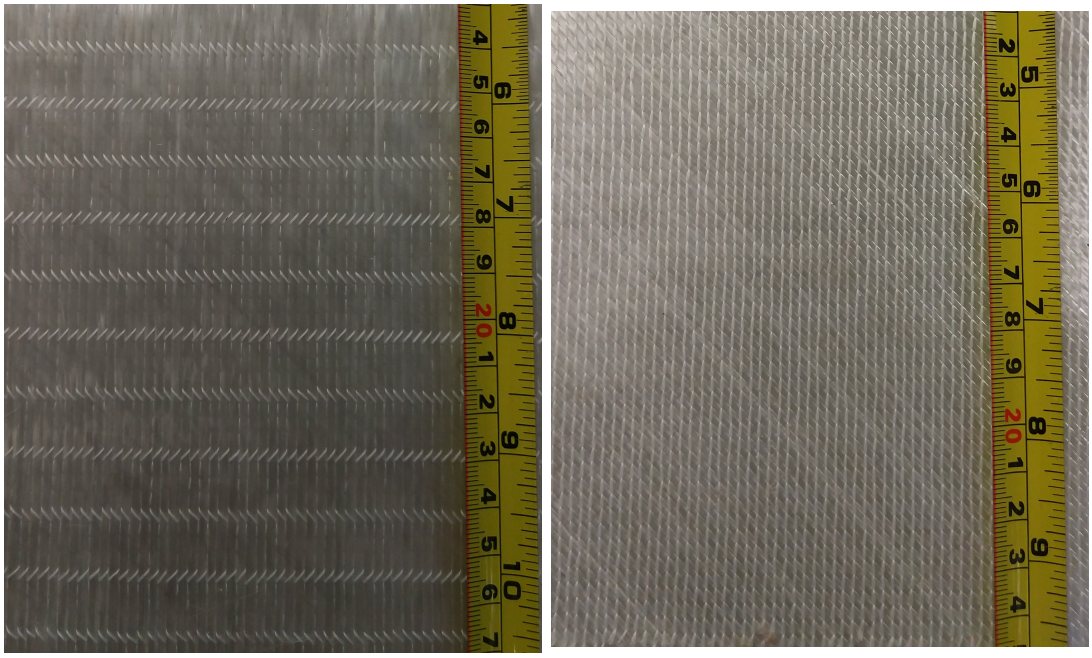

(a) Top Surface.

(b) Bottom Surface.

Figure 4.14: Glass fibre reinforcement used in vacuum infusion.

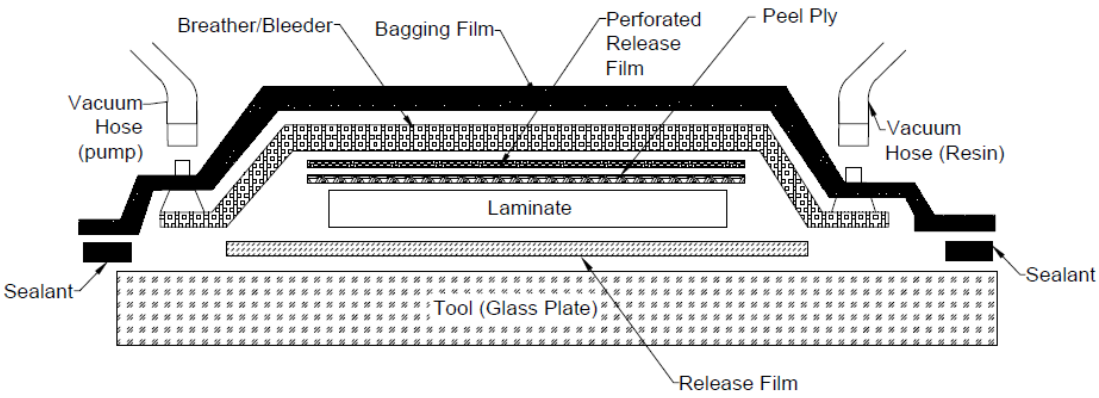

Figure 4.15: Vacuum infusion composite layup sequence.

is to ensure that all fibres are thoroughly wetted by the resin so that there are no un-impregnated areas, which could completely jeopardise the final product. Therefore the resin used must be very low in viscosity which reduces the mechanical properties of the resultant material. The procedure is also fairly labour-and time-intensive with a degree of skill and understanding required to produce laminates of acceptable quality.

The process was performed in-house at the university and prepared using the fol-

lowing steps:

1. A flat glass plate (34 cm x 34 cm) was used as the bottom tool plate. The plate was treated with aerosol foam cleaner to remove any residuals from previous lay-ups and then is treated with 'mould release' in the proposed laminate area to aid easy removal of the laminate from the glass. Care was taken to ensure that the application of mould release does not extend to the edges, where sealant tape was to be placed. Originally, instead of mould release a non-porous release film was used but after several iterations, the film was found to reduce the surface quality, with the addition of small pin like impressions.

2. A 28 cm x 28 cm piece was placed in the centre, ensuring even margins on each edge of the plate and secured using masking tape,

3. The fabric reinforcement was cut to the appropriate dimensions, in this case, 20 cm x 24 cm. It was then weighed and placed upon the release film. Any dust outside the area of the layup was removed.

4. Peel-ply was cut just slightly bigger than the reinforcement, as it does not need to overlap the edges but provide full coverage. The purpose of the peel-ply was to be peeled from the composite, following the cure phase, to leave a clean, contaminant-free, textured surface. This layer also absorbs some resin from the laminate, which had to be accounted for.

5. Perforated release film (same size as the peel ply) was then applied on top of the layup, with a breather fabric (30 cm x 30 cm) placed above that. The first function of the fabric was to ensure the efficient extraction of the air that was sealed under the vacuum bag and to allow a path for any entrapped air to flow out from during the cure cycle ("breather"). The second function, in combination with the perforated release film, was to absorb any excess resin that is bled from the laminate ("bleeder").

6. Spiral tubing was situated either end of the breather fabric and held down with small strips of masking tape. The purpose of the tubing was to improve the evenness of the resin flow from the initial feed into the laminate and across to the other side. Silicone connectors, with underside channels, were inserted into the middle of the spiral tubing. A small amount of mould release was applied to the connectors to prevent damage upon de-moulding.

7. Sealant tape is placed upon the edge of the tool plate; its pliable nature makes it highly effective at providing an air-tight seal.

8. The whole layup was covered with a vacuum bag, which was held to the bottom plate by the sealant tape. This was the most delicate and important part of the operation. Imprecise application could result in an imperfect seal. It was imperative that there was sufficient slack in the bagging film to cover all the contours and edges of the set-up. Any 'bridging' of the bag material would create voids which will result in resin-rich areas that would reduce the strength and quality of the finished product. Creating raised sections (or 't-joints') of the sealant tape edge helped prevent this bridging but it also made it harder to eliminate bag leaks. Wrinkles and folds were also to be avoided as these can affect air flow. Before the bag is completely sealed, small incisions were made directly above both resin feed connectors. PVC Vacuum hose (6 mm ID) was inserted into these breaches. Sealant tape was also applied to areas between the hose and bag to prevent air leakage.

9. One end of the hose was connected securely to the resin feed pot and the other was connected to a vacuum pump/catch-pot arrangement. The resin feed line was clamped to ensure a tight seal. The vacuum pump was switched on and the bag tightened around the mould surface as the air was removed. The bag was manually manipulated to move slack into areas that required it. Attention was paid to possible leak areas where the bag and sealant tape interface. The bag is adjusted and massaged onto the tape until the pressure gauge on the catch-pot reads close to 100%. The sound and opacity of oil vapour emitting from the vacuum pump also gave indication of how hard the pump was working. Corners where different sections of tape overlapped were typical areas of concern which required the most massaging. When full vacuum was reached the sound of the pump will diminish and oil vapour was no longer vented. The vacuum pump valve was closed and power switched off. The pressure gauge was monitored for a period of time to ascertain if there were any small leaks that were not immediately apparent. Ideally the number of times the release and application of vacuum was kept to a minimum. Weights were placed on top of the laminate to aid consolidation.

Once there was acceptable confidence in the sealed nature of the vacuum, the infusion process could then be initiated:

1. The appropriate amount of total resin (resin + hardener) for this process was estimated from the overall weight of the reinforcement and desired composite volume/weight fraction. An additional amount was also accounted for wastage caught in the distribution mesh and feed lines/tubes. This was verified by carrying

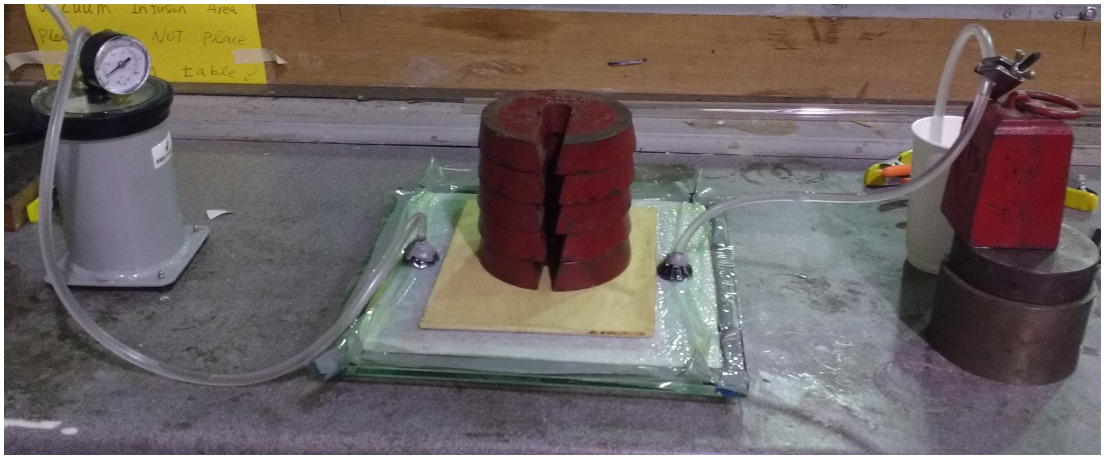

Figure 4.16: Infusion process set-up.

out trial runs of the infusion and altered accordingly. The correct weight-ratio of resin and hardener was stated by the manufacturer and the correct weight of each determined using digital scales. Once combined the mixture was stirred for a set period of time.

2. After sufficient stirring the resin mixture was degassed to allow the removal of as much air from the solution as possible. The suction of the air caused the level of solution in the receptacle to rise, so care was taken to reduce the vacuum to prevent overflowing. Once the level no longer rises, the initial surface bubbles were removed using the wooden stirrer. The mixture was placed back in the chamber for final degassing, ceasing when all visible bubbles had dissipated.

3. With the vacuum pump running and the resin feed hose now connected to the resin mixture, the clamp holding the hose was gently released to a restricted amount and the resin drawn through into the infusion. A reduced flow rate (approximately 1 hour) allowed efficient wetting of the fibres.

4. The infusion process was monitored up until the point where resin has travelled roughly 2/3 of the distance through the reinforcement. Once this had been achieved, the line to the vacuum pump was closed off and the resin feed hose clamped again, prohibiting the accumulation of excess resin.

5. The laminate was now allowed to cure. There is an earliest theoretical vacuum-off time which was dependent on both the type of hardener used and the environmental temperature. Due to the varying levels of temperature within the lab, this had to be carefully monitored and the vacuum-off time adjusted. Once concluded,

the part was post-cured in the oven at a set temperature and fixed period of time detailed by the manufacturer's instructions.

6. The final stage is de-moulding, in which the vacuum bag and other components are removed from the mould. Using 5 layers of reinforcement produced composite plates of 4 mm thickness. The part was cut and finished to the desired form. For the purpose of future experimental testing, the university engineering technicians were able to create 57 mm discs from the final product using a water-jet cutter. Sandwich plates were used as sacrificial material to reduce the damage at the edge of the discs.

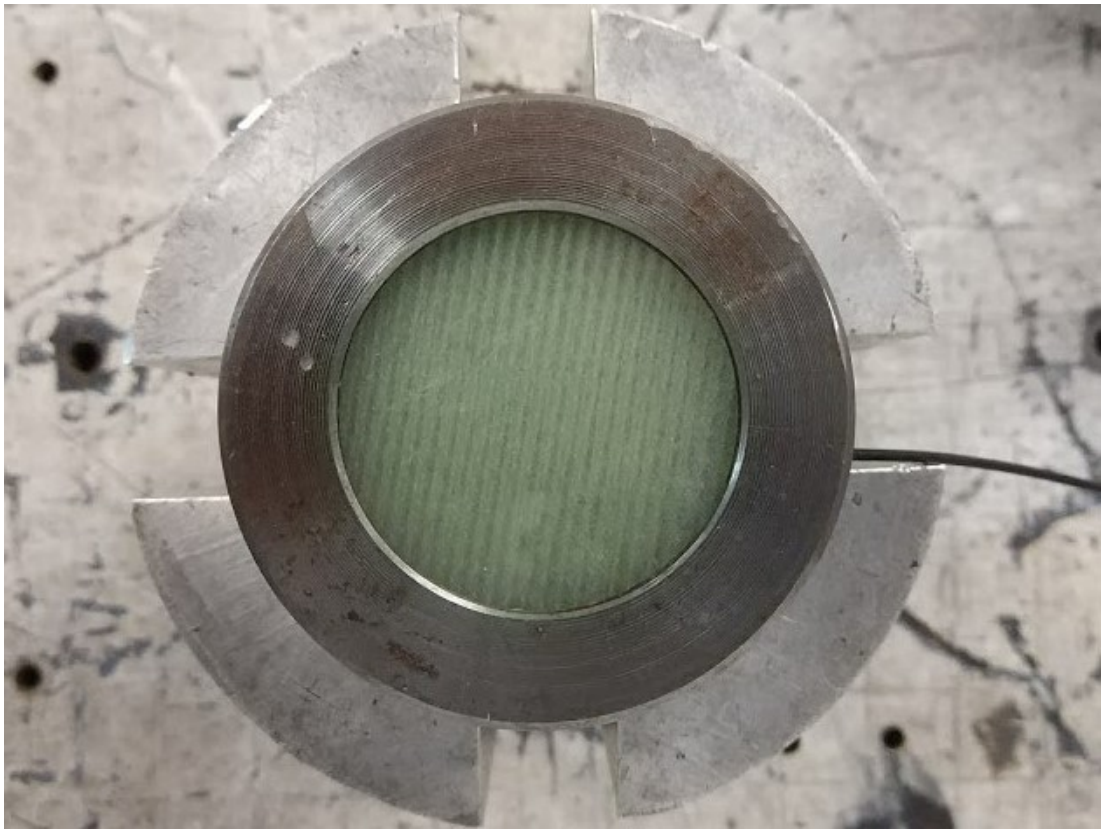

Figure 4.17: A composite sample in the clamping arrangement.

4.4.2 Composite Properties

One of the most influential mathematical factors in the determination of composite mechanical properties is the fibre volume fraction, which is essentially the ratio of reinforcement to matrix in the material. The selection of the individual components

are of course important but as the mechanical properties of the fibres are generally much greater then that of the resin, the greater the fibre volume fraction, the higher the mechanical properties of the composite will be.

The fibre volume fraction can also be expressed using the densities of the different constituents. Assuming an ideal composite with no porosity, the sum of the volume fractions will be equal to 1.

$$V_f = \frac{\rho_c - \rho_m}{\rho_f - \rho_m} \tag{4.3}$$

Considering the area weight of a certain ply, the volume fraction can be given by:

$$V_f = \frac{nA_W}{\rho_f t} \tag{4.4}$$

The volume fraction can also be estimated from the weight fraction of the constituent materials:

$$V_f = \frac{w_f}{(1 + \frac{\rho_f}{\rho_m})(\frac{1}{V_w} - 1)} \tag{4.5}$$

Where $V_w = \frac{m_f}{m_c}$

A void is an region unoccupied by composite material, which is deemed undesirable as it can affect the mechanical properties and lifespan of the composite [118]. The presence of voids will add to the total volume, but not the weight of the composite. If V_v is the void content, Equation 4.3 becomes:

$$V_f = \frac{\rho_c - \rho_m(1 - V_v)}{\rho_f - \rho_m} \tag{4.6}$$

If the fibre content is known and density can be measured with sufficient accuracy, then the void content can be estimated. From ASTM standard D2734—16, "*Standard Test Methods for Void Content of Reinforced Plastics*" the void content is calculated by

$$V_v = \frac{(\rho_T - \rho_M)}{\rho_T} \tag{4.7}$$

where ρ_T and ρ_M are the theoretical and measured density respectively.

There are various destructive and non-destructive methods which can be used to determine this fraction. Those involving resin removal are the most recognisable such acid digestion and resin burn-off. Burn-off was selected and the process is detailed in the following section.

4.4.3 Samples

The composite manufacturing process yielded eight plates of decent quality yet consistent GFRP. From each plate nine 56.68 mm diameter, composite discs could be extracted using a water jet cutter. Initially the process was effective, with no visible surface defects or delamination when sacrificial protection was employed on top of the composite. Unfortunately, a considerable number of samples were damaged due to the accidental neglect of this protection later and positioning of the sample templates too close together. This unfortunate mishap was compounded by the exhaustion of our supply of tri-axial glass fibre. This meant that the total number of composite samples available that were in optimal condition was 35. It was decided that the less damaged samples would still be suitable for calibration of the hail cannon pressure.

Three of the optimal samples were used for separate burn-off tests, to determine the volume fraction and void content of the composites. The diameter and thickness of each disc was measured and the weight taken. Before each test, the sample would be placed in a tray, with the total weight of tray and sample noted. The burn-off test involves heating the composite in a pre-heated oven to a specific temperature whereby the resin will oxidise (burn-off) but is low enough so that the fibres will remain intact [119]. It cannot be used for carbon-fibre composites. E-glass does not actually melt but "softens" at point of over 800 °C. Whereas the cured epoxy resin involved in experimental testing will soften much lower. For the ∼57 mm, ∼4 mm thick sample used in experimentation, the resin was left to burn off at 550 °C until all traces of blackness had disappeared. In this case an hour was found to be sufficient. Afterwards the total weight of tray and sample were measured again to find out the difference in weight of the sample. The remaining fibre could not be weighed separately as the stitching holding the fibre sheets together had also burned-off. This stitching thread constituted less than 1% of the total fibre areal weight and was neglected from the calculations. The fibre weight fraction from all three samples was determined (an average of 0.782 ± 0.025) and implemented in Equation 4.5 to find out the fibre volume fraction. The average value of V_f was found to be roughly 0.6. Using Equation 4.7 the average void content from the samples was found to be $2.12\% \pm 1.89\%$.

As part of the impact analysis, samples were examined under electron microscope. In addition to inspection of an undamaged sample as a control, two samples from the early attempts of composite manufacturing were also examined, to see how a poorly wetted-out specimen would appear at a microscopic level. In these images the bottom left hand text corresponds to: the microscope model (Hitachi S3700), the accelerating voltage (kV), the zoom level ('x number') and the image type (SE - Secondary Electron). The scale in divisions of ten and associated total distance are displayed in the bottom

right corner of the image.

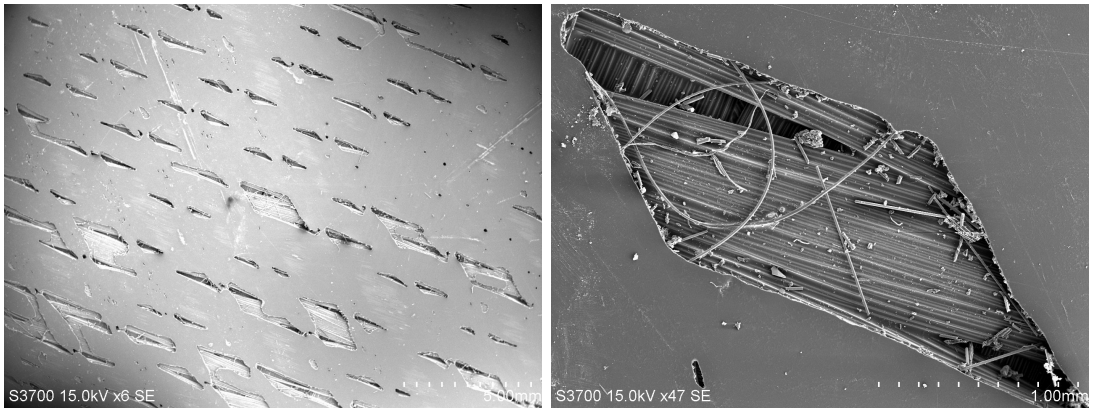

(a) (b)

Figure 4.18: SEM image of poorly-wetted composite sample.

Images taken from this lowest-quality example are displayed in Figure 4.18. The absence of matrix material in strips across the sample is all too apparent, with huge areas of exposed fibres up to 2.5 mm in length and 1 mm in width. In the slightly improved sample in Figure 4.19, these areas are somewhat less apparent and reduced in width but still of considerable length.

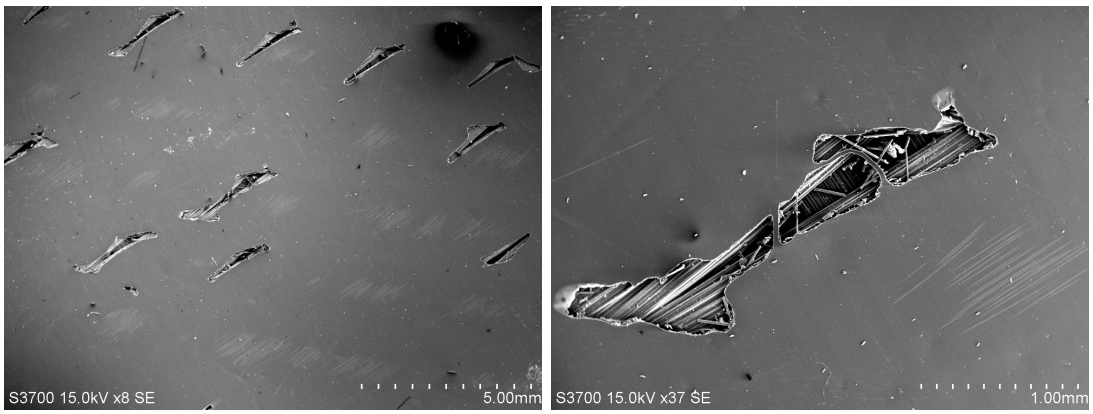

(a) (b)

Figure 4.19: SEM image of a slightly improved composite sample.

The control sample in Figure 4.20 shows a much-improved surface quality, with no immediate signs of exposed fibres as seen in the previous two figures. However, much smaller circular voids or pits appear to be present, roughly 100 µm in diameter, which are spread quite evenly about the surface, presumably caused by the presence of tiny air bubbles in the system. There also appears to be the slightest hint of fibre direction

close to the surface of the epoxy, that appear take the form of light scratches in the 45° direction.

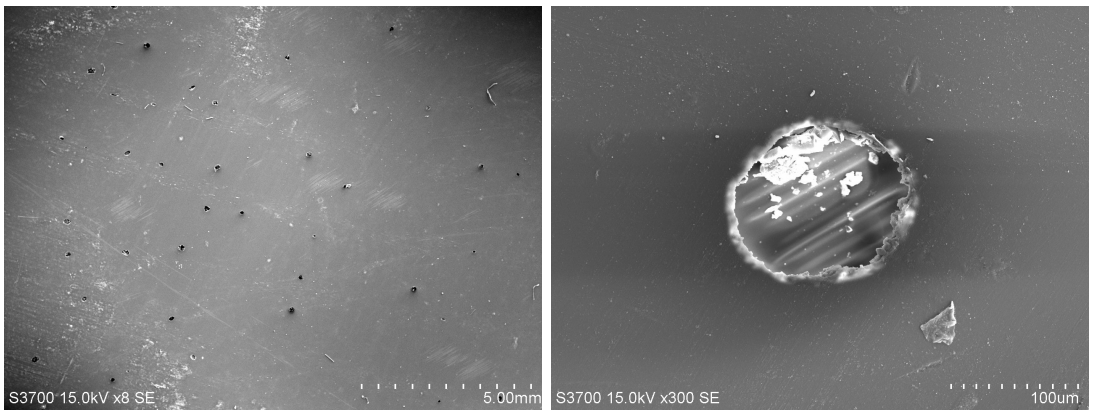

(a) (b)

Figure 4.20: SEM image of an example composite sample selected for experimentation.

The remaining 32 samples were to be used for experimental analysis. Originally, the planned matrix of variables was to involve the four different SHI diameters, at four different velocities for five different sets of number of impacts. The majority of these tests were still achieved but unfortunately there were missing data points. The SHI diameters (5 mm, 10 mm, 15 mm, 20 mm), selected from the meteorological data inspection, were fired from the different detachable barrels. The number of impacts was determined to range from Single, 5, 10, 25, 50 (roughly the maximum number of impacts in the year of one type of hail from the most prominent site in Chapter 3). The four velocities were determined from calibration of firing the ice projectiles at different pressures with the different barrels. For the reduced number of samples involved, the overall variable matrices took the form shown in Tables 4.2, 4.3, 4.4, 4.5 and 4.6. Here a particular sample is labelled 'S', for those subject to an overall total of either 5 or 10 impacts or 'M' for an overall impact of either 25 or 50 impacts. The number after this letter designation is the diameter of SHI used. The next part of the sample description is the velocity the SHI is fired at i.e the sample S10-V1 is subject to 10 mm SHI fired at the lowest specified velocity ($\sim$50 m s^{-1}).

4.5 Experimental Protocol and Calibration

An extensive calibration campaign was undertaken to not only ascertain the specified pressure/resultant velocity for each hailstone but to find an experimental procedure that would provide a sufficient level of consistency and validity amongst all the firing

Table 4.2: Diameters and velocities associated with samples used for single impacts.

	V1 $m\,s^{-1}$	V2 $m\,s^{-1}$	V3 $m\,s^{-1}$	V4 $m\,s^{-1}$
5 mm	S5_V1	S5-V2	S5-V3	S5-V4
10 mm	S10-V1	S10-V2	S10-V3	S10-V4
15 mm	S15-V1	S15-V2	S15-V3	S15-V4
20 mm	S20-V1	S20-V2	S20-V3	S20-V4

Table 4.3: Diameters and velocities associated with samples impacted 5 times.

	V1 $m\,s^{-1}$	V2 $m\,s^{-1}$	V3 $m\,s^{-1}$	V4 $m\,s^{-1}$
5 mm	**S5-V1**	S5-V2	S5-V3	**S5-V4**
10 mm	S10-V1	**S10-V2**	**S10-V3**	S10-V4
15 mm	S15-V1	**S15-V2**	**S15-V3**	S15-V4
20 mm	**S20-V1**	S20-V2	S20-V3	**S20-V4**

Table 4.4: Diameters and velocities associated with samples impacted 10 times.

	V1 $m\,s^{-1}$	V2 $m\,s^{-1}$	V3 $m\,s^{-1}$	V4 $m\,s^{-1}$
5 mm		**S5-V2**	**S5-V3**	
10 mm	**S10-V1**			**S10-V4**
15 mm	**S15-V1**			**S15-V4**
20 mm		**S20-V2**	**S20-V3**	

Table 4.5: Diameters and velocities associated with samples impacted 25 times.

	V1 $m\,s^{-1}$	V2 $m\,s^{-1}$	V3 $m\,s^{-1}$	V4 $m\,s^{-1}$
5 mm	M5-V1	**M5-V2**	**M5-V3**	M5-V4
10 mm	**M10-V1**	M10-V2	M10-V3	**M10-V4**
15 mm	**M15-V1**	M15-V2	M15-V3	**M15-V4**
20 mm	M20-V1	**M20-V2**	**M20-V3**	M20-V4

Table 4.6: Diameters and velocities associated with samples impacted 50 times.

	V1 $m\,s^{-1}$	V2 $m\,s^{-1}$	V3 $m\,s^{-1}$	V4 $m\,s^{-1}$
5 mm	**M5-V1**			**M5-V4**
10 mm		**M10-V2**	**M10-V3**	
15 mm		**M15-V2**	**M15-V3**	
20 mm	**M20-V1**			**M20-V4**

scenarios. A primary consideration in the testing procedure was SHI integrity. The volume and mass of the projectile must be maintained for the impacts to be realistic. As the sizes of the manufactured hailstones involved were a magnitude smaller than the extreme diameters in comparable studies in the literature, the sensitivity to environmental temperature were found to be markedly greater. Even with 63.5 mm, SHI Swift [120] found, through infra-red imagery, that the surface of the sphere was quickly affected by the room temperature. Originally the hailstone cannon was located in a laboratory with many other heat-producing equipment, where the environmental temperature consisted of temperatures close to 25 °C. Unfortunately, there was no cold room in the university that could fit the experimental rig and certainly not with any additional required apparatus. However, the ambient temperature in another location was found to be a lower in the region of 15 °C-20 °C, whilst still maintaining a similar distance away from the chest freezer (a transfer time of roughly thirty seconds). The justification for moving the experimental analysis to this other location, despite having carried out extensive testing already, is demonstrated below.

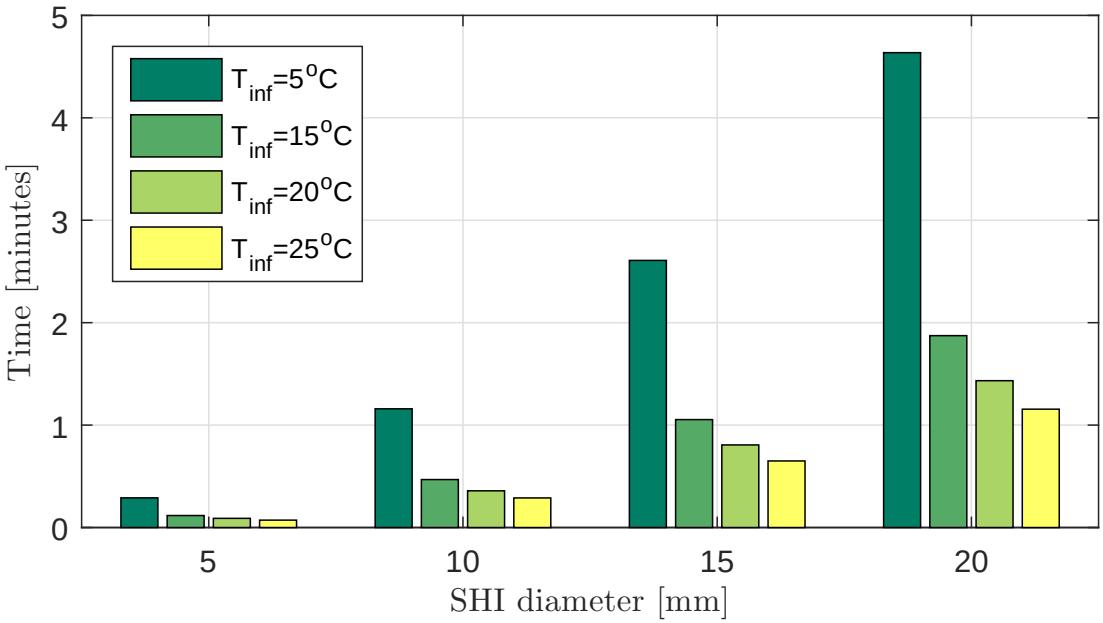

Figure 4.21: Surface melting times from Heisler equation for $T_i = -2.5\,°C$.

Figure 4.21 displays the time taken for the surface of each diameter of SHI to reach 0 °C for 3 different environmental temperatures: an elevated laboratory temperature (Tinf=25 °C), a moderate-level temperature, a lower level temperature (Tinf=20 °C) and the upper temperature limit of a cold-room (Tinf=5 °C). Although the initial temperature of the SHI could be lower, from the initial freezer storage, the initial

temperature was assumed to be −2.5 °C, the typical electric cool box temperature. Rhymer et al [85] describe firing each ice sphere 3 minutes after removal from the freezer. However, from the graph, all the projectiles would most likely be undergoing phase change after roughly a minute in the elevated temperature environment, with 5 mm the worst affected.

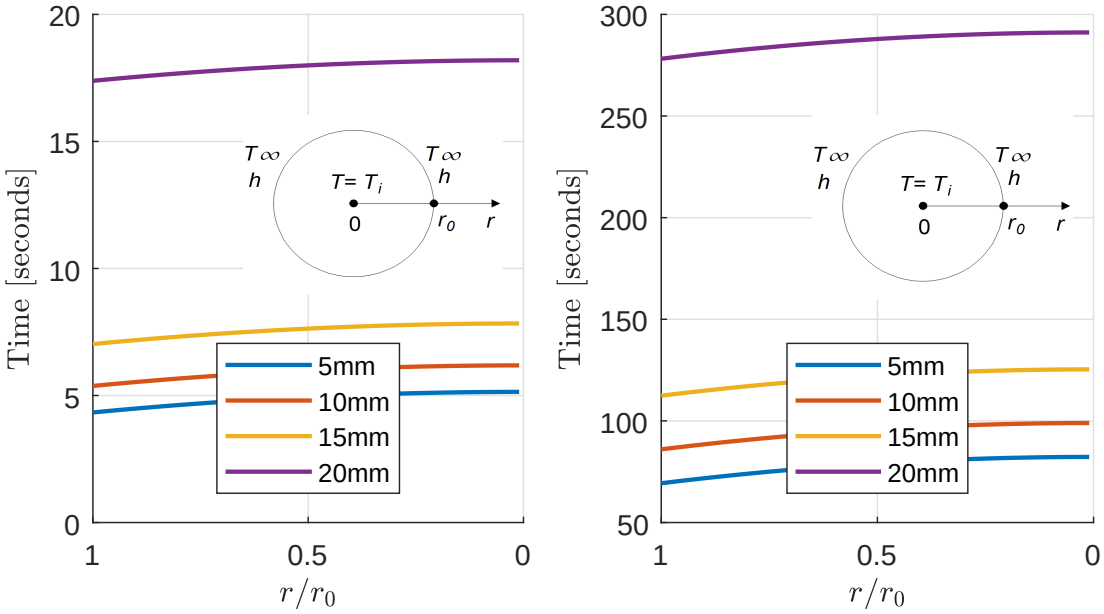

Figure 4.22: Radial melting times for different diameters of hail from Heisler equation for $T_i = -2.5\,°C$ and $T_i = -5\,°C$.

Figure 4.22 shows the time taken for the temperature to reach T_0 (0 °C) at different radial locations along the sphere and thus the time taken for the centre to reach zero once the surface has. This demonstrates, especially for 5 mm, that once the surface has been affected it did not take long for the rest of the SHI to be at risk of melting. Although from both Figure 4.21 and Figure 4.22 it appeared that only the larger sizes would benefit from a location change, it was found that the electric cool box was able to achieve temperatures of −5 °C when moved to the cooler environment.

As Figure 4.23 shows, this effectively doubled the melting times associated with Figure 4.21 across the range of diameters. It should be noted that these times should be taken more of as a comparative guide, as there are many external factors that are not considered (i.e. the transfer of heat between other solids). With the sensitive and challenging temperature requirements of the SHI in mind, other aspects of the experimental procedure were scrutinised to see if any other enhancements could be made, within the remit of the research project. Ideally a chest freezer would be located within the same room as the experimental rig. Unfortunately, for the safe operation of other

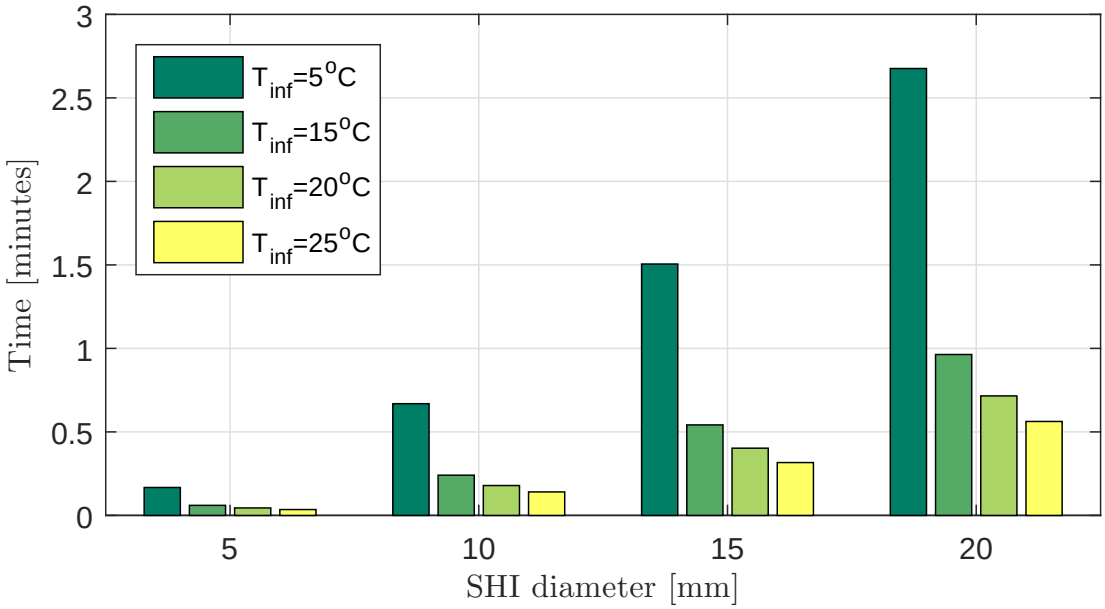

Figure 4.23: Surface melting times from Heisler equation for $T_i = -5\,°\text{C}$.

experimental equipment in the vicinity this was not possible. It should, however, be a priority for future experiments. Even excluding the moderate activity from the trips back and forth, the average metabolic rate (male, adult) from carrying out laboratory work is 130 W [121]. Therefore, care was taken to reduce the human heat impact on the experiments by wearing gloves, using tweezers to transfer the projectiles to the sabot and not directly breathing over the ice sphere. Although not considered in time for this project, a further saving could be achieved by pre-loading the projectiles into multiple sabots, much like shotgun shells. For minor gains, the detachable barrels and transporting cool box were stored in the chest freezer prior to experimental use, with the cool box also being returned immediately once the contents were delivered. Additionally, when the SHI were taken to the electric cool box, a commercial freezer/ice pack was also transported with them. With these considerations and after numerous trials, it was decided that five would be a safe but effective number of SHI projectiles to transport and store in the electric cool box for firing sessions. To reduce the amount of time outside the cool box, the pressure was built up in the reservoir prior to loading the projectile and sabot into the barrel. The pressure level was double-checked before firing for assurance. Once the overall experimental methodology had been finalised the pressure-velocity calibration could be initiated. The force information from these impacts was also recorded.

Both the pressure vessel and the pressure-reducing valve (PRV) are rated to 10 bar. Although this meant that a wide range of pressure was potentially available,

the supply pressure was limited to 5 bar. The pressure reducing valve also provided redundancy in terms of safety. The four different hailstones were fired at least five times, at intervals of 0.5 bar from ∼0.5 bar-4 bar. However, for the 20 mm case it was found that 0.5 bar of pressure was not sufficient to propel the projectile from the sabot reliably. Therefore, the pressure in this instance was increased to 0.6 bar. The average velocities and standard deviations from these tests can be seen in Figure 4.24.

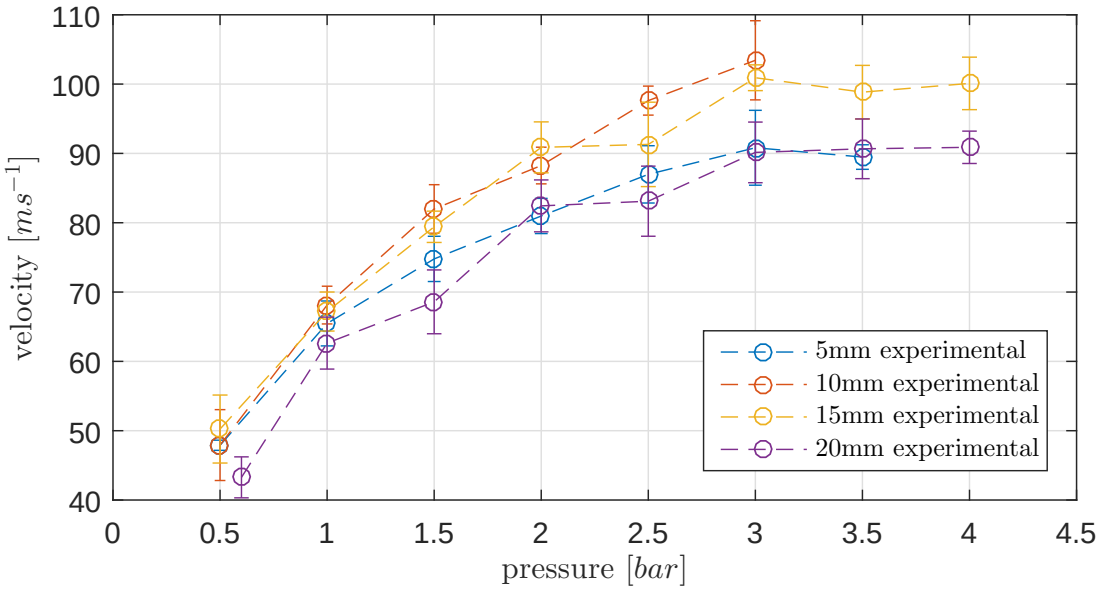

Figure 4.24: Average velocities vs. pressure for cannons of different projectile diameter.

It can be seen that for the same pressure, a higher diameter did not necessarily mean a lower velocity, as mass and air friction both play a role. It can be seen that for the most part, the pressure-velocity curves for the SHI with diameters in the mid-range (10 mm and 15 mm) were quite similar, both following higher velocities than those of the other diameters. Those at the ends of the spectrum were also quite similar to each other, although with the 20 mm variant the velocities were notably lower at lower pressures. All four experimental curves appear to follow a trend in the form of

$$u_0 = ap^{1/b} + c. \tag{4.8}$$

Fitted trend lines were generated for different root powers from 1 onwards in intervals of 0.1, with the R^2 value of the trendline observed. The curves improved with increasing root power but it was found that $p^{\frac{1}{5}}$ provided sufficient convergence. This curve is also included in Figures 4.25, 4.26, 4.27 and 4.28.

All the trendlines appeared to be visually similar to their experimental counterparts and the x-axis intersections for all four were close to zero. The 10 mm trendline showed

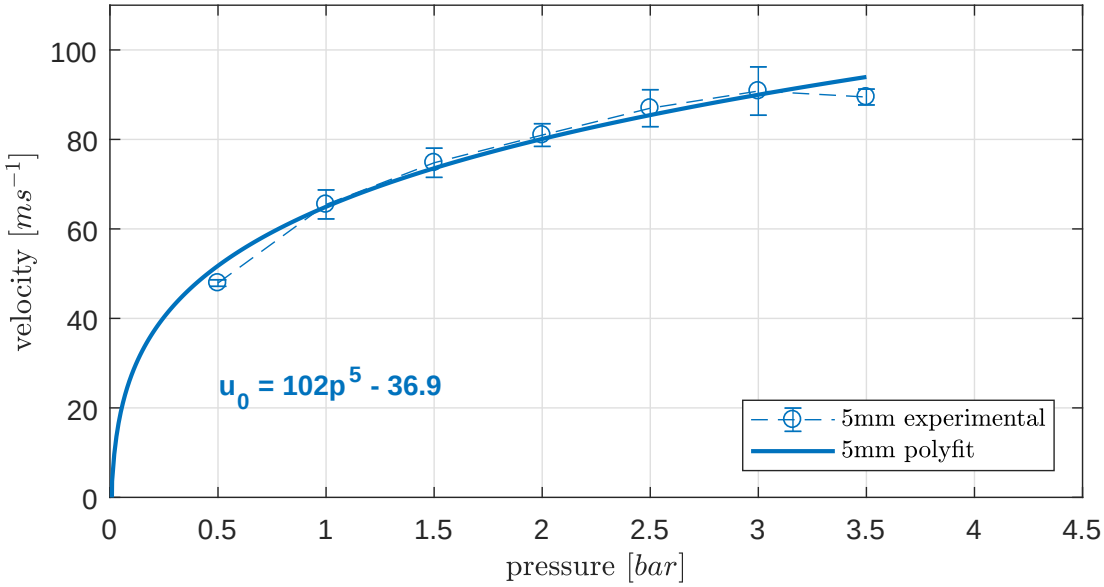

Figure 4.25: Experimental and fitted trend for 5mm SHI projectile.

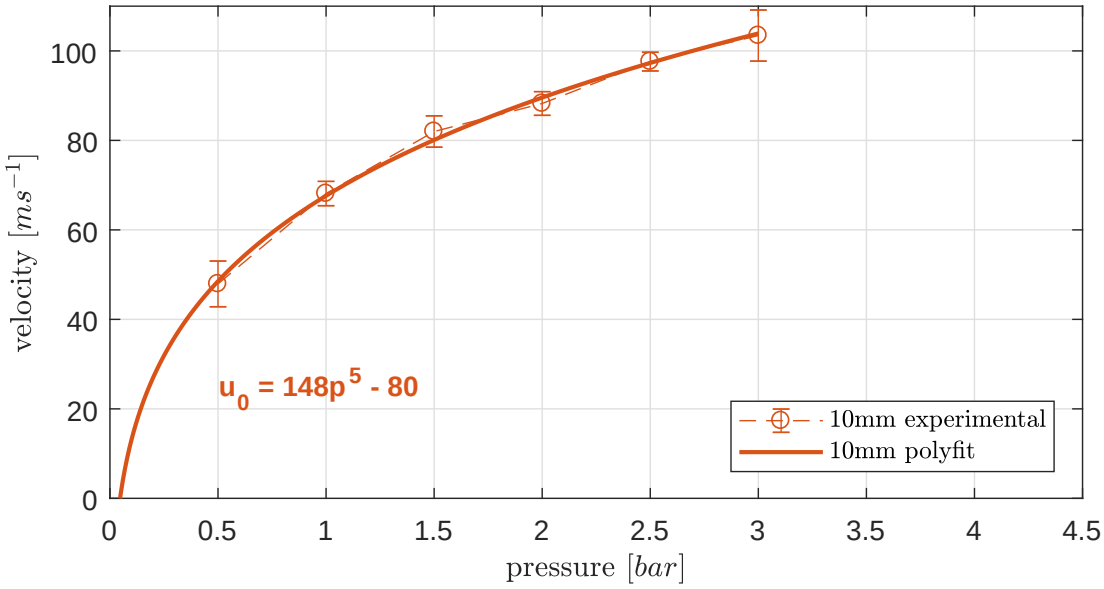

Figure 4.26: Experimental and fitted trend for 10mm SHI projectile.

the best emulation, with an overall R^2 value of 0.997, which contrasted with the 20 mm trendline having the lowest value of 0.947, which is still very favourable. However, it can also be seen that the velocity seems to level out after ~3 bar for the 5 mm, 15 mm and 20 mm SHI, which would be harder for the trendline to follow. This information was used to determine the four different pressures/velocities that would be used for experimentation in Section 4.6. With the uncertainties involved, it was important to

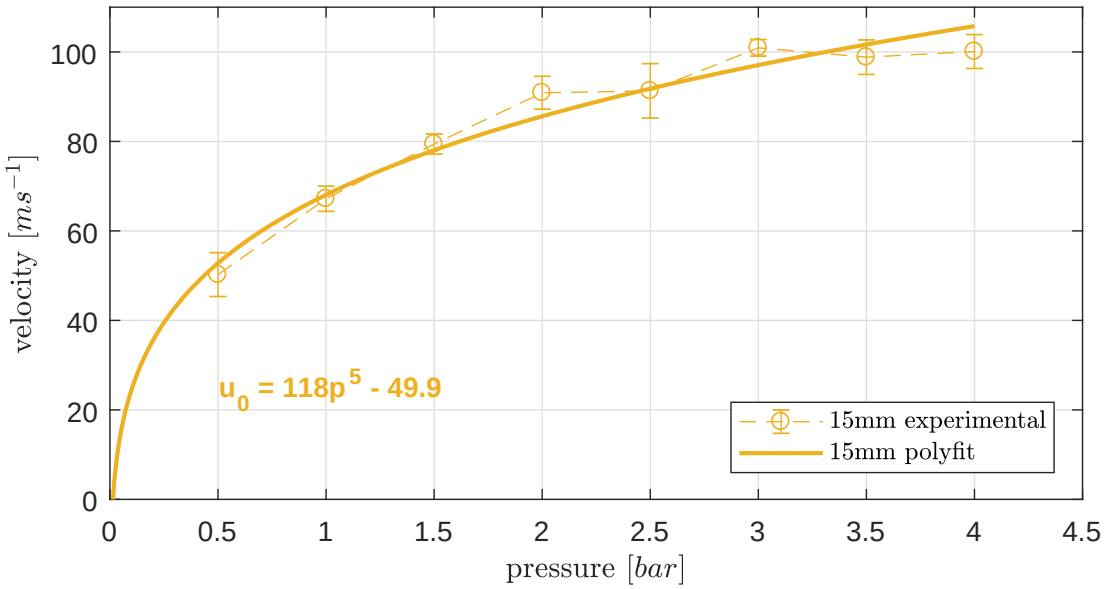

Figure 4.27: Experimental and fitted trend for 15mm SHI projectile.

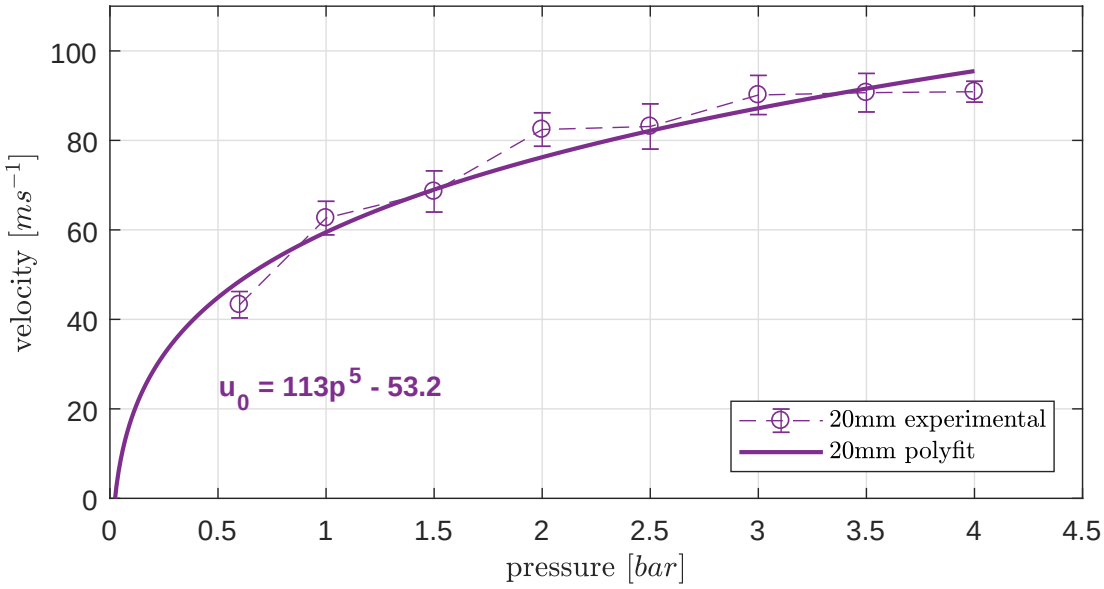

Figure 4.28: Experimental and fitted trend for 20mm SHI projectile.

try and position each velocity so that that it would be less likely to overlap another. Despite the motivation to include the highest velocity possible, in order to represent the uppermost wind turbine tip speeds, it was unlikely that this could be achieved across all the diameters. The velocities selected were $50\,\mathrm{m\,s^{-1}}$, $65\,\mathrm{m\,s^{-1}}$, $80\,\mathrm{m\,s^{-1}}$ and $95\,\mathrm{m\,s^{-1}}$. Using the trendlines a corresponding pressure was found for each of the velocities. For comparison, the linear curves between the experimental data points were also used and

often found to be more appropriate for some of the highest or lowest velocity pressure selections. These were rounded to the nearest 0.1 bar.

To further refine the calibration, the force information was also analysed to determine whether a specified velocity would result in a consistent force profile.

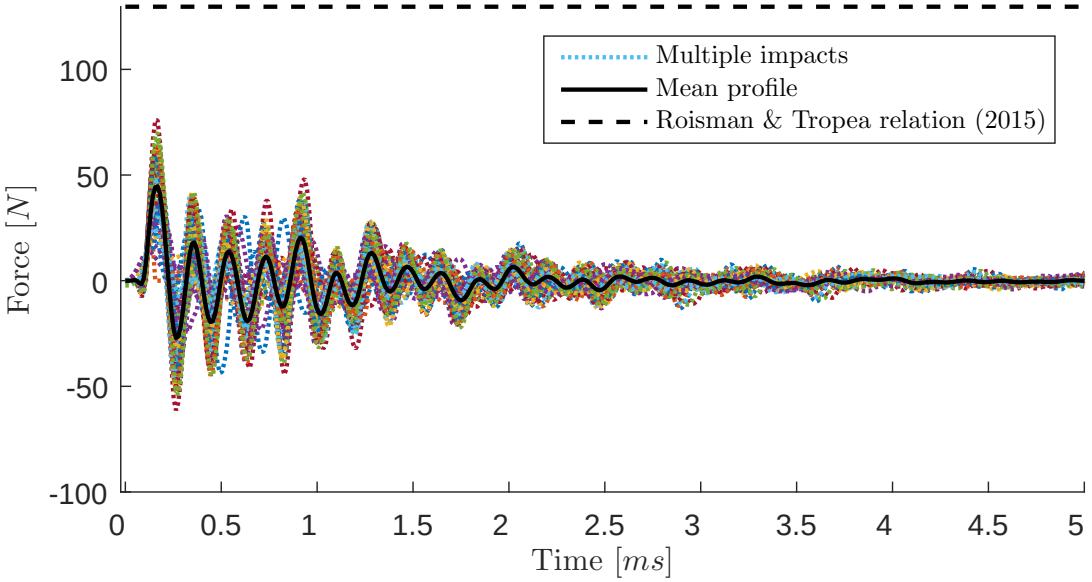

Figure 4.29: Force transducer impact profiles for 5 mm SHI fired at 0.6 bar.

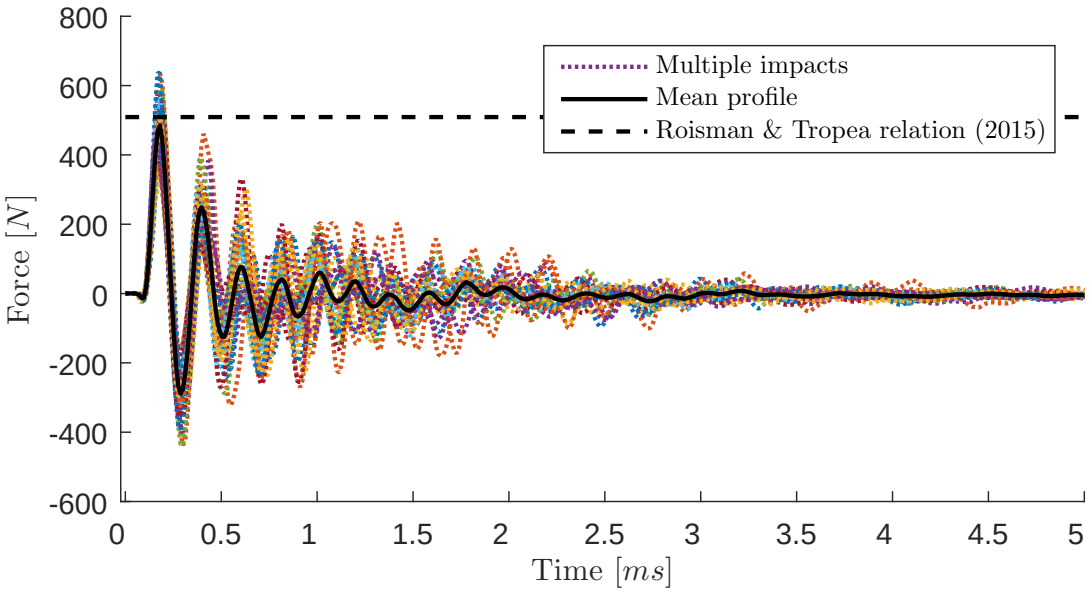

Figure 4.30: Force transducer impact profiles for 10 mm SHI fired at 0.6 bar.

Examples of the force-time relationships for the different diameter impacts at 0.6 bar

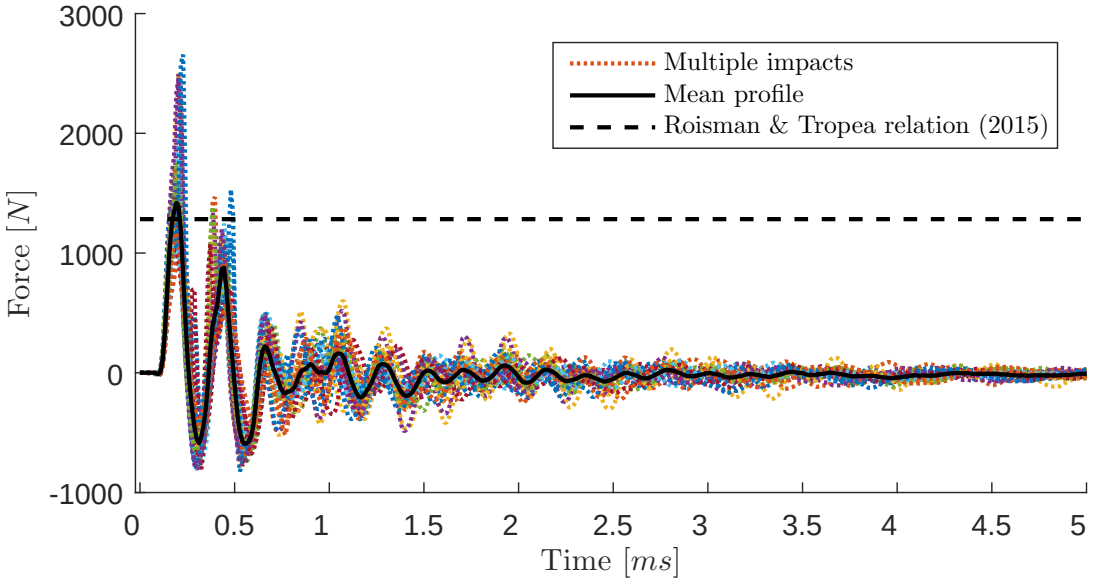

Figure 4.31: Force transducer impact profiles for 15 mm SHI fired at 0.6 bar.

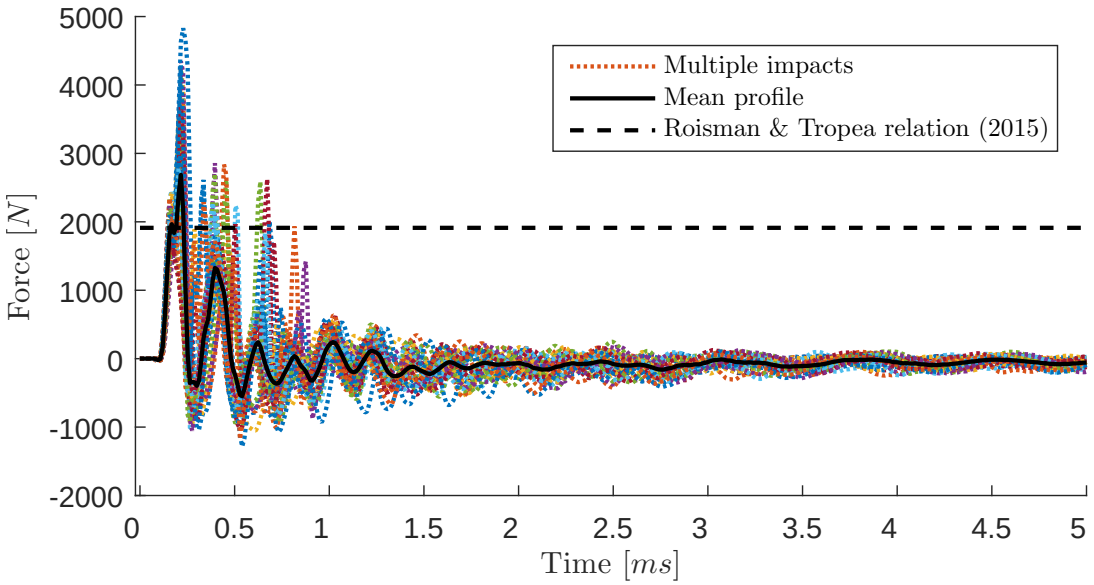

Figure 4.32: Force transducer impact profiles for 20 mm SHI fired at 0.6 bar.

are displayed in Figures 4.29, 4.30, 4.31 and 4.32, along with the mean profile of those impacts. For all cases, measured force showed a profile approximately resembling a damped sinusoidal pattern occurring at similar wavelengths for the different diameters, with the maximum force occurring at the first peak. Overall, the measured force was effectively damped out around the 5 ms mark. The peak of the mean profile for the 10 mm, 15 mm and 20 mm impacts related well to the peak force calculated using the

Roisman & Tropea [30] equation for spherical impact on a rigid wall. The empirical relation is shown in Equation 4.9, with the mean density used for each size of ice sphere.

$$F \approx \frac{4\pi}{3} r_0^2 u_0 \rho^{1/2} \Upsilon^{1/2} \tag{4.9}$$

Here the effective compressive failure stress (usually determined as a function of strain rate) is found from,

$$\Upsilon = \Upsilon_{stat} \exp \frac{0.9 u_0}{u_c} \tag{4.10}$$

The Quasi-static yield strength, Υ_{stat}, was taken to be 5.2 MPa, which applies to strain rates below $0.1\,\mathrm{s}^{-1}$.

There was a certain amount of variation for these impacts with the first two wavelengths being the most consistent in shape for the multiple measurements, although showing some variance at the local maximum/minima. However as we increased the diameter from 10 mm to 20 mm, there were notable 'spikes' in and around this region, with some major differences from the mean.

Comparatively in Figure 4.29, the peak of the mean 5 mm experimental profile fell well short of the predicted peak. The difference between the second and third positive peak was also less pronounced, compared with the other sizes of SHI.

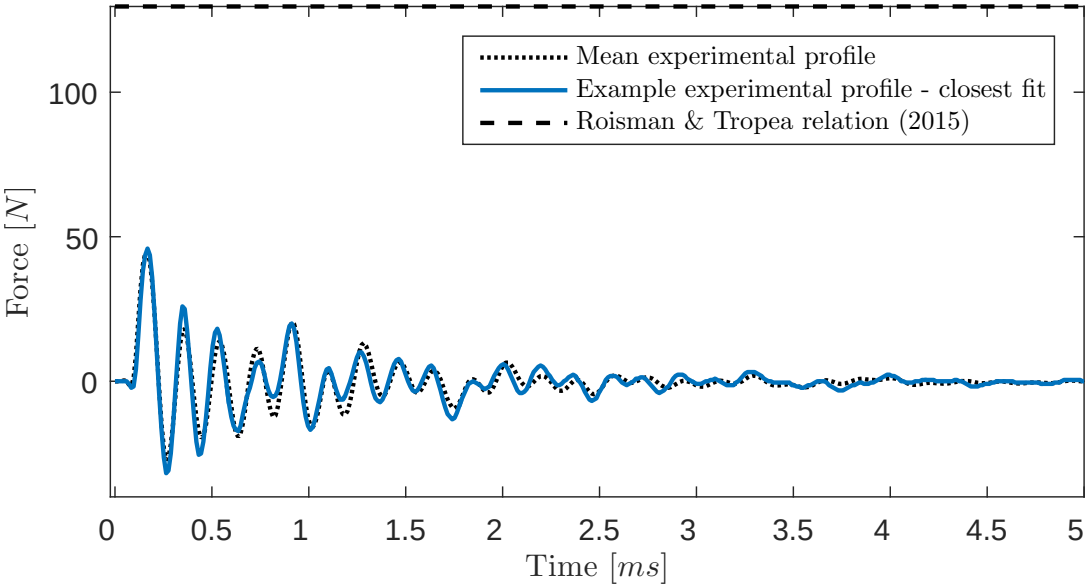

Figure 4.33: Mean force transducer impact profiles for 5 mm SHI fired at 0.6 bar compared to most similar individual example.

As there can be considerable variation amongst the different impacts for the same diameter at this pressure, Figures 4.33, 4.34, 4.35 and 4.36 describe the mean profile for

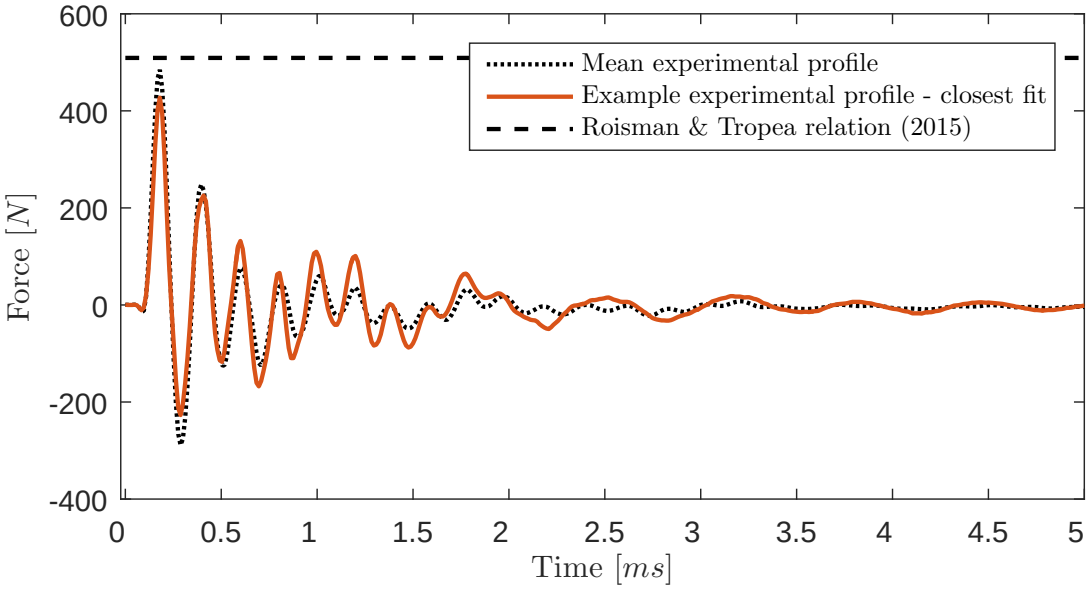

Figure 4.34: Mean force transducer impact profiles for 10 mm SHI fired at 0.6 bar compared to most similar individual example.

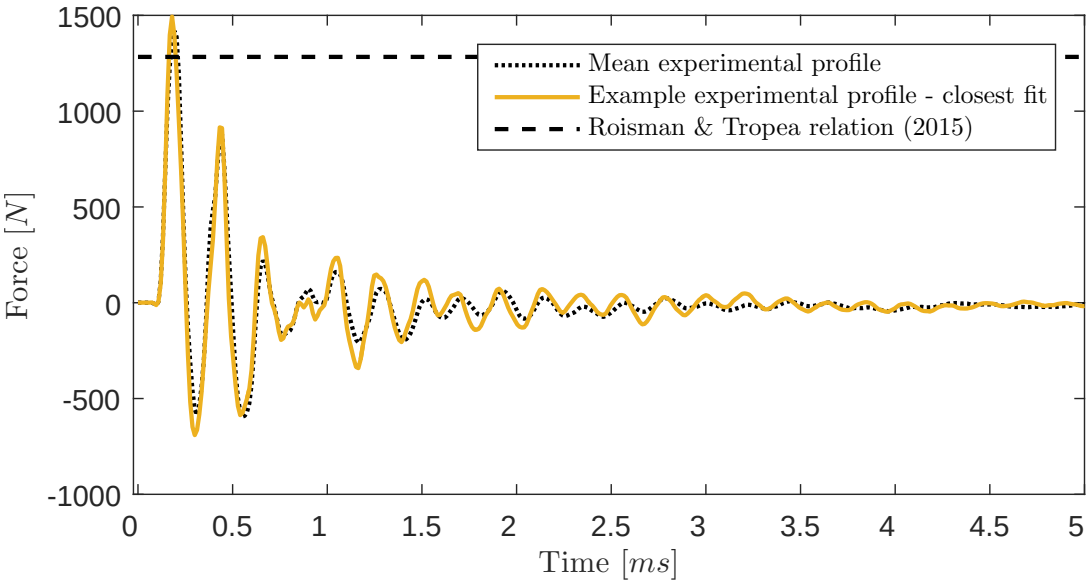

Figure 4.35: Mean force transducer impact profiles for 15 mm SHI fired at 0.6 bar compared to most similar individual example.

each diameter of SHI, as well as the nearest actual experimental recording. We can see that, the 5 mm mean was in fact quite similar to its nearest experimental counterpart, capturing the overall trend quite well with a RMSE value of roughly 0.5. The 10 mm comparison was slightly worse in terms of amplitude throughout and lost correlation

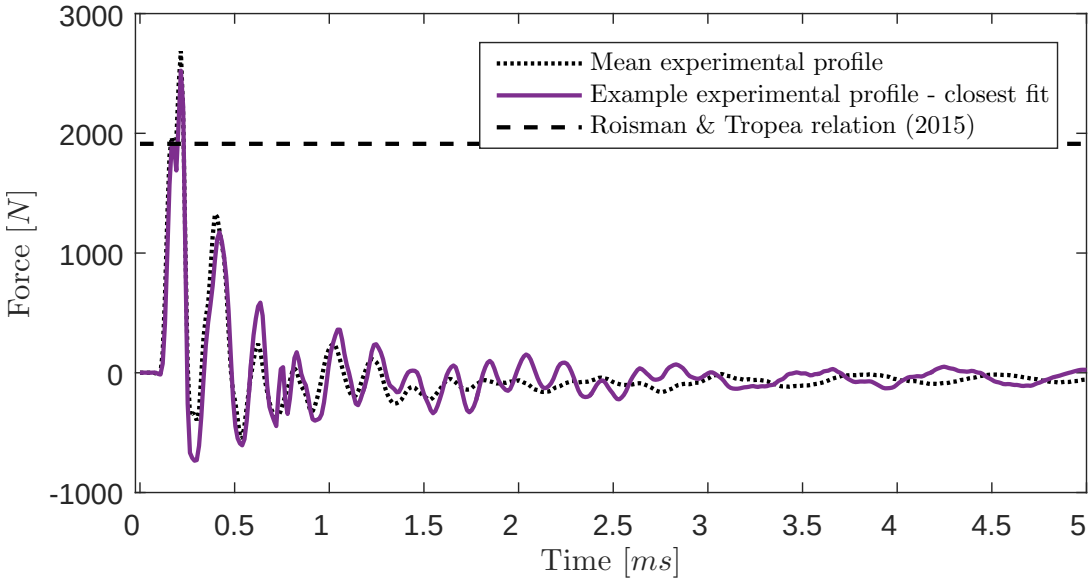

Figure 4.36: Mean force transducer impact profiles for 20 mm SHI fired at 0.6 bar compared to most similar individual example.

after the 2 ms mark, resulting in a RMSE of approximately 5. The 15 mm may have had an increased RMSE of 11.5 but the mean captured the experimental trend, including the distinctive feature just before 1 ms had passed. Despite the spikes observed in Figure 4.32, the mean of multiple 20 mm impacts bore some resemblance to an actual experimental profile with an RSME of around 25. This similarity holds less well between 1.5 ms to 3 ms, with the mean unable to produce the higher frequency response of the example, due to the positional variance between the different impacts. The average RSME from all the comparisons between the mean and experimental profiles at this pressure were 1.23, 8.92, 22.07 and 47.44 for the 5 mm, 10 mm comparison, 5 mm and 20 mm diameters of SHI respectively, which was close to a cubic relationship.

The corresponding multiple-impact figures for the highest selected pressure at each diameter are exhibited in Figures 4.37, 4.38, 4.39 and 4.40. There was a marked increase in high force 'spikes' across the diameters, particularly for the 15 mm and 20 mm variants where the multiple impacts made it difficult to discern the sinusoidal trend. The mean profile showed a less smooth trend but the mean peak force still matched the Roisman Tropea relation fairly well for the 10 mm, 15 mm and 20 mm, albeit marginally under the estimation. Again the 5 mm impacts were well below the predicted value for this relationship.

The comparisons for the individual examples are located in Figures 4.41, 4.42, 4.43 and 4.44, where the dynamic force response for each diameter can be analysed in more detail. The peak of the 5 mm impact at 3 bar was just under 50 N, similar to

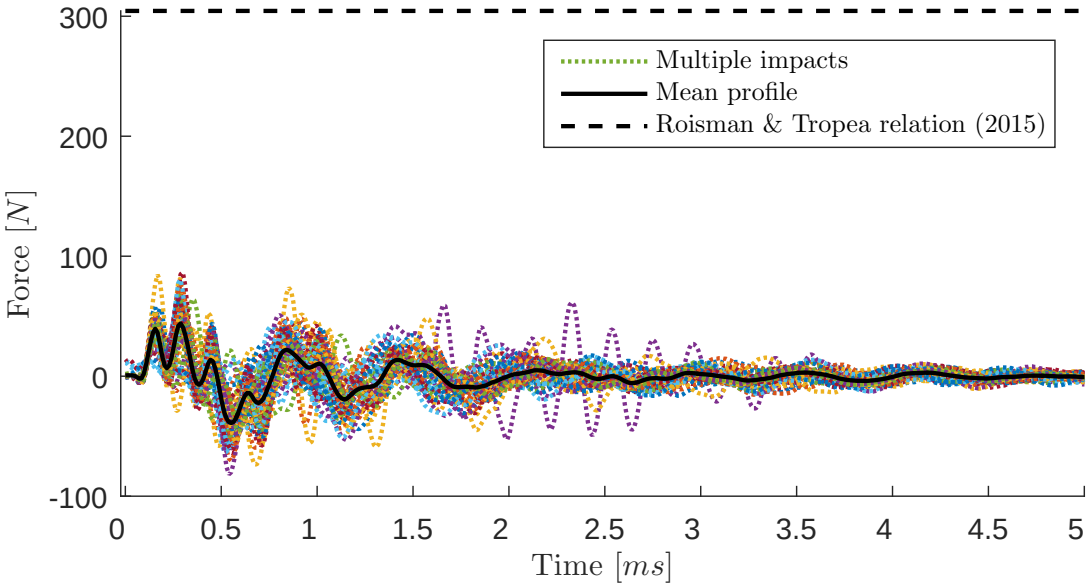

Figure 4.37: Force transducer impact profiles for 5 mm SHI fired at 3 bar.

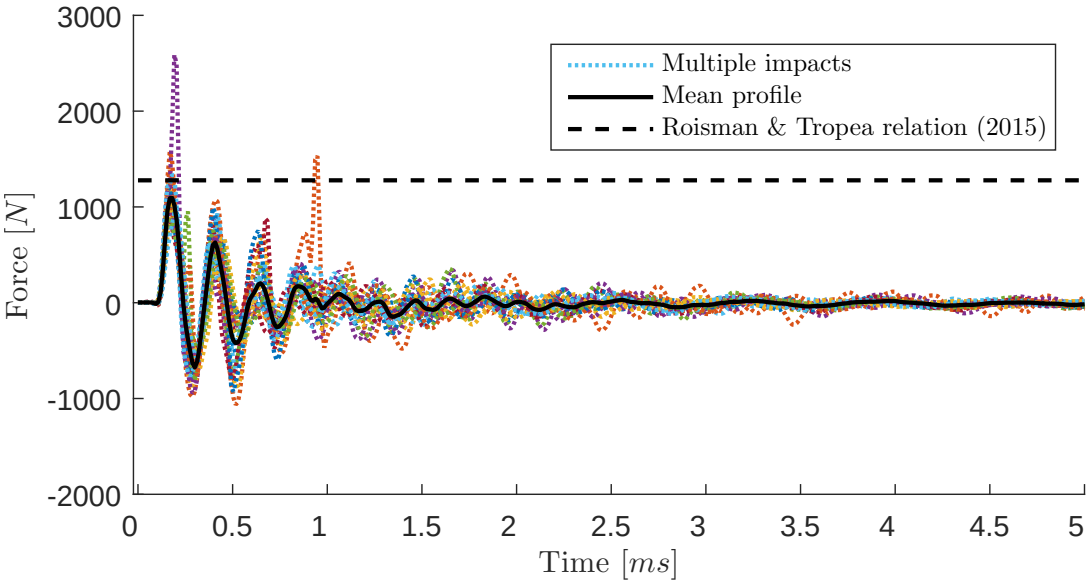

Figure 4.38: Force transducer impact profiles for 10 mm SHI fired at 2.4 bar.

the 0.6 bar impacts, although the sinusoidal trend appears to be a complex waveform, much broader than the low velocity counterpart and with additional harmonics. This could indicate that the hailstone was either interacting with the composite differently or the integrity of the sphere could be have been compromised. The form of the 10 mm response at 3 bar was similar to the 0.6 bar appearance. Apart from the first peak, the structure of the 15 mm mean curve was inconsistent, with the spikes from the different

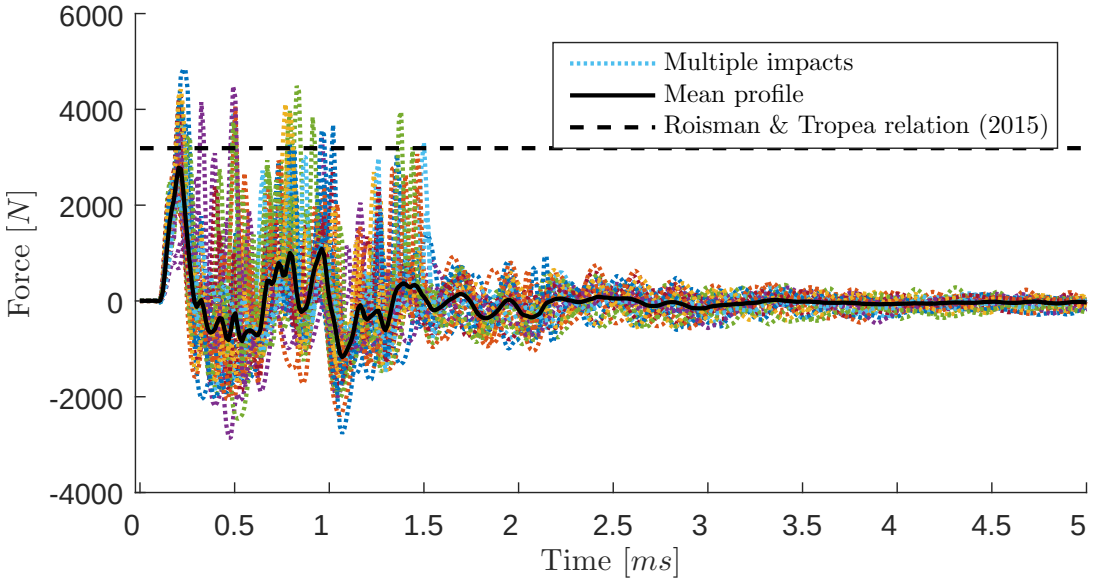

Figure 4.39: Force transducer impact profiles for 15 mm SHI fired at 2.8 bar.

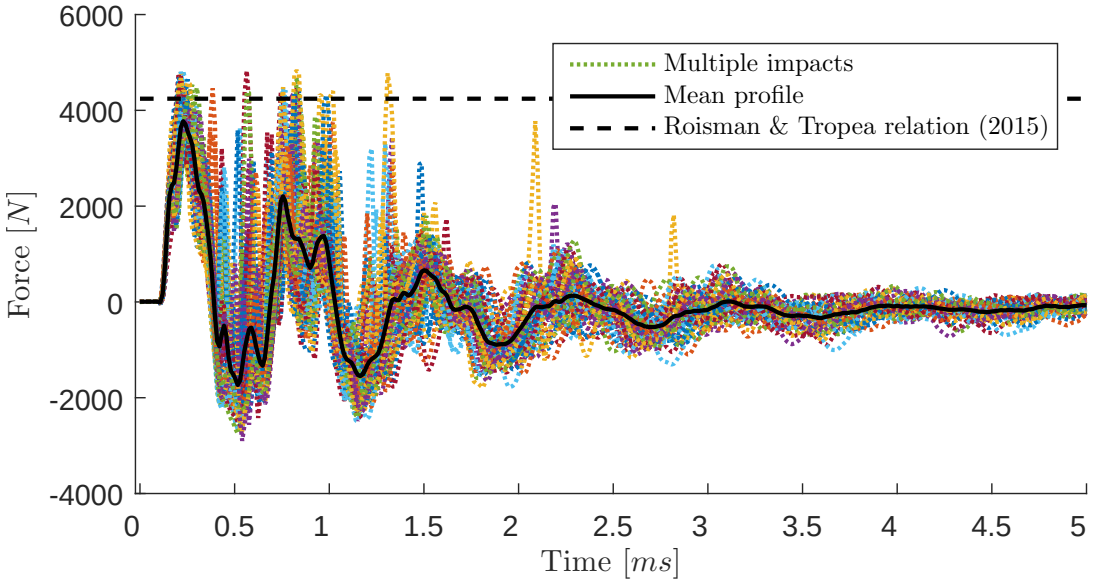

Figure 4.40: Force transducer impact profiles for 20 mm SHI fired at 3.4 bar.

examples resulting in a jagged profile. Lastly, the 20 mm had a longer wavelength but with small irregularities and harmonics spread throughout. Overall, the RMSE between the mean profile for the greatest pressure and the best-fit example were 1.96, 22.7, 96.5 and 106 for 5 mm, 10 mm, 15 mm and 20 mm respectively.

The first peak in all cases provided the maximum force measured by the transducer and this was analysed in more detail. Tippmann *et al.* [19] described the relation-

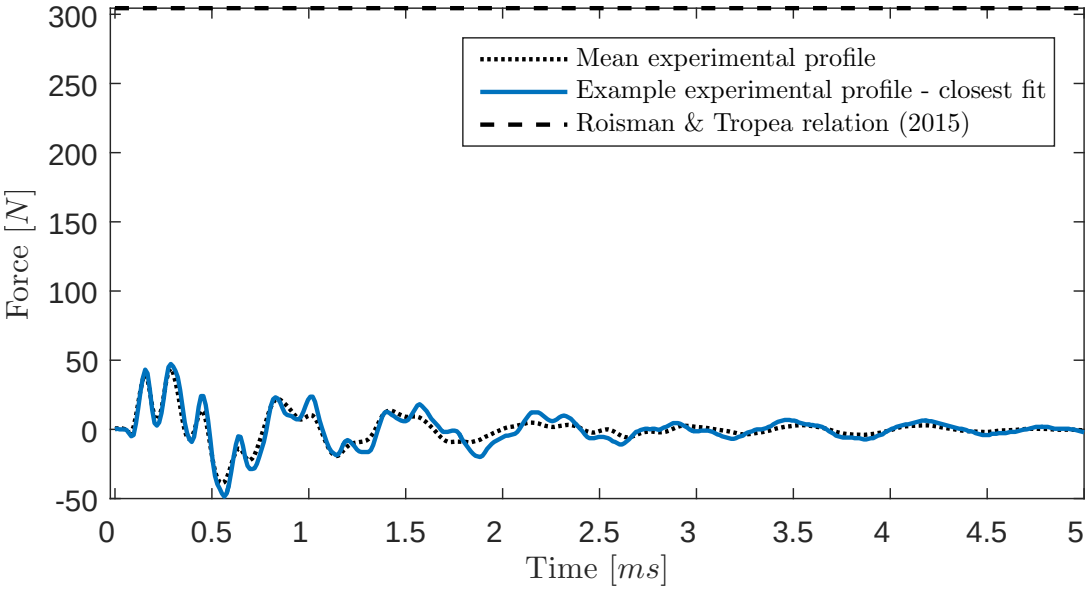

Figure 4.41: Mean force transducer impact profiles for 5 mm SHI fired at 3 bar compared to most similar individual example.

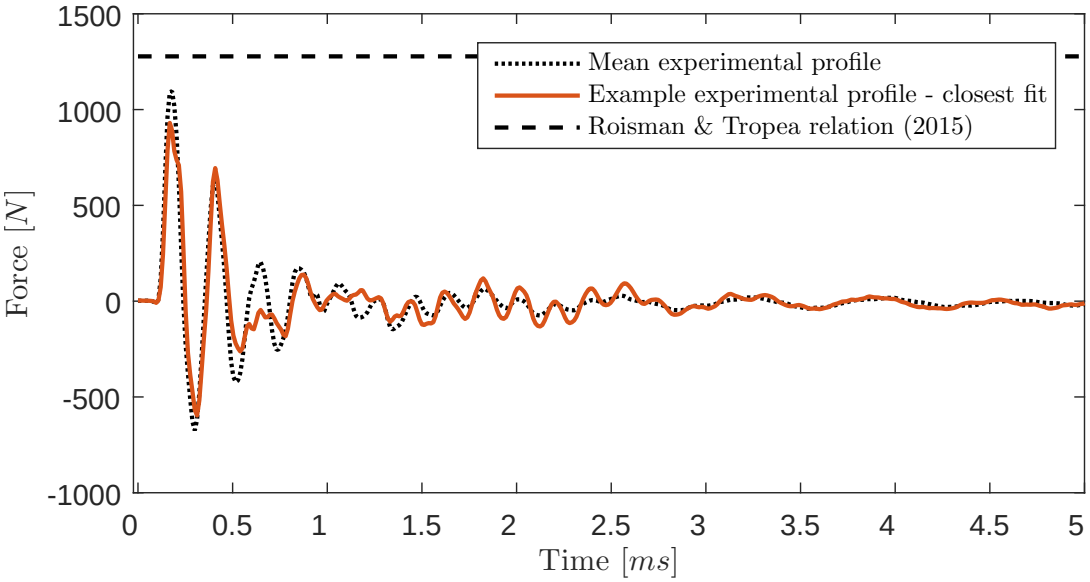

Figure 4.42: Mean force transducer impact profiles for 10 mm SHI fired at 2.4 bar compared to most similar individual example.

ship between the kinetic energy of SHI of large diameters with the measured peak force (also see Figure 2.22 in the Literature Review). In this study, three trendlines were produced: 'experimental (filtered) data', 'computer simulated data' and 'all data'. These along with disseminated impacts and trendlines taken from this study are displayed in

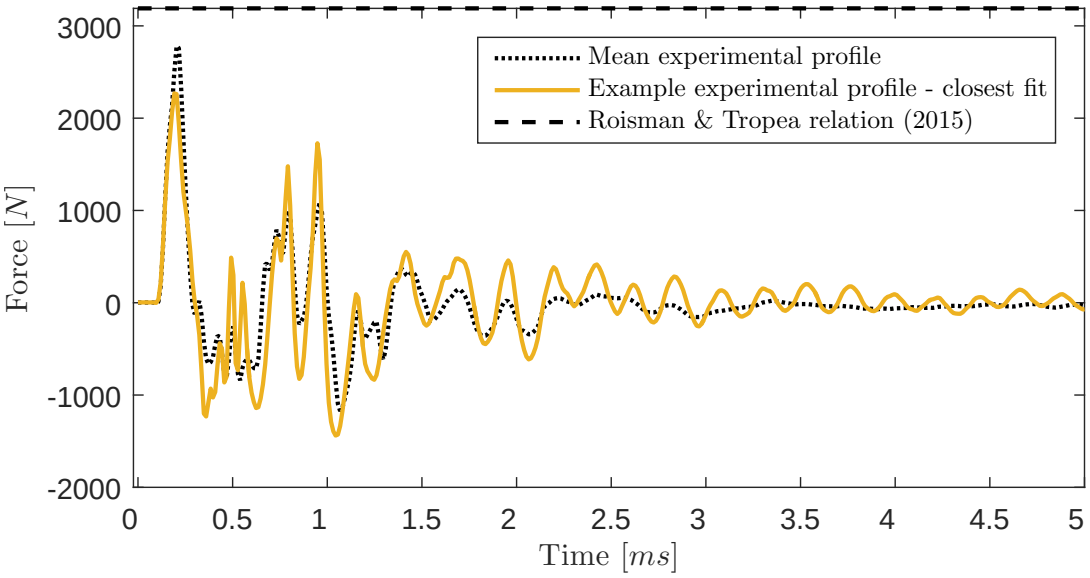

Figure 4.43: Mean force transducer impact profiles for 15 mm SHI fired at 2.8 bar compared to most similar individual example.

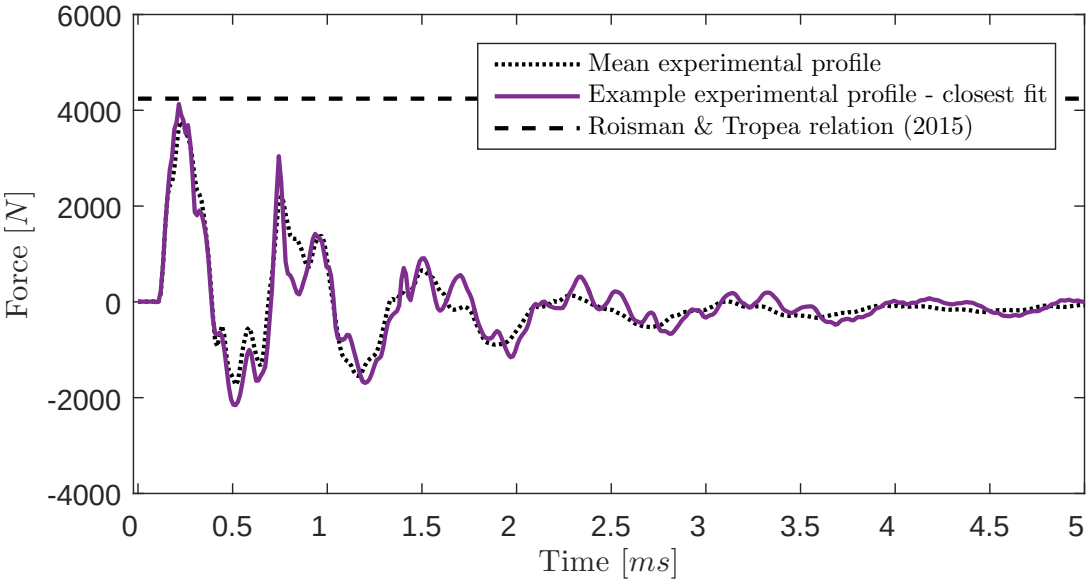

Figure 4.44: Mean force transducer impact profiles for 20 mm SHI fired at 3.4 bar compared to most similar individual example.

Figure 4.45a and Figure 4.45b.

The kinetic energy range in Figure 4.45a was 0 J to 400 J, whereas in Figure 4.45b the range was 0 J to 2500 J. Similar to the velocity profile, the trendlines were in the form of Equation 4.8. The difference in impact energy and force between the smaller diameters investigated in this thesis and the extreme studies in other hail-

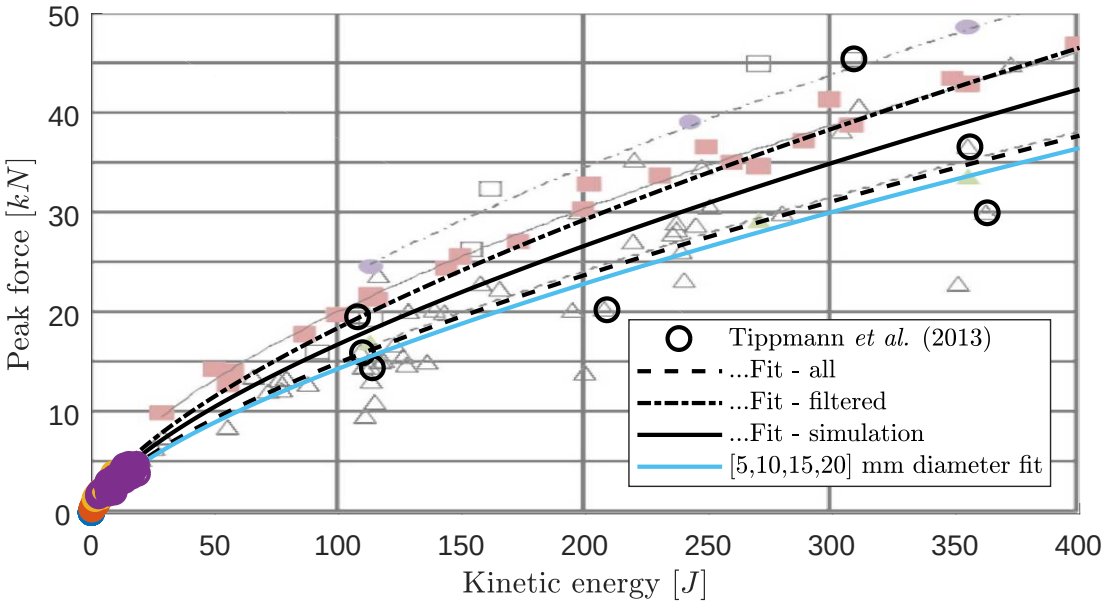

(a) Less than 400J

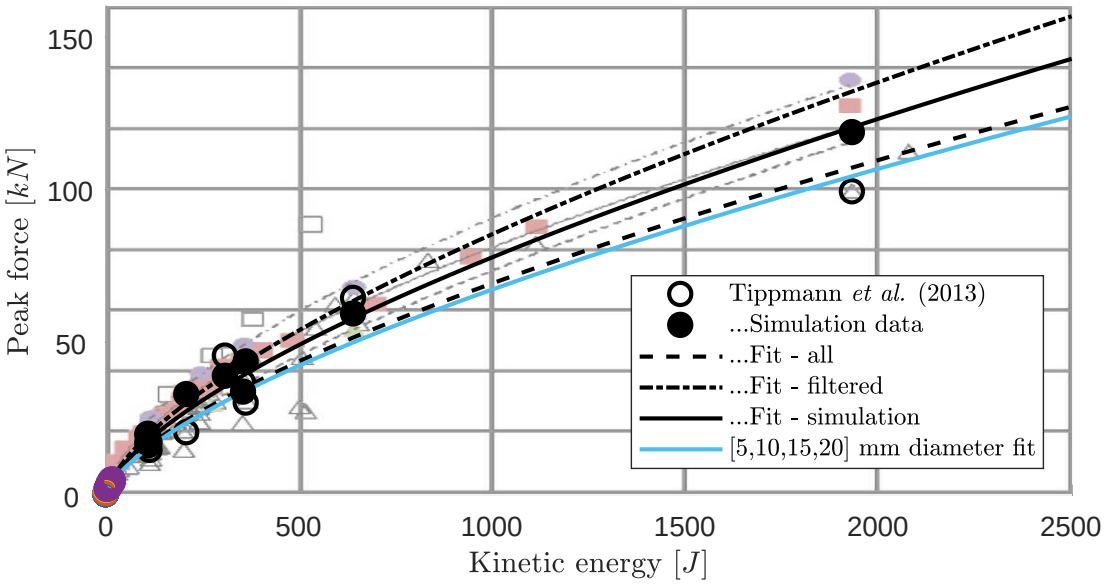

(b) Less than 2500J.

Figure 4.45: Peak force versus kinetic energy relationship (all diameters) compared with Tippmann *et al.* [19] data.

impact literature were certainly highlighted here. The trendline for the SHI of all the smaller diameters compared well with the data of Tippmann *et al.* [19]. Closer inspection of the individual lower-diameter impacts is available in Figure 4.46. At this resolution, the 10 mm, 15 mm and 20 mm diameters still favour the Tippmann data to a reasonable fit but the spread of the 15 mm and 20 mm was more apparent. One of

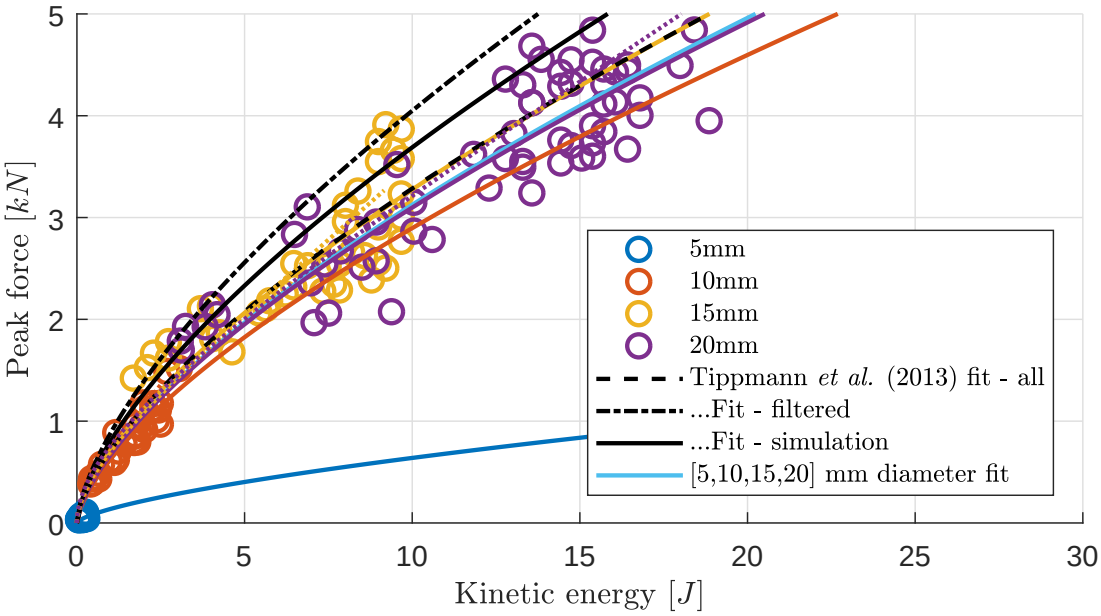

Figure 4.46: Peak force versus kinetic energy relationship (individual diameters) compared with data from Tippmann *et al.* [19].

the most of prominent features of this graph, was that the 5 mm data and trendline did not match the trend of the other diameters. Instead, the increase in peak force for an increase in kinetic energy at this diameter was much less than expected.

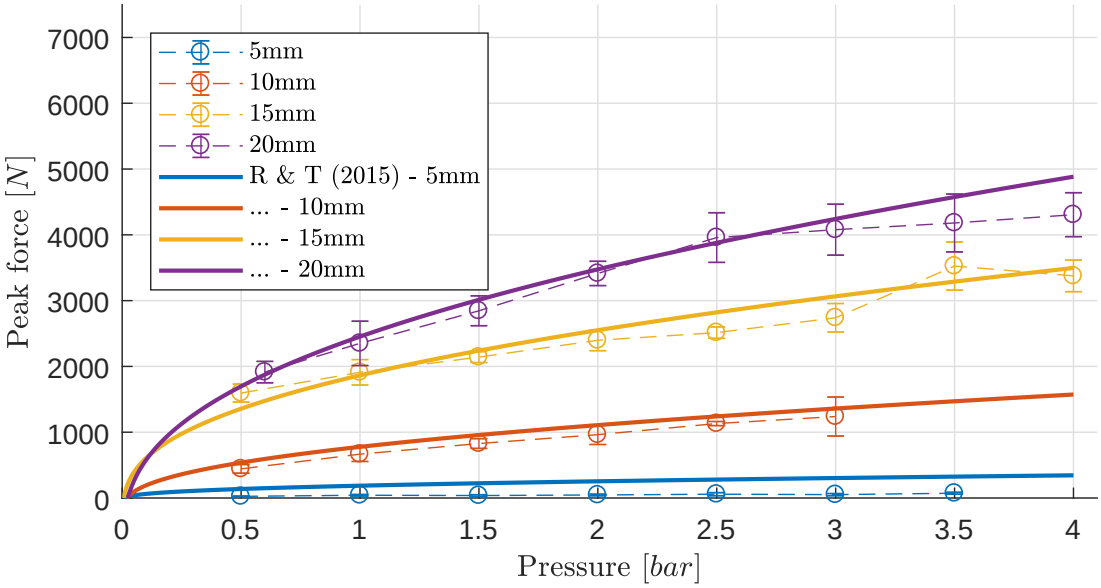

Figure 4.47: Peak force vs. selected pressure compared with estimated values from Roisman & Tropea [30].

The resultant peak force for a selected pressure is explored in Figure 4.47. Using the pressure/velocity relationship given by Figures 4.25, 4.26, 4.27 and 4.28, the trendlines from the experimental data were evaluated against the empirical relation developed by Roisman & Tropea [30]. The 10 mm, 15 mm and 20 mm variants compared very well to the empirical prediction, with again a greater spread experienced by the 15 mm and 20 mm diameters, especially at higher velocities. There appeared to be higher-than-expected forces for the 15 mm firings at 0.5 bar. However, the 5 mm forces were again under-represented. Only the slightest increasing trajectory was observed, which appeared to be horizontal at first glance but this is also due to the scale of the y-axis. Unfortunately, the ± 10 V restraint of the DAQ used for collecting force measurement was exceeded during the testing of 20 mm impacts at maximum pressure, with some peaks restricted to the equivalent force limit. It may mean that at these higher velocities, the force profile and thus maximum force was not properly represented. Other miscellaneous factors that could affect the experimental results were also discovered throughout the calibration campaign. Unlike other hail propulsion rigs [19, 34] the vertical configuration meant that a certain amount of residual water/ice mixture could be left stagnant on the sample following impact. The quantity of liquid left on top would obviously depend on the volume of ice particle and also on the velocity of impact, with higher-velocity examples spreading wider and further. Composites are known to absorb water, which can alter the mechanical properties [122] and have affected the results obtained for each case. For this reason, the stagnant solution was gently dabbed away after each firing, using an absorbent cloth. Utmost care was taken not to rub against the surface itself, as that could be a source of wear.

4.5.1 High Speed Video

A high-speed video camera was employed in order to ascertain, primarily, whether the impacts were genuinely hitting the composite surface and secondly whether each type of SHI was still intact prior to impact. Regrettably, the capabilities of the camera would not allow for the high-quality footage exemplified by other sources of literature and thus detailed analysis of the sphere and sample upon impact was not possible. Additionally, several halogen lamps had to be shone onto the target area for the footage to be visible at the maximum possible frame rate of 5000 frames per second. To obtain a sufficient number of images, each projectile had to be fired at the lowest possible pressure/velocity, which meant neglecting the possible differences of higher velocity examples. The heat generated by the lamps made for an even more challenging experimental environment, despite only being utilised for the duration of filming (a matter of seconds). At this rate the resolution was reduced to 128 x120 pixels, diminishing the

quality of images even further. Fortunately, some discernible footage was obtained. A secondary use of the video camera was to verify that the velocity measured by the light gate was accurate. Placing a right-angled rule onto the metal support and fixing it to the middle of the clamp/composite arrangement, where the hailstone would pass by allowed the position of hailstone to be observed with respect to the ruler divisions and the associated time stamp. This enabled a rough approximation velocity to be calculated, which could be compared to the corresponding light gate reading. Although this method was quite crude, it was found to match closely with the actual measurement for all four hailstone sizes. Scale bars are not included in the images but from the ruler divisions the estimated width of the image was 30 mm.

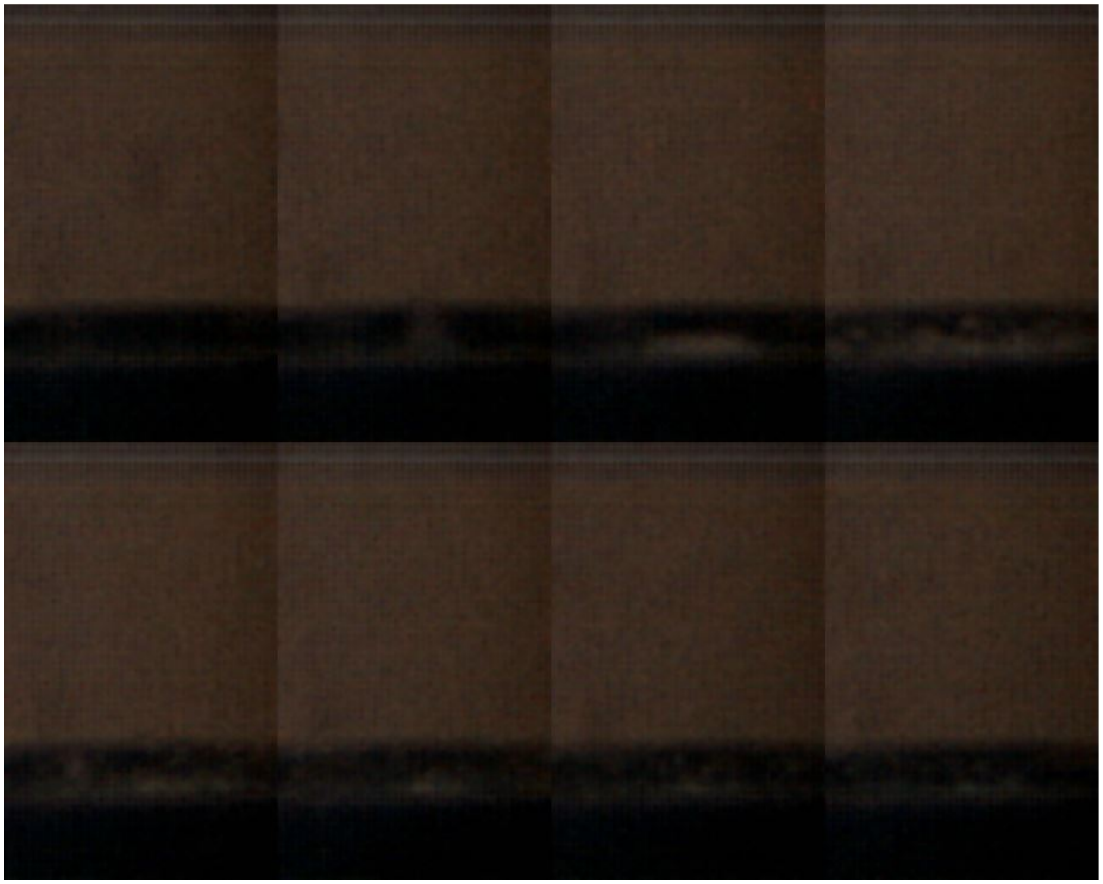

Figure 4.48: High speed video footage of 5 mm SHI impact.

From the previous force analysis, there was some suggestion that the 5 mm diameter SHI may not have been hitting the sample correctly or in a different manner to that of the other hailstones. In Figure 4.48 the blurry but intact form of the 5 mm shape is vaguely distinguishable, especially in video format. In the next images, the actual impact is more or less in the centre of the disc. Shattering of the SHI was not entirely

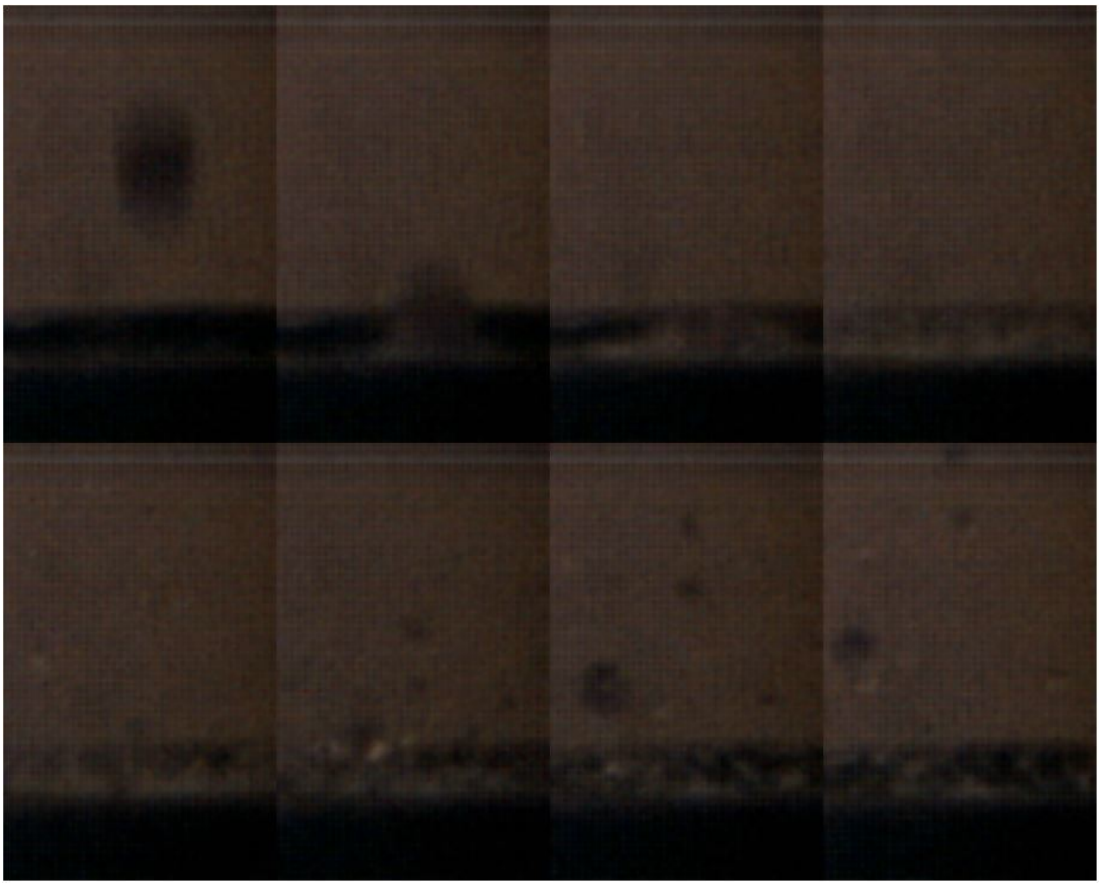

Figure 4.49: High speed video footage of 10 mm SHI impact.

clear due to the resolution and associated noise of the image but was slightly more obvious in motion. It appeared that most of particles spread along the surface of the disc but again this was not completely clear due to noise and the size of these tiny fragments. This might suggest that overall the failure behaviour in the case of the 5 mm SHI was still brittle but to a lesser degree. Unfortunately the higher pressure firings that exhibited different dynamic force readings could not be examined.

The 10 mm projectile was a little more detectable in Figure 4.49 even prior to impact. The initial contact was observed in the second frame, the crushing of the particle and lateral jetting in the subsequent two frames. In the lower half of the figure, the ricocheting of fragments off the surface and spreading outward was a lot more discernible. In the last two images, a particularly large fragment was observed.

As diameter was increased, the initial impact becomes more recognisable. Figure 4.50 depicts the footage of a 15 mm collision. Again the top row displayed the crushing of the particle in the early stages of impact. Larger fragments are seen in the bottom row, with the entire picture being covered with the radial spread of different

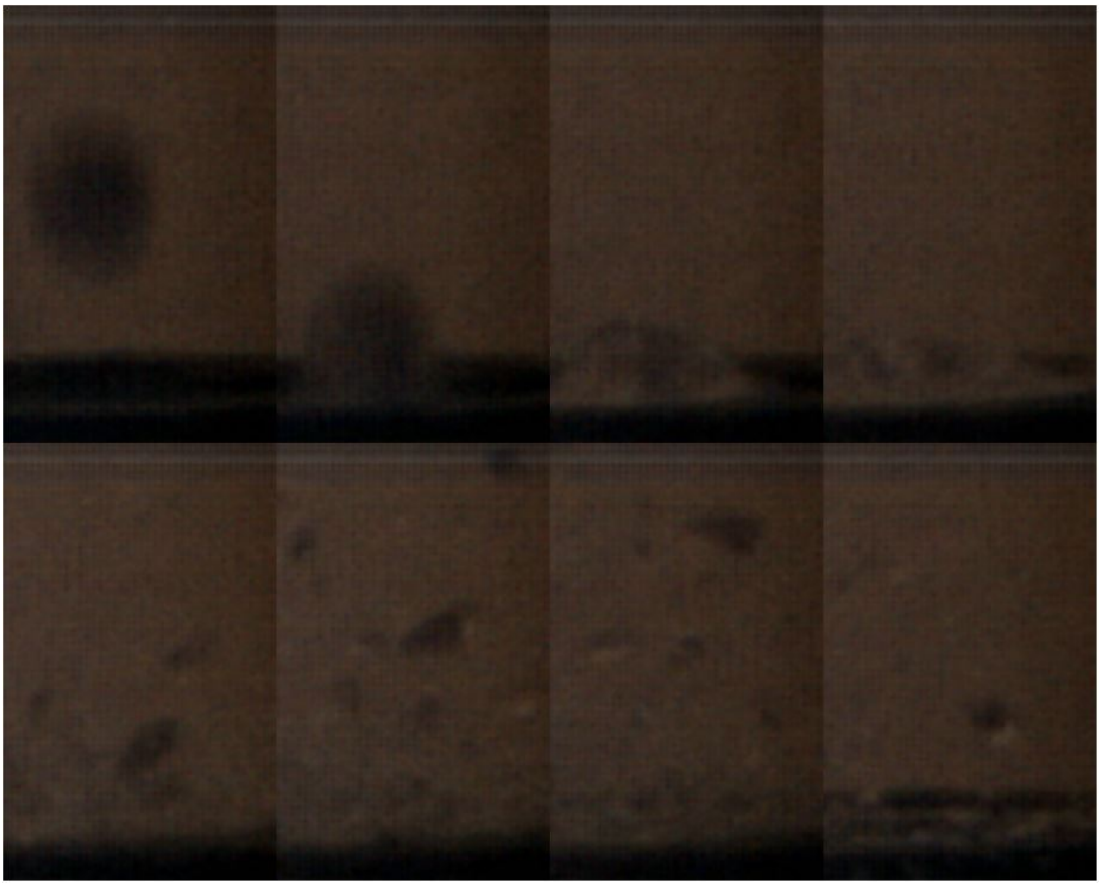

Figure 4.50: High speed video footage of 15 mm SHI impact.

sized ice segments.

The disintegration of the 20 mm ice sphere is even more apparent in Figure 4.51, with the third and fourth image starting to resemble the higher quality footage filmed by Tippmann *et al.* [19]. However, the referenced material did not describe the presence and subsequent motion of dissimilar sized fragments that were clearly visible in Figure 4.51. These bulkier segments could be the reason behind the less smooth, spikier force profiles seen in the larger diameter SHI.

According to Kim and Kedward [17], the time of peak force is evident when only a small portion of the sphere's volume has been disintegrated. The difference between the second and third image in Figure 4.51 is 0.2 ms. Comparing this to the force-time history in Figure 4.32, the peak force occurred around 0.1 ms, in between these two frames. From all the HSV footage, there was clear indication that the projectile hit the surface correctly but there would most likely be some disparity from the exact centre of the disc.

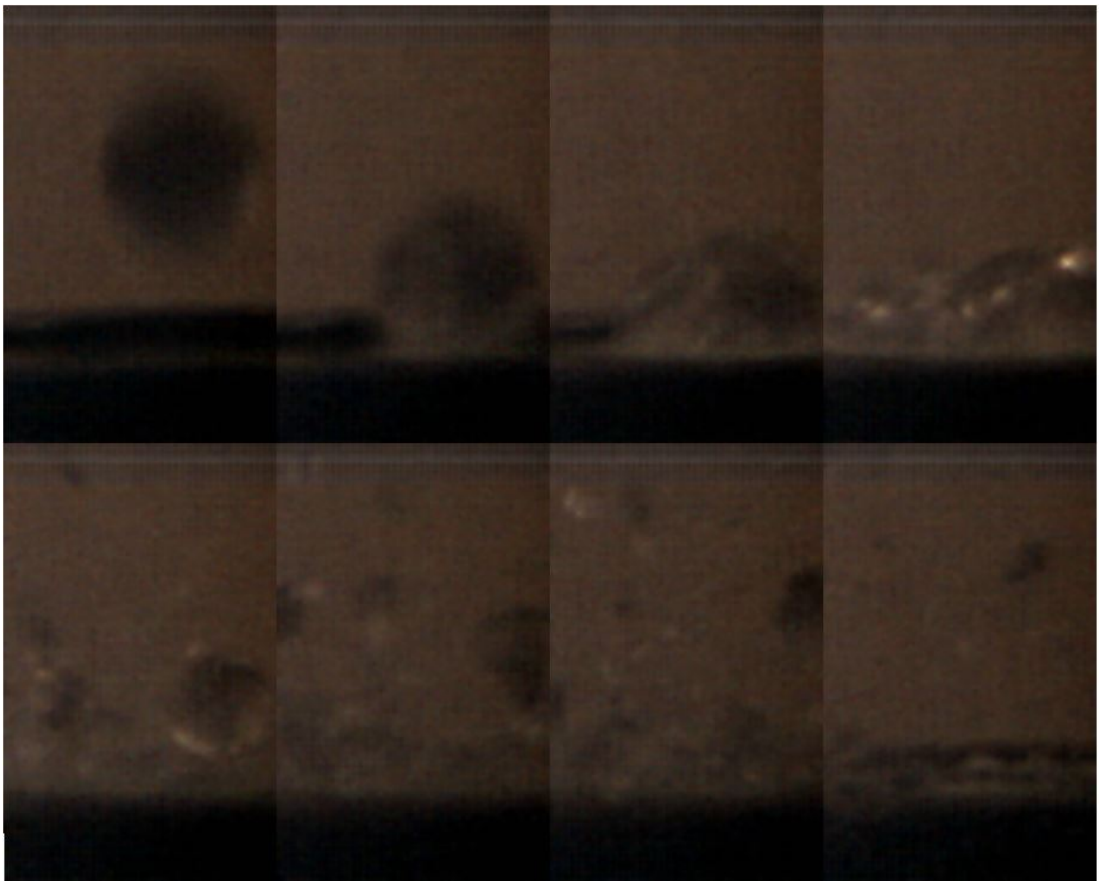

Figure 4.51: High speed video footage of 20 mm SHI impact.

4.6 Experimental Forces and Velocities

After developing and calibrating an experimental methodology in the previous sections, the composite samples described in Tables 4.2, 4.3, 4.4, 4.5 and 4.6 could now be impacted. Throughout the experimentation, the force and velocity information was measured so that any inconsistencies between the expected and captured values could be determined.

Figures 4.52, 4.53, 4.54 and 4.55 describe the velocities that were produced for the defined pressures for each of the SHI diameters. For the most part, four distinct and consistent velocity regions of $50\,\mathrm{m\,s^{-1}}$, $65\,\mathrm{m\,s^{-1}}$, $80\,\mathrm{m\,s^{-1}}$ and $95\,\mathrm{m\,s^{-1}}$ were achieved. However, there were certain instances where this was not the case. As can be expected, there are examples of higher or lower speeds for the single impacts. Overall, the error bars for all the multiple impact velocities were smallest for the 10 mm SHI, with 15 mm and 20 mm SHI equally variable. Both SHI of diameters 5 mm and 20 mm struggled to reliably reach the higher-end velocity of $95\,\mathrm{m\,s^{-1}}$, meaning that the difference between

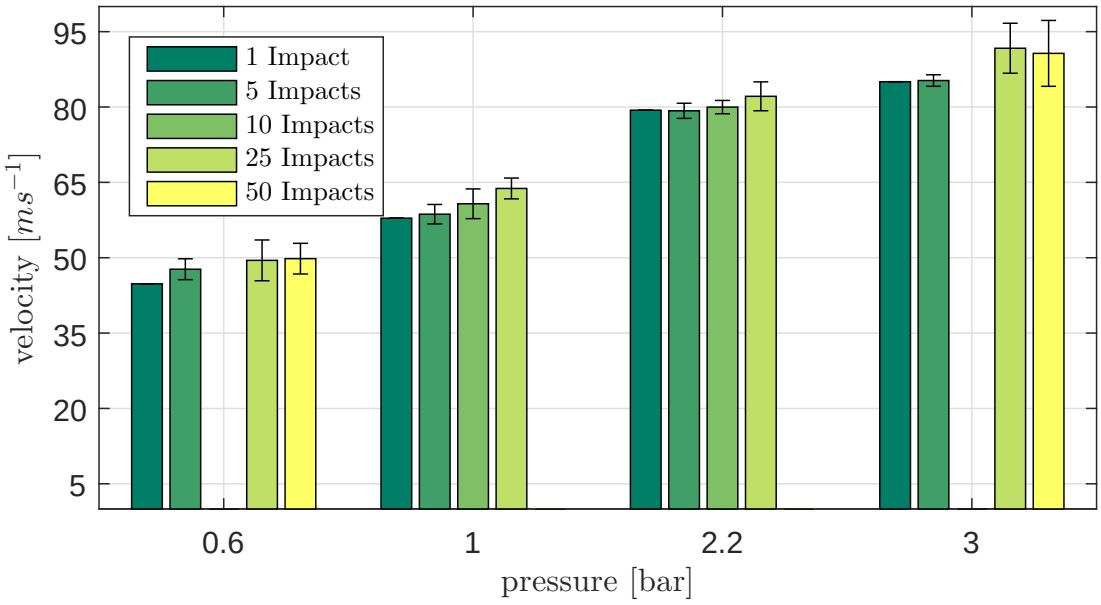

Figure 4.52: Average velocities for samples impacted by 5 mm SHI for a selected firing pressure and number of impacts.

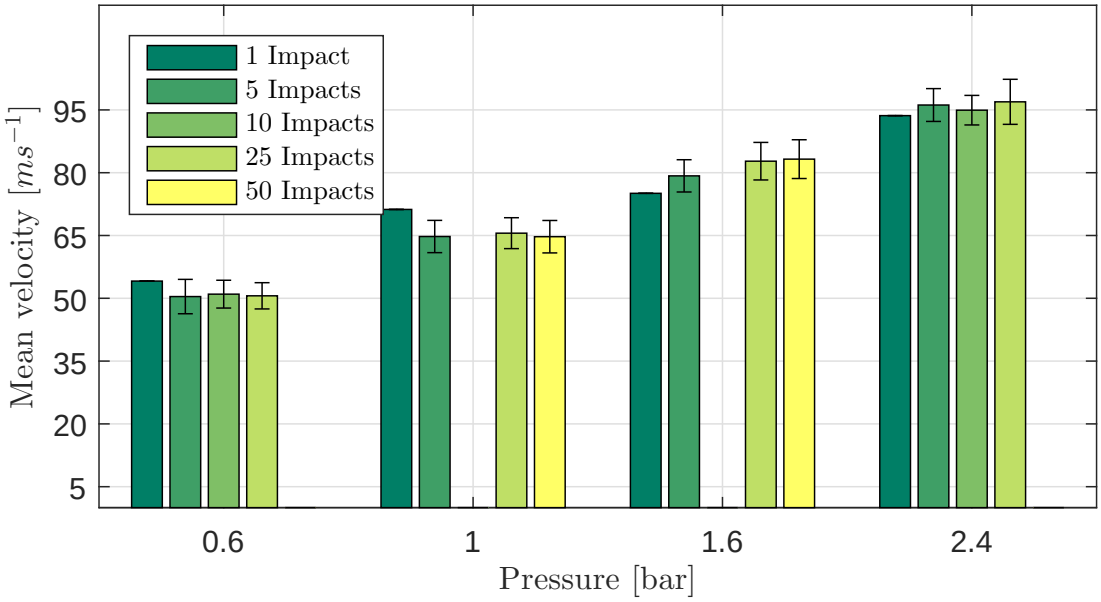

Figure 4.53: Average velocities for samples impacted by 10 mm SHI for a selected firing pressure and number of impacts.

these impacts and the projected 80 m s^{-1} variants was not as pronounced, especially for the 20 mm case. Similarly, the lowest pressure for the 15 mm version produced velocities that were very close to the higher selected speed of 65 m s^{-1}.

The mean forces measured by the transducer for the previously described mean

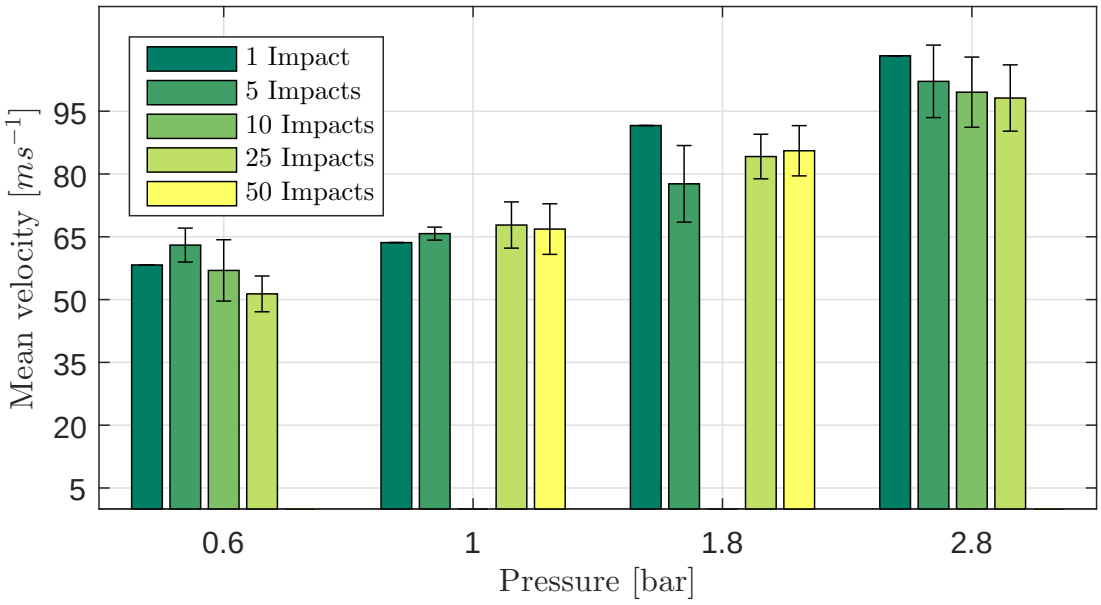

Figure 4.54: Average velocities for samples impacted by 15 mm SHI for a selected firing pressure and number of impacts.

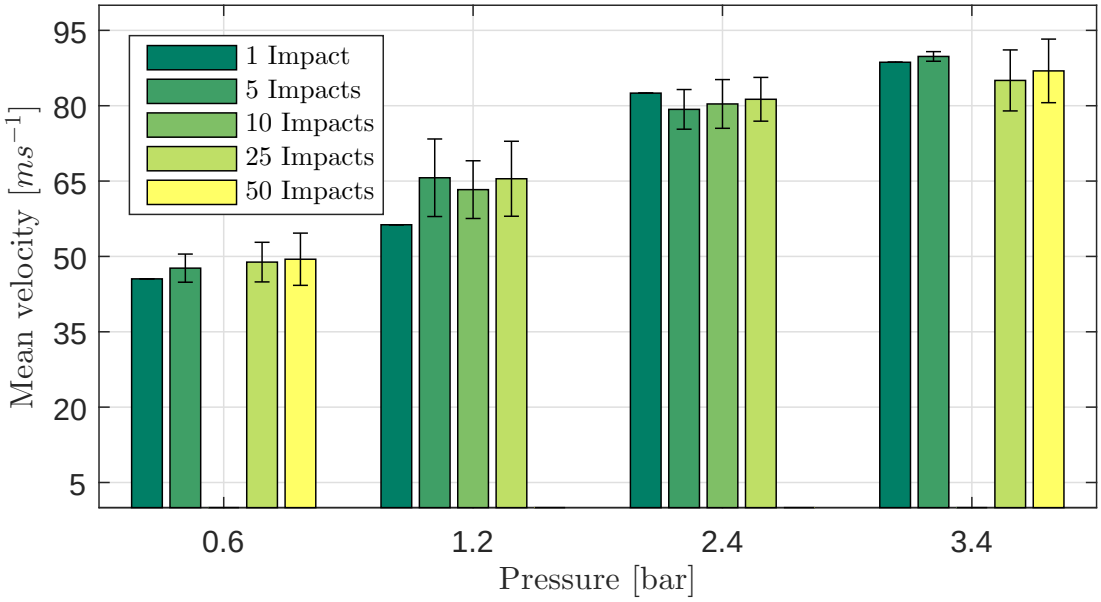

Figure 4.55: Average velocities for samples impacted by 20 mm SHI for a selected firing pressure and number of impacts.

velocities and separate SHI diameters cases are displayed in Figures 4.56, 4.57, 4.58 and 4.59.

The difference of mean force between the different diameters was quite clear. The mean force ranges for the 5 mm, 10 mm, 15 mm and 20 mm hailstones were approxi-

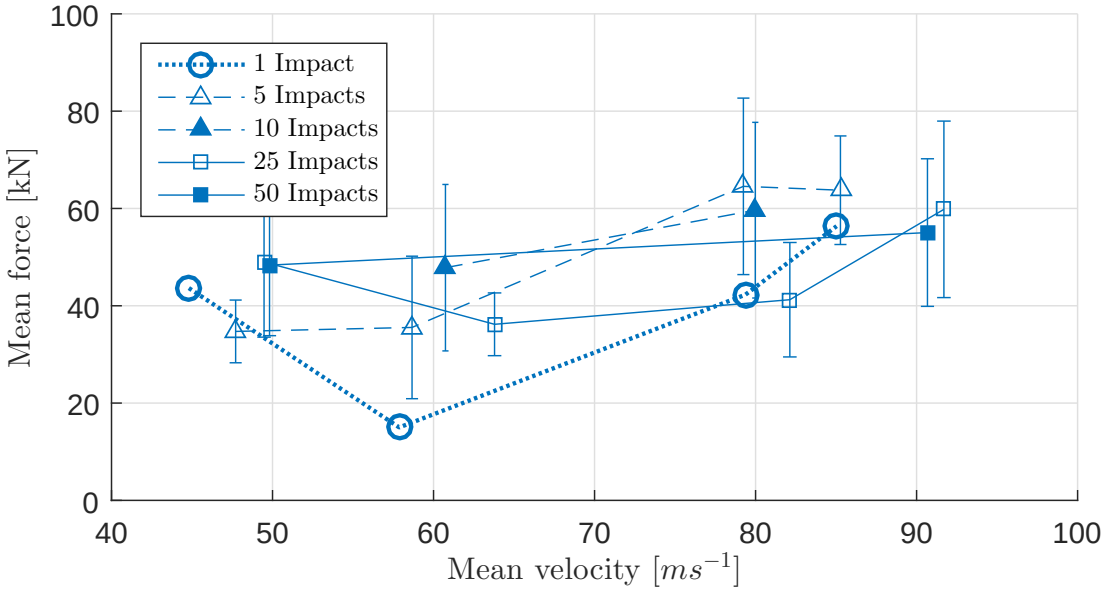

Figure 4.56: Average peak force for each set of 5 mm impacts at a certain mean velocity.

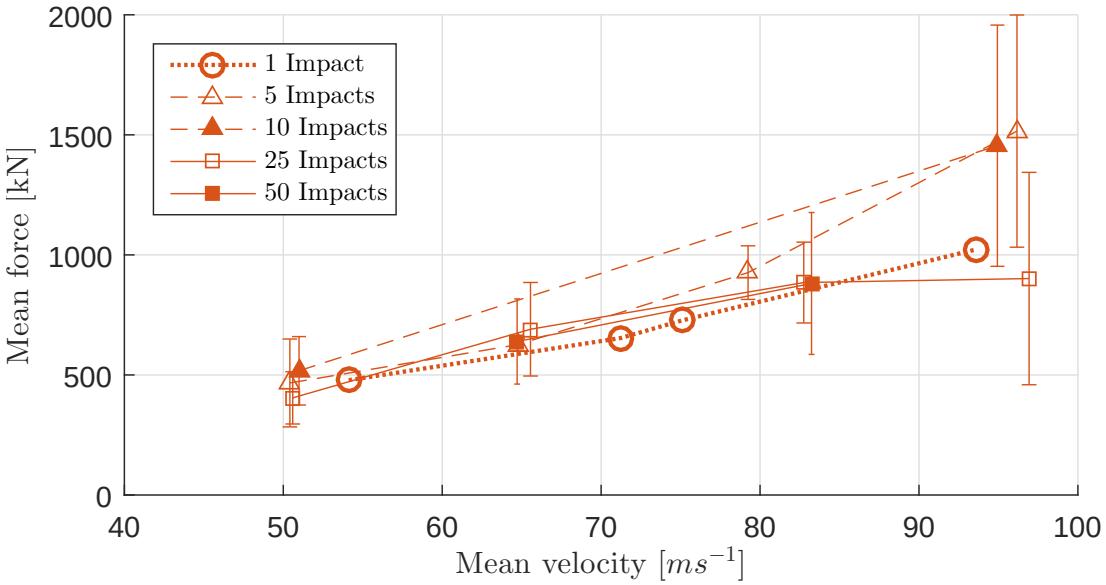

Figure 4.57: Average peak force for each set of 10 mm impacts at a certain mean velocity.

mately 15 N – 65 N, 400 N – 1500 N, 1350 N – 3960 N and 2300 N – 4820 N, respectively. There was some overlap amongst the 10 mm, 15 mm and 20 mm diameters but the 5 mm forces were demonstrably lower than the rest. The increasing force trend with increasing velocity was not completely obvious, particularly for the 5 mm case although the highest forces tended to be at the higher velocities. Again, the 10 mm impacts were the

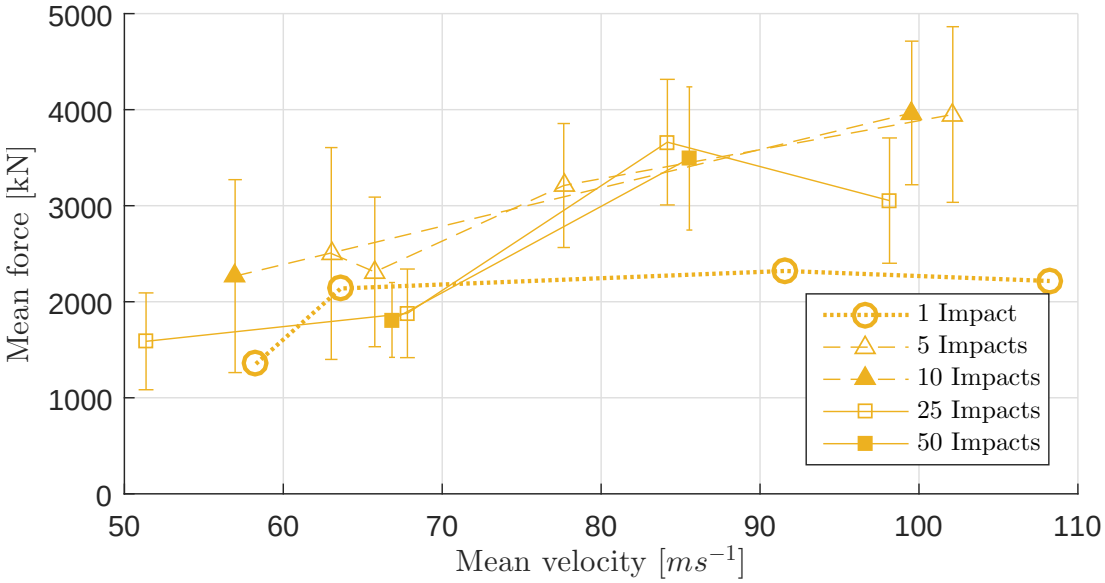

Figure 4.58: Average peak force for each set of 15 mm impacts at a certain mean velocity.

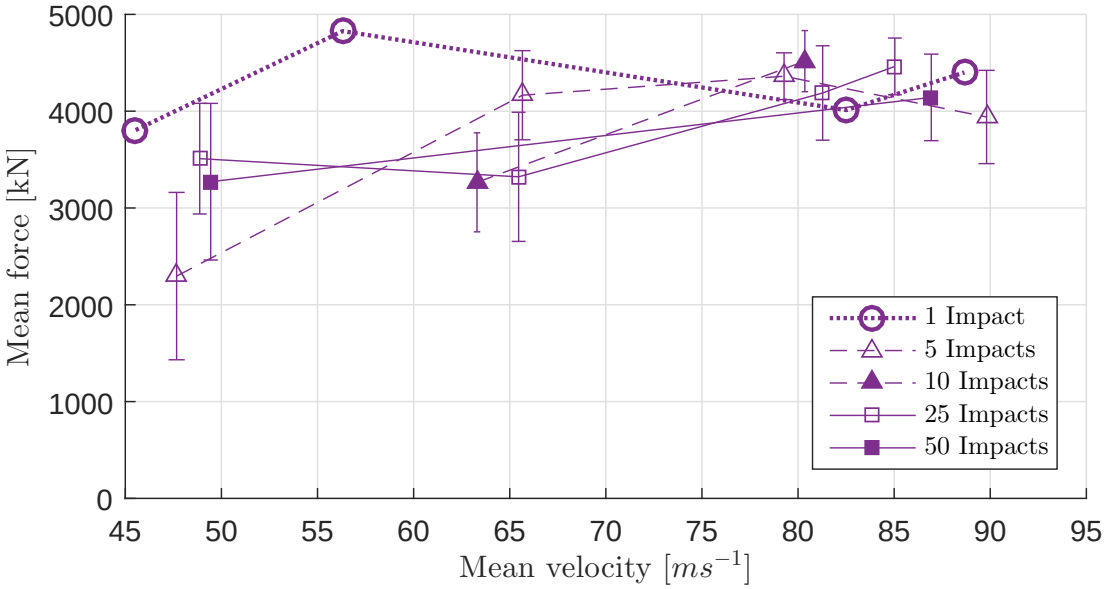

Figure 4.59: Average peak force for each set of 20 mm impacts at a certain mean velocity.

most reliable and followed the trend the best. The variance in force was related more to the diameter than the velocity. The voltage limit of the DAQ input limit may have been diminishing the higher velocity 20 mm force measurements. The total subjected force on a sample was useful for highlighting how similar a higher diameter SHI fired at

a lower velocity compares to a lower diameter SHI fired at a higher velocity. This can be examined in Figure 4.61. For this and subsequent figures, the legend can be viewed in figure

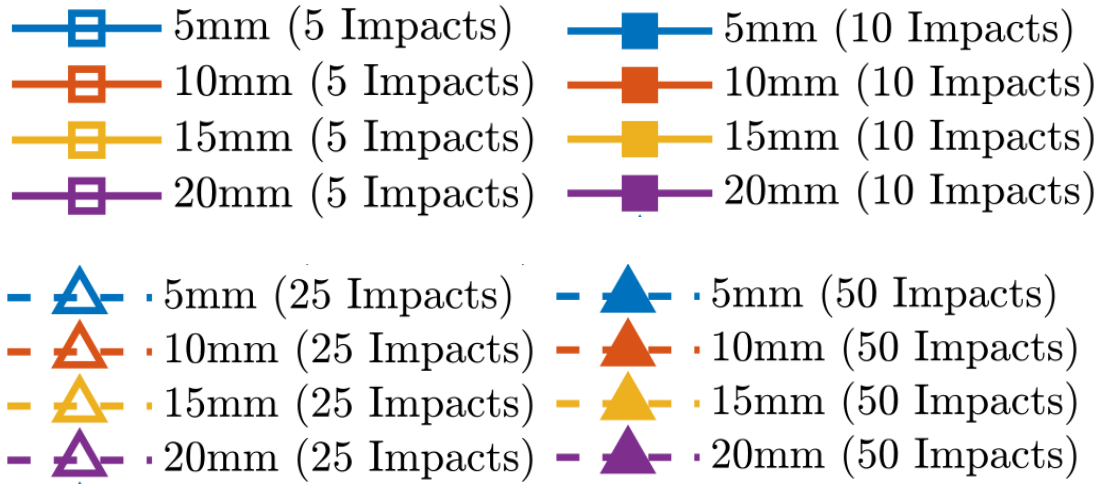

Figure 4.60: Legend for Figures 4.61, 4.62, 4.63, 4.64, 4.65 and 4.66.

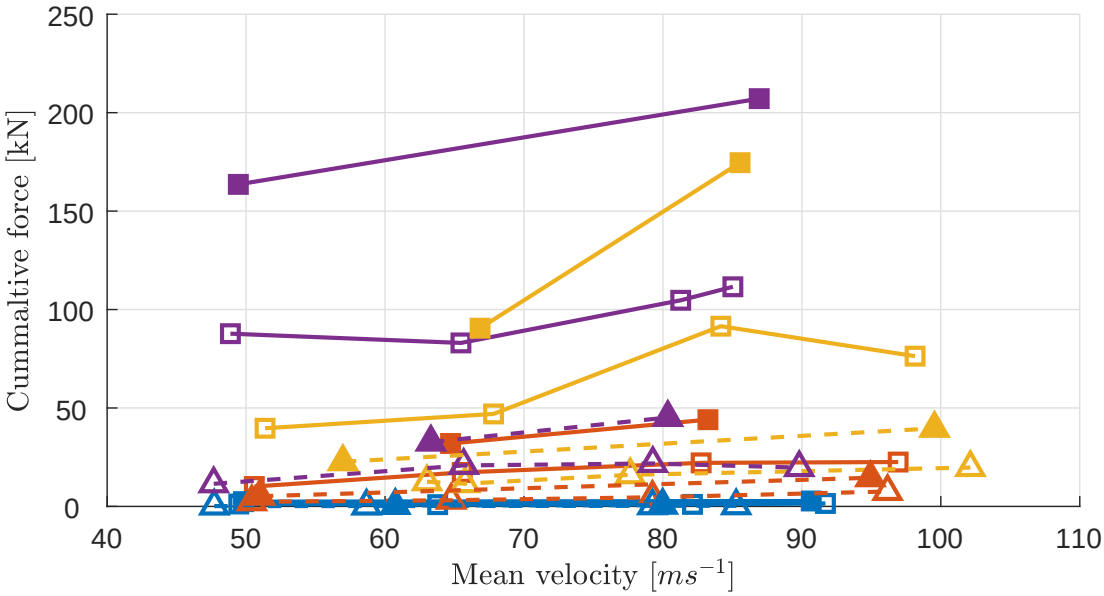

Figure 4.61: Total *measured* force subjected to each sample.

The single impact version is excluded here and instead can be extracted from the previous Figures 4.56, 4.57, 4.58 and 4.59. The force imparted by the 5 mm ice projectile was substantially less than the other sizes. If the force is scaled to a maximum 50 N, as in Figure 4.62, this is more apparent. Only after 50 impacts did the total force

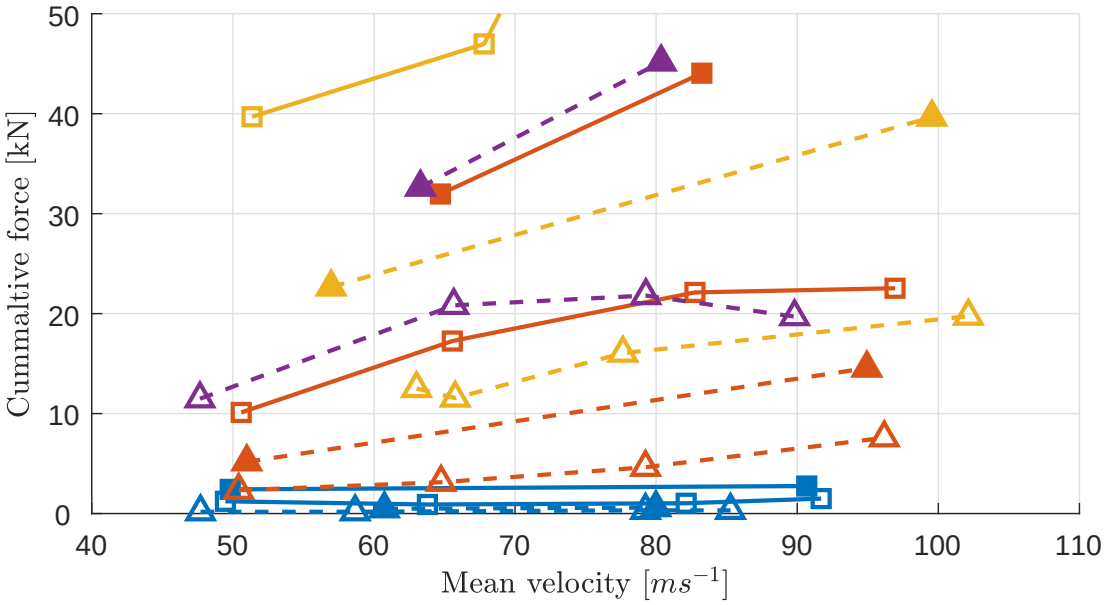

Figure 4.62: Total *measured* force subjected to each sample (reduced force range).

start to compare to the nearest counterpart of 10 mm at 5 impacts, at the lowest velocities. There are several other crossover examples that made interesting comparisons, including: 10 mm at 50 impacts vs. 20 mm at 10 impacts; and the specific case of 50 impacts of 15 mm at $\sim$85 m s^{-1} vs. 50 impacts of 20 mm at $\sim$50 m s^{-1}, to name but a few.

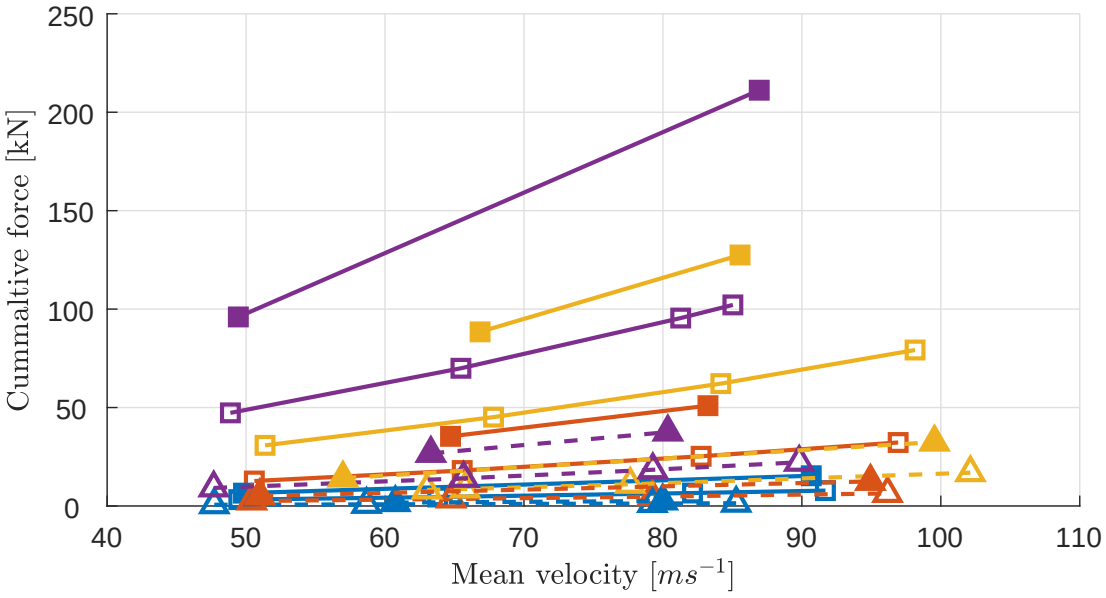

Figure 4.63: Total *projected* force subjected to each sample.

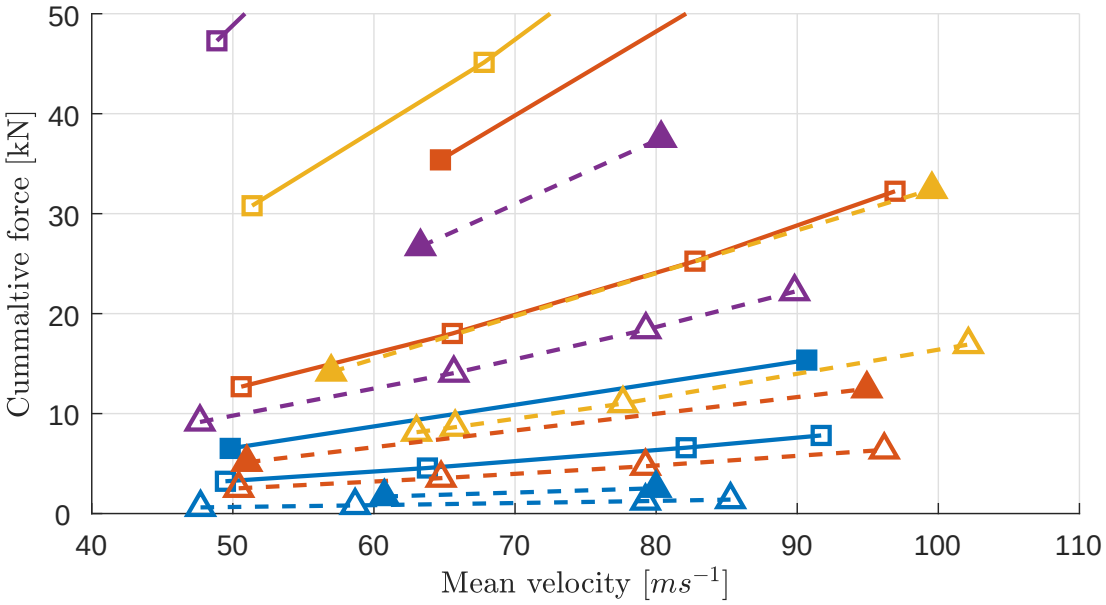

Figure 4.64: Total *projected* force subjected to each sample (reduced force range).

These cumulative forces can be compared with the predicted values in Figures 4.63 and 4.64 calculated from Roisman & Tropea (Equation 4.9). Overall, the totals were fairly similar however, there were some clear exceptions. Even when the multiple impacts were accumulated, the experimental trend for force against velocity was not always as obvious as the empirical calculation. The abatement of the 5 mm impact is again highlighted in the close-up view of Figures 4.62 and 4.64. Fifty and twenty five impacts of 20 mm SHI at $\sim$50 m s^{-1}, 15 mm SHI at $\sim$80 m s^{-1} were the most obvious cases where the total experimental force exceeded the prediction.

For reference, the aggregated estimates of projectile kinetic energy experienced by each sample are shown in Figure 4.65. Similar to the cumulative force diagrams, a version with a scaled down y-axis is made available in Figure 4.66 to better inspect the lower energy cases. The influence of diameter is highlighted here, with smaller hailstones displaying proportionally reduced totals in agreement with the force aggregation. These figures are also useful for the discussion of failure threshold energy (FTE) often utilised in the literature with respect to simulated hail ice (SHI).

4.7 Damage evaluation

As evident in Tables 4.2, 4.3, 4.4, 4.5 and 4.6, certain samples would be need to be analysed multiple times once a required number of impacts was reached. After either 1, 5, 10, 25 or 50 impacts were reached, the sample was left to dry for 24 hours at

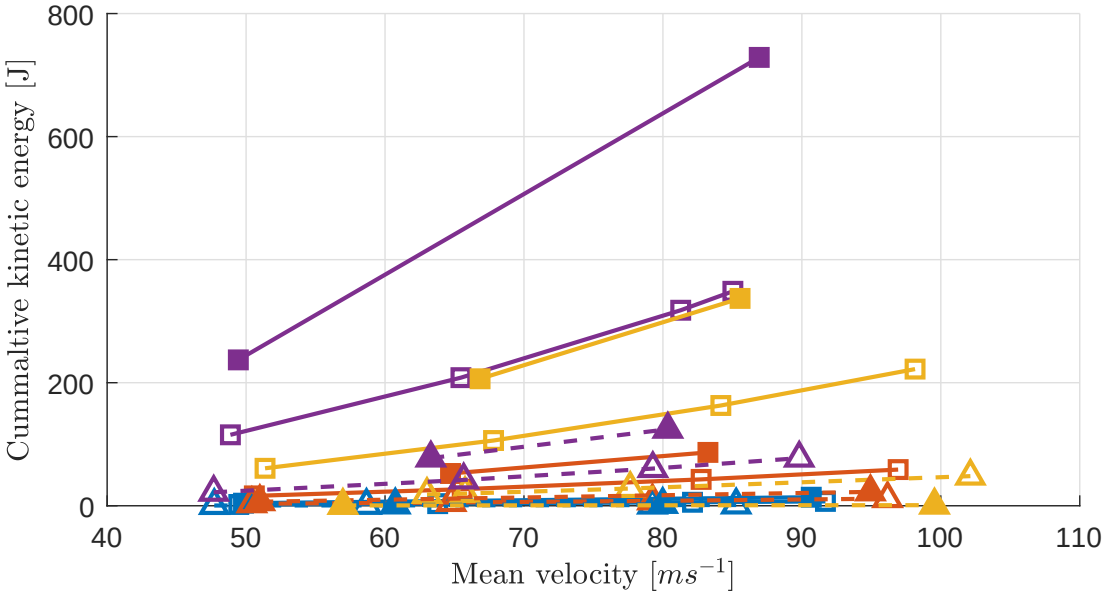

Figure 4.65: Cumulative kinetic energy subjected to each sample.

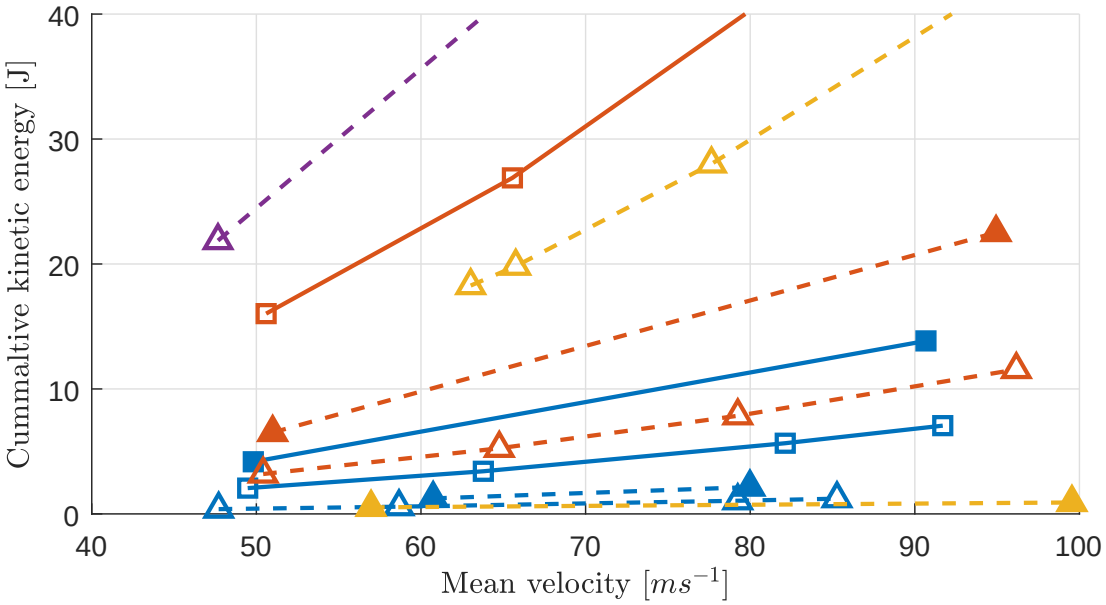

Figure 4.66: Cumulative kinetic energy subjected to each sample (reduced KE range).

a slightly elevated temperature of 30 °C. The analysis of damage from the analysed in three different ways, mass loss, visual inspection and inspection using an electron microscope. Once the sample was dried, it was weighed and compared to the weight before experimentation, using a Mettler College 150 measuring balance with a resolution of 0.000 01 g. It was then visually inspected and images taken using a VEHO

VMS-004 USB microscope at 20x magnification and a distance of 1 cm from the target. Three images taken at different LED light levels (none, minimum and maximum) to see if at these contrasting levels, certain surface defects became more or less apparent. The highest LED light level was found to highlight any discrepancies on the immediate surface the best. The reason why not all samples could be inspected by electron microscope was that because a composite is non-metallic, sample surfaces had to be applied with a conductive gold coating, to enable detailed imaging. This would affect the surface properties, as well as the sample mass for future impacts. The Hitachi S-3700N microscope allowed for 4 samples to be examined at the one time in the chamber, which had to be brought to vacuum before inspection could take place.

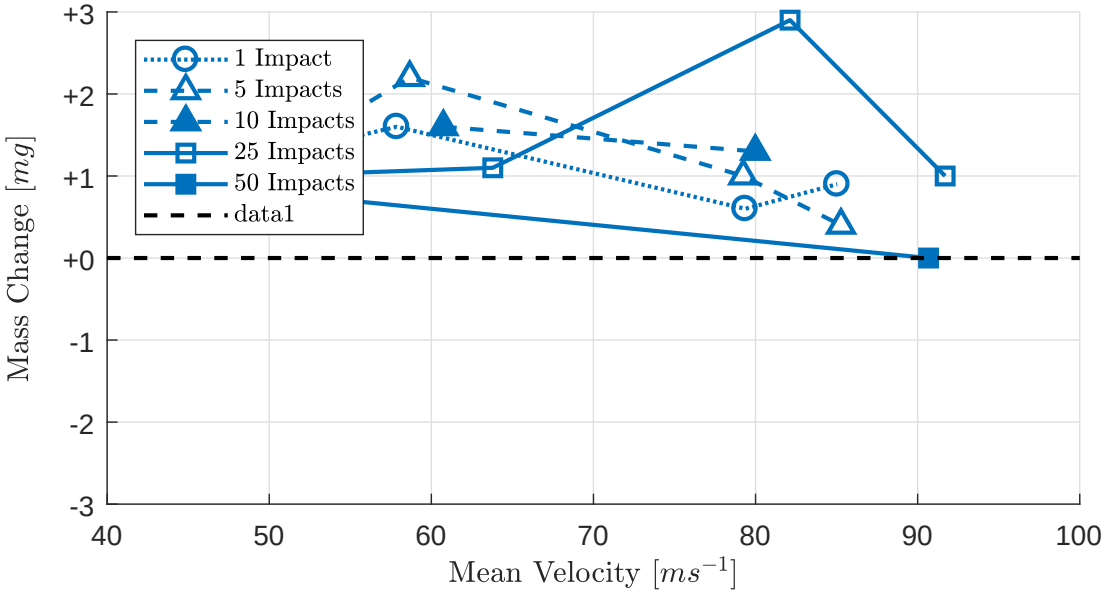

Figure 4.67: Mass loss for each sample subject to 5 mm impacts

The difference in mass loss against mean velocity for each SHI diameter can be seen in Figures 4.67, 4.68, 4.69 and 4.70. Note that the error in mass measurement will equate to 0.05 mg, which is less than the length of point markers. Unfortunately, despite the efforts to avoid any water absorption there were definite instances of a small amount mass gain across the different sizes. Because of this, any observations made will have to be tentative. The maximum mass loss/gain range did not exceed 4 mg. This equates to approximately 0.02% mass change of the mean sample weight (measured prior to impact). The average weight change was roughly 0.0043% of the mean sample weight. As the overall mass loss across the specimens is so low, it is difficult draw any meaningful comparisons or conclusions for this form of analysis.

One other form of analysis was the visual inspection using reflected light microscopy

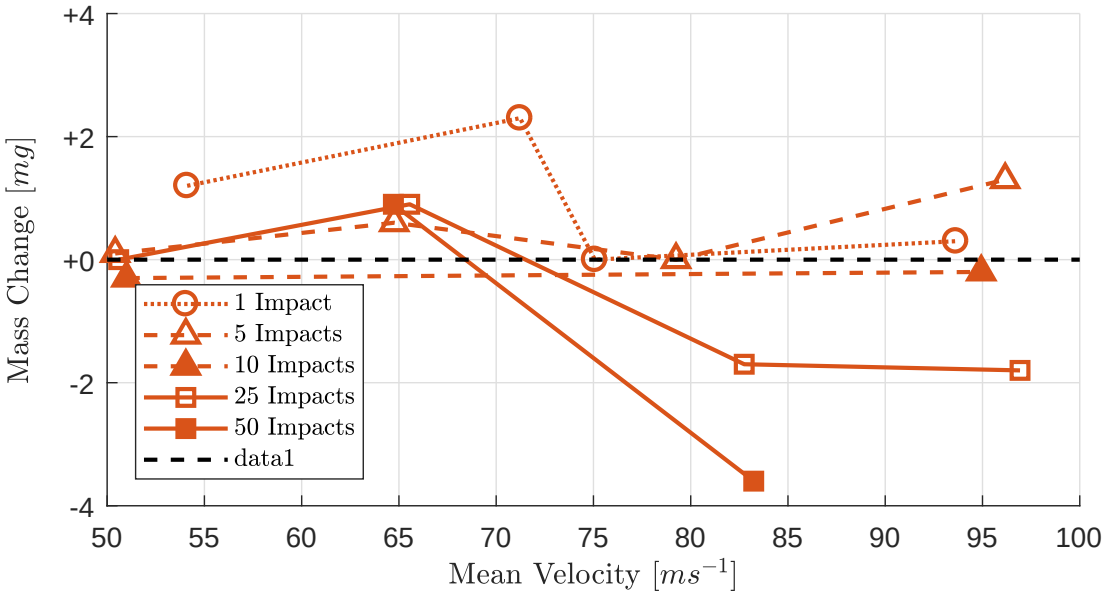

Figure 4.68: Mass loss for each sample subject to 10 mm impacts

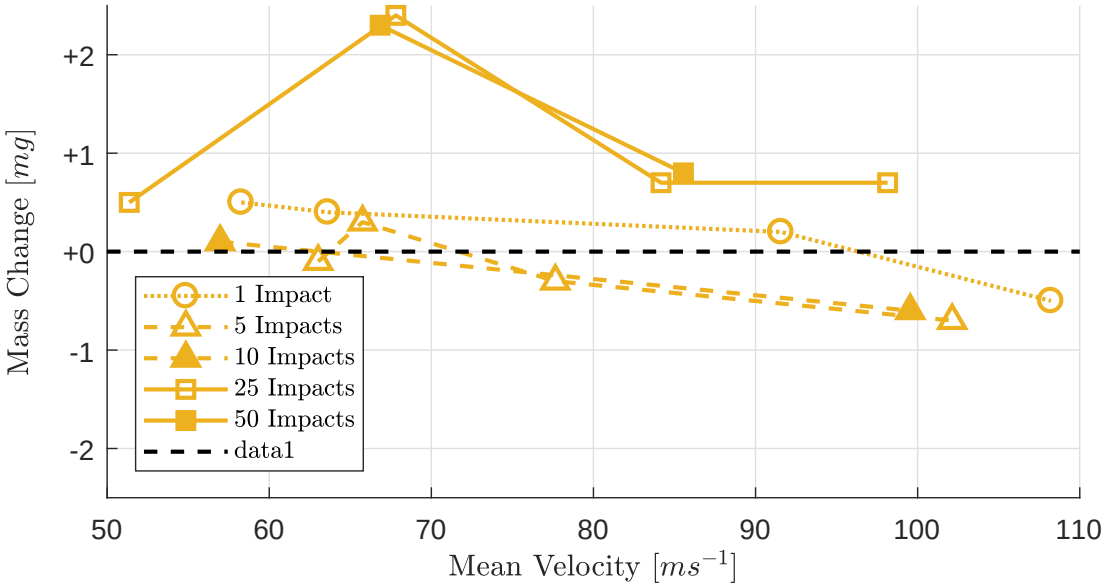

Figure 4.69: Mass loss for each sample subject to 15 mm impacts

of the samples after impact, to see if there was any damage apparent before utilising the electron microscope. Due to the variation in quality of the in-house manufacturing of composite, the condition of the disc prior to experimentation was used for comparison. Figures 4.71, 4.72, 4.73 and 4.74 show images before and after impacts at the centre of the disc (approximately 20 mm in width in each case), for the different diameters at the maximum number of impacts (50) and the highest velocity tested for this number. Out

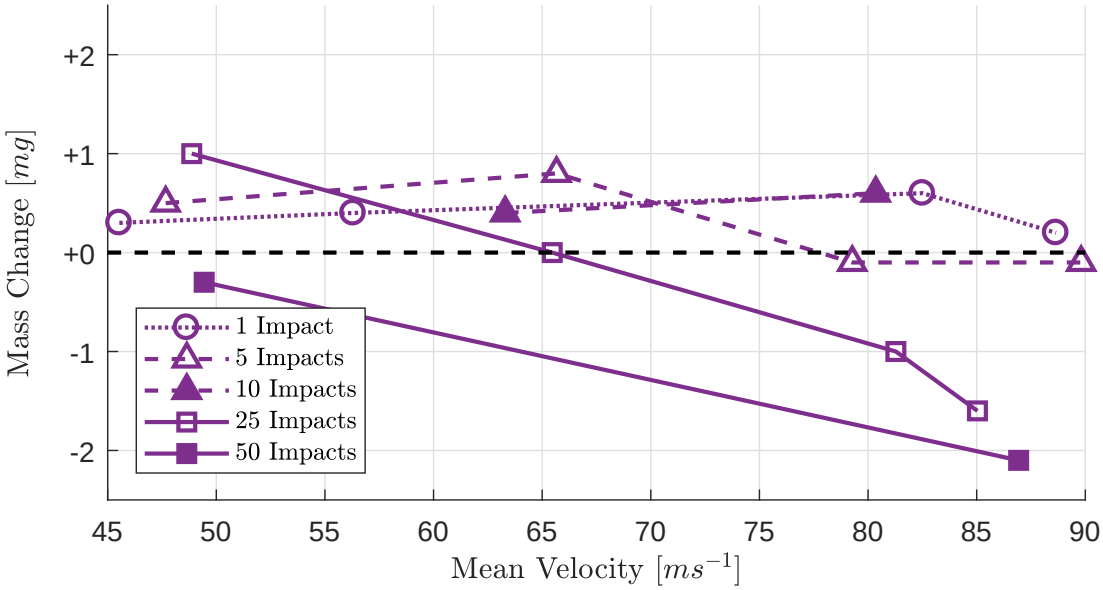

Figure 4.70: Mass loss for each sample subject to 20 mm impacts

of these examples, only the 15 mm variant seemed to show any notable change after experimentation, with −45 deg and 45 deg scores as evident in Figure 4.73b. However, it should be noted that the condition of the composite in Figure 4.73a, prior to impact, was most likely the worst out of the four samples. It was difficult to determine any remarkable changes in Figure 4.74b, where the SHI used is larger and on average, fired at a slightly great velocity. No other noteworthy damage indicators were found in any other samples besides these examples.

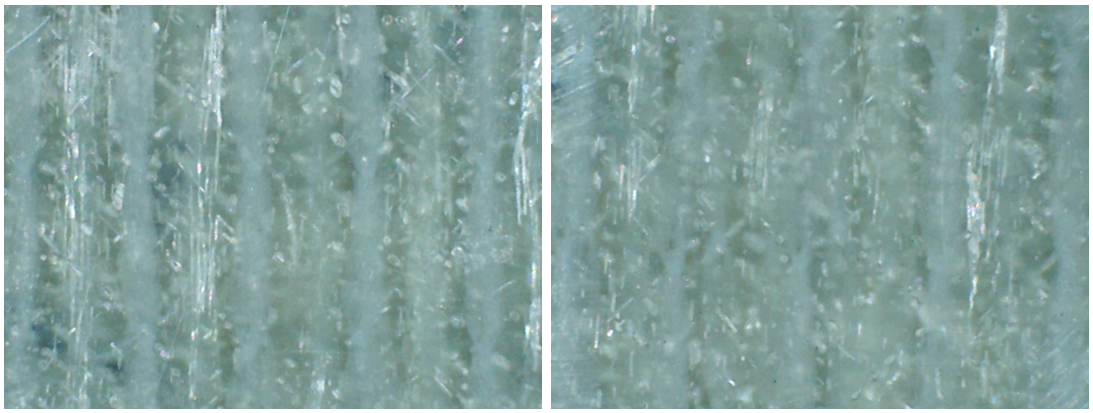

(a) Before (b) After

Figure 4.71: Visual surface quality of sample M5-V4.

Scanning electric microscopy was carried out for all samples. Out of the full survey,

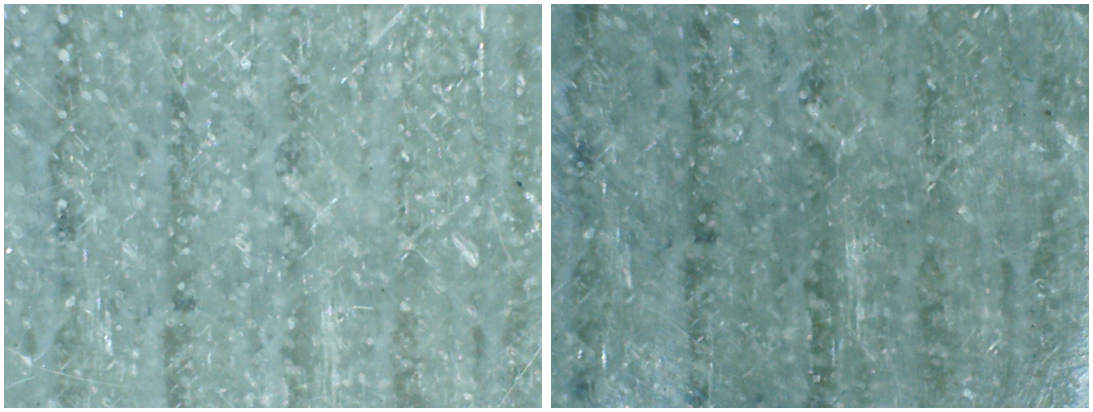

(a) Before (b) After

Figure 4.72: Visual surface quality of sample M10-V3.

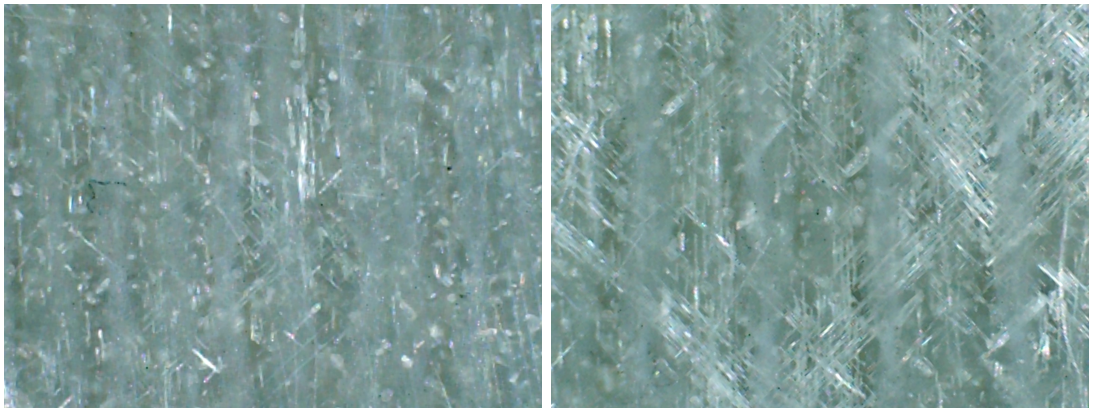

(a) Before (b) After

Figure 4.73: Visual surface quality of sample M15-V3.

the following samples were found to yield interesting comparisons, particularly in reference to the cumulative forces exacted on the composite, as described in Figures 4.61 and 4.62. Here the images for each sample are collated in the form of: one large figure taken at the widest possible shot (both in terms of zoom and distance from the specimen) and further close-up sub-figures of detailed features. The text displayed at the bottom of the image is in the same format, except for the inclusion of the vertical distance of the stage (specimen holder) to the microscope.

The first images displayed in Figures 4.75 and 4.76 are of the 15 mm sample (M15-V3), which previously had the most obvious change in surface quality in the USB microscope images. The ∼15mm wide image in Figure 4.75 shows the aftermath of 50 impacts of 15 mm SHI at a mean velocity of $85.6\,\mathrm{m\,s^{-1}}$. There appear to be several small voids no greater 500 µm scattered across the surface. Although it is difficult

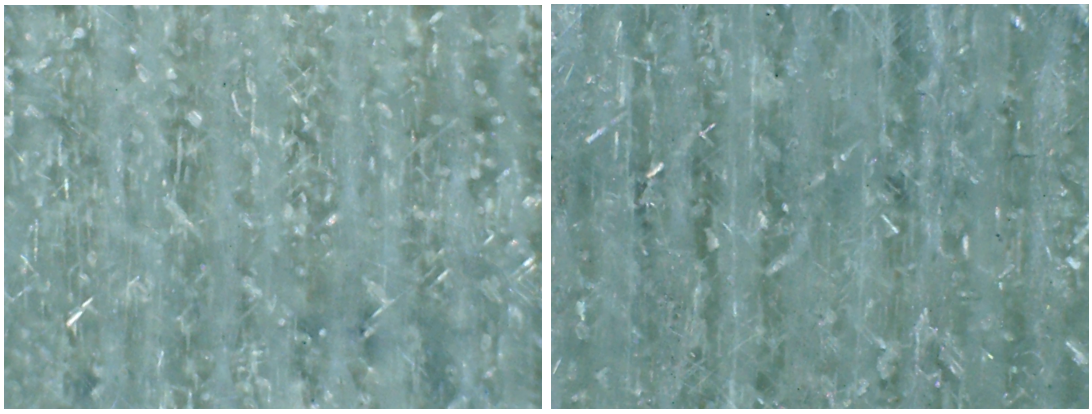

(a) Before (b) After

Figure 4.74: Visual surface quality of sample M20-V4.

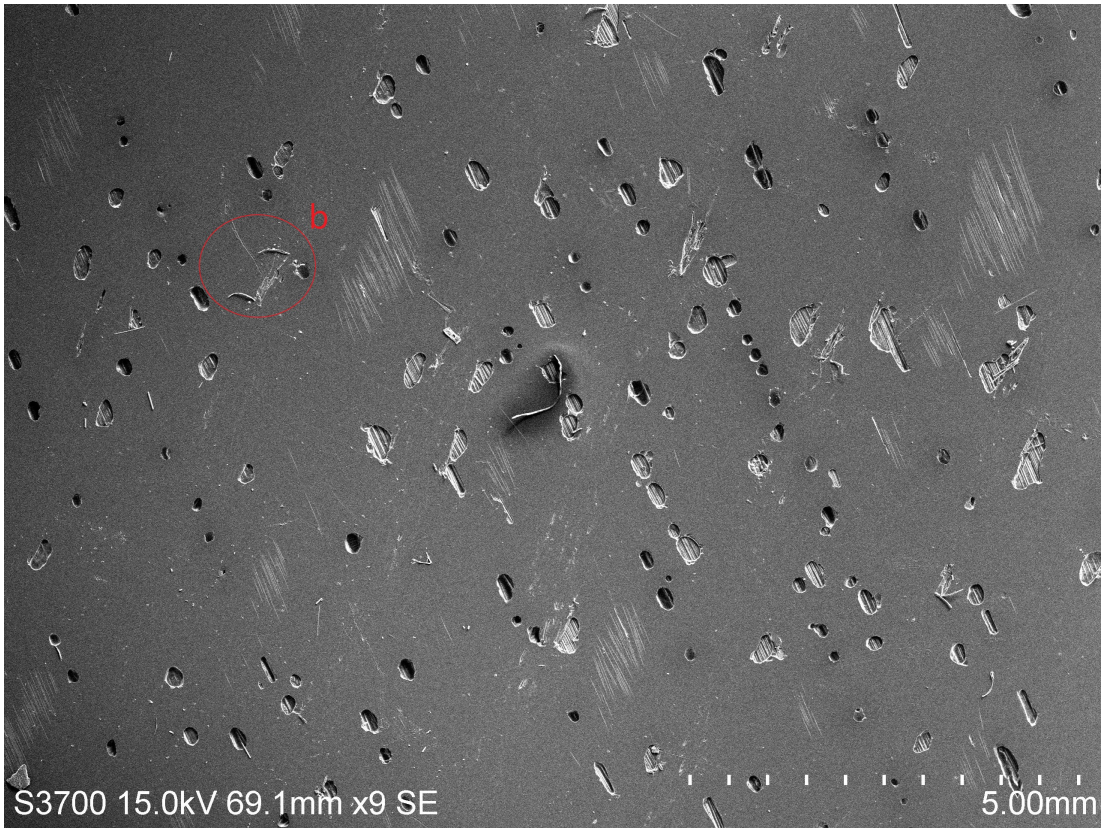

Figure 4.75: Overview SEM image for sample M15-V3.

to ascertain for certain without the exact control image prior to impact, these voids could have been produced during manufacturing process rather than a consequence of hailstone impact. They pertain to the voids exhibited by the improved composite

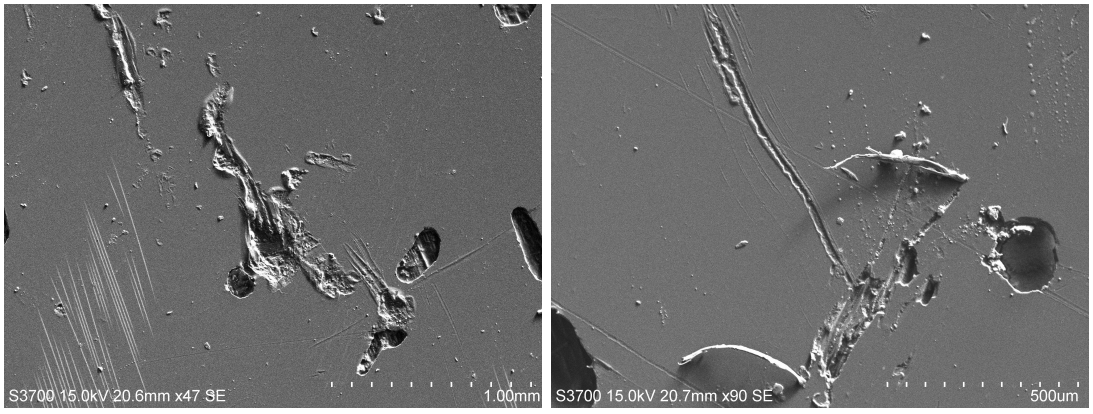

(a) (b)

Figure 4.76: Close-up SEM images for sample M15-V3.

sample not used for experimentation in Figure 4.20b. There was a cleanness and depth around the edge of where fibres underneath were revealed, suggesting the presence of air bubbles. There were however, a number of other features present that are more clear indicators of surface damage inflicted by the experimental campaign. Figure 4.76a displays the removal of resin material just outside the wider view of Figure 4.75. A circular crater of around 400 µm is shown in the centre. There was evidence of 'cutting' wear from the irregular grooves connected and in close proximity to the crater site. Smaller indentations no bigger than 100 µm were also observed, with tiny granules close to the area of incidence. Whereas Figure 4.76b reveals one of a handful of separate instances, the top left of Figure 4.75 shows whole fibres detaching from the epoxy and exposing more of the material underneath the resin. A long, narrow scar was also present, describing the path of the erodent.

Despite not being discernable on the 20x images taken with the USB light microscope, the level of damage is clearly increased for the M20-V4 specimen, that was subject to fifty impacts of 20 mm SHI at a mean velocity of 86.9 $\mathrm{m\,s^{-1}}$. Increased and larger illustrations of damage are observable in the overview snapshot displayed in Figure 4.77. As well as a smattering of longer fibres detached from the surface, there were long, deep scars localised in the centre of the image. Figure 4.78a captures a localised area of damage roughly 400 µm in width and greater than 1 mm in length. As well as the enlarged area, the severity of the damage has increased. There was possible interaction with the original voids, enlarging the exposed area and pulling fibres away. This was more obvious in the top right of Figure 4.78b, where there appeared to be increased wear "stamped" around the outside of the original void imprint. Figures 4.78c and 4.78d show not only the violent pulling of fibres to the surface but also

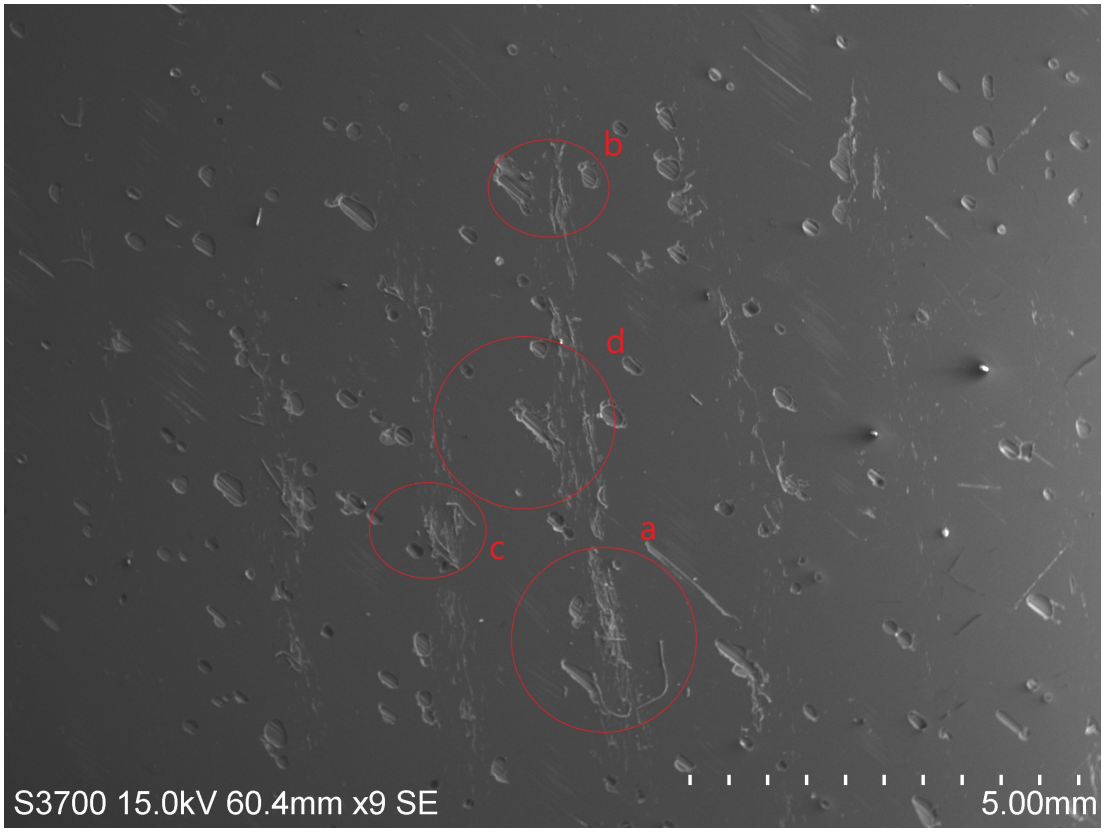

Figure 4.77: Overview SEM image for sample M20-V4.

the emergence of small scars, in-line and parallel to these cases.

Figure 4.79 presents an interesting case for discussion but also a result that is tentative. The image again shows the effect of fifty impacts of 20 mm projectiles but this time at a mean velocity of $49.4\,\mathrm{m\,s^{-1}}$. A notable but irregular area absent of epoxy is evident in the centre of the image. Unfortunately there also appeared to be a reduced quantity of smaller voids associated with the other specimens, surrounding this main feature. This suggests a marked increase in surface quality compared to the other experimental and control samples, which may have influenced the lack and confined nature of the damage. Other small characteristics included a small indent to the left of the 'v-shape' at the tip of the shape and a couple of loose fibres either side. The edges of the feature are, for the most part, quite sharp and clean but there are certain details that are rougher and harsh, as shown in Figure 4.80a, which allude to wear by erosion. A long scar implying the effects of cutting wear is shown in Figure 4.80b, as well as a particularly deep gouge from the feature for comparison.

These aforementioned samples (M15-V3, M20-V4 and M20-V1) are decisively the three that experienced the greatest cumulative force, as displayed in Figure 4.61. For

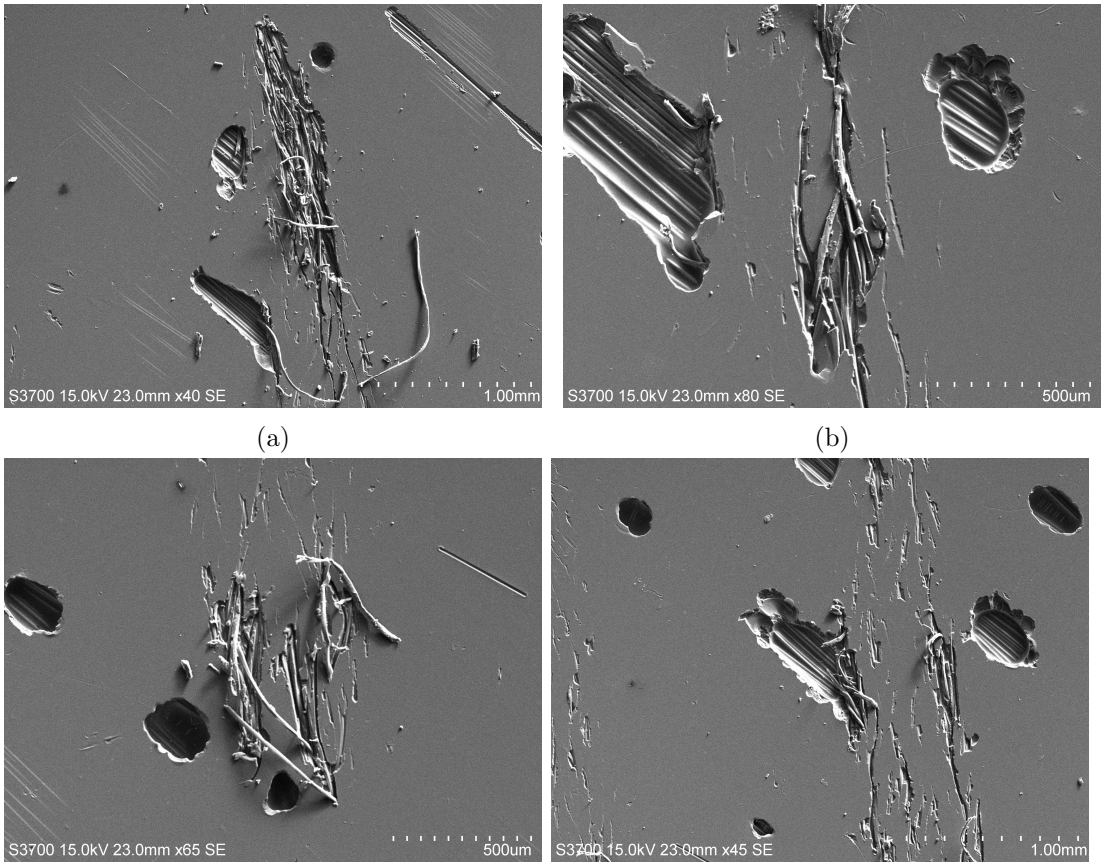

Figure 4.78: Close-up SEM images for sample M20-V4.

the next set of comparisons, the extreme of the 'x-axis' variable is now scrutinised. The projectile with the greatest mean velocity when fired at the highest selected pressure was the 15 mm diameter SHI. Figure 4.81 displays the widest snapshot of the M15-95 sample that was subject to twenty five impacts of this hailstone at a notable mean velocity of $98.2\,\mathrm{m\,s^{-1}}$. Although possibly not to the same degree as the M20-V4 sample, the localised damage was certainly more severe than fifty impacts of equivalent diameter at a lower pressure. Large areas of broken fibres were visible, as well as the associated debris. Figure 4.82a describes an expanse of damage greater than 500 µm in diameter and of convincing width, certainly greater in magnitude than Figure 4.76a. Figure 4.82a shows another location of marked damage dissociated with any pre-experimental voids.

A composite subject to 15 mm SHI at an even greater mean velocity is sample S15-V4, with ten impacts at an average of $99.5\,\mathrm{m\,s^{-1}}$. In fact the first five impacts of the total were averaged at $102.1\,\mathrm{m\,s^{-1}}$, approaching the upper limit of large scale industry wind turbine tip speeds. Even for these reduced number of impacts, examples of severe

Figure 4.79: Overview SEM image for sample M20-V1.

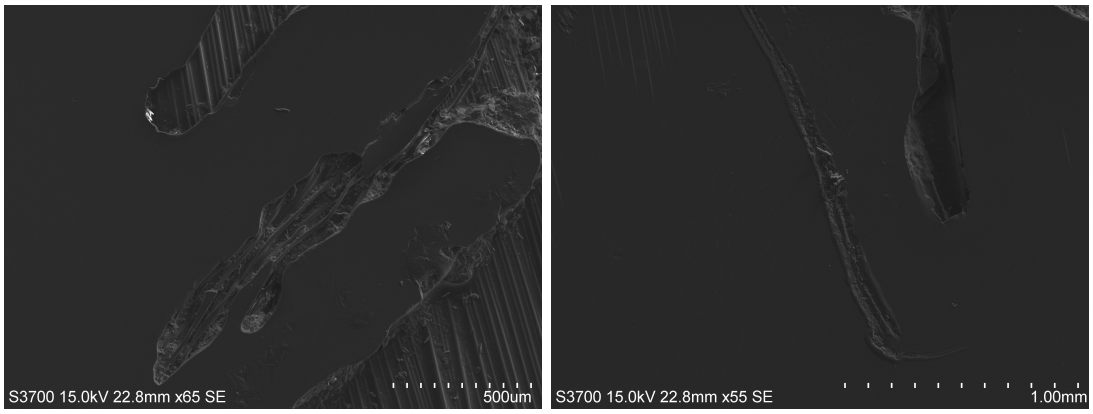

(a) (b)

Figure 4.80: Close-up SEM images for sample M20-V1.

damage at this speed were apparent. In the left hand side of Figure 4.83, we can see a ∼2 mm scar and two other sites abundant with loose fibres and debris. A close-up of the scar is exhibited in Figure 4.84a, where cutting/ploughing wear is obvious.

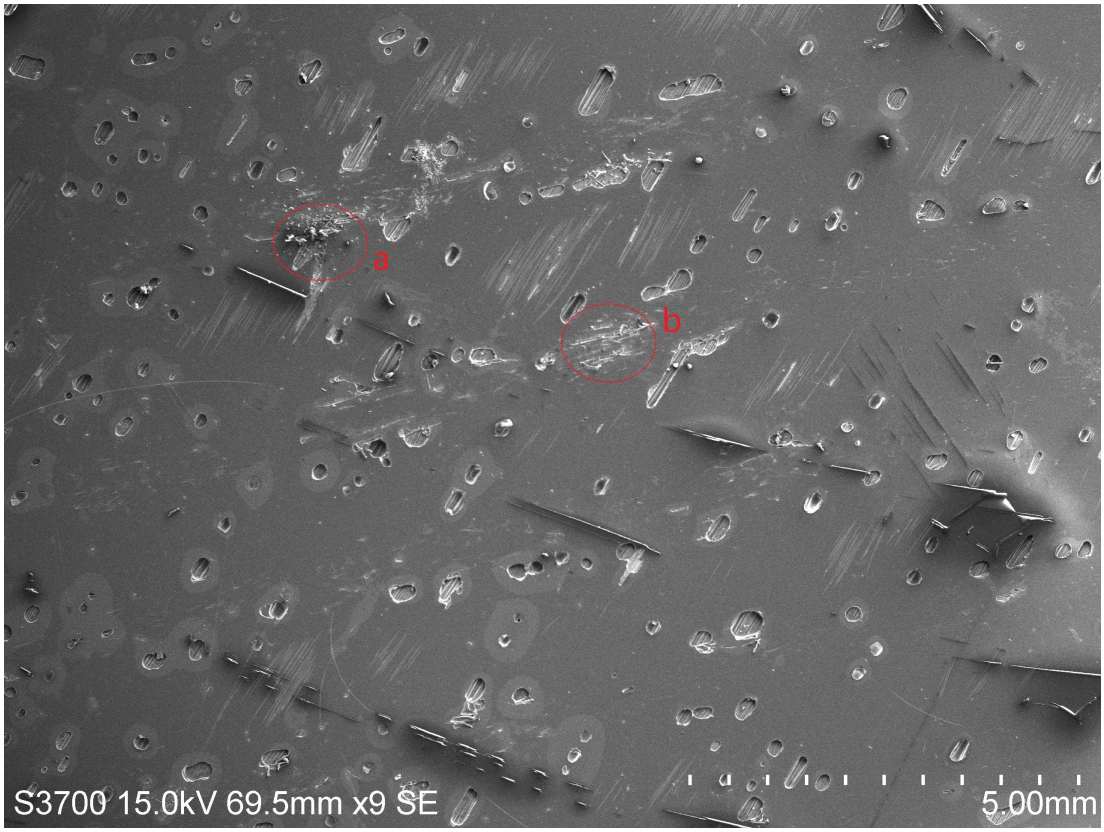

Figure 4.81: Overview SEM image for sample M15-V4.

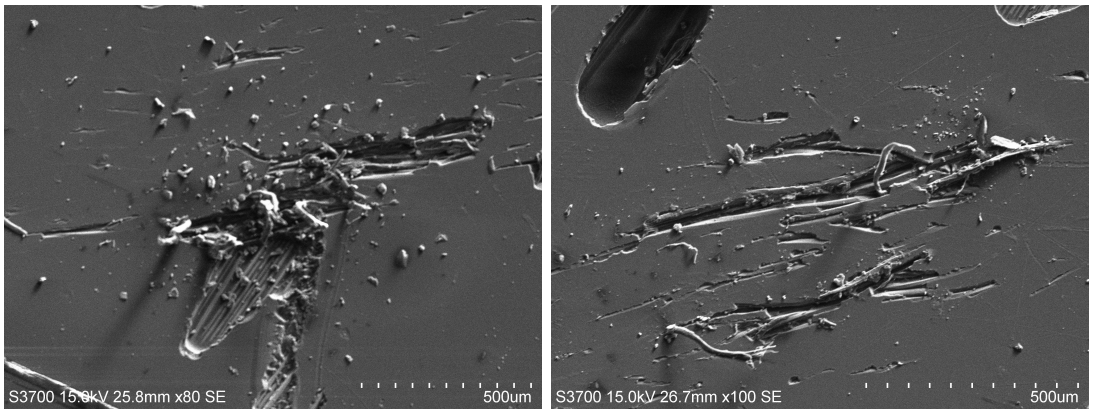

(a) (b)

Figure 4.82: Close-up SEM images for sample M15-V4.

The plastic deformation of the matrix is showcased but also the deeper exposition of fibres underneath is evident, which were unconnected with any void caused by the manufacturing process. This defect was bigger than seen in any previous examples of

Figure 4.83: Overview SEM image for sample S15-V4.

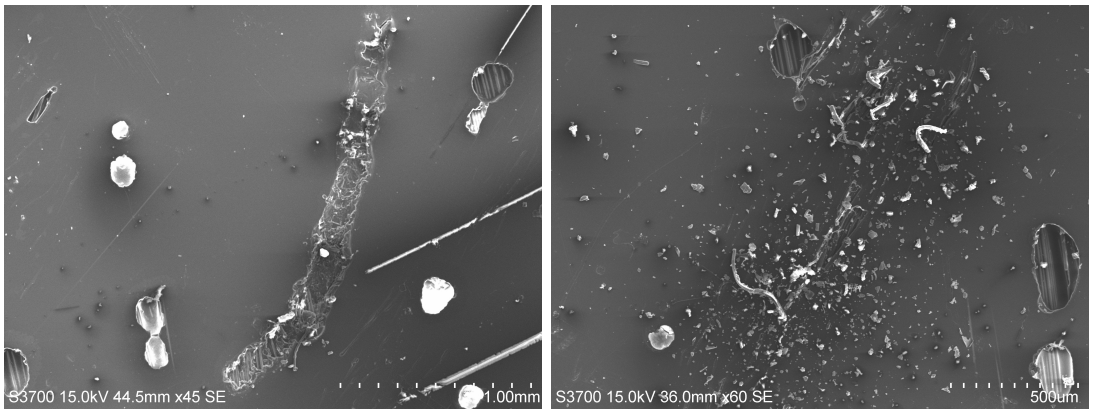

(a) (b)

Figure 4.84: Close-up SEM images for sample S15-V4.

this category of damage, even for the larger diameter at a greater number of impacts. It should be noted, however, that the mean velocity was close to $13\,\mathrm{m\,s^{-1}}$ more than that of the greatest mean velocity experienced by the 20 mm SHI. Fibres breaching

the epoxy were also apparent in Figure 4.84b but in a localised manner. Instead of the larger areas of subsurface damage, the trenches were smaller, although with an increased clutter of small debris and detritus. Overall the scene appears 'messier' compared with, for instance, Figure 4.78a where the level of damage is heightened but the aftermath was less chaotic and spread out.

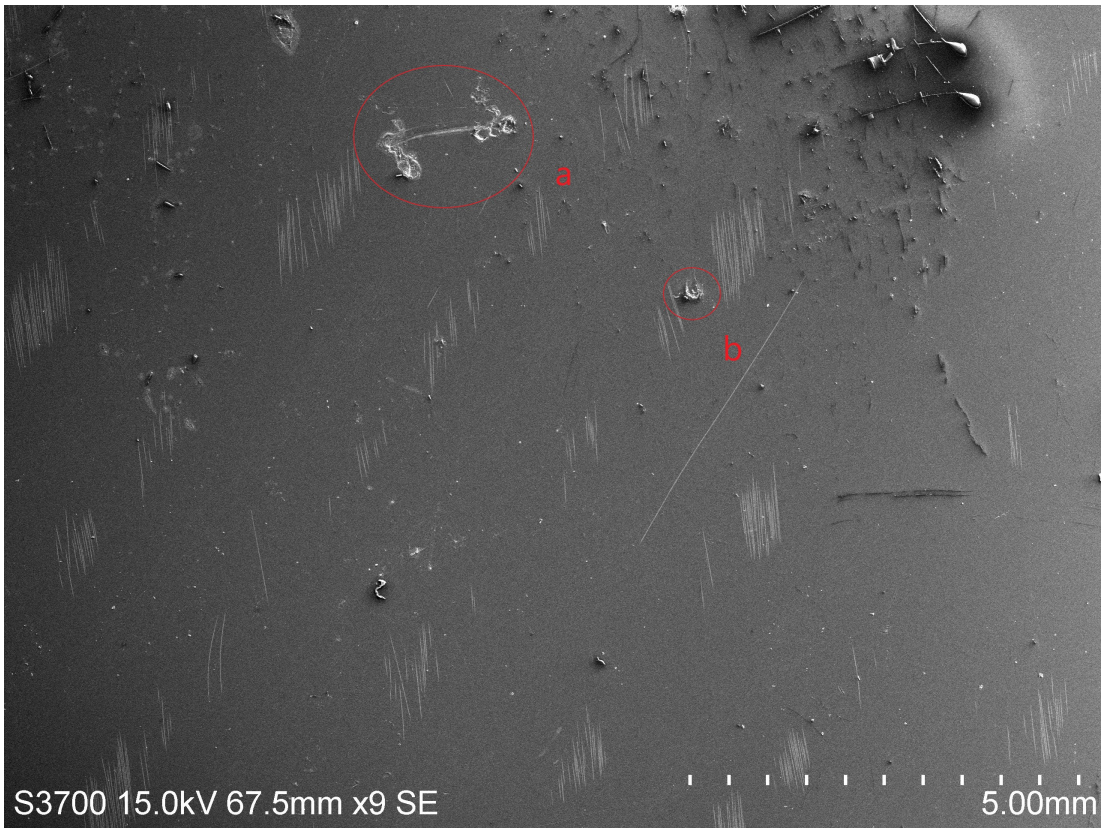

Figure 4.85: Overview SEM image for sample S20-V3.

Attention was now shifted to other samples which had aggregated forces close to S15-V4 (roughly 40 kN). This presents an opportunity to compare specimens where different diameters, velocities and number of impacts crossover, which result in a similar total subjected force. In this region, the following specimens were examined for comparison: S20-V3, M15-V1 and M10-V3. Figure 4.85 shows the resultant damage from ten impacts of 20 mm SHI at 80.4 $\mathrm{m\,s^{-1}}$. There were a small number of features found in the main overview but the extent of damage was not as prominent. There were also a lack of detached fibres. Disregarding these details, the condition of the rest of the surface was of noticeably higher quality and this should be taken into account. An enlarged view of the largest feature is shown in Figure 4.86a, where two separate areas of indentations, approximately 500 µm wide, were interconnected by a shallow groove

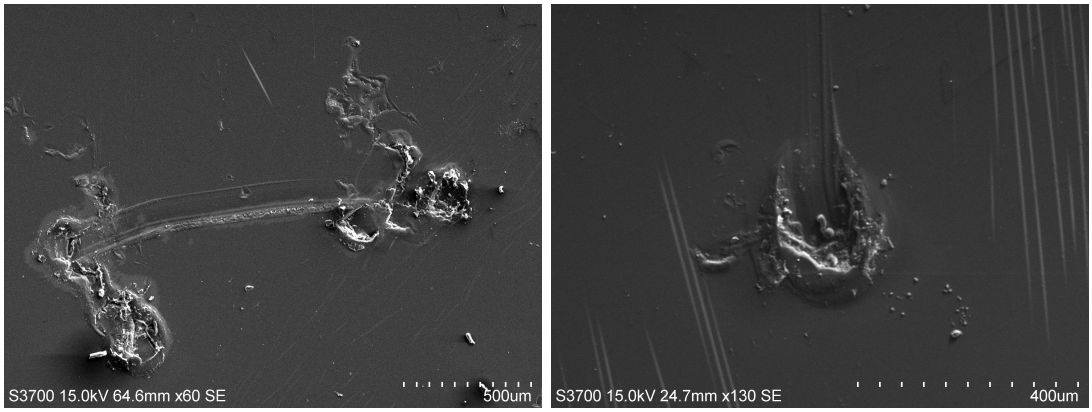

(a) (b)

Figure 4.86: S20-V3.

roughly 1.5 mm. Another gouge around 120 µm is displayed in Figure 4.86b. In both cases, these depressions do not appear to result in the exposition of fibres underneath the epoxy topcoat.

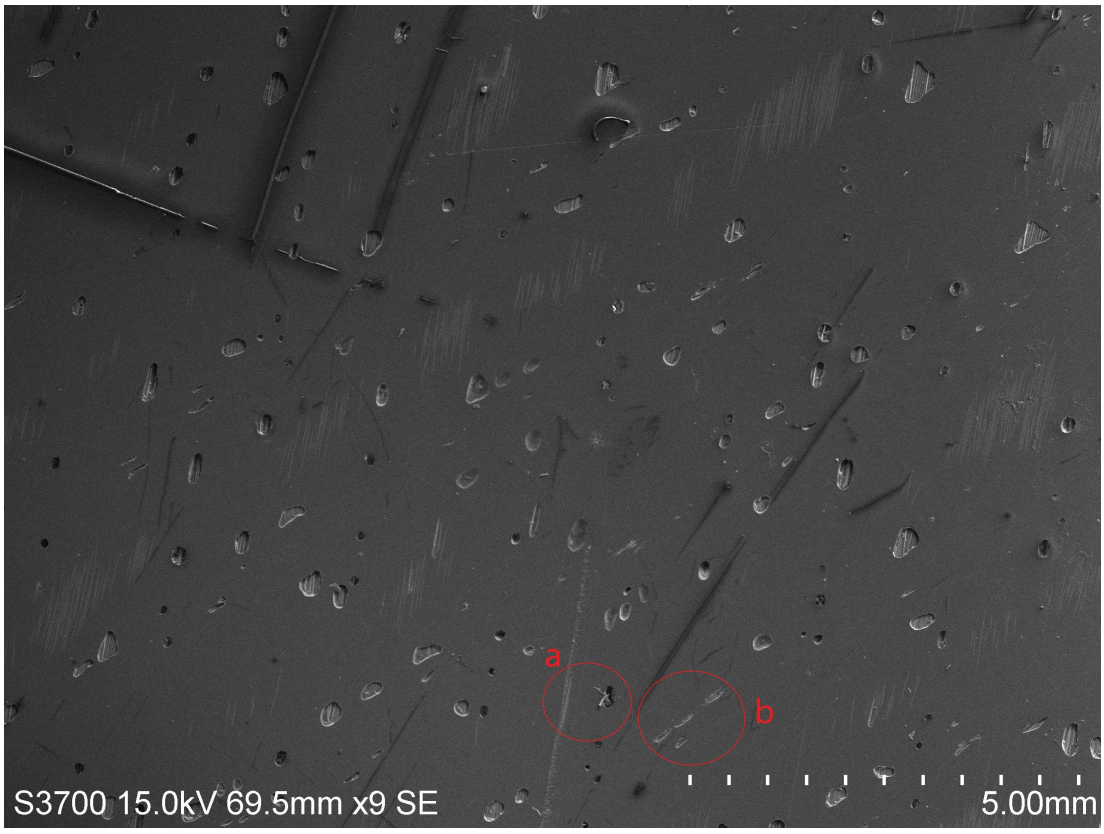

Figure 4.87: Overview SEM image for sample M15-V1.

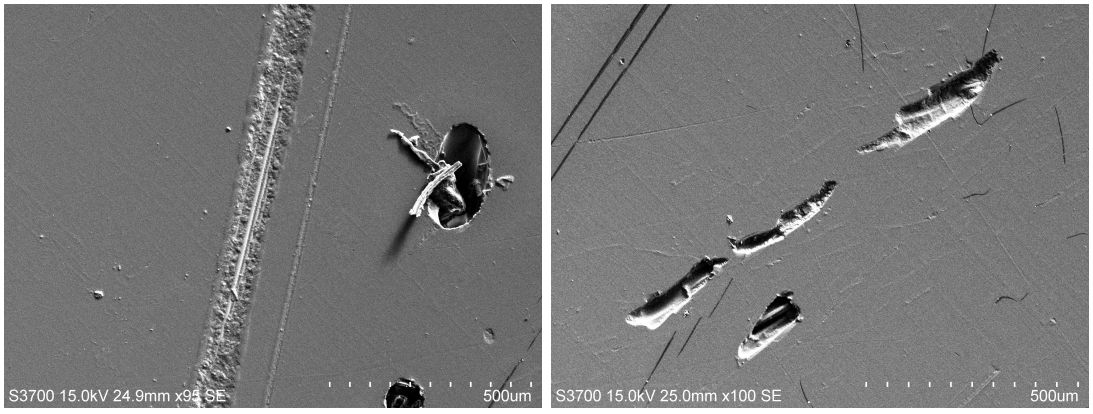

(a) (b)

Figure 4.88: Close-up SEM images for sample M15-V1.

The sample hit with twenty five impacts of 15 mm SHI at 51.4 m s^{-1} mean velocity is presented in Figure 4.87. A long scratch that travels more than 2.5 mm in length is visible in the bottom portion of the image. A close-up of this is shown in Figure 4.88a. This image also depicts loose material collected in a nearby void. There were also numerous occurrences of the furrows as shown in Figure 4.88b throughout the main overview. These marks appeared narrower than the other voids present in the composite.

The final specimen in this cumulative force region is the first example of 10 mm hailstone impact. The composite shown in Figure 4.89 is hit fifty times at a mean velocity of 83.2 m s^{-1}. Despite displaying by far the greatest mass loss change of all the samples, there are no obvious differences in the composite surface compared to the previous samples. There a certain amount of matrix debris shown in Figures 4.90a and 4.90a but there are only a few examples of individual detached fibres.

For completeness, the sample subject to 10 mm at a higher mean velocity of 96.9 m s^{-1} at a lower number of impacts (twenty five) is also shown in Figure 4.91. We can see a few indications of loose fibres spread around and regions of localised damage shown in Figures 4.92a and 4.92b. As well as the deeper lacerations, there were many smaller abrasions close by, possible hallmarks of repeated impact.

. Figure 4.93 displays the aftermath of fifty impacts from the most common and yet smallest size of hail, at a mean velocity of 90.7 m s^{-1}. There were instances of fibres removed from the matrix but no obvious individual areas of severe damage. There are a few examples, as shown in Figure 4.94a, of depressions roughly the same size as other voids but of slightly different form. These measured no more than 30 µm across. A small disfigurement of around 500 µm is shown in Figure 4.94b but with very little

Figure 4.89: Overview SEM image for sample M10-V3.

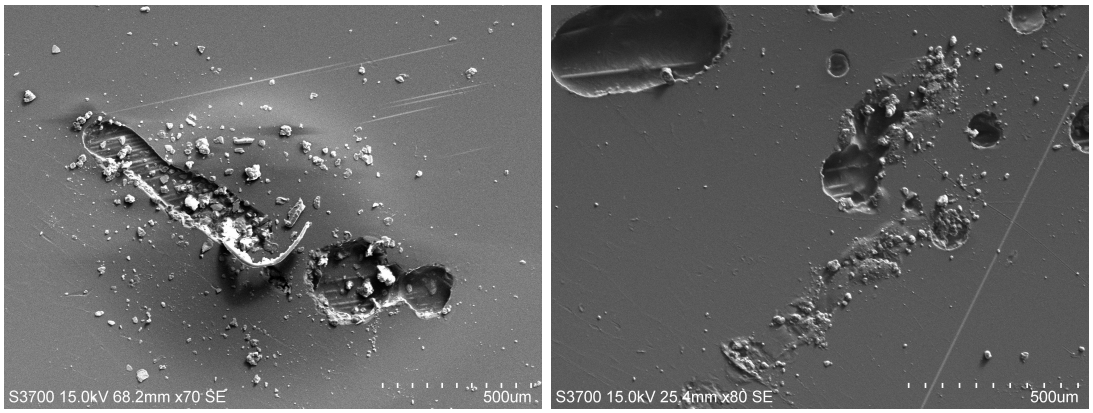

(a) (b)

Figure 4.90: M10-V3.

debris.

The nearest comparable 10 mm sample, in terms of cumulative force, is shown in Figure 4.95. Despite being subject to only ten impacts of 51.0 $\mathrm{m\,s^{-1}}$ mean velocity, the

Figure 4.91: Overview SEM image for sample M10-V4.

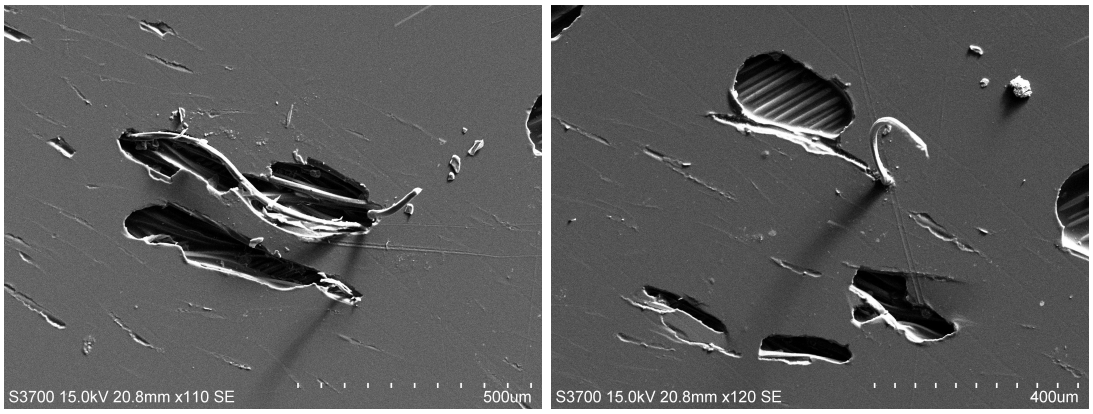

(a) (b)

Figure 4.92: Close-up SEM images for sample M10-V4.

damage is at least of a similar degree to that of the maximum 5 mm variant, with loose fibres and debris scattered around. There are also small indications of wear, as shown in Figure 4.96a

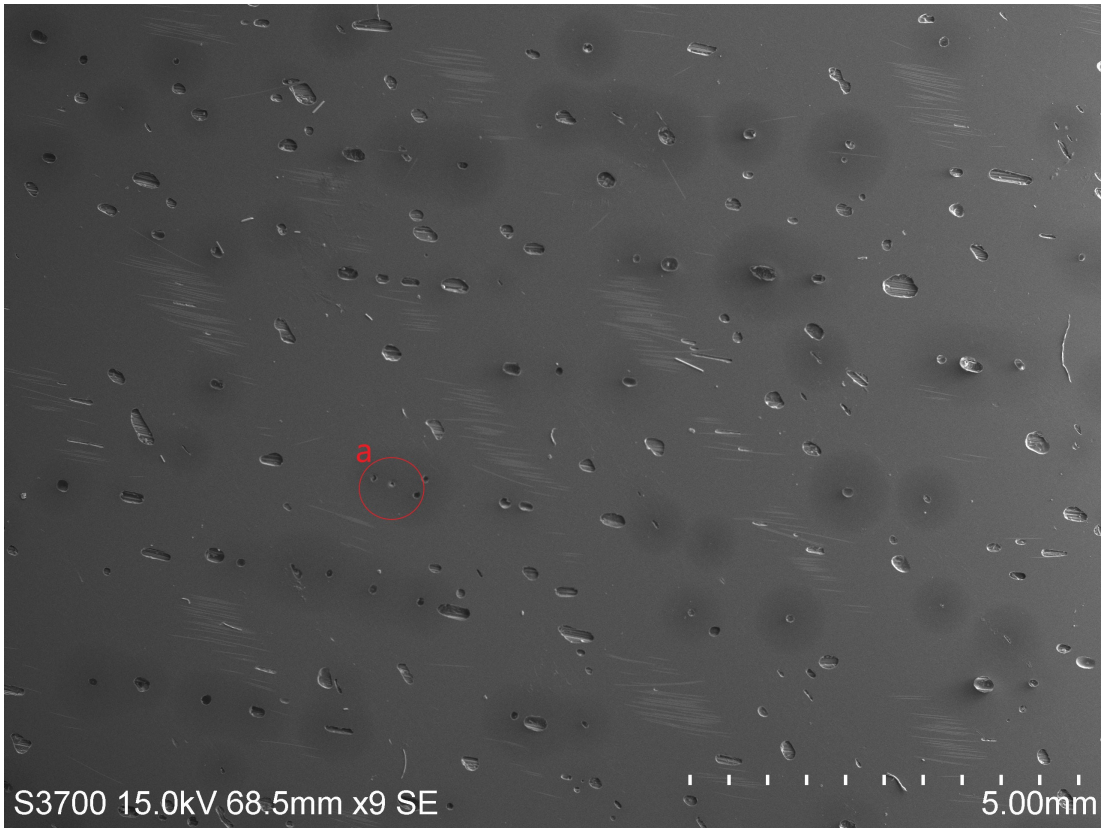

Figure 4.93: Overview SEM image for sample M5-V4.

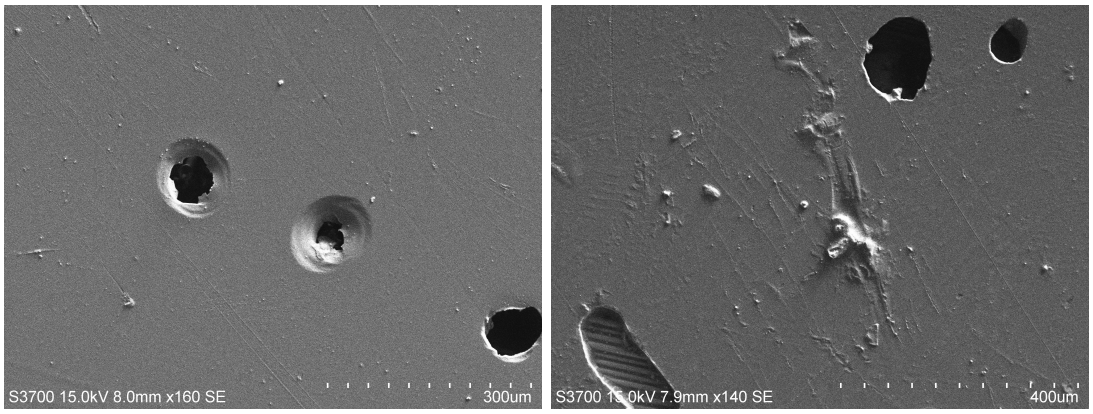

(a) (b)

Figure 4.94: Close-up SEM images for sample M5-V4.

4.8 Discussion

Over the course of this experimental campaign, several interesting results were found that are unique to the field of ice impact on composites. Along with these findings,

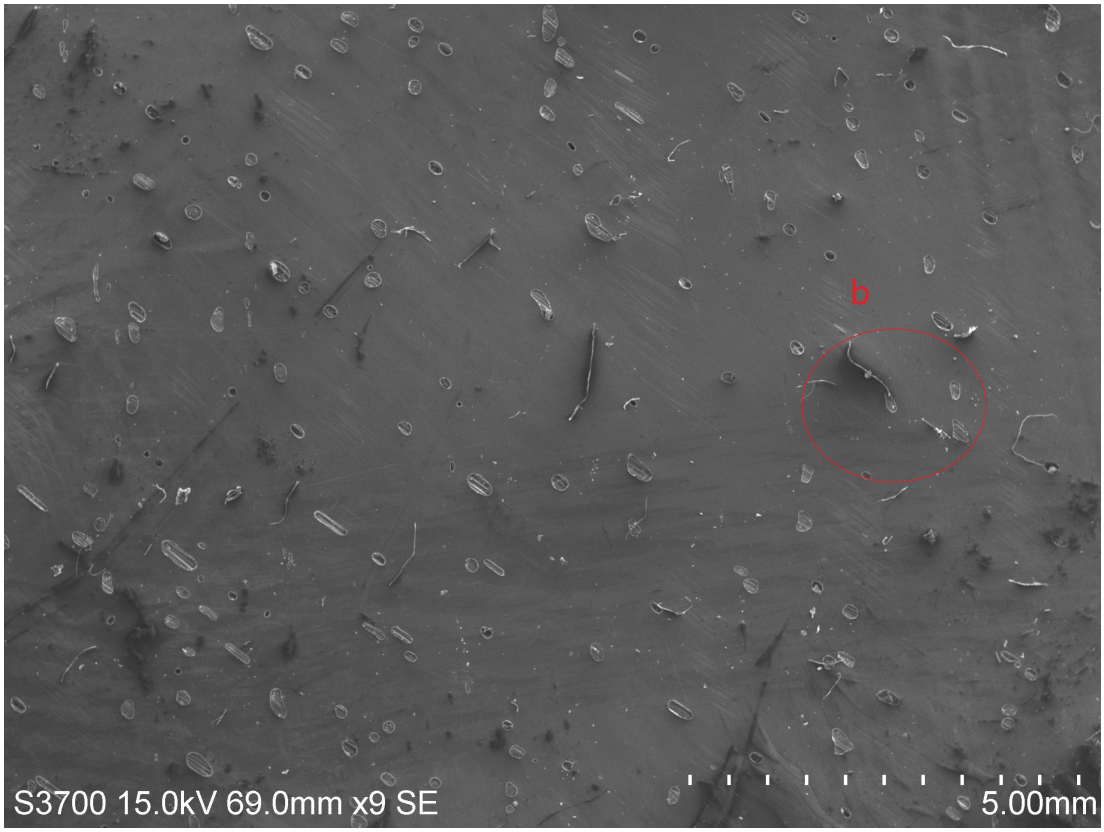

Figure 4.95: Overview SEM image for sample S10-V1.

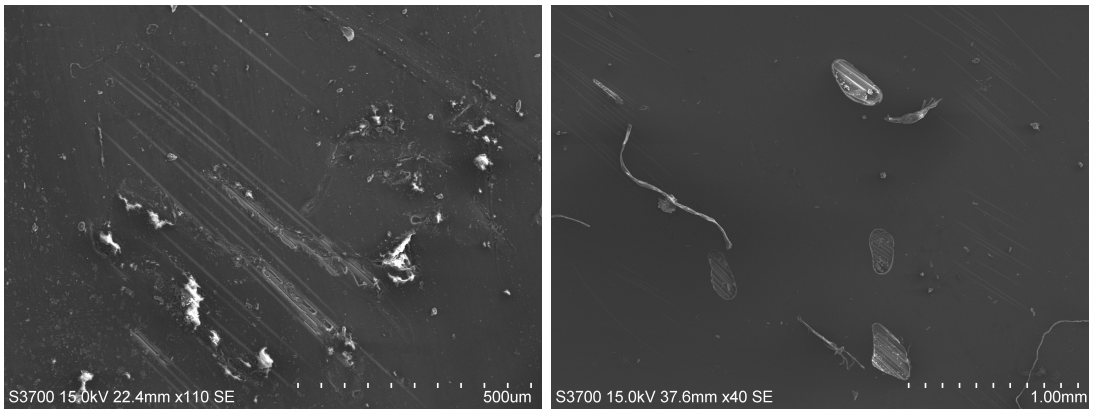

(a) (b)

Figure 4.96: Close-up SEM images for sample S10-V1.

various experiences provided many opportunities to reflect upon and examine further.

The use of smaller sizes of simulated hail ice (SHI) that are more commonly experienced in the UK is novel compared with other investigations. However, as demon-

strated, these modest diameters of hail were far more sensitive to the laboratory environment than the extreme sizes would be. With the information obtained from meteorological data, the ambition was to use the lowest possible but more prevalent 5 mm diameter on the TORRO hail intensity scale. Despite a lengthy calibration to ascertain a consistent experimental procedure, from the estimated melting times and force transducer measurements, concerns must be raised regarding the integrity of this category of hail. Unlike SHI of larger diameters, the peak impact force from 5 mm diameter SHI was significantly undervalued; and beyond a certain firing pressure, the force pattern appeared to behave differently. It is certainly likely that although the inner structure of the SHI maybe be solid ice, the outer surface may have started to melt, resulting in a different consistency of projectile and thus mechanism of impact. Unfortunately video evidence to confirm this finding was not of sufficient detail clear and unobtainable beyond a certain projectile velocity.

The remaining diameters compared well with peak force vs. kinetic energy relationships of the larger sizes of SHI investigated Tippmann *et al.*. The restrictive (± 10 V) voltage requirements of data acquisition device is exceeded by some higher velocity impacts of the largest diameter SHI, curbing the initial peak force in some cases. There was also a limitation on the highest achievable and reliable velocity for each diameter. Regardless, maximum velocities of $90\,\mathrm{m\,s^{-1}}$, $96\,\mathrm{m\,s^{-1}}$, $98\,\mathrm{m\,s^{-1}}$ and $85\,\mathrm{m\,s^{-1}}$ were achieved for 5 mm, 10 mm, 15 mm and 20 mm diameter SHI respectively; indicative of many large-scale commercial wind turbines. Any unpredictability in the resultant velocity/force production was taken into account and represented in the results. Although the capabilities of the high speed camera were limited, the footage showed that considerable shards were often created upon impact, instead of a spread of more uniform, smaller particles. This was especially evident at the larger diameters, which could account for erosion of the composite, secondary to the initial contact. The pressure required to cause a phase change from solid to liquid in ice, taken from adiabatic shock Hugoniot curves [34], is thought to be extremely large ($\geq$23.5 GPa). The maximum pressures from all diameters of SHI, taken from peak force measurements and the estimated contact area at that time, are found to be less than 0.09 GPa. Therefore the generation of any liquid solution on the surface of the composite sample was not caused by impact in this scenario and must instead be driven by temperature. It

The selection of the composite materials was driven by the more recent tendency of using multi-axial glass fibres in wind turbine skins. With the gap in research of glass fibre analysis in spherical ice impacts, a simple five layered configuration was used to provide thickness without any additional structure. There is certainly much room for further investigation into coatings and additional composite features for future

research. Composite samples were manufactured in-house using vacuum infusion and the differences in quality between samples were immediately apparent. Originally, the scope of the investigation considered including composite properties and orientation as an experimental variable. Once discounted, hindsight concluded that obtaining samples directly from a manufacturer would have been beneficial. Once samples of consistent condition (to the naked eye) were obtained, three separate burn-off tests were carried out and yielded an average void content of close to 2%. However, when examining the experimental specimens under an electron microscope there appeared to be slightly more variation in surface quality then originally anticipated. The investigation was hampered by the reduced number of samples available, as SEM analysis was not possible for the full range of total impacts and impact velocities, necessitating concessions to the original methodology.

Mass loss did not appear to be a valid indicator of damage for these investigations. This could be influenced by the absorption of residue by the composite, due to the vertical orientation of the hailstone firing rig. Examining the composite surface immediately did not yield any major differences, except in the case of fifty impacts of $\sim$80 m s^{-1} 15 mm SHI. There were, however, several observations of damage using the electron microscope. Unsurprisingly, the more severe damage was experienced using the 15 mm and 20 mm impacts at higher velocity, for a higher number of impacts. The 10 mm damage was visible but noticeably less and damage sustained from the 5 mm is minor, even cumulatively. The resultant effects caused by extreme velocity impacts $\geq$ 95 s^{-1} of 15 mm SHI were still apparent at twenty five or even at ten impacts.

4.9 Conclusion

An experimental investigation was carried out to examine the damage caused by repeated impact of smaller-sized Simulated Hail Ice (SHI) on Glass Fibre Reinforced Polymer GFRP composites. Diameters of 5 mm, 10 mm, 15 mm and 20 mm were chosen to better reflect the more common sizes of hailstones experienced in the UK, rather than focussing on extreme cases. Each diameter was fired at four proposed velocities ranging from $\sim$50 m s^{-1} to $\sim$95 m s^{-1}. Different sets of "number of impacts" included: singular, 5, 10, 25 and 50. Dynamic force measurement profiles were also captured, for use in calibrating future computational modelling of the SHI impacts.

Although visual inspection and mass loss measurements did not produce meaningful results or particularly discernible damage, the effects of impact were apparent using scanning electron microscopy. Two main forms of damage were encountered. The first and most common involves glass fibres being "torn-out" from underneath, dislodging

the epoxy resin on the surface and exposing more of the reinforcement. There was also evidence of a secondary form of damage, with cutting/ploughing scars similar to solid particle erosion found at elevated velocities. High speed video footage added weight to this observation, with larger, angular fragments found amongst the jetting particles.

As anticipated, the most extreme form of damage came from the largest diameter of SHI at the highest selected velocity, at the highest number of impacts. Obvious areas of ripped fibres were found across the specimen. Similar investigations of 5 mm and 10 mm diameter SHI displayed some disfigurements but only minor damage in comparison. There was a noticeable influence of velocity on the defacement of the composite. The violent effects of 15 mm hail when speeds reach greater than $95\,\mathrm{m\,s^{-1}}$ were evident, even after ten or twenty five impacts. The lowest velocity impacts would correspond to, at most, the tangential velocity at half the wind turbine blade length but the difference in surface quality was clear.

Once again, we must refer back to Chapter 3 where the practical scenarios of hailstone impact were reported. Even at a wind farm site where hail was prevalent, the incidences would be as such that the damage caused by 5 mm or 10 mm hailstones is likely to be minor, even before taking protection methods into account. The likelihood of 15 mm and 20 mm hail, where the effects are much more apparent, is significantly low. However, the trend for increased wind turbine tip speeds for the larger MW machines is certainly a concern, due to the influence of impact velocity. For a wind turbine blade to experience leading edge erosion after just a number of years other factors must be involved. The practical limitations of this part of the investigation have been discussed but there would certainly be a case for expanding upon the experimental findings as part of a future investigation.

Chapter 5

Computational Modelling

List of Symbols

Symbol	Definition	Units
A	surface area	m^2
E	Youngs modulus	Pa
F	failure	
G	shear modulus	Pa
K	bulk modulus	Pa
S	strength	Pa
V	volume fraction	
W	weight fraction	
f	fibre (subscript)	
m	matrix (subscript)	
c	composite (subscript)	
ν	Poissons ratio	
ρ	material density	$\mathrm{kg\,m}^{-3}$
σ	Stress	Pa

The experimental study carried out in Chapter 4 tested a portfolio of hailstone impact variables and inspected the resultant damage. This chapter attempts to create a computational model that would replicate the experimental set-up and analyse in more detail the behaviour of the composite subject due to hailstone impact. LS DYNA ®, a multi-purpose explicit and implicit finite element program designed to analyse the non-linear response of structures was selected as the most appropriate software as it is proficient in high-velocity impact scenarios and has been employed previously numerous hailstone impact investigations in the literature [17, 19, 60, 123]. For this project, the model was originally created in LS-PrePost 4.3. An exported "keyword" file (.k) from the model was run through the ANSYS LS-DYNA solver at the command level and the results analysed using LS-PrePost 4.3 Unfortunately the capabilities of the software limited the simulations to single-impact scenarios but investigating the other variables, hail size and velocity, would still provide valuable insight into their influence on composite damage. Unless additional literature or support information is cited, simulation recommendations are taken from either the LS DYNA ® keyword user's manual (Volume1) [124] or LS DYNA ® theory manual [125].

5.1 Methods of Determining Composite Characteristics

Even within the category of polymer matrix composites (PMC's) that are used for wind turbine blades, there are a range of fibres and resins that are combined to form the final form. The choices of these constituent materials will result in different characteristics which are of particular significance when modelling the structure computationally. After selection the micromechanics of the resultant composite structure are largely determined by: the properties of the fibre, the properties of the resin, the ratio of fibre to resin (volume fraction) and the geometry and orientation of the fibres. There are many material modelling methods and relationships that seek different configurations in order to obtain particular material properties. The various material models available in LS DYNA® for modelling composites require specific material characteristics in order to perform accurate simulations of impact behaviour. The majority of examples use at least the following properties: Material Density (ρ), Young's Modulus (E), Shear Modulus (G), Poisson's Ratio (ν), Tensile Strength (S_x), Compressive Strength (C_x) and Shear Strength (S_{xy}). Carrying out physical mechanical testing to determine these properties was not within the scope of this project, so other means had to be employed. Fortunately there are some simple mathematical methods that, if treated with care, can give useful approximations for the behaviour of composite materials. A range of these micromechanical models were assessed. The material density can be determined

Table 5.1: Properties of reinforcement and matrix materials

Property	Glass fibre	Epoxy resin
Young's modulus (GPa)	80	3.6
Poisson's ratio	0.25	0.35
Shear modulus (GPa)	339	3.6
Tensile strength (MPa)	2400	72
Density ($\mathrm{kg\,m^{-3}}$)	2.54	1.14

easily thanks to the simple geometry of composite samples but the other properties need to be analysed in more detail. Fibre and matrix information was obtained from the associated manufacturers. Acquisition of the volume fraction for the experimental composites are described previously in Chapter 4.

5.1.1 Rule of Mixtures

One of the most well-known methods for approximating material characteristics is the rule or law of mixtures. This approach assumes the structure to be a simple beam, in which the fibre and matrix are perfectly bonded together so they deform together in unison and the load on the overall composite is shared equally between them [118]. The strain in the two phases is assumed to be the same as that in the full composite. Stress is defined by load divided by area, therefore:

$$\sigma_c A_c = \sigma_f A_f + \sigma_m A_m$$

From the isotropic strain condition ($\epsilon_c = \epsilon_f + \epsilon_m$), we have a relationship between the longitudinal moduli:

$$\frac{\sigma_c A_c}{\epsilon_c} = \frac{\sigma_f A_f}{\epsilon_f} + \frac{\sigma_m A_m}{\epsilon_m}$$

This is more commonly represented in terms of volume (Vf and Vm) fractions, which we know the sum of to be equal to one, to form the familiarly recognised *rule of mixtures* for the longitudinal Young's modulus:

$$E_x = E_f V_f + E_m(1 - V_f) \tag{5.1}$$

Similarly the major Poisson's ratio is determined by

$$\nu_{xy} = \nu_f V_f + \nu_m(1 - V_f) \tag{5.2}$$

The transverse modulus is determined by assuming an "iso-stress model" ($\sigma_c = \sigma_f +$

σ_m), resulting in the *inverse rule of mixtures*

$$E_y = \frac{E_f E_m}{V_f E_m + (1 - V_f) E_f} \tag{5.3}$$

The shear modulus is calculated similarly as shown below

$$G_{xy} = \frac{G_f G_m}{V_f G_m + (1 - V_f) G_f} \tag{5.4}$$

The estimates for the Young's moduli using these formulae apply only to unidirectional laminates ($E11$;$E22$). A correction or efficiency factor ($\eta_{xy}\theta$) is typically applied to include the effect of the fibre orientation in the calculation of the Young's modulus. Here the factor takes into the account the angle of each of fibres (θ) and the proportion of total fibre content in that direction (a_n). The angle is taken appropriately for the cases of longitudinal or transverse modulus:

$$\eta_\theta = \sum a_n \cos^4(\theta)$$

5.1.2 Hart-Smith Rule (10%)

The Hart-Smith or more commonly the "Ten-Percent rule" is a quick and easy approximation method. Here each 45° or 90° ply is considered to contribute one tenth of the strength or stiffness of a 0° equivalent. The sum of these percentages results in a laminate factor, that can be applied to the unidirectional value (usually obtained from the Rule of Mixtures), i.e:

$$\eta = \%\text{ of } 0^\circ \text{ plies} + 0.1 \times \%\text{ of } \pm 45^\circ, 90^\circ \text{ plies} \tag{5.5}$$

Expanding the rule, the major Poisson's ratio and shear modulus are estimated by:

$$\nu_{xy} = \frac{\%\text{ of } \pm 45^\circ + 40 \times 0.3}{\%\text{ of } \pm 45^\circ + (3.6 \times \%\text{ of } \pm 90^\circ) + 40} \tag{5.6}$$

and:

$$G_{xy} = E_{11}(0.028 + 0.0234 \times \%\text{ of } \pm 45^\circ) \tag{5.7}$$

The formula is limited to 0°, 45°, and 90°, plies and is typically utilised in the aerospace industry where balanced laminates are used.

5.1.3 Classical Laminate Analysis

In this method, each fibre-reinforced lamina (or ply) is treated as a orthotropic sheet and the overall composite is analysed using classical theory of laminated plates. The elasticity properties (E, G, ν) are required as initial values and are taken from rule of mixtures calculations described previously. The theory uses 'ABD' stiffness matrices ($\begin{bmatrix} A & B \\ B & D \end{bmatrix}$), that connect applied loads and resultant strains in the laminate, in order to derive the following equations [126]:

$$\frac{1}{E_x} = \frac{m^4}{E_{11}} + \frac{n^4}{E_{22}} + (\frac{1}{G_{12}} - \frac{2\nu_{12}}{E_{11}})m^2n^2 \tag{5.8}$$

$$\frac{1}{E_y} = \frac{n^4}{E_{11}} + \frac{m^4}{E_{22}} + (\frac{1}{G_{12}} - \frac{2\nu_{12}}{E_{11}})m^2n^2 \tag{5.9}$$

$$\nu_{xy} = E_x[\frac{\nu_1}{E_{11}} - (\frac{1}{E_{11}} + \frac{2\nu_{12}}{E_{11}} + \frac{1}{E_{22}} + \frac{1}{G_{12}})m^2n^2] \tag{5.10}$$

$$\frac{1}{G_{xy}} = 4[\frac{1+2\nu_{12}}{E_{11}} + \frac{1}{E_{22}} - \frac{1}{2G_{12}}]m^2n^2 + \frac{1}{G_{12}}(m^4+n^4) \tag{5.11}$$

where $m = \cos\theta$, $n = \sin\theta$ and θ is the angle from the reference direction. Each property is calculated for each applicable fibre direction (0°, −45°, +45°) and then multiplied by the % of total fibres in that direction (i.e. 1/3). The summation of these equates to the overall property value for that layer.

5.1.4 Engineering Sciences Data Unit (ESDU)

The Engineering Sciences Data Unit (ESDU) is a national (UK) engineering advisory organisation that provides methodologies, design guides, equations and software tools for a broad range of engineering problems. As part of the ESDU "composites" series, Section 2: Laminated Composites, ESDU 83035 describes the "Estimation of the stiffnesses and apparent elastic properties of laminated at plates". The associated software ESDUpac A8335 allows for the estimation of these properties. The data input is structured with the respective matrix and fibre Young's Moduli, shear moduli, major Poisson's ratio, as well as the fibre volume fraction, entered initially. Then the composite of the laminate, including angle of orientation and thickness of each layer was included. The laminate has to be classified as either symmetric, anti-asymmetric or asymmetric. First, the output file described the input of fibre and matrix data, then a lamina composed of unidirectional properties. The geometry of the asymmetric layers is then shown including the angle, thickness and distance from the reference plane, with

the moduli and Poisson's ratio of each layer detailed subsequently. This is followed by the 'ABD' stiffness matrices of classical laminate analysis form with the overall 'laminate' properties detailed at the end. A statement is made at the end regarding whether the plate stiffness-matrices satisfy the conditions for special orthotropy.

5.1.5 Autodesk Helius Composite Simulation Design

Another form of programmed analysis is Autodesk Helius Composite. Formally known as Simulation Composite Design, the software can be used to create a library of fibres, matrices and assemble laminae and laminates. The inclusion of other materials such as metals and cores in the overall plate construction is also possible. A particularly attractive feature is the fabric builder, which can be used to create different fibre types such as: random continuous mat, woven fabric or the stitched fabric type under consideration, certain weave orientations and custom constituent materials. From these constructs, detailed information on either the 2D and 3D mechanical properties can be obtained within the software. The 3D computed laminate properties are designed for symmetric laminates, so caution must be taken for asymmetric cases. Laminate-analysis tool sets are also available to perform "First Ply Failure", "Failure Envelope" or "Progressive Failure" (further behaviour after failure has taken place) techniques to acquire particular strength properties. For the purposes of this investigation, the "First Ply Failure" strength will suffice.

5.2 Comparison of Elastic Properties

Before a calculation method was selected, properties assessment for an example of a glass-epoxy laminate was carried out for comparison. Samborsky *et al.* [127] provided an ideal case study for this validation, with detailed experimental testing carried out and information provided on six-ply glass/epoxy test coupons at a similar volume fraction, as well as for just the neat epoxy resin. The Young's and shear moduli predictions are shown in Figure 5.1 along with the actual mechanical properties. Every procedure gave a reasonable approximation for E_x, with the ESDU and Autodesk methods marginally closer. Whereas the estimations for E_y were a lot more spread out. Here the calculated value from ESDU was the closest match and the Rule of Mixtures was notably lower than the experimental value. All the G_{xy} estimations were very accurate apart from the Hart-Smith (10%) rule, which was about double the magnitude. Only the Autodesk software gave an estimate for E_z, G_{xz} and G_{yz}. The shear modulus values were quite accurate but the E_z modulus was moderately undervalued.

The major and minor Poisson's ratios in all orthogonal directions are displayed

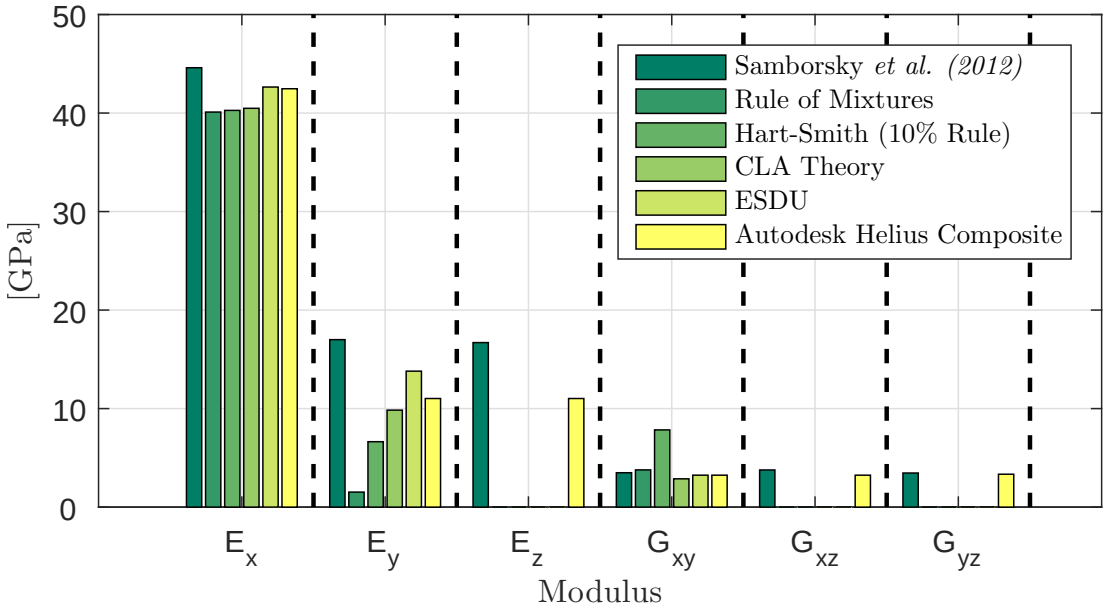

Figure 5.1: Experimentally determined modulus properties of a six ply unidirectional glass/epoxy composite by Samborsky *et al.* compared with various estimation methods.

in Figure 5.2. Again, only the Autodesk software could make an approximation that considered for the other direction. Every method made a very good prediction for the major Poisson's ratio describing axial to transverse strain but similarly to Figure 5.1, the corresponding minor-ratio estimations were dispersed. Once more, the Hart-Smith(10%) rule performs the worst and ESDU the best. The remaining ratios are fairly well predicted by Autodesk, although with a marginal overestimation for ν_{yz} and ν_{zy}.

From these initial validations, confidence in estimation leant towards either ESDU or the Autodesk Helius Composite software. In terms of capability, Autodesk provided features; including, most importantly, strength properties albeit only for 2D arrangements. Attempts were made to find a similar ESDU package to calculate strength but the nearest applicable tool, 96036 - "Design of Laminated Plates Subjected To In-Plane Loads and Bending Moments", was unable to handle asymmetric or unidirectional laminates. Therefore Autodesk Helius Composite was selected as the preferred calculation method. Using this software, the 2D strengths and ultimate strains for the 'Samborsky *et al.*' laminate were calculated and are collated in Figures 1.3 and 1.4 respectively. The predictions were well matched for each case, with only marginal differences noted.

For comparison, the properties for the composite used for hailstone impact were calculated using all previously discussed methods. Whereas for the 'Samborsky *et al.*' composite the 2D and 3D properties were identical for the unidirectional laminate,

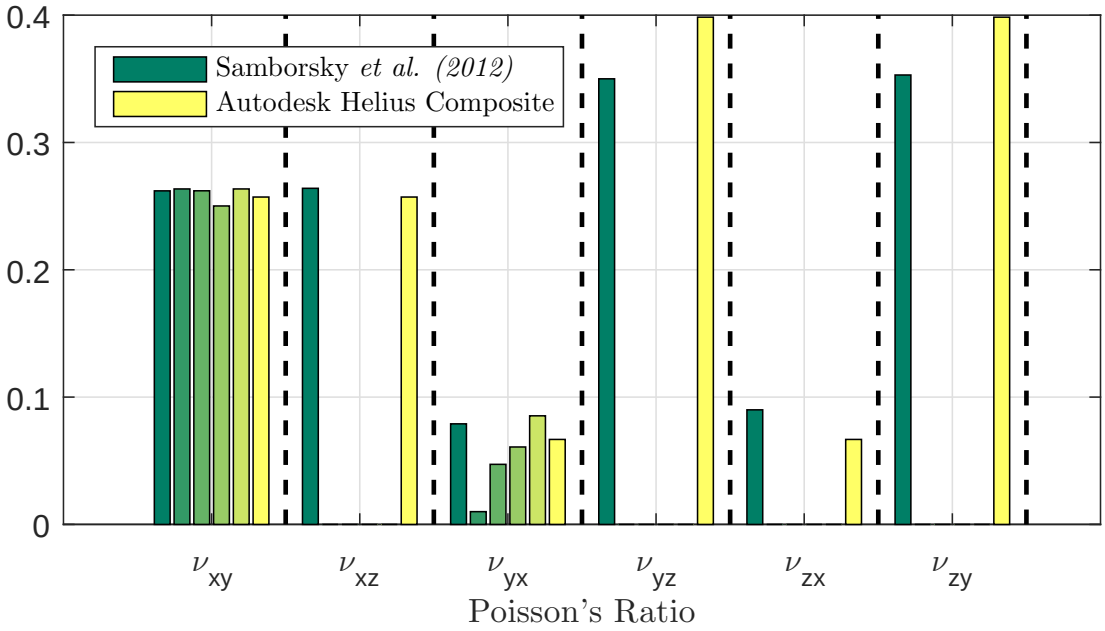

Figure 5.2: Experimentally determined Poisson's ratios of a six ply unidirectional glass/epoxy composite by Samborsky *et al.* compared with various estimation methods (see Figure 5.1 for full legend).

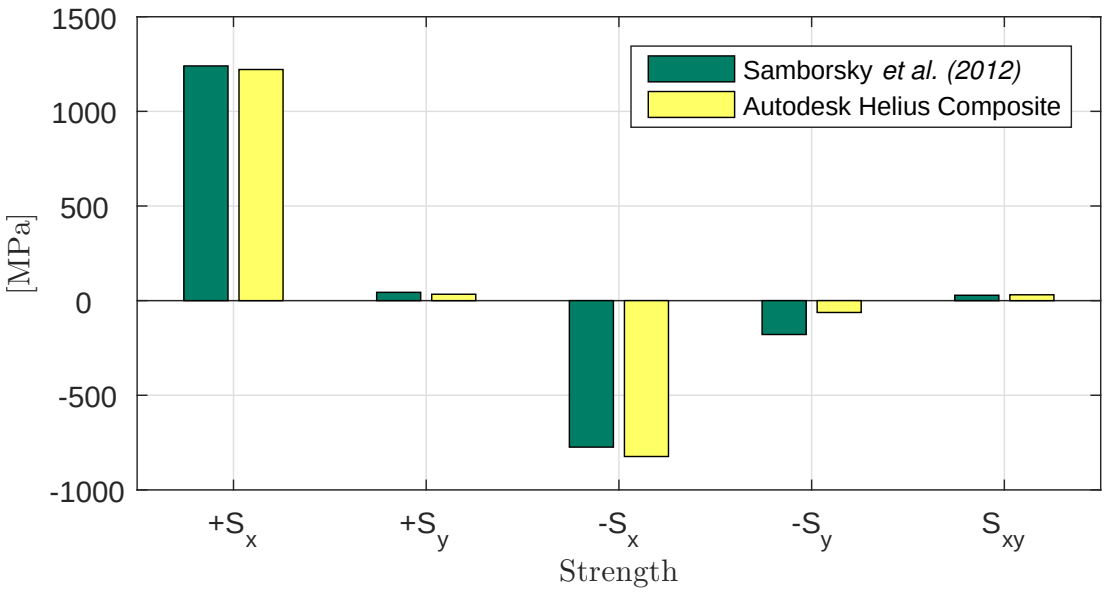

Figure 5.3: Strength properties of the 'Samborsky *et al.* composite' compared with estimations by Autodesk Helius Composite.

they were slightly different for the triaxial glass-epoxy case and both were taken into consideration. The calculated moduli are displayed in Figures 1.5. The Autodesk and

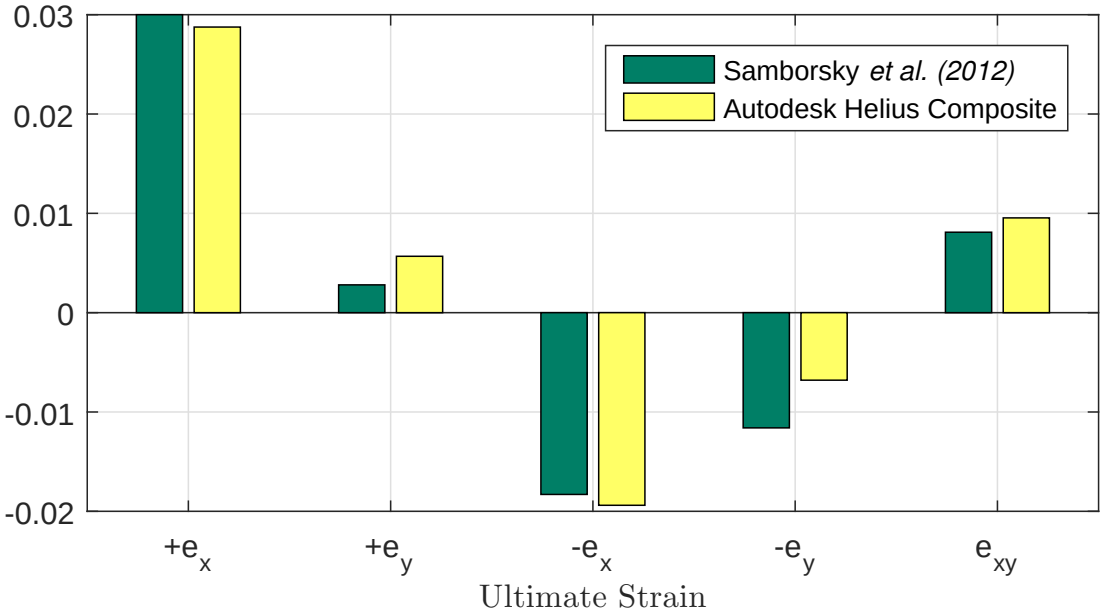

Figure 5.4: Ultimate strain properties of the 'Samborsky *et al.*' composite compared with estimations by Autodesk Helius Composite.

ESDU methods show similar values of and were greater for the most part than the alternative theories across the Young's moduli. The 2D Autodesk provided values that were marginally lower than the 3D alternative for E_x but almost identical for estimates of E_y and G_{xy}. The Poisson's ratios for the experimental composite are also shown in Figure 1.6. The Rule of Mixtures and Hart-Smith (10%) rule showed a ν_{xy} of under 0.3, whereas for the other methods ν_{xy} was closer to 0.4 and 0.45. The difference was more noticeable for ν_{yx} where the $\sim$0.1 obtained from the quick estimation methods contrasts to $\sim$0.2 to $\sim$0.3 using the other techniques.

The range of values obtained for the mechanical properties clearly shows that the selection of a certain method could result in different behaviour of the computational model. Although determination by physical mechanical testing was not possible, this extensive investigation of calculation practices, which was the next best alternative, provided a method that could determine properties with a reasonable degree of confidence.

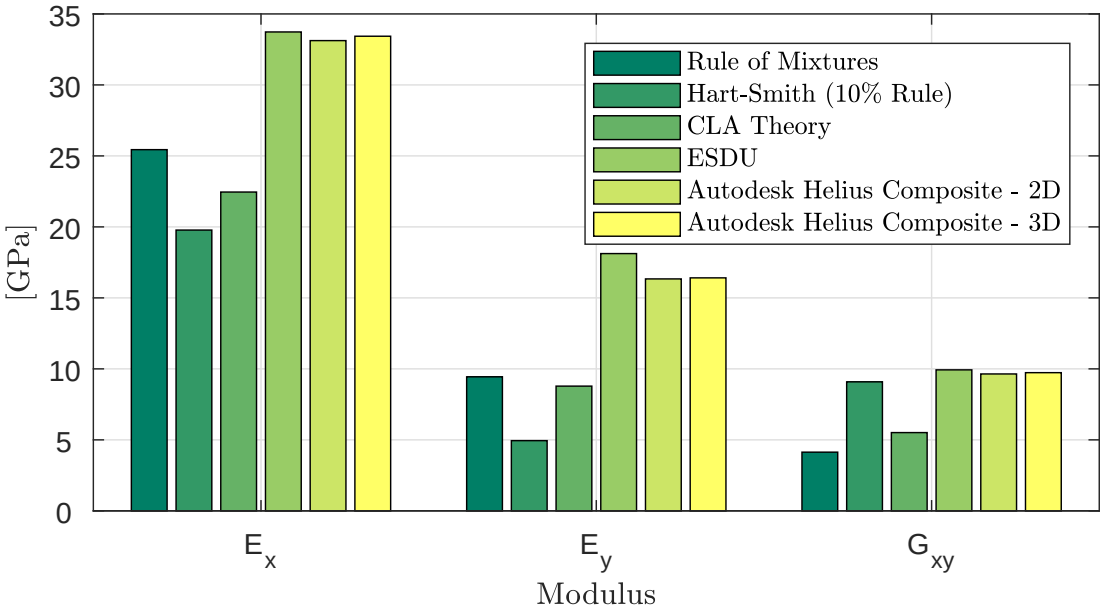

Figure 5.5: Various estimated modulus properties for the 5-ply triaxial glass/epoxy composite used for hailstone impact.

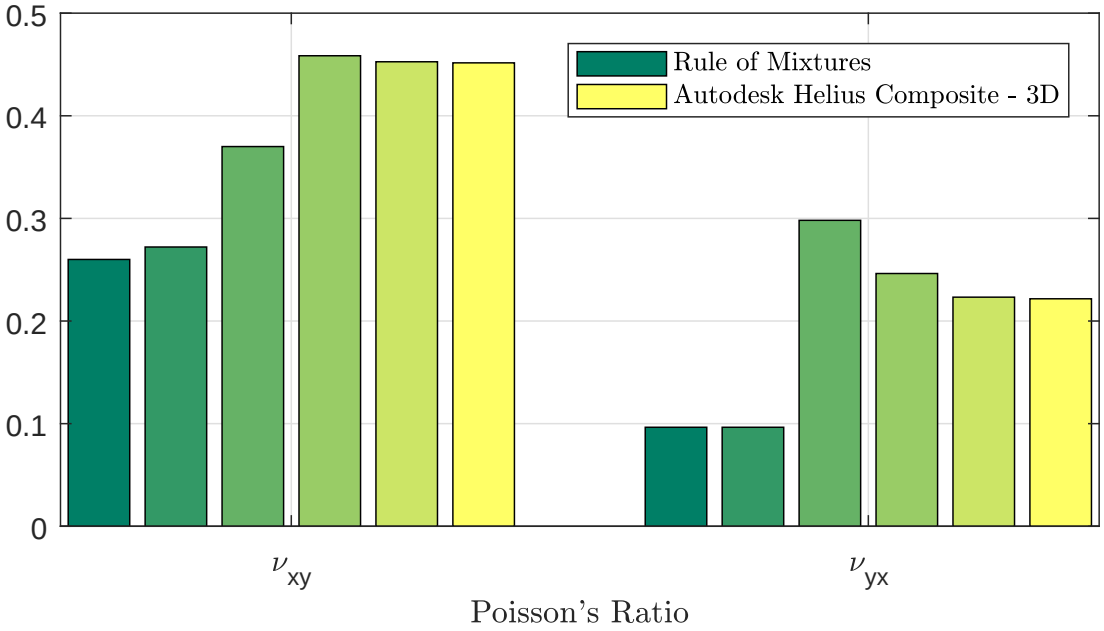

Figure 5.6: Various estimated Poisson's ratios properties for the 5-ply triaxial glass/epoxy composite used for hailstone impact (see Figure 5.5 for full legend).

5.3 Computational Model Geometry and Material Characteristics

5.3.1 Composite

The geometry of the composite laminae were created in LS PrePost using the block mesher function. This represents each element as a solid, applicable to the simplified structure. Creating the composite "disc" in block mesher, utilised butterfly blocks of a specified radial, perimeter and thickness density and thickness density, In order to confirm that the specified mesh was of sufficient refinement, a small study was undertaken to compare the convergence of a solution. This is described later in Section 5.4.6. The overall composite was modelled as a singular part, consisting of the five layers of reinforcement together with the matrix. The overall composite radius of 28.34 mm was taken from the average dimensions of the burn-test samples. The thickness of the disc, 3.803 mm, was also determined from the average thickness of the burn-test samples, which is actually slightly less than the 3.846 mm and 3.8425 mm calculated from ESDU and Autodesk Helius Composite respectively. There are several different material models that could be used to represent composites in LS DYNA, even when using solid elements. Many of the advanced damage models require specific parameters that are not easily obtained and many values would be assumed. *MAT 022-COMPOSITE DAMAGE, the Chang-Chang Composite Failure Model, has been reliably used in impact analysis [123] and only requires five material parameters for three failure criteria. These include the longitudinal tensile strength (S_x), transverse tensile strength (S_y), shear strength (S_xy) and transverse compressive strength (C_y). An additional term, the nonlinear shear stress parameter (α), is also needed. In-plane strain is related to the stress in Equation 5.12, where the third equation defines the nonlinear shear stress parameter.

$$\begin{aligned} \epsilon_x &= \frac{1}{E_x}(\sigma_x - \nu_{zy}\sigma_y) \\ \epsilon_y &= \frac{1}{E_y}(\sigma_y - \nu_{yz}\sigma_z) \\ 2\epsilon_{xy} &= \frac{1}{G_{xy}}(\tau_{xy} - \alpha\tau_{xy}^3) \end{aligned} \tag{5.12}$$

LS DYNA ® recommended setting the value in the range of 0 - 0.5. Due to a lack of information, the default value of 0.1 was accepted. The fibre matrix shearing term (τ) augments each of the three damage modes, defined by the ratio of shear stress to shear strength as shown in Equation 5.13.

$$\bar{\tau} = \frac{\frac{\tau_{xy}^2}{2G_{xy}} + \frac{3}{4}\tau_{xy}^4}{\frac{S_{xy}^2}{2G_{xy}} + \frac{3}{4}\alpha S_{xy}^4} \tag{5.13}$$

The failure criteria are defined as follows [124]

- Matrix-cracking failure

$$F_{matrix} = (\frac{\sigma_y}{S_y} + \bar{\tau}) \tag{5.14}$$

  where failure is assumed whenever $F_{matrix} > 1$. If this occurs then the material constants Ey, G_{xy}, ν_{xy} and ν_{yx} are set to zero.

- Compression failure

$$F_{comp} = (\frac{\sigma_y}{2S_{xy}})^2 + [(\frac{C_y}{2S_{xy}})^2 - 1]\frac{\sigma_y}{C_y} + \bar{\tau} \tag{5.15}$$

  where failure is assumed whenever $F_{comp} > 1$. If this occurs then the material constants E_y, ν_{xy} and ν_{yx} are set to zero.

- Fibre-breaking failure

$$F_{fibre} = (\frac{\sigma_x}{2S_x})^2 + \bar{\tau} \tag{5.16}$$

  where failure is assumed whenever $F_{fibre} > 1$. If this occurs then the material constants E_y, E_y, G_{xy} ν_{xy} and ν_{yx} are set to zero.

A fourth mode of failure, which is unique to solid elements, is noted in the LS-DYNA ® literature as a delamination failure mode. Definition of this flag is not openly described in either the keyword or theory manuals. From the material source code, it is achieved in relation to the shear strengths in all directions. For solid elements the bulk modulus is also utilised by the material model to calculate a hydro-static pressure in the element after it has failed in terms of tensile fibre. This applies only for a volumetric state of compression (i.e. when the volume is less than the initial volume). Summerscales [119] proposes a prediction for the bulk modulus for a square symmetric material based on Maxwell's reciprocal theorem in Equation 5.17. For this composite it was determined to be 12.01 GPa. The rule of mixtures approximations, which required bulk moduli for the fibre and matrix, were also implemented and provided a value of 10.09 GPa. In the end, the higher value from the Summerscales theorem was entered in the model.

$$K = \frac{\sqrt[3]{E_x E_y E_z}}{3(1 - 2\sqrt[3]{\nu_{xy}\nu_{zx}\nu_{yz}})} \tag{5.17}$$

Table 5.2: Mechanical properties of the *MAT 022 COMPOSITE DAMAGE model.

Material Parameter		Value
Density [kg m^{-3}]	ρ	2004
Young's Modulus [GPa]	E_a	33.4
	E_b	16.4
	E_c	14.2
Poisson's Ratio	ν_{ba}	0.227
	ν_{ca}	0.0796
	ν_{cb}	0.274
Shear Modulus [GPa]	G_{ab}	9.73
	G_{bc}	4.86
	G_{ca}	4.83
Shear Strength [MPa]	S_{ab}	97.2
	S_{bc} (Solid Elements Only)	97.2
	S_{ca} (Solid Elements Only)	97.2
Tensile Strength [MPa]	S_a	253
	S_b	73.5
	S_c (Solid Elements Only)	73.5
Compressive Strength [MPa]	C_b	123

Strength properties were taken from Autodesk Helius composite using the first ply failure survey. Nine separate techniques were possible including: Max. Stress, Max. Strain, Tsai-Wu, Tsai-Hill, Hashin, Christensen, PUCK and MCT. The methods were almost identical for determining y-axis tension and compressional strength but there was some variation among the x-axis counterparts and shear strength. The Hashin, Christensen, Puck and MCT criteria could differentiate between fibre and matrix failure, which would be more alike to the computational Chang Chang damage model. There was not much difference between these four methods and no inferred preference, so average values were taken. A summary of the composite properties used in the material card are displayed in Table 5.2.

5.3.2 Metals

The clamp could also be created using the block mesher function, although with a reduced mesh. The upper and lower sections of the clamp were generated separately but labelled as one part for ease of computation. The slightly more complicated angles of the force transducer and support meant that the respective shapes were difficult to create using the same function. Instead the structures were created in Autodesk Inventor and imported into LS Prepost to be meshed using the auto mesher. The support was represented with solid elements, whereas the shape of the force transducer

meant it could only be accurately meshed as a shell. The support, force transducer and clamp materials were all defined as *MAT 020-RIGID, which requires only the isotropic input of material density, Elastic Modulus and Poisson's ratio. The force transducer case is made from 17-4 PH stainless steel, for which the physical properties are easily attainable but slightly variable, depending on the condition. Although the exact material used for the manufacture of the clamp and the support block were not known, the mass density of the part was calculated and an approximation of the properties assumed.

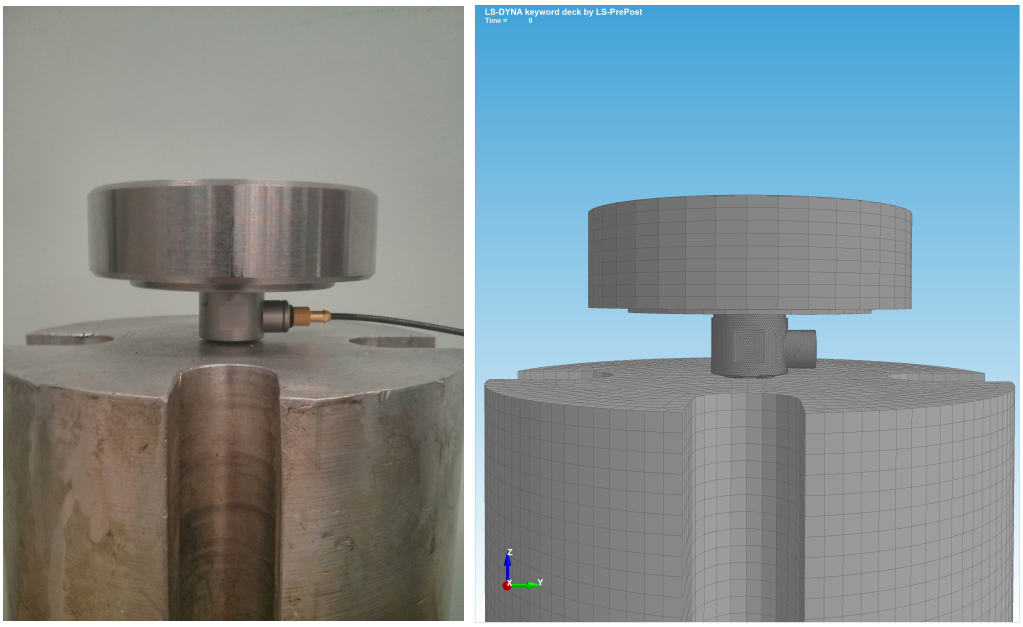

(a) Experimental

(b) Computational

Figure 5.7: Dynamic force transducer and clamping arrangement.

Table 5.3: Metal material properties.

Part	Material	ρ [kg m^{-3}]	E [GPa]	ν
Force Transducer	17-PH Stainless Steel	7725	200	0.285
Support	Aluminium 2024-T5	2793	73.1	0.33
Clamp	AISI 1005 Steel	7575	200	0.29

The rigid material allows for the centre of mass constraint in the six translational and rotational directions. The force transducer and clamp were left unconstrained, whereas the support was constrained in the z direction, to model the restriction of

displacement due to the floor of the hail rig. Alternatively this could be represented either restraining the nodes on the bottom surface of the support or inserting a rigidwall at the bottom. No convincing difference was found for the three approaches, so the first method was chosen as it was less taxing, computationally.

5.3.3 Ice

As described previously in Chapter 2, there are three main approaches for simulation of ice: the Lagrangian finite element formulation; the Arbitrary Lagrangian Eulerian (ALE) method; and the Smooth Particle Hydrodynamic (SPH) method. All three are shown to model behaviour to a reasonable degree of accuracy but depending upon the geometry and scenario involved, opinion differs about which method is more appropriate [81, 123, 128]. For the case of hailstone ice, the SPH formulation has typically been employed and is the method selected here, as the Lagrangian types are adequate only in the initial stages of the impact [22]. Keegan [60] found that the greater the number of SPH nodes, the more accurate the results but overall a total of 33000 nodes provided satisfactory performance without being too computationally taxing. SPH geometry works best when uniformly spaced: so the number of particles generated was set to 40 in each orthogonal direction (x, y, z). The Carney [23] model for ice was described using the material model *MAT PLASTICITY COMPRESSION TENSION EOS (155). The model was updated using more recent values from Tippmann *et al.* [19]. Notable changes included slightly increased values for the tensile failure pressure, quasi-static yield strength and yield strength ratios for different strain rates. The main properties can be seen in Table 5.4.

Table 5.4: Ice material properties.

Property	Material
Density [$\mathrm{kg\,m^{-3}}$] (ρ)	5mm - 1023 10mm - 953 15mm - 1037 20mm - 916
Young's Modulus [GPa] (E)	9.38
Poisson's Ratio (ν)	0.33
Tensile failure pressure [MPa]	0.517
Quasi-static yield strength [MPa]	5.2
Rate dependent yield strength	Tabular input [3]

As part of the ice material model, an equation of state had to be included through *EOS TABULATED COMPACTION. Here the pressure is related to the volume and the temperature of the material, with values taken from Carney *et al.* [23].

5.4 Control and Additional LS-DYNA Considerations

5.4.1 Termination and Timestep

For impact events that involve high strain rates, there is a likelihood that the default time step of LS-DYNA ® will be too high to ensure stability. The scale factor TSSAFC will need to be reduced to a value of 0.6 or lower in these scenarios. A reduction in DTMIN might also be necessary to ensure the simulation does not stop when the time step falls below a minimum value. The termination time was selected to be 2.5 ms. Ideally this would be around 5 ms but the computational requirement for this increase would be much greater in magnitude. It was felt the majority of the impact behaviour would occur at the lower threshold.

5.4.2 Damping

LS DYNA can add damping to a system as part of either mass damping, good for damping out low-frequency system-level oscillations or stiffness/structural damping, which is more suited to higher-frequency oscillations. Stiffness damping is an inherent property of most materials but a stiffness coefficient of 0.1 is recommended for the composite part in order to remove excess noise. No damping is included in solid element formulation, so mass damping is recommended [125]. According to the support site [129], there are no shortcuts to producing good agreement to observed loss in a test. A good judgement and a trial-and-error approach in order to tune the numerical damping was the only suggestion. *DAMPING RELATIVE was selected for all solid parts, apart from the SPH elements, as all the parts are connected. The motion was selected to be damped out relative to the rigid body of the support block. A critical damping coefficient of 2.5% was selected to apply at a frequency of 4000 Hz, taken from the experimental force measurements.

5.4.3 Contact

In order for separate or disjointed parts to interact with each other in LS DYNA, contact between them needs to be defined. The focus is primarily with the hailstone interaction with the composite but in order to authenticate the experimental regime, contact that enables forces to be experienced by the clamping arrangement and transferred to the force transducer (to be measured), is also required. Contact in LS-DYNA is defined by identifying whether a "slave" node as penetrated a "master" segment. A contact algorithm will search every time step for potential penetrations

Contact is connected by referencing geometry, in the form of a master/slave inter-

action. Simple referencing can be achieved through Part ID's or collectively as Part ID sets. If specific features of geometry are of importance, distinct nodes or segments can be selected. Certain sections and contact types are better suited to specific references. Contact occurs when one segment of the outer surface of an interface (the slave) penetrates another (the master). Contact types are broadly split between those that impact or move against each other and those that are tied together. For the case of the hailstone sphere constituting of SPH nodes upon a composite surface, contact of the form *NODES TO SURFACE was the ideal choice. Whereas *SURFACE TO SURFACE for the solid body interactions was more applicable. *CONTACT ERODING NODES TO SURFACE was chosen for the hailstone, which enables failure of elements based on material criteria. SPH particles have no associated contact thickness. The recommended way to define the particle contact thickness was to use the SST parameter in the associated *CONTACT keyword. A value of 1mm was selected. The Viscous Damping Coefficient (VDC) is frequently used in contact interface definitions to damp out oscillations normal to the contact segment. Similar to suggestions by Keegan [60], a value of 60% was selected. A soft constraint option card (i.e SOFT=1) was chosen for improved interaction of two dissimilar materials. To secure the composite to the clamp, the *CONSTRAINED EXTRA NODES command was selected, with the appropriate composite nodes added to the rigid body of the clamp. Here the forces from hailstone impact are transferred but computational time is saved by not using the standard *CONTACT keyword. The connection between the force transducer and support block is modelled in the same way, with the support block utilised as the rigid body in the case. The force of interest is the clamp upon the force transducer and so a *CONTACT keyword is necessary in this case, in order for the force-time history to be recorded. Here *CONTACT TIED SURFACE TO SURFACE OFFSET is utilised. The "offset" section of the keyword makes the contact suitable for rigid body connections. Segments along the interacting faces of each part are chosen as connecting geometry, with the force transducer the master surface.

5.4.4 Hourglass

One of the key considerations involved in finite element analysis is hourglass control. Hourglass modes are non-physical modes of deformation that occur in under-integrated elements, such as solid elements with a single integration point or Shell or Tshell elements with a single in-plane integration point. One direct solution to under-integration would be to have more elements along the length of the cylindrical mesh geometry of each composite layer. However, this would increase the total number of elements and thus the computational time. Another option would be to use tetrahedron and trian-

gular elements but these are generally not recommended due to "locking", whereby the displacements calculated by the finite element method are orders of magnitude less than expected. The most common types are pressure, when elements are subject to bending or shear locking, when the material is incompressible. The method most commonly used is the application internal forces to elements susceptible to hourglass modes, in order to resist hourglass deformation. Hourglass formulation can be set in either a part specific or a global context. The energy required for these forces to perform work is taken away from the total energy of the system. There are several different algorithms available in LS-DYNA ® for the computation of these forces which can be broken up into two main categories. Viscous forms generate hourglass forces proportional to nodal velocities that contribute to hourglass modes. Whereas stiffness forms generate them with respect to nodal displacements. The former is suited to high velocity/strain rate scenarios and the latter to lower rate simulations. Viscous forms can only inhibit additional hourglassing, whereas stiffness forms are able to reduce the overall system hourglassing, including previously accumulated hourglass deformation. One drawback of stiffness control is that it can artificially stiffen the response of contact. Therefore, it is usually appropriate to assign a lower value of hourglass coefficient to minimise this effect. With "high-velocity" not strictly defined and the many different options existing within these categories, it can be difficult to ascertain the ideal criteria. To evaluate a certain choice, the hourglass energy should be computed and included in the overall energy balance by setting HGEN=2 in *CONTROL ENERGY and paying attention to the hourglass energy levels with respect to the total internal energy over the course of the simulation. The rule of thumb is that if the ratio should be less 10% or preferably 5% otherwise the results are deemed unreliable. This can be analysed using ASCII files from the *DATABASE OPTION in terms of the overall system (GLSTAT) or on a by-part basis (MATSUM). Moderate to extreme hourglassing would only be acceptable in parts of coarse mesh away from the primary area of interest. Viscous hourglass algorithms, IHQ=2 - "Flanagan-Belytschko integration and IHQ=3 - "Flanagan-Belytschko with exact volume integration" with a QH coefficient of 0.1, were trialled first with similar results. Figure 1.8 shows the overall system hourglass and total internal energy of the largest hailstone, 20 mm in diameter, at the highest average velocity impact of $87\,\mathrm{m\,s^{-1}}$ for both algorithms. It was thought this would be the experimental scenario where hourglassing would be most prominent. The ratio of hourglass to internal energy is also displayed for the y-axis on the right hand side. Straight away there appears to be an issue for the viscous forms, with the hourglass energy following the trend of internal energy quite closely at first, resulting in a maximum ratio of over 0.8, after which both levels appear to stabilise around 0.65.

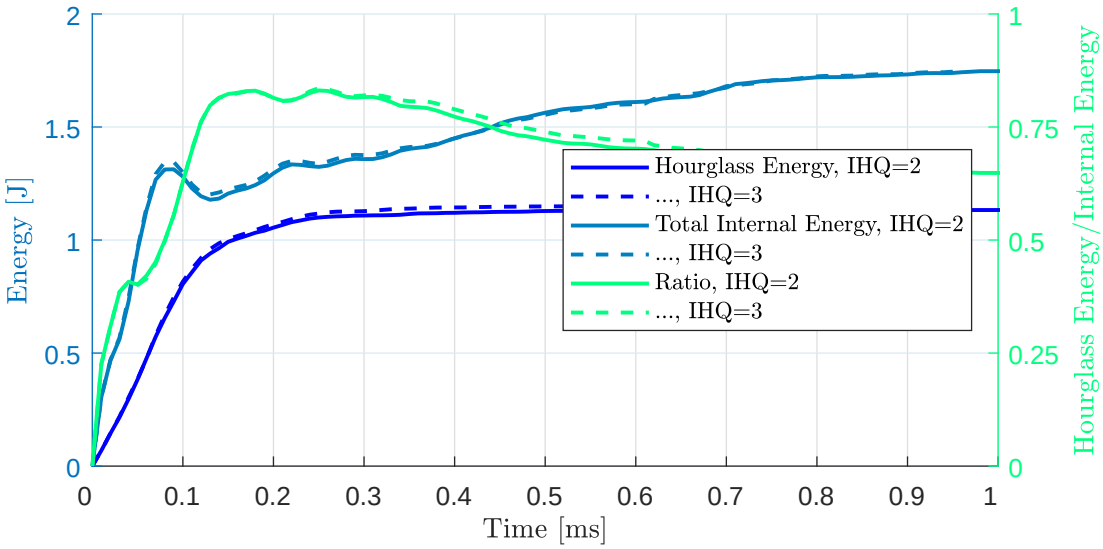

Figure 5.8: System internal energy, hourglass energy and the respective ratios for viscous hourglass algorithms (IHQ=2, IHQ=3).

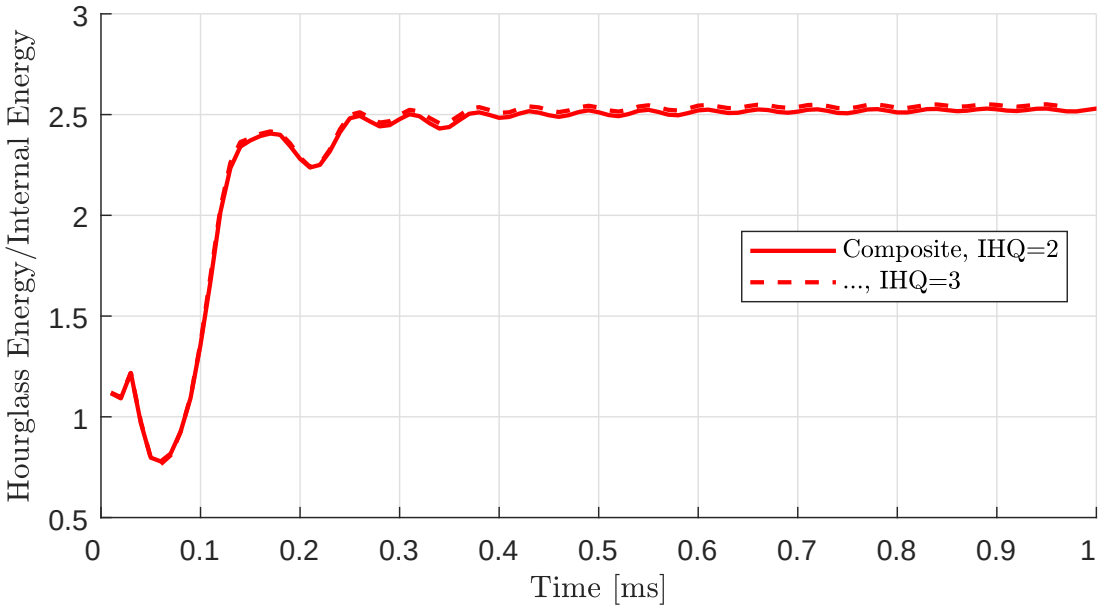

Figure 5.9: Part internal energy/hourglass energy ratios for viscous hourglass algorithms (IHQ=2, IHQ=3).

For closer inspection, the influence of the hourglass energy ratios was examined for each part, displayed in Figure 5.9. Only the composite part was found to have visible hourglassing. Upon convergence, the hourglass energy for this part is roughly 250% greater than the internal energy, raising definite concerns of the validity of any results. Stiffness approaches were utilised next, with the chosen algorithms IHQ=4, IHQ=5 the stiffness forms of IHQ=2 and IHQ=3. IHQ=6 is stated to be "Belytschko-Bindeman assumed strain co-rotational stiffness form for 2D and 3D solid elements only". Reduced hourglass coefficients of QH=0.03 were employed for each method. The overall energies can be seen in Figure 5.10. The difference in hourglass energy is immediately apparent, resulting in a much improved converged ratio of less than 5% for all three algorthims. The ratios for the various parts can be inspected in Figure 5.11. Here the variance amongst the stiffness algorithms is visible. Following this short study, it was decided a stiffness hourglass algorithm would be utilised. The algorithm, IHQ=6, was chosen as it had the best performance when analysing the composite part.

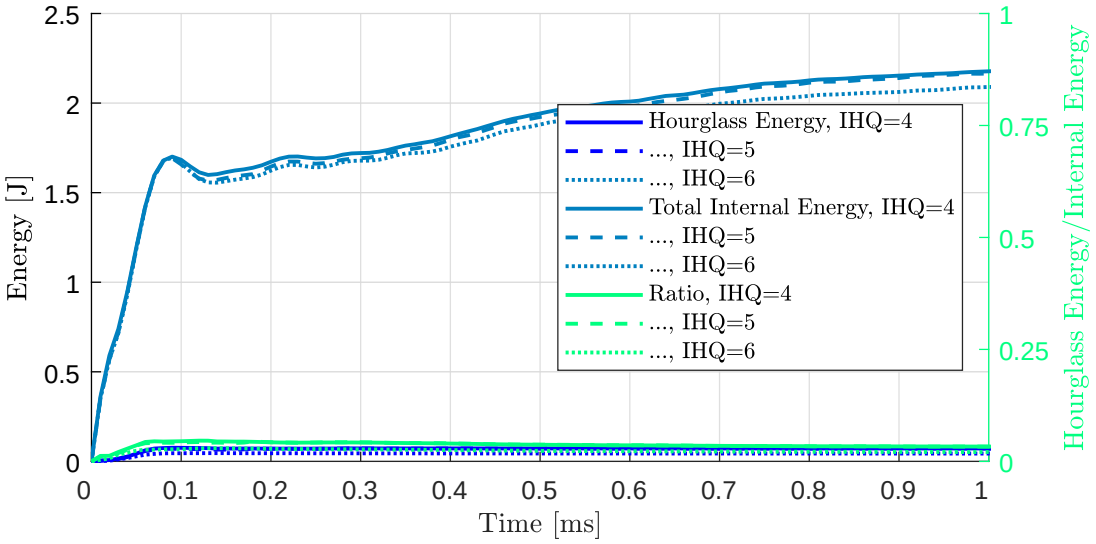

Figure 5.10: System internal energy, hourglass energy and the respective ratios for stiffness hourglass algorithms (IHQ=4, IHQ=5, IHQ=6).

5.4.5 Gravity

Initially the presence of gravitational forces was considered to influence the force measurements and the motion of the SPH particle spread and was included for comparison. The effects of gravity can be simulated in LS-DYNA in the following explicit manner. A 'positive' accelerative constant of $9.806\,55\,\mathrm{m\,s^{-2}}$ was defined in *LOAD BODY Z to represent gravitational force in the 'negative' z direction. Pre-loading the simulation

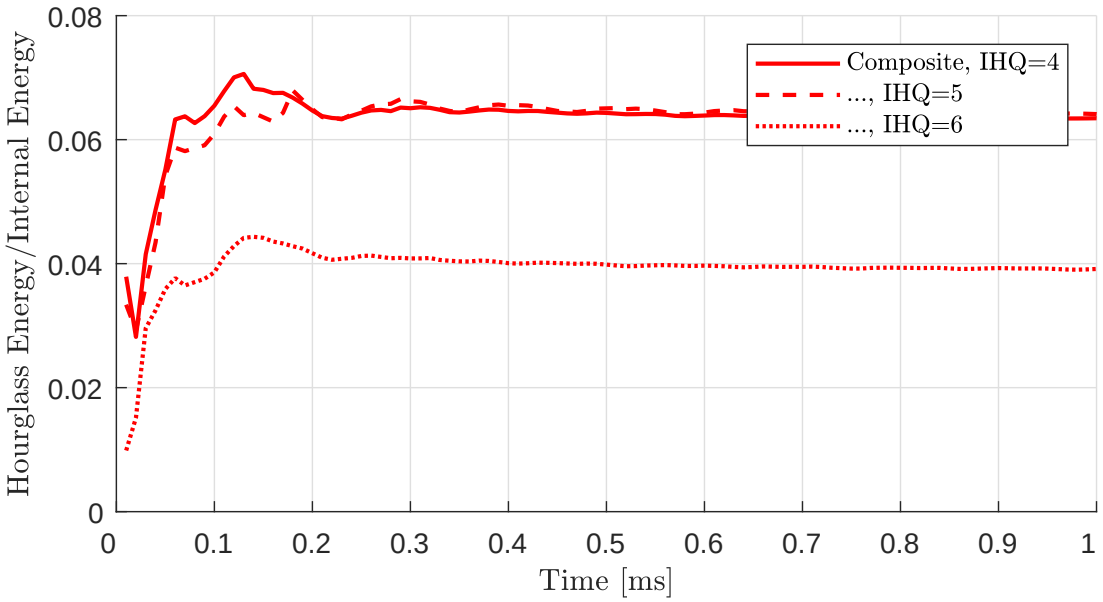

Figure 5.11: Part internal energy/hourglass energy ratios for stiffness hourglass algorithms (IHQ=4, IHQ=5, IHQ=6).

with gravity can be accomplished by either an explicit or implicit dynamic relaxation analysis. Two curves of gravity acceleration are assigned to *LOAD BODY Z. One designation (LCID) set a constant gravity acceleration to take place over only the transient phase. In the other (LCIDDR), the gravitational acceleration was ramped linearly from zero to the constant value over a very short period of time, over only the dynamic relaxation phase. Mass damping is also invoked only for the early portion of an explicit dynamic analysis in order to reduce the oscillations caused by the gravitational load, then removed. The dynamic relaxation phase took place before the regular transient loading, whereby the distortional kinetic energy was monitored and once it reached a sufficiently low level (in this case a convergence tolerance of 0.01), the dynamic relaxation phase terminated and the simulation proceeded to the transient analysis phase. The distortional kinetic energy and tolerance over this transient stage can be viewed in Figure 5.12.

The differences in force, stress distribution were minor, with no obvious changes in SPH particle spread. However, the additional computational time was noteworthy and for these reasons the analysis was performed without the presence of gravity.

5.4.6 Mesh Refinement

For this study, the contact of interest is between the SPH form of the hailstone and the composite part. Therefore for the purpose of this study, the model was simplified to

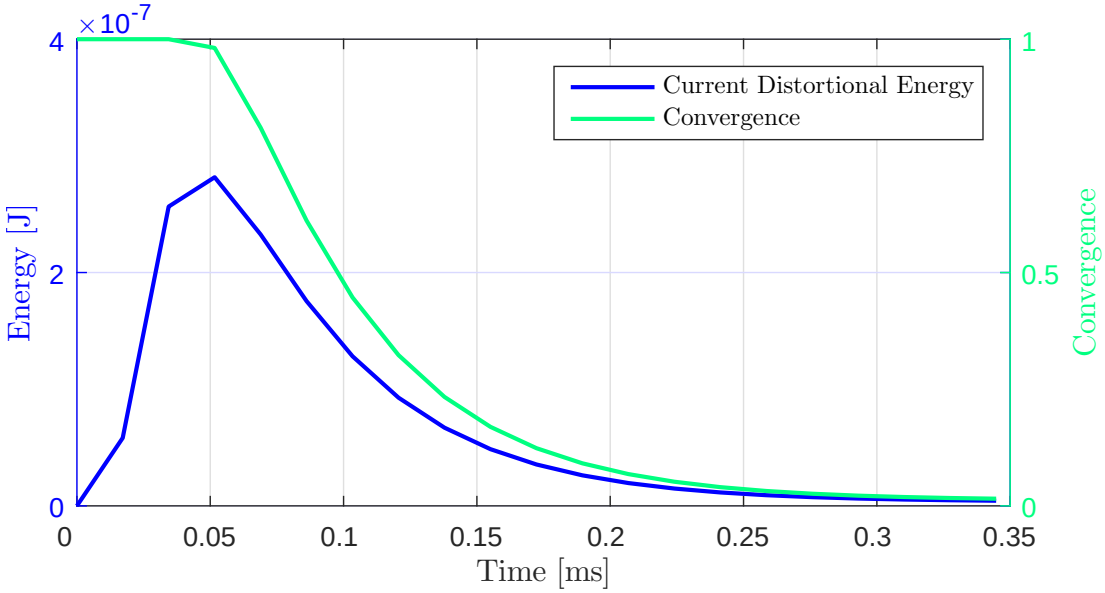

Figure 5.12: Distortional kinetic energy and convergence factor during dynamic relaxation phase.

just increased these two parts. Five different variants of mesh, with their mesh details and associated computational time described in Table 5.5. It should be noted that the times associated with would be markedly and proportionally increased for the full simulation model. Although all diameters of SHI were tested, the 5 mm diameter case was of greatest interest, with contact between the composite and hailstone confined to a smaller area. This was carried out for an initial hailstone velocity of $100\,\mathrm{m\,s^{-1}}$.

Table 5.5: Mesh computational times.

Selection	Density			Time
	Radial	Perimeter	Thickness	
1	12	12	2	12 min
2	26	26	3	13 min
3	50	50	6	14 min
4	100	100	12	42 min
5	200	200	24	402 min

The contact force on the composite by the hailstone for the different selections of mesh is displayed in Figures 5.13 and 5.14. The finest mesh, "Selection 5" is displayed on both figures. The differences between the force profiles of hte relatively coarse meshes of Selections 1 and 2 compared with Selection 5 are immediately apparent, with large deviations and spikes observable in Figure 5.13. Selections 3 and 4 show a much closer resemblance to the force profile exhibited by the finest mesh, shown in Figure 5.14.

When examining the animation of impact in the D3PLOT file, there were examples of missed contact for Selections 1 and 2.

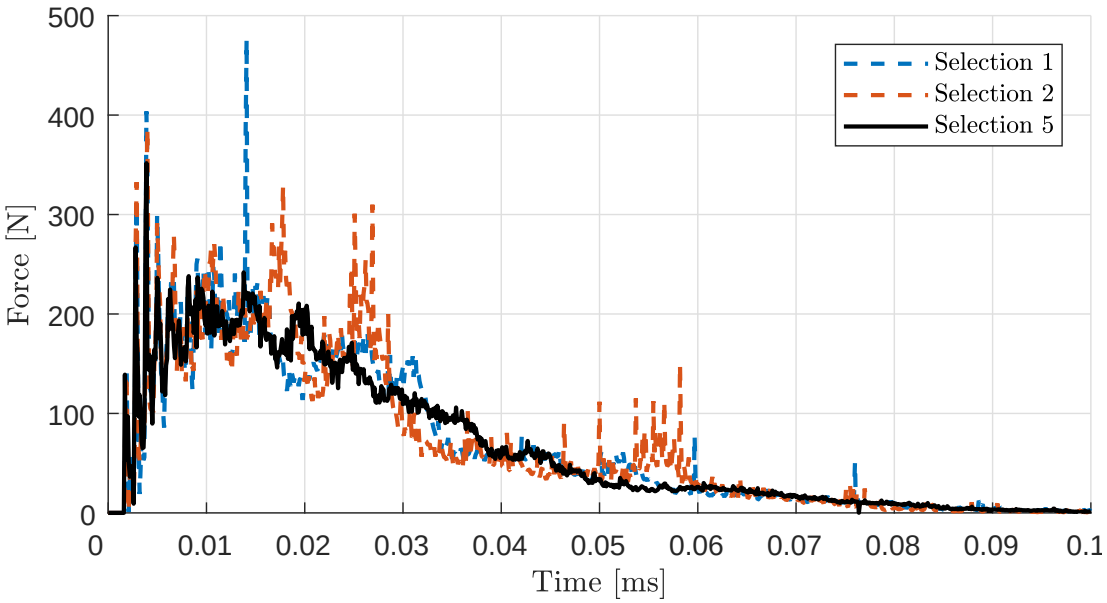

Figure 5.13: Contact force between composite and hailstone shown for coarser mesh generations (Selections 1 and 2) the converged profile (Selection 5).

When taking all these aspects into consideration, it was decided that Selection 3 would offer both a close-to converged solution and a less computationally taxing geometry. Therefore it was chosen for use in the full model .

5.5 Model Calibration

Before inspecting the computational damage, the force developments would be compared and validated against the experimental measurements. This was carried out for each of the SHI diameters (5 mm, 10 mm, 15 mm and 20 mm) at their lowest and highest mean velocities measured experimentally. Force histories for each contact were obtained by enabling RCFORC in *DATABASE ASCII OPTION at a output time interval of 1×10^{-7} s. The force output from the *CONTACT TIED SURFACE TO SURFACE between the clamp and force transducer was used as the comparison. This was evaluated against the mean measured force profile in each case but also the nearest "actual" experimental force profile, determined by minimum root mean squared error. The comparisons for the lowest and highest mean velocity at each velocity are displayed below. The Roisman & Tropea relation [30] is also included for reference. For the lowest mean velocities, the 10 mm and 15 mm versions in Figures 5.16 and 5.17

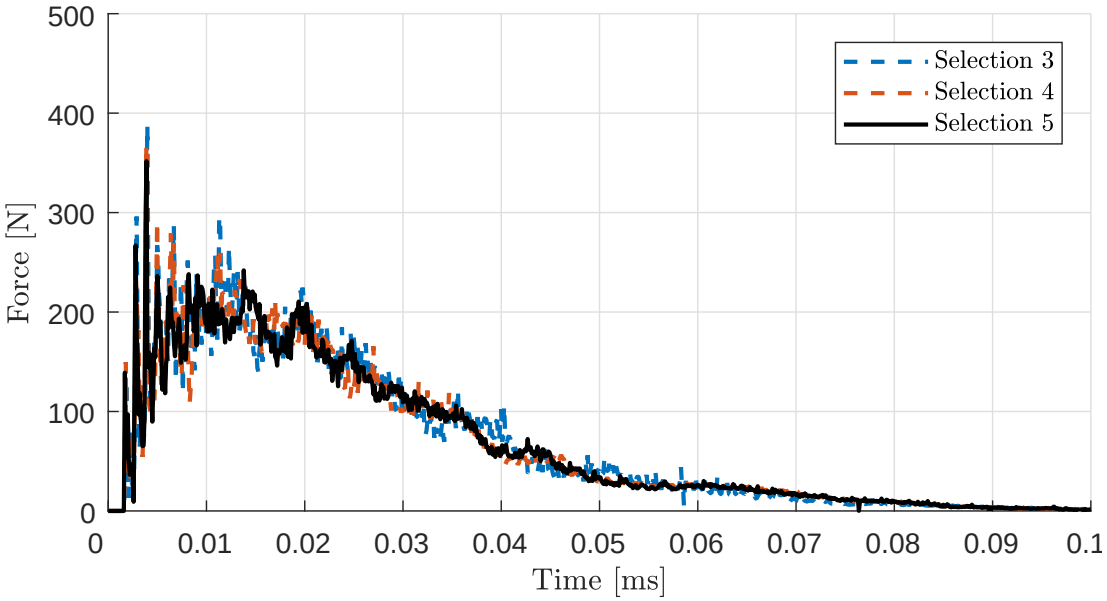

Figure 5.14: Contact force between composite and hailstone shown for finer mesh generations (Selections 3 and 4) the converged profile (Selection 5).

compared best with the smooth force measurements from the experiments. In all cases the amplitude of later force peaks were perhaps not as damped as the experimental data but adding additional damping to the simulation would have also diminished the initial peaks. This region was felt to be more important to replicate, as this would be when the majority of damage would occur. The 20 mm profile in Figure 5.18 matched fairly well to the example experimental profile. However, the first peak of the mean experimental profile was a lot larger. The forces generated by the 5 mm simulation in Figure 5.15 are notably greater than the measured counterparts across the profile, again hinting that the constitution and behaviour of the smallest diameter SHI in the experiments have been affected by the environmental temperature.

The simulations for the highest mean velocities were less comparable to the experimental examples. The 10 mm variant was still the closest performing, as shown in Figure 1.18, where the behaviour of the experimental profiles was damped more abruptly after 0.8 ms. The initial peak of the 15 mm simulated profile in Figure 1.19 was notably greater than both the experimental counterparts and the Roisman & Tropea relation. The subsequent second and third simulation peaks are not represented experimentally and the overall trend did not coincide until close to 1.5 ms. Despite the spikes observed in measurement, the 20 mm case in Figure 1.20 was a closer resemblance to an example experimental profile, although this was performed at a markedly lower velocity than the other sizes. Again the second and third simulation peaks are not

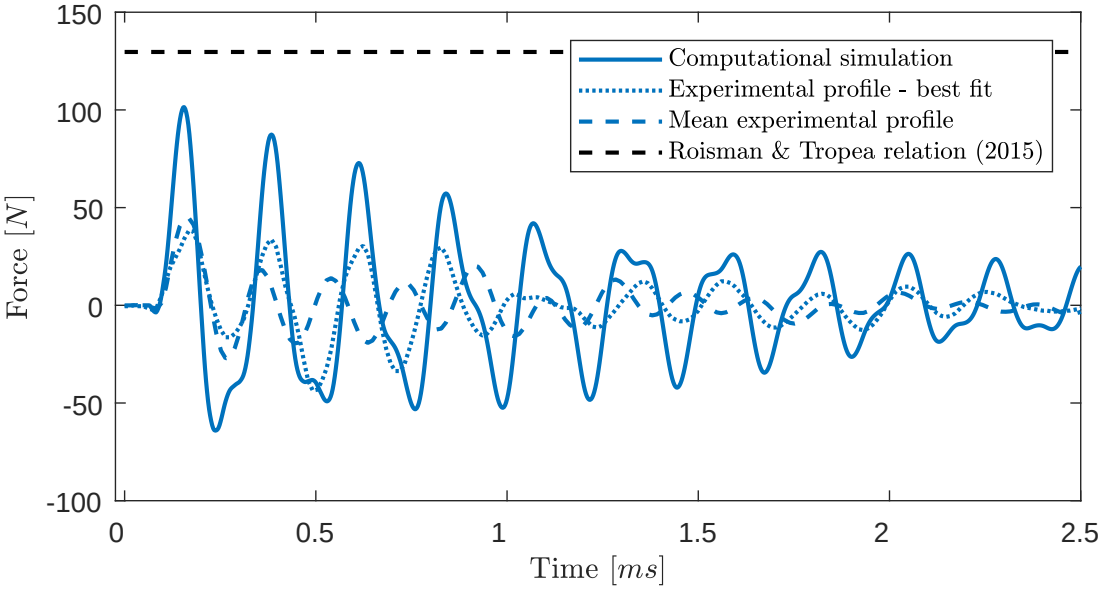

Figure 5.15: Simulated force profile for a 5 mm hailstone at 49.6 m s^{-1} and experimental counterparts.

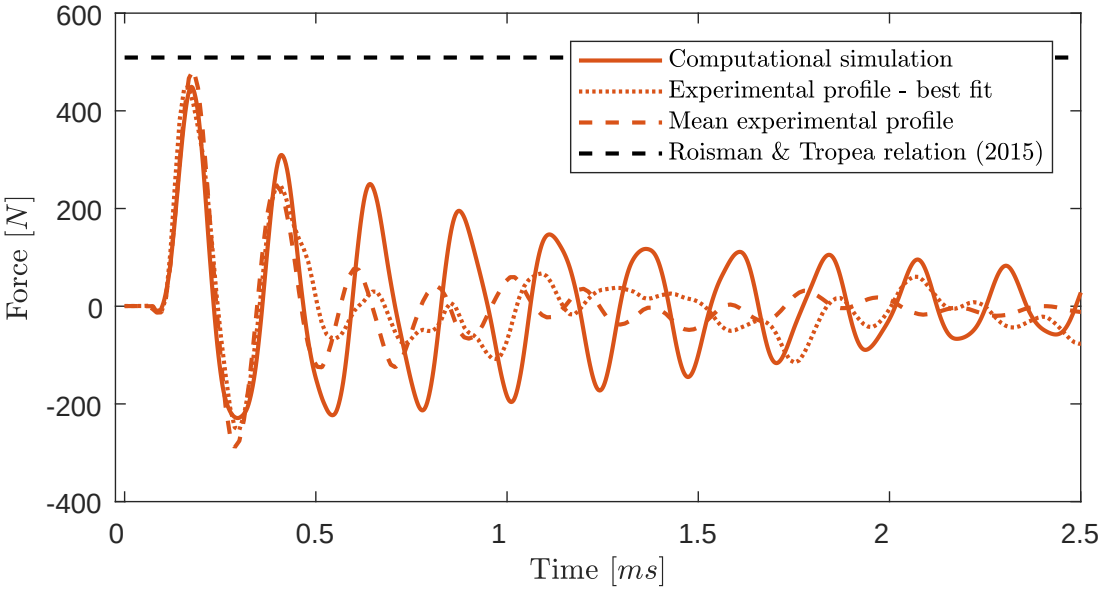

Figure 5.16: Simulated force profile for a 10 mm hailstone at 50.7 m s^{-1} and experimental counterparts.

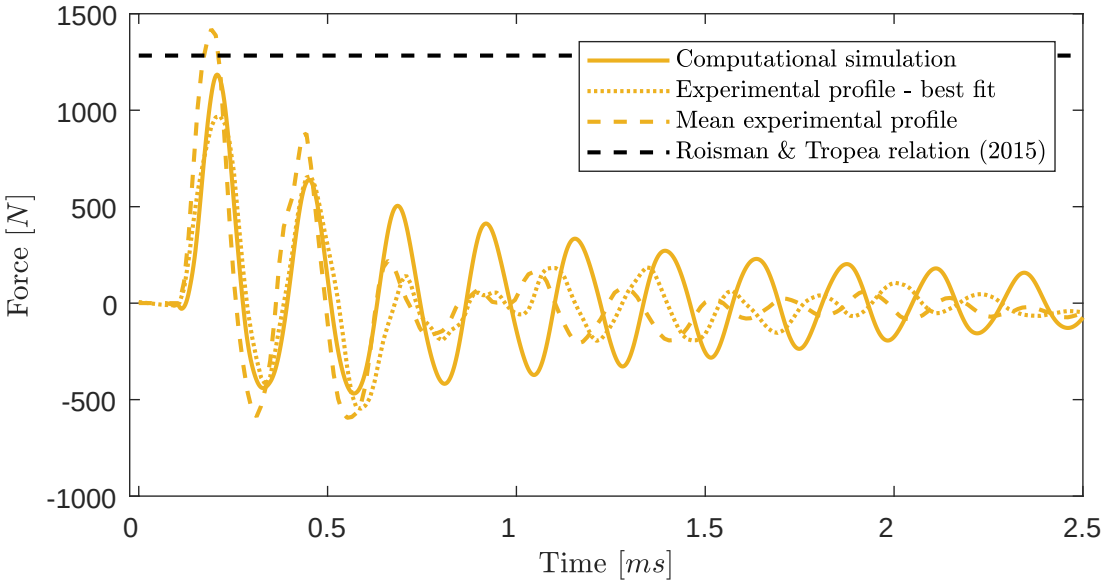

Figure 5.17: Simulated force profile for a 15 mm hailstone at 53.0 m s^{-1} and experimental counterparts.

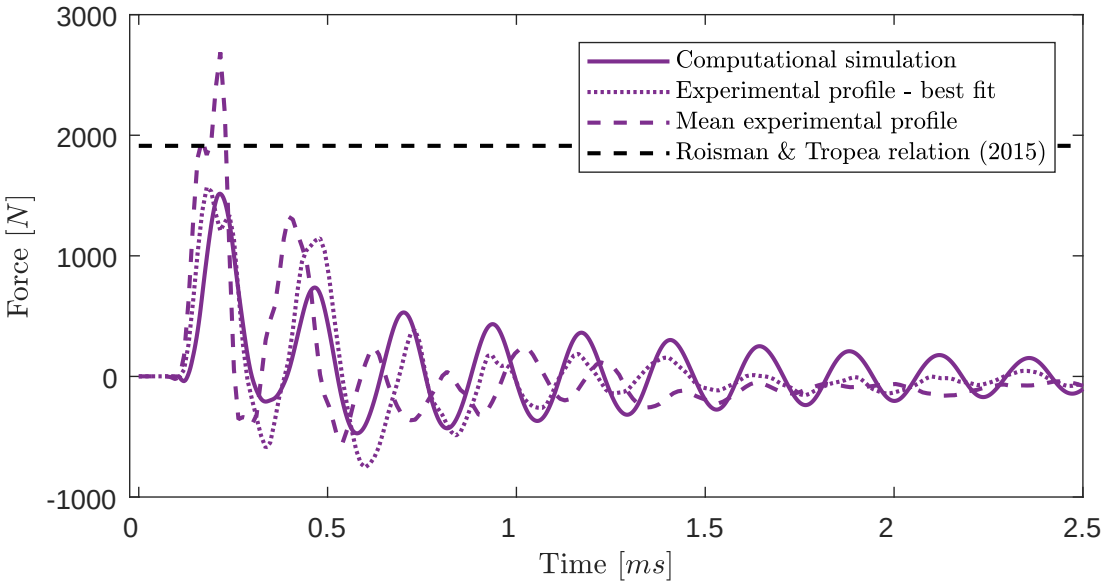

Figure 5.18: Simulated force profile for a 20 mm hailstone at 49.3 m s^{-1} and experimental counterparts.

represented in practice. The experimental force measurements of 5 mm seemed almost flat in comparison with the simulated force profile displayed in Figure 1.20. The initial maximum of 85 N from the example experimental reading was dwarfed by the peak of 242 N from the simulation and by subsequent positive (compressional force) peaks. The difference in the 5 mm profile compared with the other sizes of SHI was notable, particularly in terms of the shape of the negative (tension) peaks which appeared to consist of harmonic components.

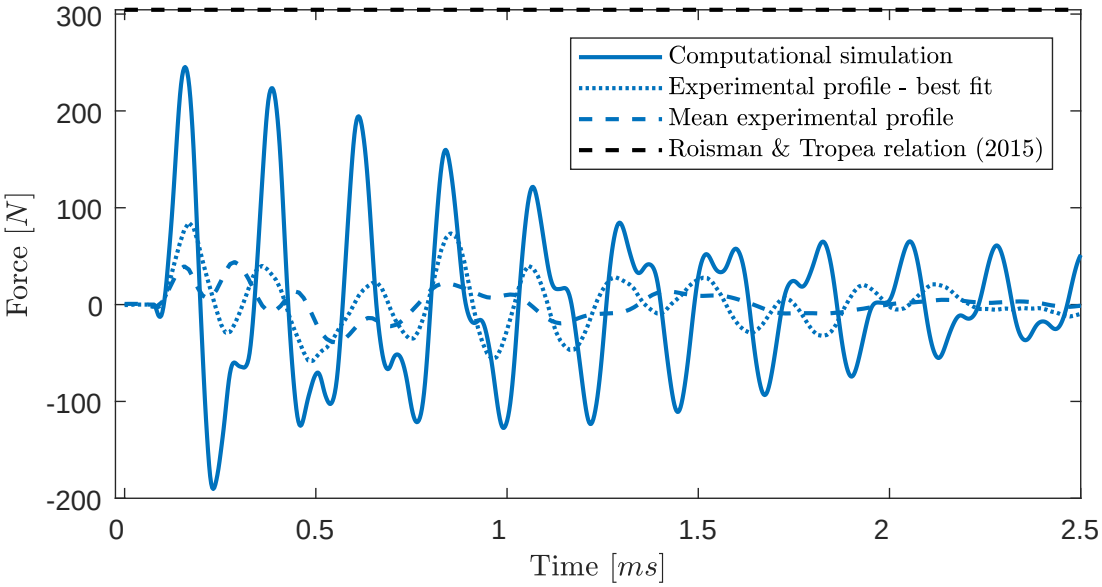

Figure 5.19: Simulated force profile for a 5 mm hailstone at 90.2 m s^{-1} and experimental counterparts.

The visualisations of the lowest velocity impacts for each hailstone impact were also analysed and compared to the high speed camera footage taken during the experimental investigation. Visualisations were created by enabling *DATABASE BINARY D3PLOT to be created at a time interval of 0.01 ms. The initial impact of all four hail diameters on the composite diameters, at approximately the same stage and at the highest mean experimental velocity, can be observed in Figure 5.23. In these images the clamp, support and force transducer have been removed for clarity. Apart from the obvious differences in size, there were only a few separate distinctions. There was some slight displacement of the bottom surface of the composite disc due to the compressional action, that increased with increasing SHI diameter. The 5 mm cases showed no visible distortion at all. In addition, the angle at which the majority of particles spread away from the impact area appeared to vary with diameter, with the 20 mm displaying more lateral jetting. This trend was difficult to verify against the low resolution and grainy high speed camera footage.

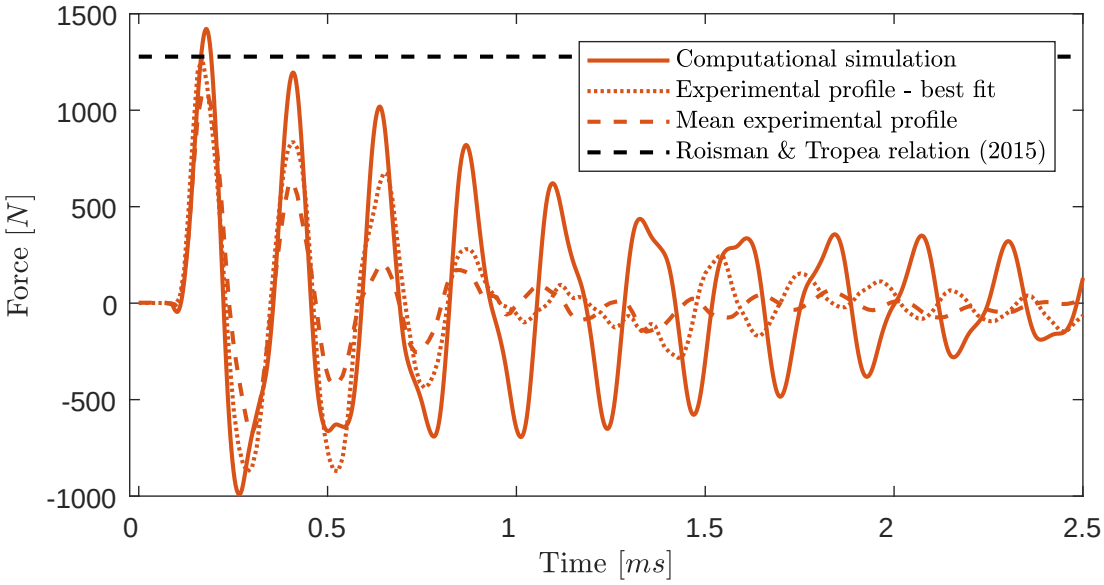

Figure 5.20: Simulated force profile for a 10 mm hailstone at 96.4 m s^{-1} and experimental counterparts.

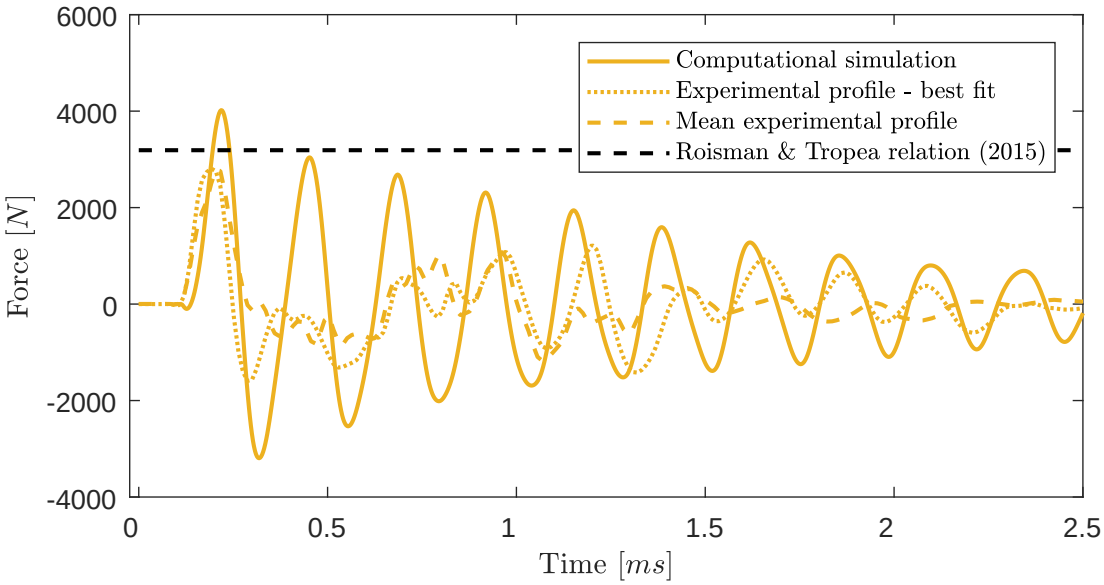

Figure 5.21: Simulated force profile for a 15 mm hailstone at 98.6 m s^{-1} and experimental counterparts.

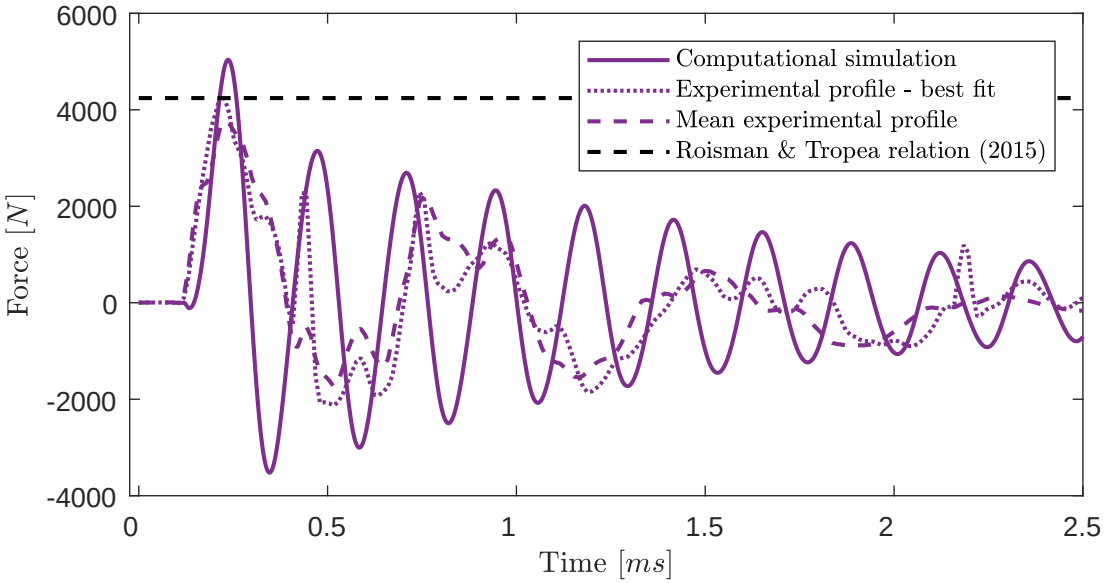

Figure 5.22: Simulated force profile for a 20 mm hailstone at 87.2 m s^{-1} and experimental counterparts.

The velocity of fragments after initial contact can be observed in Figure 5.24, demonstrating that the particles involved in lateral "jetting" are of a higher velocity than the initial vertical speed of the ice sphere.

The initial stress shockwave as described by Olsson and Juntikka [34] can also be viewed in Figure 1.23. The stress spread rapidly upwards in a "ring-like" outline, dissipating after reaching the top third of the spherical nodes.

5.6 Damage Analysis

The identification of damage from the interaction of hailstone on the composite was evaluated in separate ways. Firstly, as part of the D3PLOT, the Von-Mises Stress (or Effective Stress) can be observed to confirm when the material was yielding. The time-history of the composite element with the maximum Von-Mises stress was extracted for the lowest and highest mean velocities. The time history plots for the former can be examined in Figure 5.26. The peak stress value occurred before 0.1 ms for all four diameters, with increasing values of 5.28 MPa, 19.2 MPa, 51.2 MPa and 194 MPa for increasing diameter. The 5 mm, 10 mm, 15 mm curves then began to approach zero, with minor ripples less than 5 MPa observed after 0.5 ms. The 20 mm curve, however, seemed to converge towards 20 MPa, indicating that the element has undergone permanently yielding and damage has occurred.

The same plot for the highest mean velocities is shown in Figure 1.25. The difference

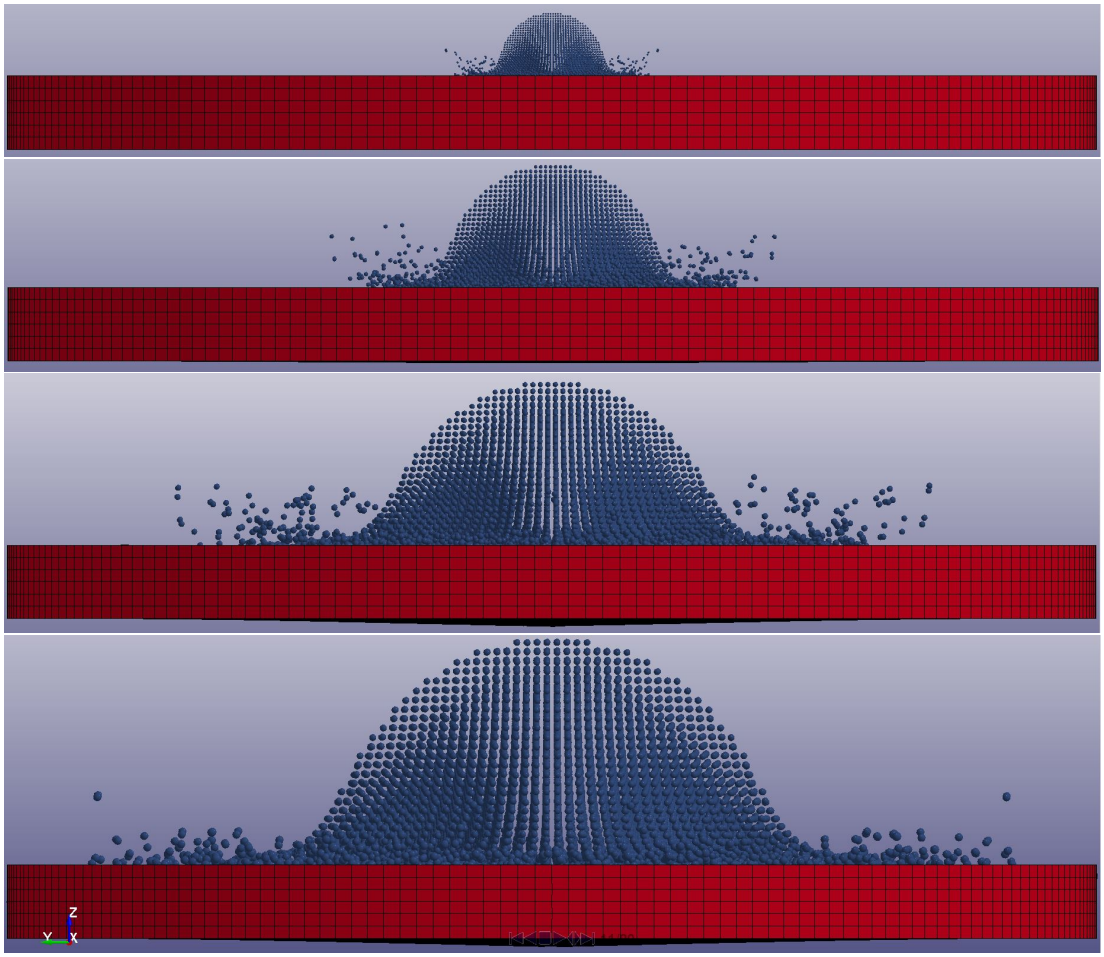

Figure 5.23: Visualisation of 5 mm, 10 mm, 15 mmand 20 mm simulated impact on a composite disc at the highest mean experimental velocities.

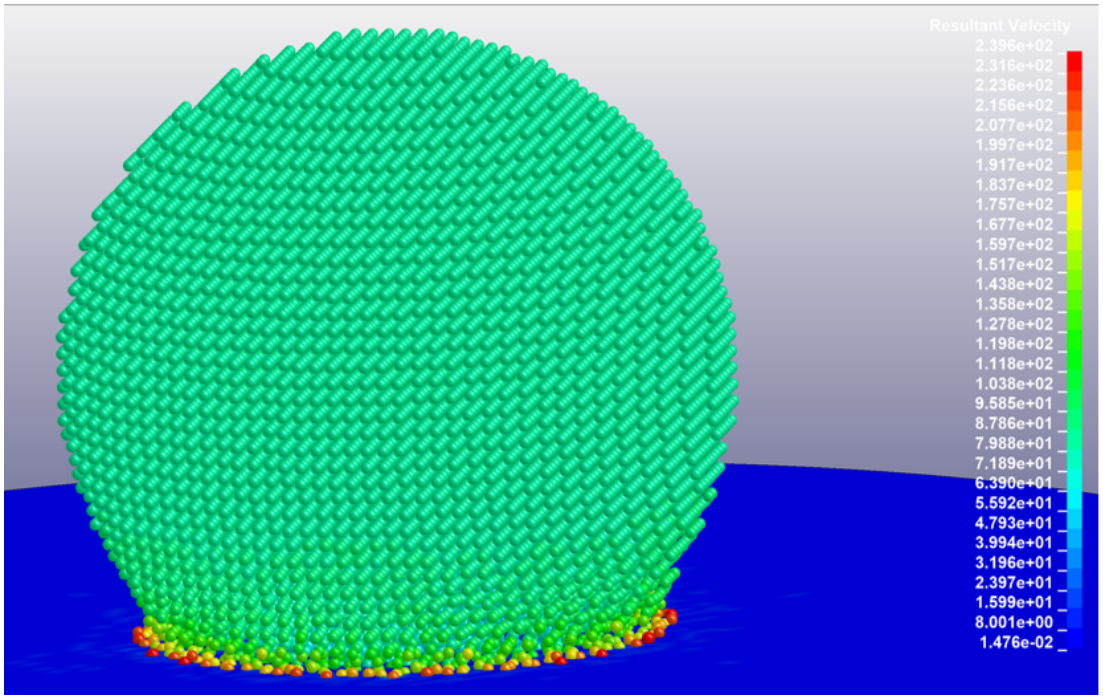

Figure 5.24: Velocities of individual SPH nodes upon contact of 20 mm hailstone with the composite disc (legend units in $\mathrm{m\,s^{-1}}$).

between the time histories of the larger 15 mm and 20 mm diameters compared with the smaller 5 mm and 10 mm diameters is observed immediately. Both the 15 mm and 20 mm quickly shot up to a large Von-Mises stress of around 250 MPa in less than 0.05 ms. Both then started to settle to just below this mark, with the 15 mm curve reaching a global maximum of 252.48 MPa and the corresponding 20 mm plot experiencing the greater value of 294.30 MPa. The 5 mm and 10 mm followed roughly the same trend as the previous figure, reaching maximum values of 12.42 MPa and 62.31 MPa respectively before moving towards zero, albeit at a gradual rate.

By assigning extra values in the *DATABASE EXTENT BINARY keyword, the four yield criteria of the Chang-Chang damage model in *MATERIAL 022 - COMPOSITE DAMAGE could also be observed in the D3PLOT visualisation. In the following figures the damage was inspected for each mode and displayed in images taken from above, below and an isometric view. The first row is the tensile fibre mode, the second the tensile matrix mode, the third the compressive matrix mode and finally the fourth row the delamination mode. When any failure has occurred, the non-failed elements were removed from the isometric projection. Here the colour contours range from blue (1-elastic) to red (0-failed), for a element to node averaging scheme.

The first case examined in Figure 5.28 is for a 20 mm diameter hailstone at a

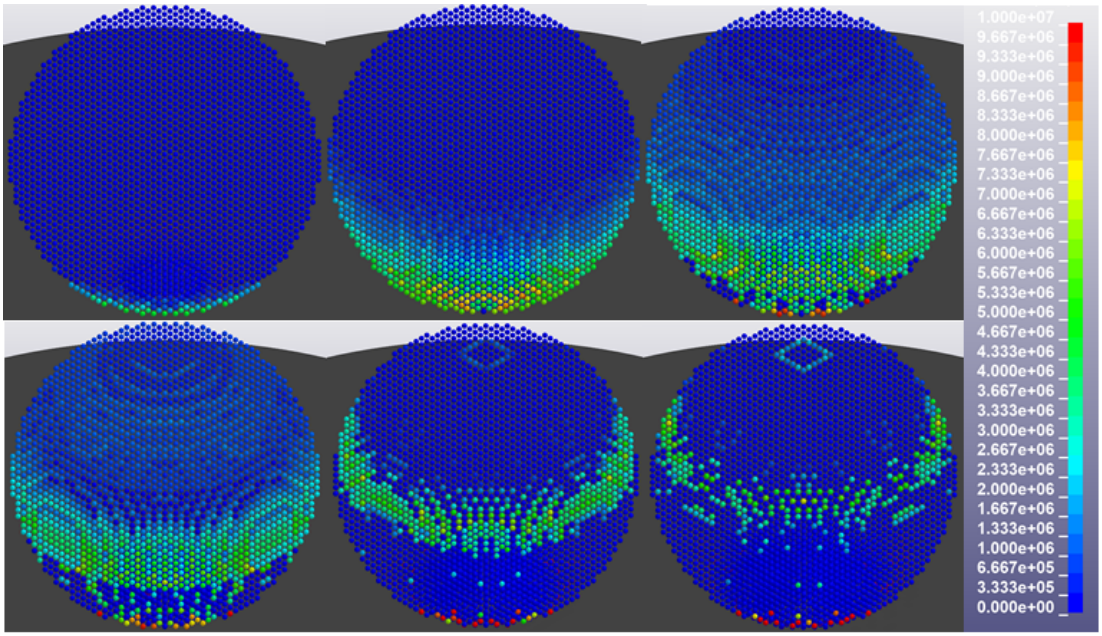

Figure 5.25: Stress contours in the form of a shockwave during simulated impact of 20 mm hailstone with an initial velocity of 87.2 $\mathrm{m\,s^{-1}}$ (legend units in Pa).

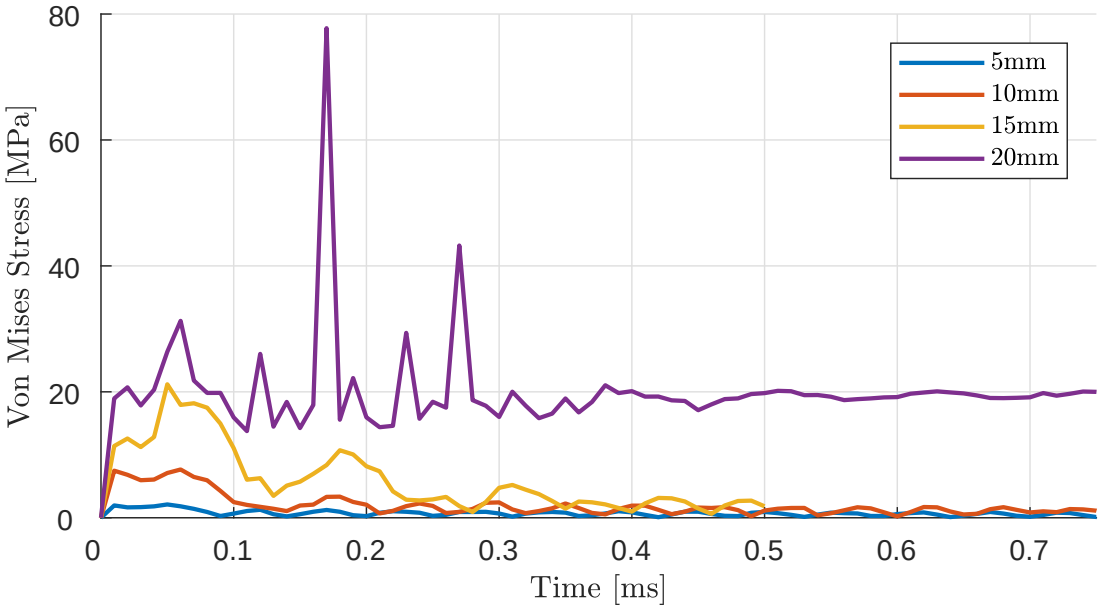

Figure 5.26: Von-Mises histories for the element of the composite experiencing the maximum stress for the lowest respective mean velocities for each diameter.

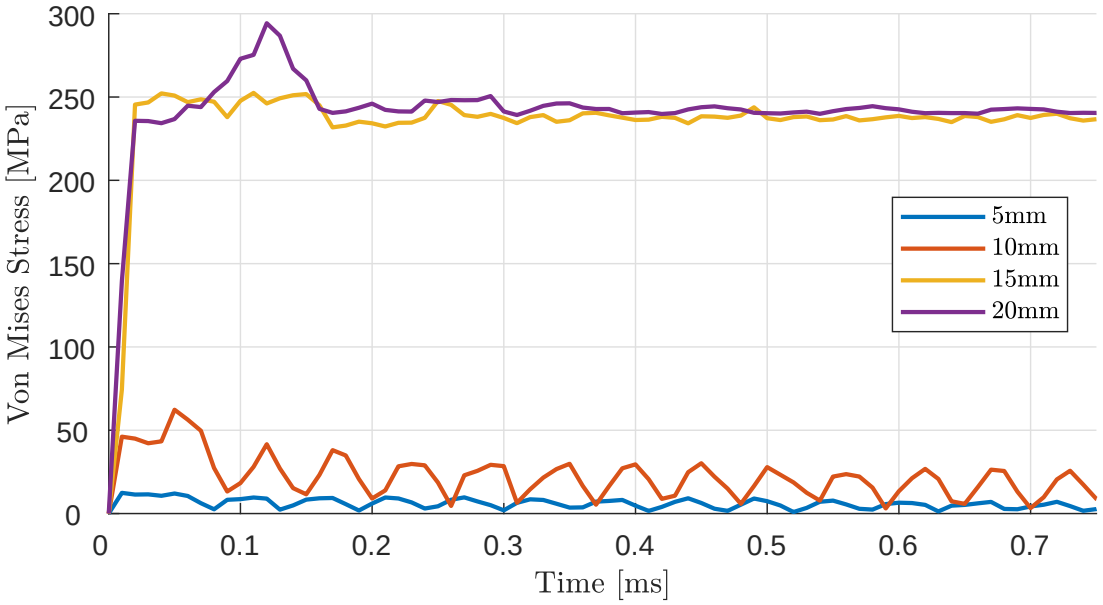

Figure 5.27: Von-Mises histories for the element of the composite experiencing the maximum stress for the highest respective mean velocities for each diameter.

velocity of $49.3\,\mathrm{m\,s^{-1}}$. No failure was found for the first three modes of failure. Only a smattering of delamination failure was found for a small number of elements at the very top of the composite.

The damage of the next investigated scenario, 15 mm at $98.6\,\mathrm{m\,s^{-1}}$, is more apparent in Figure 5.29. All four modes of failure are flagged, with visible damage on both the top and bottom surfaces of the, as well as through the composite disc. The emergence of tensile fibre (fibre-breakage) and tensile matrix (matrix-cracking) failure was found in the form of a long stip roughly 3/4 the length of the disc, with a very small amount of fully-failed elements due to matrix cracking centred on the bottom surface. Compressive matrix failure was the most obvious overall damage indicator with many red elements produced in a cigar-like formation, centred on the top and bottom surfaces. Scattered flags of element delamination were visible on the top surface, as well as the originations of damage in the aforementioned strip-like structure.

The damage from 20 mm hailstone impact at $87.2\,\mathrm{m\,s^{-1}}$ was slightly more severe and spread out than the previous case, displayed in Figure 1.28. The development of tensile fibre and matrix damage was again shown to occur in the form of a thin strip through the centre of the disc, predominately near the bottom surface. There existed a number of both fibre - and matrix tensile - failed elements centred on the top surface, roughly the diameter of the ice sphere. There was also some moderately damaged elements present around the perimeter of the disc, where the upper surface

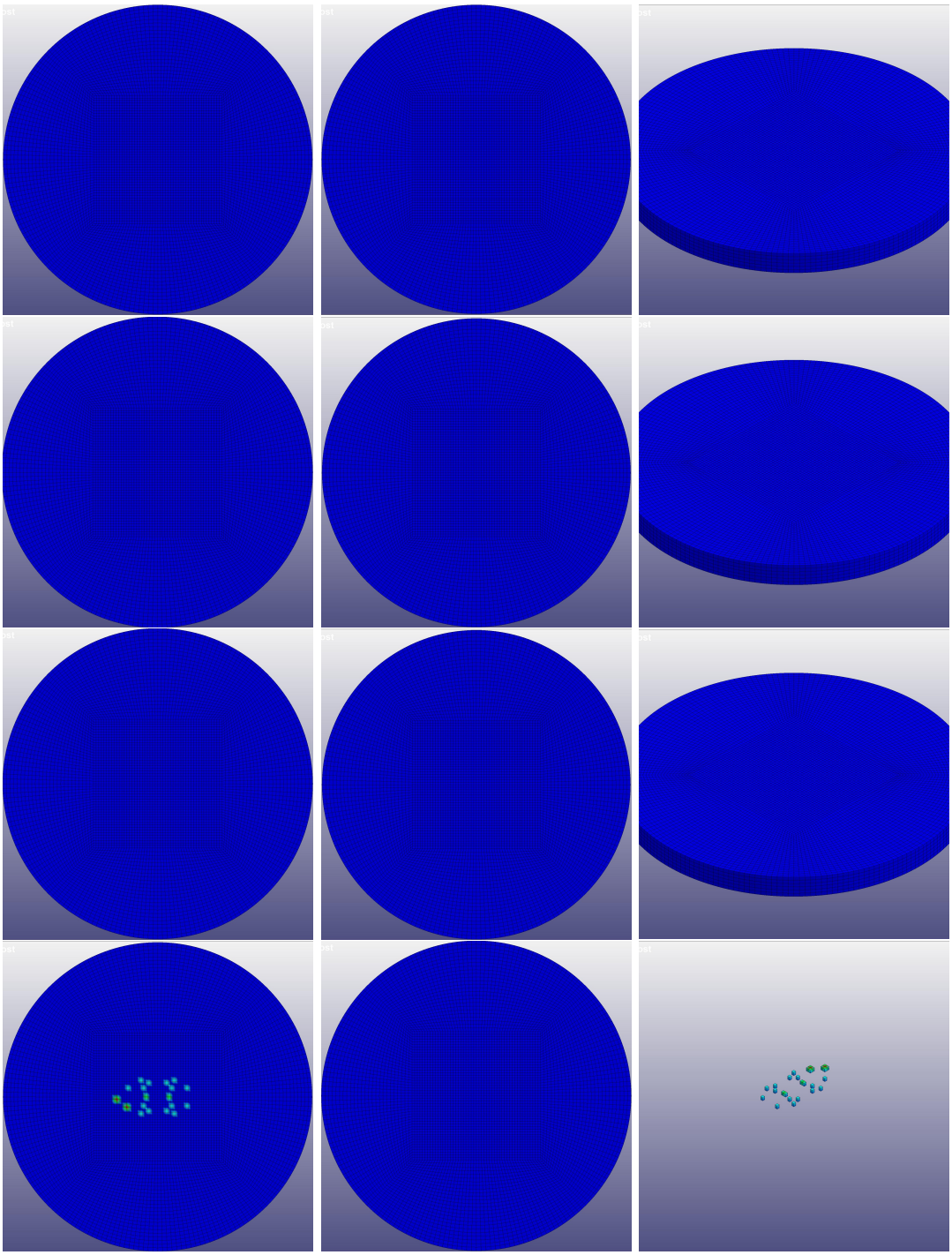

Figure 5.28: Failure flags for 20 mm composite impact at 49.3 $\mathrm{m\,s^{-1}}$ viewed from top, bottom and isometric perspectives (top row - fibre tensile failure, 2nd row - matrix tensile failure, 3rd row - matrix compressive failure, bottom row - delamination).

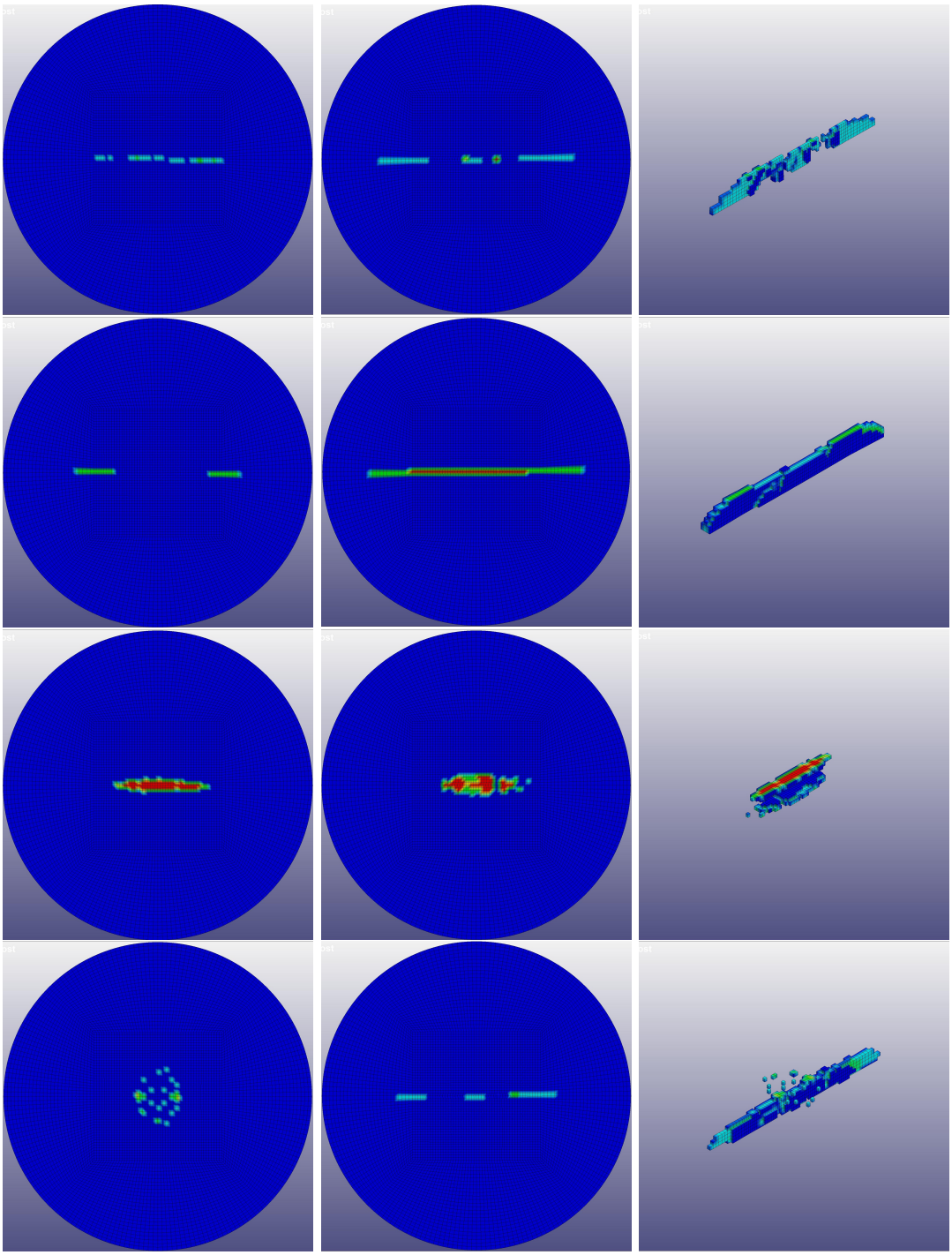

Figure 5.29: Failure flags for 15 mm composite impact at 98.6 $\mathrm{m\,s^{-1}}$ viewed from top, bottom and isometric perspectives (top row - fibre tensile failure, 2nd row - matrix tensile failure, 3rd row - matrix compressive failure, bottom row - delamination).

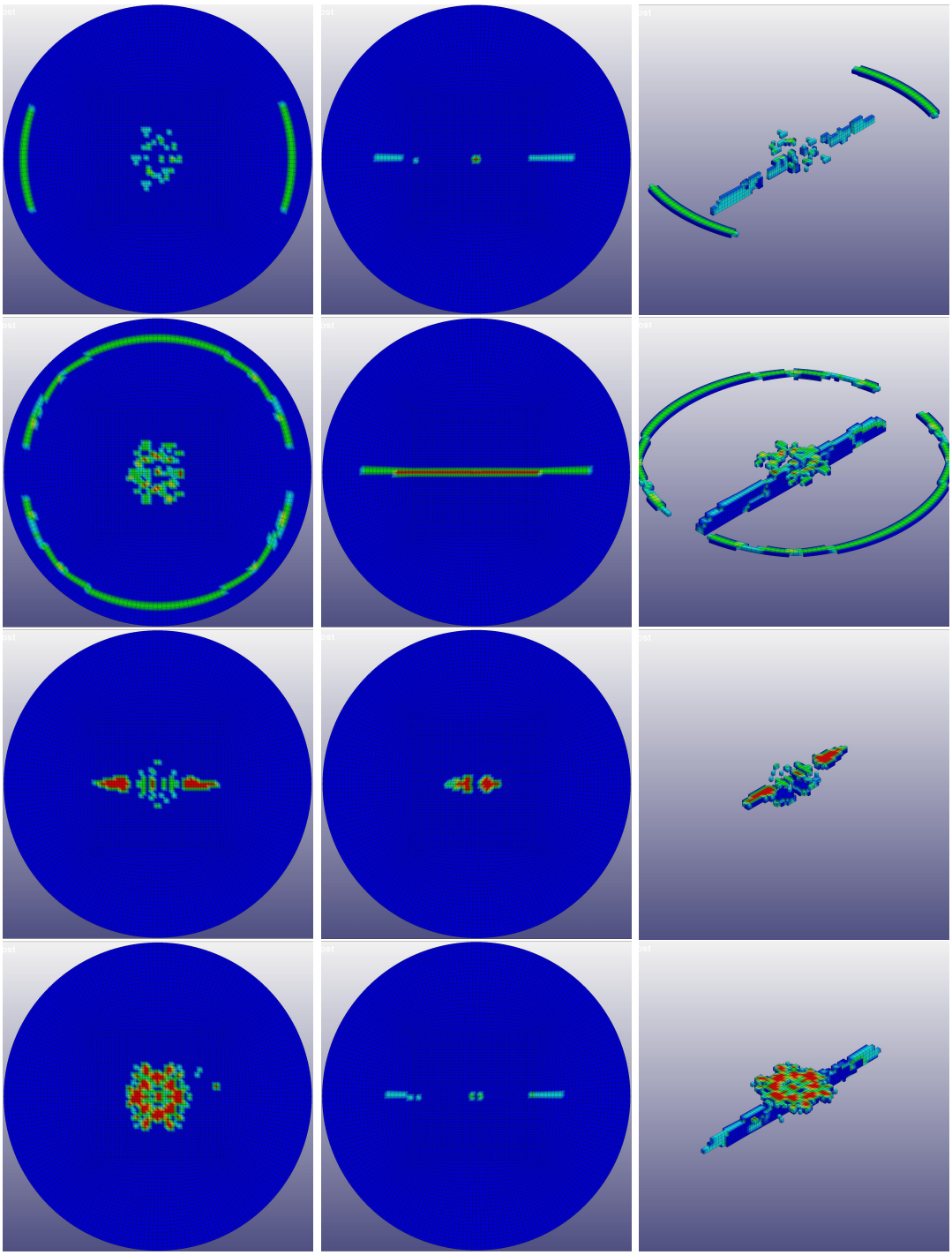

Figure 5.30: Failure flags for 20 mm composite impact at 87.2 $\mathrm{m\,s^{-1}}$ viewed from top, bottom and isometric perspectives (top row - fibre tensile failure, 2nd row - matrix tensile failure, 3rd row - matrix compressive failure, bottom row - delamination).

of the composite came into contact with the clamp. The compressive matrix failure was similar in severity to the 15 mm scenario but with a wider impression on the upper surface and less failure in the very centre. The compressive matrix failure on the bottom surface of the composite was fractionally less pronounced than for the smaller 15 mm hailstone fired at a higher speed. Delamination was noticeably more severe than Figure 1.27 with more fully-failed elements spread out on the centre of the upper surface.

The bottom surfaces of a selection of experimental composite discs were re-examined and example images are shown in Figure 5.31. There appeared to be some evidence of fibre damage for the samples used in the single impact of both 15 mm and 20 mm diameter SHI at high velocities, which was not observed in the low velocity counterparts. The damage exhibited was exacerbated in the multiple impact variants.

Following these damage inspections at velocities taken from the mean of experimental measurements, the simulations were repeated so that the predicted damage threshold energies and velocities for each diameter of hailstone could be determined, performed in step-sizes of $5\,\mathrm{m\,s^{-1}}$. The threshold was determined to be when the onset of damage was noticeable in any of the four modes of failure (i.e. a failure flag greater than zero), rather full failure of elements (failure flag = 1). The emergence of failure was assumed to indicate that through further impact, the form and appearance of damage would escalate. A plot of threshold velocities and associated initial kinetic energy taken from LS-DYNA is shown in Figure 5.32. The slightest amount of delamination for largest diameter hailstone (20 mm) was found to emerge at $35\,\mathrm{m\,s^{-1}}$. The 15 mm hailstone was found to experience this same mode of damage first at an increased velocity of $60\,\mathrm{m\,s^{-1}}$. The 10 mm diameter did not experience any damage until it experienced delamination failure in the centre of the top surface of the disc. This occurred at $120\,\mathrm{m\,s^{-1}}$, just outside the range of nominal tip speeds of wind turbines. The threshold velocity of the 5 mm case was much greater, with the slightest delamination damage, as well as strips of matrix - and fibre - tensile failure found on the bottom surface only at a velocity $260\,\mathrm{m\,s^{-1}}$. The figure displays notable differences in the failure threshold energy (FTE) for the the different diameters of hail. Both the 5 mm and 20 mm diameter cases had FTEs lower than 2.4 J, whereas the 10 mm and 15 mm variants experienced the onset of failure at around 3.6 J and 3.3 J respectively.

5.7 Discussion

As an investigation into repeated hailstone impact was not feasible using the finite element software, this computational analysis was always intended to be ancillary to the other chapters. However, the results offer some further insight to into low-diameter

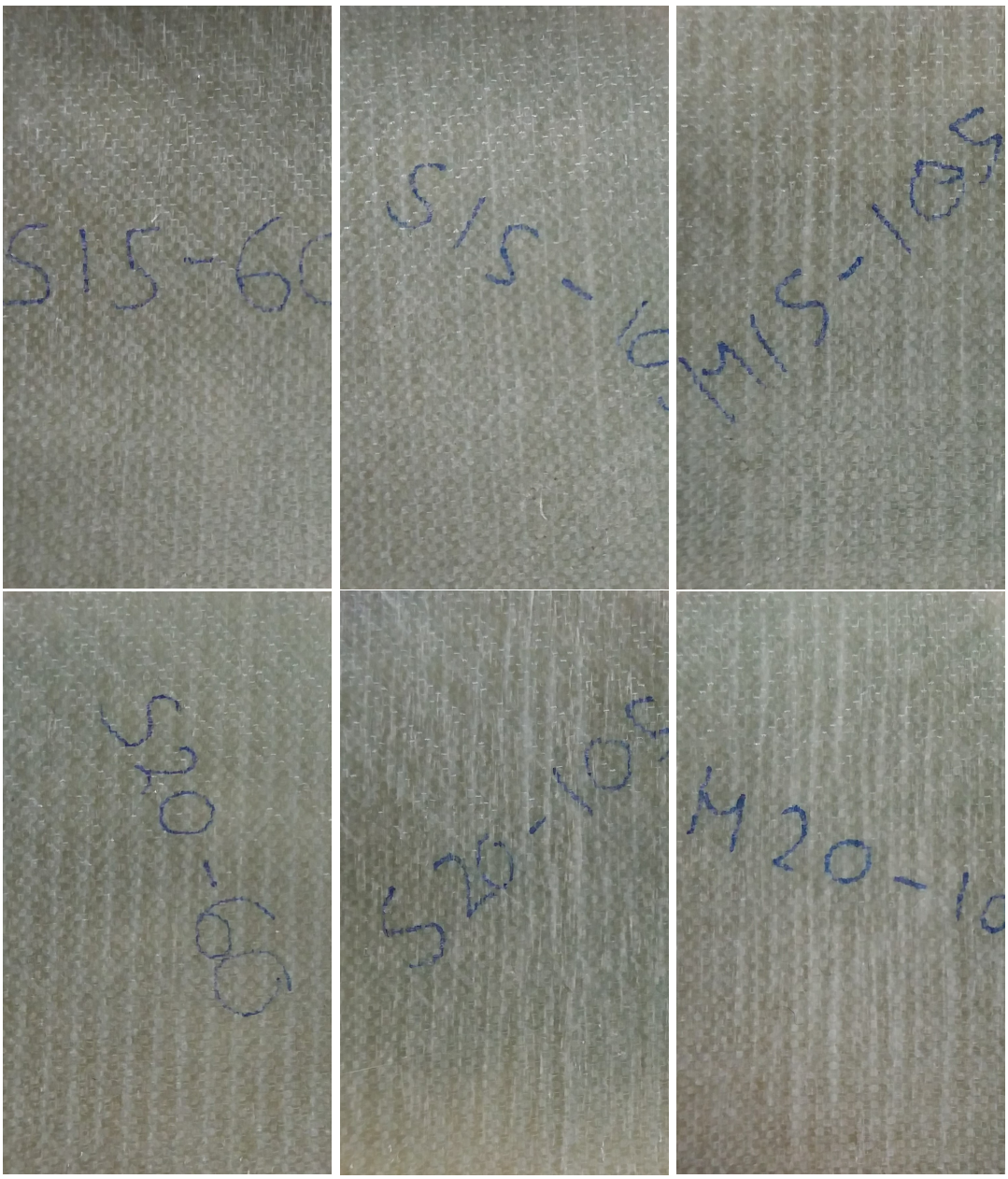

Figure 5.31: Bottom surfaces of experimental discs for 15mm and 20mm SHI impacts (1st Row L-R) S15-V1, S15-V4, M15-V4; (2nd Row L-R) S20-V1, S20-V4, M20-V4 (Note that the velocity description on each sample label in the images are $10\,\mathrm{m\,s^{-1}}$ less than the subjected velocity, for all samples).

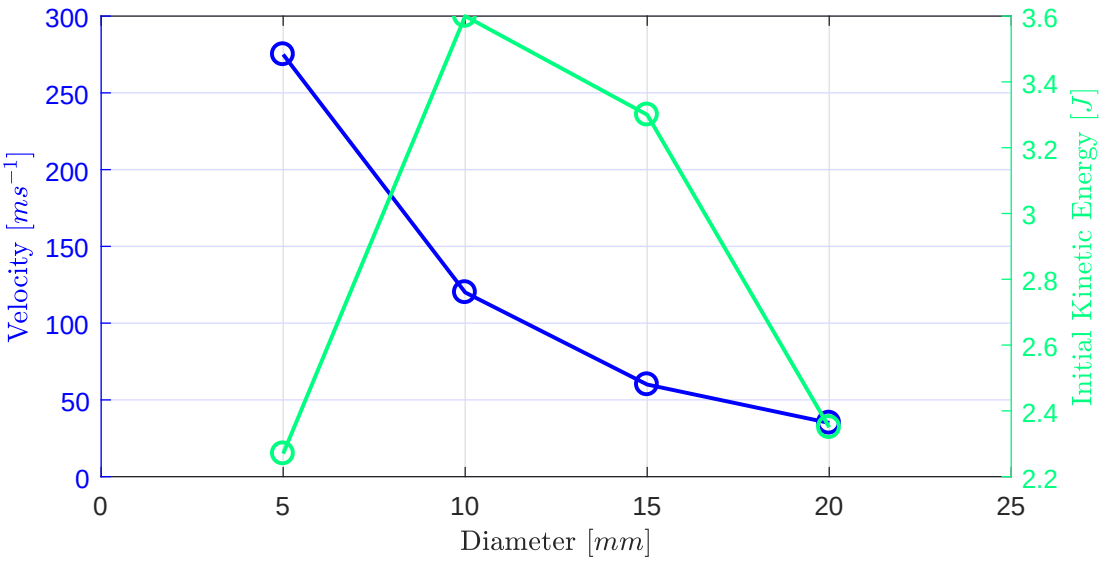

Figure 5.32: Simulated damage threshold velocities and energies for each diameter of hail.

hailstone impact behaviour on composite materials. With the limited composite material information, only a simplified damage model was possible for use in the LS-DYNA simulation. The use of other advanced composite material models that were available would require many more assumptions. Despite the lack of mechanical testing, there was a reasonable degree of confidence in the properties obtained, as concluded from the survey of the various calculation methods. The study also showed that the range of methods could produce differing values. The model constructed compared fairly well with the measured force profile, however there were some concerns regarding the behaviour subsequent to the initial peak in higher velocity cases. The force profiles obtained from the 5 mm simulations reinforced the belief that this unwieldy size of hail, was behaving differently in experimental practice, either losing structure due to the environmental temperature or the pressure from the air cannon. Unfortunately the quality of the high speed camera footage meant that the visual behaviour of the hailstone impact could not compared and analysed in detail.

One of the more interesting observations was the increase in velocity of the SPH nodes spreading outwards after contact with the composite. This high speed lateral jetting could explain some of the "cutting" and "ploughing" type of wear observed in a small collection of the SEM images involved in high speed impact.

The small amount of damage observed for singular impact of the 20 mm diameter ice sphere at the lowest mean velocity may not even cause complete delamination of the composite but it is possible that with repeated impact, the stripping back of matrix

material would be similar to that observed in the SEM for fifty impacts in Chapter 4.

The other two cases of damage surmise that even at a marginally reduced velocity, singular impact of the larger 20 mm diameter hailstone could still cause more matrix cracking, fibre breakage and delamination on the top surface of the composite, than the 15 mm variety. The compressional damage on the upper and lower surfaces in both cases seemed exceptionally more grevious than observed experimentally. Only at a microscopic level, could evidence be found of fibres pushing through the matrix.

A more sophisticated composite material model may be more appropriate for future analysis of this type of behaviour. Overall the damage of 15 mm and 20 mm sizes of hail at high velocity was far greater than for the low speed situations.

The indication is that the onset of failure for single impacts of 5 mm and 10 mm may be outside the range of wind turbine operational tip speeds, especially for the former. Very minor damage was found from multiple impacts at these diameters in practice which was only evident from investigations under the electron microscope and certainly diminutive compared to that inflicted by the larger diameter SHI.

5.8 Conclusion

A computational model was used to simulate the experimental set-up involved in the SHI impact on a composite disc, including the clamp, force transducer and support block. Composite material properties were selected after a survey of calculation methods, involving a case study of a glass-epoxy example composite in the literature [127]. The model was calibrated against force information obtained from each experimental impact.

Damage was established for three singular impact experimental scenarios: a 20 mm diameter hailstone at $49.3\,\mathrm{m\,s^{-1}}$, a 15 mm diameter hailstone at $98.6\,\mathrm{m\,s^{-1}}$ and a 20 mm diameter hailstone at $87.2\,\mathrm{m\,s^{-1}}$. Only a minimal amount of delamination damage was observed on the surface for the low velocity, 20 mm case, whereas all four modes of damage were flagged for the high velocity examples of 15 mm and 20 mm. The 20 mm damage was the more severe of the two even at a slightly reduced velocity. The simulated compressional matrix failure was more extreme for both than anticipated from the experimental results. Further simulations to determine failure thresholds suggest that the onset of damage for singular impact would not occur for 10 mm diameter hail until $120\,\mathrm{m\,s^{-1}}$ and $260\,\mathrm{m\,s^{-1}}$ for 5 mm.

Chapter 6

Overall Discussion and Future Work

In this section, discussions from the three main areas of investigation (Meteorological, Experimental and Computational) are collated and compared to conduct an overall examination of the findings. Although interesting results have been obtained, there are still numerous areas where the phenomenon of hail impact could be explored further, for each of these areas of investigation. The effects of leading edge erosion and damage on wind turbine blades are still an ongoing concern for the industry and until the causes has been completely understood, there will be potential for future developments.

6.1 Meteorological

The majority of available literature into hail damage on composite materials have explored the effects of singular, extreme sizes of hail (greater than 20 mm) that impact subsonic aircraft or aerospace structures at a range of speeds, with some exceeding $200\,\mathrm{m\,s^{-1}}$. After reviewing the type of damage associated with wind turbine blades and a thorough study into the activity of hail in the UK, it became clear that a different approach was required. The conclusions drawn from the meteorological data, particularly in terms of prevalence, indicated that repeated impact from smaller sizes of hail (less than 20 mm) would be a much more realistic scenario for wind farms installed in the UK. The rotational speeds of commercial wind turbines were confirmed to be the determining factor of the velocity at which hailstones impact the blades and restricted the speeds of investigation to just over $100\,\mathrm{m\,s^{-1}}$.

The meteorological study was taken from data harnessed in the UK but on a global scale there are other countries, such as the USA and China, that have a higher capacity of wind turbines, in addition to both a greater frequency and larger, more extreme

sizes of hail. For the hail-specific instruments used at CFARR and NERC stations, the absence of hail events did constrain the depth of analysis. A similar, multi-faceted approach could also be carried out to ascertain the full range of environmental parameters subject to certain wind farm locations. There is also a particular lack of information regarding the prevalence of hail impacts offshore, to accompany the growing trend of hail turbines in this setting. Additional interpretations from the meteorological data present that those locations that experience a greater number of days of hail, are also exposed to very high rainfall rates, categorised as "violent". This demonstrates an interesting case for further exploring the interaction of rain and hail as factors for wind turbine blade leading edge erosion and damage. Even as a short review, future installations of wind turbines would surely benefit from the inclusion of an assessment of other weather effects, in addition to wind, in the planning stage. Without the availability of detailed weather information it would be difficult at this stage to extrapolate these considerations to the offshore environment.

6.2 Experimental and Computational

The outcome from the meteorological study was a proposed experimental campaign, from which a number of challenges were encountered and future recommendations generated. These primarily centred around the sensitivity of smaller sizes of simulated hail ice (SHI) to the laboratory environment. Even with all the steps taken to reduce this detrimental influence, it is clear that a temperature-regulated room should be employed to ensure this effect is negated, especially for 5 mm diameter SHI. Any additional sources of heat should be mitigated. For example, when carrying out future high speed camera work, LED lighting should used in place of halogen lighting. Other constraints of the experimental rig, such as: the limit of force measurement input, maximum firing velocity and reduced resolution of high speed camera footage were not as imperative but could definitely have enhanced the analysis. One of the noteworthy absences of the experimental investigation, that limits its connection to the realistic wind turbine environment, is the use of a coating on the composite samples. While this is still an important avenue of scrutiny, it was felt that due to the lack of examples of ice impact on glass-fibre composites, as opposed to carbon-fibre, the use of protection measures would not be included in the scope of this work. The experimental analysis was predominately concerned with erosion of composite material, that would affect the aerodynamic properties of the wind turbine blade. However, the reduction in strength properties has been carried out for other forms of ice projectiles [35] and could be of interest for future studies.

There were several challenges experienced throughout the experimental campaign which, as a consequence, resulted in a more narrowly defined investigation. Even within the confines of the same experimental apparatus, different types of composites relevant to current wind turbines could be tested for hail impact. More importantly, for the direct representation of leading edge erosion, blade coatings should be included. Although it would involve a long, time-consuming process there would be a motivation to expand upon the variables utilised, including the number of impacts investigated to what a wind turbine would experience over the course its lifetime, in an extreme setting. The study of smaller diameter hailstones was an unique aspect of this experimental investigation but also made for a more environmentally-sensitive application. Future research into these sizes of hail would certainly benefit from a more controllable and sophisticated operation. The dynamic force profile of the 5 mm diameter sphere was notably different to the other, larger sizes Similar to the recommendations for meteorological research, there would be definite potential in investigating the interaction of hailstone impact with different environmental parameters (rain, UV, dust etc.) on composite materials.

One of the most unfortunate restrictions of the computational study was the inability to carry out multiple impact scenarios, for comparison to the experimental findings. Even for a simplified model the computational requirements placed on the finite software would be monumental, though this may be a more plausible task in the future. The model in this investigation could be developed further by implementing of a more sophisticated damage model, through the gathering of additional composite characteristics.

With the mass measurements before and after SHI impacts found to be inconclusive, the survey of damage from the experimental campaign had to be appropriated from the SEM images alone. The results obtained are more qualitative but can be summarised in terms of the experimental variables, shown in the table below.

Preliminary inspections of the meteorological data had highlighted the occurrence of the smallest forms of hail compared with the larger sizes. However, the results obtained from both the cumulative nature of the experimental investigation and the singular impact capabilities of the computational investigation indicate that, even for an increased number of impacts, the cumulative damage caused by 5 mm and 10 mm diameter hail is not as severe compared with the far less prevalent, 15 mm and 20 mm diameter cases, at a lower number of impacts. The relationship between SHI velocity and the level of damage sustained was evident across the composite samples.

As the terminal velocities of each hailstone were less than the respective threshold velocity, the importance of the motion of the blade was highlighted. The "nowcasting"

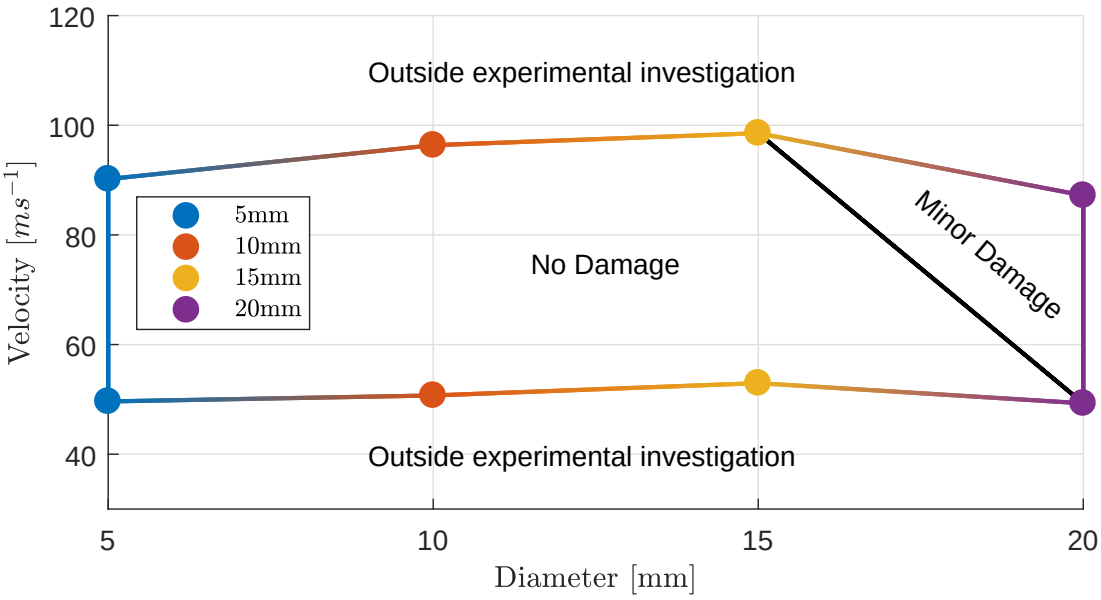

Figure 6.1: Levels of computer simulated damage on GFRP samples obtained from single impact of hailstones of different diameters, fired at different speeds.

of hail still requires some development but shows satisfactory results in the prediction of the kinetic energy of hailstones in a hailstorm. For those rare situations where wind turbines would encounter large sizes of hailstones, there would certainly be a case for reducing the rotational speed of the blades or curtailment of operation. The severity of damage from these early hailstones experiments are not indicative of the serious level of blade damage and erosion observed in the field and that other factors (such as rain) must also play a role. This should also be verified, in future research, for protection measures used in actual wind farm installations.

The main stakeholders of the wind turbine industry would also benefit more from this particular category of research if the "threat" of hail and other environmental parameters to wind turbine blades could be more easily quantifiable. For key decision makers involved in the manufacturing, owning and operation of wind turbines this still ultimately comes down cost. Although the form of blade damage is complex and the acquisition of cost data difficult, the research should still be directed towards the goal of assisting these stakeholders, for the development of solutions to this issue.

Table 6.1: Damage observed under SEM of different diameters of SHI, fired at low and high velocities, for different numbers of impacts.

Mean Velocity	Diameter	Number of Impacts	
		Low	High
Low	5 mm	[49.5 m s^{-1}, 5 impacts] **minimal** surface damage;	[49.8 m s^{-1}, 50 impacts] **minimal** surface damage;
	10 mm	[51.0 m s^{-1}, 10 impacts] **minimal** surface damage;	[50.6 m s^{-1}, 25 impacts] **minimal** surface damage; individual loose fibres
	15 mm	[57.0 m s^{-1}, 10 impacts] **minimal** surface damage;	[51.4 m s^{-1}, 25 impacts] **minimal** surface damage; minor gauges and scarring
	20 mm	[47.7 m s^{-1}, 5 impacts] **minimal** surface damage; minor gouges	[49.4 m s^{-1}, 50 impacts] **notable** surface damage; large area of removed matrix; no debris or loose fibres; minimal scarring
High	5 mm	[91.7 m s^{-1}, 5 impacts] **minimal** surface damage; localised areas of shallow scarring	[90.7 m s^{-1}, 50 impacts] **minimal** surface damage; individual loose fibres and minor defects
	10 mm	[94.9 m s^{-1}, 10 impacts] **minimal** surface damage; minor debris and individual loose fibres	[96.9 m s^{-1}, 25 impacts] **minimal** surface damage; minor fibre breakage, gouges and debris
	15 mm	[99.5 m s^{-1}, 10 impacts] **notable** surface damage; large gouges; significant debris; minor fibre breakage; one long furrow	[98.2 m s^{-1}, 25 impacts] notable surface damage; large gouges; debris; areas of major fibre breakage; shallow scarring
	20 mm	[89.8 m s^{-1}, 5 impacts] **notable** surface damage; gouges; minor debris; scattered individual fibres	[86.9 m s^{-1}, 50 impacts] **notable** surface damage; large gouges; debris; numerous areas of major fibre breakage; deep scarring spread throughout.

Chapter 7

Summary of Conclusions

From the results in each chapter an overall conclusion of the influence of hail impact on wind turbine blade leading edge erosion has been derived. From the meteorological investigation undertaken, the likelihood of hail events at wind turbine locations were gathered. It was determined that even for those locations where hail events were more frequent, the overwhelming majority of incidents in the UK were comprised of hailstones less than 10 mm.

A experimental campaign was devised to evaluate the cumulative effect of 5 mm, 10 mm, 15 mm and 20 mm hailstones impacting on glass fibre reinforced polymer samples, at speeds associated with wind turbine operation. The use of these sizes of hailstones is novel to the field of ice impact analysis on composites. Even for a greater number of impacts, the severity of damage associated with smaller sizes of hail was minimal compared with that of the larger sizes, at a reduced number of impacts. The influence of velocity on the severity of damage was also apparent, of which the operational speed of the turbine is the primary factor.

Simulated analysis of single-impact examples using LS DYNA ® confirmed these impressions for the range of variables carried out in the practical experiments; whereby damage was only encountered for 15 mm diameter hail at high velocity ($98.6\,\mathrm{m\,s^{-1}}$) and 20 mm at both low velocity ($49.3\,\mathrm{m\,s^{-1}}$) and high velocity ($87.0\,\mathrm{m\,s^{-1}}$). The threshold velocities for the onset of damage computed for the single-impact of 5 mm and 10 mm diameters of hail were found to occur outside the range of conventional wind turbine tip speeds.

Early recommendations for the wind turbine industry were formed but further research into the interaction of both hail and the other multitude of environmental factors is still required.

Bibliography

[1] WWEA, "World Wind Energy Report 2013," in *14th World Wind Energy Conf. Renew. Energy Exhib.*, 2014.

[2] UK Meteorological Office, "Weather and Climate," Met Office, Tech. Rep., 2012.

[3] International Energy Agency, "How2Guide for Wind Energy - Roadmap Development and Implementation," IEA, Tech. Rep., 2014.

[4] P. Gipe, "Smith-Putnam Industrial Photos," aug 2014. [Online]. Available: http://www.wind-works.org/cms/index.php?id=223

[5] University of Cambridge - Materials Group, "Specific stiffness - Specific strength," 2011. [Online]. Available: http://www-materials.eng.cam.ac.uk/mpsite/interactive{_}charts/spec-spec/basic.html

[6] Gurit, "Wind Energy Compsite Materials Handbook," Gurit, Tech. Rep., 2013.

[7] B. F. Sørensen, E. Jørgensen, C. P. Debel, F. M. Jensen, H. M. Jensen, T. K. Jacobsen, and K. M. Halling, "Improved design of large wind turbine blade of fibre composites based on studies of scale effects (Phase 1) - Summary Report," Ris National Laboratory, Tech. Rep., 2004.

[8] T. Zander, "Benefits of Long Term Service Strategy," Hamburg, 2013.

[9] C. E. Claus, "Effects of Leading Edge Erosion on Wind Turbine Efficiency & Innovative Erosion Protection Solutions," 2013.

[10] G. W. Stachowiak and A. W. Batchelor, *Engineering Tribology.* Elsevier, 2006. [Online]. Available: http://www.sciencedirect.com/science/article/pii/B9780750678360500122

[11] R. List, "Properties and growth of hailstones," in *Thunderst. Morphol. Dyn.*, 2nd ed., E. Kessler, Ed. University of Michigan Library, 1982, ch. XII, pp. 409–446. [Online]. Available: http://babel.hathitrust.org/cgi/pt?id=mdp.39015013049716;view=1up;seq=431

[12] C. A. Knight and N. C. Knight, "The Falling Behavior of Hailstones," *J. Atmos. Sci.*, vol. 27, no. 4, pp. 672–681, jul 1970.

[13] P. R. Field, W. Hand, D. Cappelluti, G. McMillan, A. Foreman, A. Stubbs, and M. Willows, "Hail Threat Standardisation - Final report," EASA, Research Project EASA.2008/5, 2008.

[14] British Atmospheric Data Centre, "The Natural Environment Research Council (NERC) Mesosphere-Stratosphere-Troposphere (MST) Radar Facility at Aberystwyth Data," 2014. [Online]. Available: http://badc.nerc.ac.uk/view/badc.nerc.ac.uk{_}{_}ATOM{_}{_}dataent{_}MST

[15] E. M. Schulson, "The structure and mechanical behavior of ice," *JOM*, vol. 51, no. 2, p. 21, feb 1999.

[16] H. Kim and J. N. Keune, "Compressive strength of ice at impact strain rates," *J. Mater. Sci.*, vol. 42, no. 8, pp. 2802–2806, 2007.

[17] H. Kim and K. T. Kedward, "Modeling Hail Ice Impacts and Predicting Impact Damage Initiation in Composite Structures," *AIAA J.*, vol. 38, no. 7, pp. 1278–1288, 2000.

[18] H. Kim, D. A. Welch, and K. T. Kedward, "Experimental investigation of high velocity ice impacts on woven carbon/epoxy composite panels," *Compos. Part A Appl. Sci. Manuf.*, vol. 34, no. 1, pp. 25–41, 2003.

[19] J. D. Tippmann, H. Kim, and J. D. Rhymer, "Experimentally validated strain rate dependent material model for spherical ice impact simulation," *Int. J. Impact Eng.*, vol. 57, no. 0, pp. 43–54, 2013. [Online]. Available: http://dx.doi.org/10.1016/j.ijimpeng.2013.01.013

[20] R. Olsson, M. V. Donadon, and B. G. Falzon, "Delamination threshold load for dynamic impact on plates," *Int. J. Solids Struct.*, vol. 43, no. 10, pp. 3124–3141, may 2006. [Online]. Available: http://www.sciencedirect.com/science/article/pii/S0020768305002568

[21] R. Juntikka and R. Olsson, "Experimental and modelling study of hail impact on composite plates," in *ICCM Int. Conf. Compos. Mater.*, 2009.

[22] M. Anghileri, L. M. L. Castelletti, F. Invernizzi, and M. Mascheroni, "A survey of numerical models for hail impact analysis using explicit finite element codes," *Int. J. Impact Eng.*, vol. 31, no. 8, pp. 929–944, 2005.

[23] K. S. Carney, D. J. Benson, P. DuBois, and R. Lee, "A phenomenological high strain rate model with failure for ice," *Int. J. Solids Struct.*, vol. 43, no. 2526, pp. 7820–7839, 2006.

[24] N. Li, Q. Zhou, X. Chen, T. Xu, S. Hui, and D. Zhang, "Liquid drop impact on solid surface with application to water drop erosion on turbine blades, Part I: Nonlinear wave model and solution of one-dimensional impact," *Int. J. Mech. Sci.*, vol. 50, no. 1011, pp. 1526–1542, 2008.

[25] M. H. Keegan, D. H. Nash, and M. M. Stack, "On erosion issues associated with the leading edge of wind turbine blades," *J. Phys. D. Appl. Phys.*, vol. 46, no. 38, p. 383001, 2013.

[26] G. Giller, "Wind Turbines Generate Upside-Down Lightning [Video]," 2014. [Online]. Available: http://blogs.scientificamerican.com/observations/2014/03/03/wind-turbines-generate-upside-down-lightning-video/

[27] H. Zell and V. Carl, "Wind Turbine Inspection: new Methods of Remote Non-Destructive Inspection of Rotorblades," *DEWI Mag.*, 2012. [Online]. Available: http://www.dewi.de/dewi{_}res/fileadmin/pdf/publications/Magazin{_}40/03.pdf

[28] B. Xie, Q. Zhang, and Y. Wang, "Observed Characteristics of Hail Size in Four Regions in China during 1980-2005." *J. Clim.*, vol. 23, no. 18, pp. 4973–4982, 2010.

[29] M. Cox and P. R. Armstrong, "Statistical model for assessing the risk of hail damage to any ground installation. Technical report, June 1978-March 1979," Albuquerque Operations Office, Albuquerque, NM (United States), Tech. Rep., sep 1979. [Online]. Available: http://www.osti.gov/scitech/biblio/5385433

[30] I. V. Roisman and C. Tropea, "Impact of a crushing ice particle onto a dry solid wall," *Proc. R. Soc. A Math. Phys. Eng. Sci.*, vol. 471, no. 2183, p. 20150525, nov 2015. [Online]. Available: http://rspa.royalsocietypublishing.org/content/471/2183/20150525.abstract

[31] International Electrotechnical Commission (IEC), *61400-1 Wind Turbines - Part 1: design requirements*, 3rd ed. International Electrotechnical Commission (IEC), 2015.

[32] A. Sareen, C. A. Sapre, and M. S. Selig, "Effects of leading edge erosion on wind turbine blade performance," *Wind Energy*, vol. 17, no. 10, pp. 1531–1542, 2013.

[33] M. Sioutas, G. T. Meaden, and J. D. C. Webb, "Hail frequency, distribution and intensity in Northern Greece," *Atmos. Res.*, vol. 93, no. 1-3, pp. 526–533, jul 2009. [Online]. Available: http://www.sciencedirect.com/science/article/pii/S0169809508002512

[34] R. Olsson, R. Juntikka, and L. E. Asp, "High Velocity Hail Impact on Composite Laminates - Modelling and Testing," in *Dyn. Fail. Compos. Sandw. Struct.*, ser. Solid Mechanics and Its Applications, S. Abrate, B. Castanié, and Y. D. S. Rajapakse, Eds. Springer Netherlands, 2013, vol. 192, pp. 393–426.

[35] G. J. Appleby-Thomas, P. J. Hazell, and G. Dahini, "On the response of two commercially-important CFRP structures to multiple ice impacts," *Compos. Struct.*, vol. 93, no. 10, pp. 2619–2627, 2011.

[36] World Meteorological Organisation, "Manual on Codes: Part A - Alphanumeric Codes," World Meteorological Organisation, Geneva, Tech. Rep. 2, 2011.

[37] D. Dawson, E. Mansell, Y. Jung, L. Wicker, M. R. Kumjian, and M. Xue, "Low-Level {Z_{DR}} Signatures in Supercell Forward Flanks: The Role of Size Sorting and Melting of Hail." *J. Atmos. Sci.*, vol. 71, no. 1, pp. 276–299, 2014.

[38] EU, "Directive 2009/28/EC Of The European Parliament And Of The Council," *Off. J. Eur. Union*, vol. L 140, pp. 16–62, apr 2009. [Online]. Available: http://ec.europa.eu/clima/policies/package/

[39] EWEA, "Pure Power - Wind energy targets for 2020 and 2030," The European Wind Energy Association, Tech. Rep., jul 2011.

[40] ——, "Wind in power - 2013 European statistics," The European Wind Energy Association, Tech. Rep., feb 2014.

[41] UNFCCC, "Kyoto Protocol Reference Manual on Accounting of Emissions and Assigned Amount," *United Nations Framew. Conv. Clim. Chang.*, 2008.

[42] T. Burton, *Wind Energy Handbook:*. John Wiley & Sons Inc, may 2011. [Online]. Available: https://www.dawsonera.com:443/abstract/9781119992721

[43] P. Jones, "Wind energy in cold climates to increase by 72%," jun 2013. [Online]. Available: http://www.ewea.org/blog/2013/06/wind-energy-in-cold-climates-to-increase-by-72/

[44] Z. J. Westgate and J. T. DeJong, "Geotechnical Considerations for Offshore Wind Turbines," US Offshore Wind Collborative, Tech. Rep., 2005.

[45] GL, "Guideline for the Certification of Offshore Wind Turbines," Germanischer Llyod, Tech. Rep., 2012.

[46] C. Moné, T. Stehly, B. Maples, and E. Settle, "2014 Cost of Wind Energy Review," NREL, Tech. Rep., 2014. [Online]. Available: http://www.nrel.gov/docs/fy16osti/64281.pdf

[47] M. A. S. Shohag, E. C. Hammel, D. O. Olawale, and O. I. Okoli, "Damage mitigation techniques in wind turbine blades: A review," *Wind Eng.*, vol. 41, no. 3, pp. 185–210, jun 2017. [Online]. Available: http://journals.sagepub.com/doi/10.1177/0309524X17706862

[48] T. J. Price, "Blyth, James (1839-1906)," Oxford University Pres, oct 2009. [Online]. Available: http://www.oxforddnb.com/view/article/100957

[49] J. F. Manwell, J. G. McGowan, and A. L. Rogers, *Wind energy explained: theory, design and application.* John Wiley & Sons Inc, sep 2010. [Online]. Available: https://www.dawsonera.com:443/abstract/9780470686287

[50] P. Jamieson, *Innovation in Wind Turbine Design:.* John Wiley & Sons Inc, jul 2011. [Online]. Available: https://www.dawsonera.com:443/abstract/9781119975458

[51] C. Bak, "Aerodynamic design of wind turbine rotors," in *Adv. Wind Turbine Bl. Des. Mater.* Elsevier, 2013, pp. 59–108. [Online]. Available: http://www.sciencedirect.com/science/article/pii/B9780857094261500039

[52] S. Tegen, E. Lantz, M. Hand, B. Maples, A. Smith, and P. Schwabe, "2011 Cost of Wind Energy Review," National Renewable Energy Laboratory, Tech. Rep., mar 2013.

[53] S. Krohn, P.-E. Morthorst, and S. Awerbuch, "The Economics of Wind Energy," EWEA, Tech. Rep., 2009.

[54] P. W. Carlin, A. S. Laxson, and E. B. Muljadi, "The History and State of the Art of Variable-Speed Wind Turbine Technology," *Wind Energy*, vol. 6, no. 2, pp. 129–159, 2003. [Online]. Available: http://dx.doi.org/10.1002/we.77

[55] E. N. Kablov, O. V. Startsev, A. S. Krotov, and V. N. Kirillov, "Climatic aging of composite aviation materials: I. Aging mechanisms," *Russ. Metall.*, vol. 2011, no. 10, pp. 993–1000, feb 2012. [Online]. Available: http://link.springer.com/10.1134/S0036029511100065

[56] ——, "Climatic aging of composite aviation materials: II. Relaxation of the initial structural nonequilibrium and through-thickness gradient of properties," *Russ. Metall.*, vol. 2011, no. 10, pp. 1001–1007, feb 2012. [Online]. Available: http://link.springer.com/10.1134/S0036029511100077

[57] L. Merugula, V. Khanna, and B. R. Bakshi, "Reinforced Wind Turbine Blades - An Environmental Life Cycle Evaluation," *Environ. Sci. Technol.*, vol. 46, no. 17, pp. 9785–9792, 2012.

[58] Siemens, "IntegralBlade® - A key technology unique to the wind industry," Siemens, Tech. Rep., 2012. [Online]. Available: http://www.energy.siemens.com/mx/pool/hq/power-generation/renewables/wind-power/Integral{_}Blades{_}brochure.pdf

[59] B. Kjærside Storm, "Surface protection and coatings for wind turbine rotor blades," in *Adv. Wind Turbine Bl. Des. Mater.* Elsevier, 2013, pp. 387–412. [Online]. Available: http://www.sciencedirect.com/science/article/pii/B978085709426150012X

[60] M. H. Keegan, "Wind Turbine Blade Leading Edge Erosion: An investigation of rain droplet and hailstone impact induced damage mechanisms," Ph.D. dissertation, University of Strathclyde, 2014.

[61] G. A. O. Davis and R. Olsson, "Impact on composite structures," *Aeronaut. J.*, vol. 108 (1089), pp. 541–563, 2004. [Online]. Available: http://aerosociety.com/News/Publications/Aero-Journal/Online/594/Impact-on-composite-structures

[62] Wind Power Monthly, "2nd Annual Blade Inspection Damage And Repair Forum," Hamburg, sep 2014. [Online]. Available: http://www.windpowermonthly.com/wind-blade-inspection-damage-repair-conference-2014

[63] L. Kumosa, M. Kumosa, and D. Armentrout, "Resistance to stress corrosion cracking of unidirectional ECR-glass/polymer composites for high voltage composite insulator applications," *Compos. Part A Appl. Sci. Manuf.*, vol. 34, no. 1, pp. 1–15, jan 2003. [Online]. Available: http://linkinghub.elsevier.com/retrieve/pii/S1359835X02002609

[64] I. M. Giammanco and T. M. Brown, "Characteristics of Severe Hail 2012 Pilot Field Study : Data Analysis Summary," Insurance Institute for Business & Home Safety, Tech. Rep., 2012. [Online]. Available: https://www.disastersafety.org/wp-content/uploads/

Characteristics-of-Severe-Hail-2012-Pilot-Field-Study-Data-Analysis-Summary{_}IBHS.pdf

[65] ——, "2013 IBHS Characteristics of Severe Hail Field Research Summary," Insurance Institute for Business & Home Safety, Tech. Rep., 2013. [Online]. Available: https://www.disastersafety.org/wp-content/uploads/2013-Characteristics-of-Severe-Hail-Field-Research-Summary{_}IBHS.pdf

[66] M. M. Barros and L. Bevilacqua, "Elastic fractal trees: a correspondence among geometry, stress, resilience and material quantity," *J. Brazilian Soc. Mech. Sci. Eng.*, vol. 37, no. 5, pp. 1479–1483, sep 2015.

[67] I. M. Hutchings, D. W. T. Deuchar, and A. H. Muhr, "Erosion of unfilled elastomers by solid particle impact," *J. Mater. Sci.*, vol. 22, no. 11, pp. 4071–4076, nov 1987.

[68] R. Kaundal, A. Patnaik, and A. Satapathy, "Solid Particle Erosion of Short Glass Fiber Reinforced Polyester Composite," *Am. J. Mater. Sci.*, vol. 2, no. 2, pp. 22–27, aug 2012. [Online]. Available: http://article.sapub.org/10.5923.j.materials.20120202.05.html

[69] S. Yashiro, K. Ogi, A. Yoshimura, and Y. Sakaida, "Characterization of high-velocity impact damage in CFRP laminates: Part II prediction by smoothed particle hydrodynamics," *Compos. Part A Appl. Sci. Manuf.*, vol. 56, pp. 308–318, 2014.

[70] British Atmospheric Data Centre, "Met Office Integrated Data Archive System (MIDAS) Land and Marine Surface Stations Data (1853-current)," 2014. [Online]. Available: .nerc.ac.uk/view/badc.nerc.ac.uk{_}{_}ATOM{_}{_}dataent{_}ukmo-midas

[71] N. C. Knight and A. J. Heymsfield, "Measurement and Interpretation of Hailstone Density and Terminal Velocity," *J. Atmos. Sci.*, vol. 40, no. 6, pp. 1510–1516, jun 1983.

[72] N. E. Castellano, O. B. Nasello, and L. Levi, "Study of hail density parametrizations," *Q. J. R. Meteorol. Soc.*, vol. 128, no. 583, pp. 1445–1460, jul 2002. [Online]. Available: http://doi.wiley.com/10.1002/qj.200212858303

[73] C. Wisner, H. D. Orville, and C. Myers, "A Numerical Model of a Hail-Bearing Cloud," *J. Atmos. Sci.*, vol. 29, no. 6, pp. 1160–1181, sep 1972.

[74] B. S. Ferrier, W.-K. Tao, and J. Simpson, "A Double-Moment Multiple-Phase Four-Class Bulk Ice Scheme. Part II: Simulations of Convective Storms in Different Large-Scale Environments and Comparisons with other Bulk Parameterizations," *J. Atmos. Sci.*, vol. 52, no. 8, pp. 1001–1033, apr 1995.

[75] C. A. Knight and N. C. Knight, "Hailstorms," in *Sev. Convect. Storms.* American Meteorological Society, nov 2001, vol. 28, no. 50, pp. 223–249.

[76] P. H. Groenemeijer and A. Van Delden, "Sounding-derived parameters associated with large hail and tornadoes in the Netherlands," *Atmos. Res.*, vol. 83, no. 2-4, pp. 473–487, feb 2007. [Online]. Available: http://www.sciencedirect.com/science/article/pii/S0169809506001165

[77] N. Zhang, F. Yang, D. Guerra, C. Shen, J. Castro, and J. L. Lee, "Enhancing particle erosion resistance of glass-reinforced polymeric composites using carbon nanofiber-based nanopaper coatings," *J. Appl. Polym. Sci.*, vol. 129, no. 4, pp. 1875–1881, aug 2013. [Online]. Available: http://doi.wiley.com/10.1002/app.38899

[78] H. Harries, "The frequency, size, and distribution of hail at sea," *Q. J. R. Meteorol. Soc.*, vol. 21, no. 96, pp. 230–244, 1895.

[79] E. M. Frisby and H. W. Sansom, "Hail Incidence in the Tropics," *J. Appl. Meteorol.*, vol. 6, no. 2, pp. 339–354, apr 1967. [Online]. Available: http://journals.ametsoc.org/doi/abs/10.1175/1520-0450(1967)006{%}3C0339{%}3AHIITT{%}3E2.0.CO{%}3B2

[80] C. Berthet, E. Wesolek, J. Dessens, and J. Sanchez, "Extreme hail day climatology in Southwestern France," *Atmos. Res.*, vol. 123, pp. 139–150, 2013.

[81] J. Sánchez, L. López, E. García-Ortega, and B. Gil, "Nowcasting of kinetic energy of hail precipitation using radar," *Atmos. Res.*, vol. 123, pp. 48–60, 2013. [Online]. Available: http://www.sciencedirect.com/science/article/pii/S0169809512002578

[82] P. Melcón, A. Merino, J. L. Sánchez, L. López, and L. Hermida, "Satellite remote sensing of hailstorms in France," *Atmos. Res.*, vol. 182, pp. 221–231, 2016. [Online]. Available: http://www.sciencedirect.com/science/article/pii/S0169809516302253?dgcid=Newsletters{%}26Alerts{_}email{_}SDPR-EXP10-VAR2

[83] R. Ferraro, J. Beauchamp, D. Cecil, and G. Heymsfield, "A prototype hail detection algorithm and hail climatology developed with the advanced microwave sounding unit (AMSU)," *Atmos. Res.*, vol. 163, pp. 24–35, 2015.

[84] H. Park and H. Kim, "Damage resistance of single lap adhesive composite joints by transverse ice impact," *Int. J. Impact Eng.*, vol. 37, no. 2, pp. 177–184, 2010.

[85] J. D. Rhymer, H. Kim, and D. Roach, "The damage resistance of quasi-isotropic carbon/epoxy composite tape laminates impacted by high velocity ice," *Compos. Part A Appl. Sci. Manuf.*, vol. 43, no. 7, pp. 1134–1144, 2012.

[86] E. M. Schulson, "Brittle failure of ice," *Eng. Fract. Mech.*, vol. 68, no. 17-18, pp. 1839–1887, dec 2001. [Online]. Available: http://www.sciencedirect.com/science/article/pii/S0013794401000376

[87] J. J. Petrovic, "Review Mechanical properties of ice and snow," *J. Mater. Sci.*, vol. 38, pp. 1–6, 2003. [Online]. Available: http://dx.doi.org/10.1023/A:1021134128038

[88] M. Mahinfalah and R. A. Skordahl, "The effects of hail damage on the fatigue strength of a graphite/epoxy composite laminate," *Compos. Struct.*, vol. 42, no. 2, pp. 101–106, jun 1998. [Online]. Available: http://www.sciencedirect.com/science/article/pii/S0263822398000567

[89] A. Combescure, Y. Chuzel-Marmot, and J. Fabis, "Experimental study of high-velocity impact and fracture of ice," *Int. J. Solids Struct.*, vol. 48, no. 20, pp. 2779–2790, 2011.

[90] R. Olsson, "Closed form prediction of peak load and delamination onset under small mass impact," *Compos. Struct.*, vol. 59, no. 3, pp. 341–349, feb 2003. [Online]. Available: http://www.sciencedirect.com/science/article/pii/S0263822302002441

[91] T. Sain and R. Narasimhan, "Constitutive modeling of ice in the high strain rate regime," *Int. J. Solids Struct.*, vol. 48, no. 5, pp. 817–827, 2011.

[92] J. E. Field, "ELSI conference: invited lecture: Liquid impact: theory, experiment, applications," *Wear*, vol. 233 235, pp. 1–12, 1999.

[93] M. Lesser, "Thirty years of liquid impact research: a tutorial review," *Wear*, vol. 186-87, Pa, no. 0, pp. 28–34, jul 1995.

[94] M. H. Keegan, D. H. Nash, and M. M. Stack, "Modelling rain drop impact on offshore wind turbine blades," in *ASME Turbo Expo*, Copenhagen, 2012.

[95] O. Gohardani, "Impact of erosion testing aspects on current and future flight conditions," *Prog. Aerosp. Sci.*, vol. 47, no. 4, pp. 280–303, 2011.

[96] N. Wilson, K. Cummins, A. Nag, and J. Myers, "Lightning Attachment to Wind Turbines in Central Kansas: Video, Observations, Correlation with the NLDN and in-situ Peak Current Measurements," in *EWEA*, Hamburg, 2013. [Online]. Available: http://proceedings.ewea.org/annual2013/programme-final/info2.php?id2=1024{&}id=167{&}ordre=1

[97] E. Sagol, M. Reggio, and A. Ilinca, "Issues concerning roughness on wind turbine blades," *Renew. Sustain. Energy Rev.*, vol. 23, pp. 514–525, jul 2013. [Online]. Available: http://linkinghub.elsevier.com/retrieve/pii/S1364032113001366

[98] Y. Han, J. Palacios, and S. Schmitz, "Scaled ice accretion experiments on a rotating wind turbine blade," *J. Wind Eng. Ind. Aerodyn.*, vol. 109, pp. 55–67, oct 2012. [Online]. Available: http://www.sciencedirect.com/science/article/pii/S0167610512001870

[99] S. Biswas, P. Taylor, and J. Salmon, "A model of ice throw trajectories from wind turbines," *Wind Energy*, vol. 15, no. 7, pp. 889–901, oct 2012. [Online]. Available: http://doi.wiley.com/10.1002/we.519

[100] Kelly Aerosoace Thermal Systems, "Wind Turbine Ice Protection System," 2011. [Online]. Available: http://www.kellyaerospace.com/wind{_}turbine{_}deice.html

[101] C. J. Spruce, "Power performance of active stall wind turbines with blade contamination," in *EWEA*. Athens: EWEC, 2006.

[102] V. Sathiesh Kumar, N. J. Vasa, and R. Sarathi, "Detecting salt deposition on a wind turbine blade using laser induced breakdown spectroscopy technique," *Appl. Phys. A*, vol. 112, no. 1, pp. 149–153, sep 2012. [Online]. Available: http://link.springer.com/10.1007/s00339-012-7219-5

[103] U. Tewari, A. Harsha, A. Häger, and K. Friedrich, "Solid particle erosion of carbon fibre and glass fibreepoxy composites," *Compos. Sci. Technol.*, vol. 63, no. 3-4, pp. 549–557, feb 2003. [Online]. Available: http://www.researchgate.net/publication/222545511{_}Solid{_}particle{_}

erosion{_}of{_}carbon{_}fibre{_}and{_}glass{_}fibreepoxy{_}compositeshttp://www.sciencedirect.com/science/article/pii/S0266353802002105

[104] M. Troedsson, "Application of Viable Inspection Methods for On-site Blade Assessment," Hamburg, pp. 1–10, 2013.

[105] K. B. Katnam, A. J. Comer, D. Roy, L. F. M. da Silva, and T. M. Young, "Composite Repair in Wind Turbine Blades: An Overview," *J. Adhes.*, vol. 91, no. 1-2, pp. 113–139, jan 2015. [Online]. Available: http://www.tandfonline.com/doi/abs/10.1080/00218464.2014.900449

[106] A. Young, A. Kay, S. Marshall, R. Torr, and A. Gray, "Hyperspetcral Imaging for Erosion Detection in Wind Turbine Blades," in *Hyperspectral Imaging Conf.*, 2016. [Online]. Available: http://strathprints.strath.ac.uk/58291/

[107] D. Li, S.-C. M. Ho, G. Song, L. Ren, and H. Li, "A review of damage detection methods for wind turbine blades," *Smart Mater. Struct.*, vol. 24, no. 3, p. 033001, mar 2015. [Online]. Available: http://stacks.iop.org/0964-1726/24/i=3/a=033001?key=crossref.2d9872ce308594acb3e4ec59d5094560

[108] G. Marsh, "The challenge of wind turbine blade repair," 2011. [Online]. Available: http://www.renewableenergyfocus.com/view/21860/the-challenge-of-wind-turbine-blade-repair/

[109] H. Macdonald, D. Infield, D. H. Nash, and M. M. Stack, "Mapping hail meteorological observations for prediction of erosion in wind turbines," *Wind Energy*, pp. n/a–n/a, apr 2015. [Online]. Available: http://doi.wiley.com/10.1002/we.1854

[110] I. M. Hutchings, *Tribology : friction and wear of engineering materials*. London : Edward Arnold, 1992.

[111] M. H. Keegan, D. H. Nash, and M. M. Stack, "Numerical modelling of hailstone impact on the leading edge of a wind turbine blade," in *EWEA Annu. Wind Energy Event*, Vienna, 2013.

[112] British Atmospheric Data Centre, "Chilbolton Facility for Atmospheric and Radio Research (CFARR): surface, radar and lidar measurements (1998-present)," 2014. [Online]. Available: http://badc.nerc.ac.uk/browse/badc/chilbolton

[113] J. Agnew and M. Brettle, "A Field Study To Characterise The Measurement Of Precipitation Using Different Types Of Sensor," in *WMO Tech. Conf. Meteorol. Environ. Instruments Methods Obs.* Brussels, Belgium: STFC Rutherford Appleton Laboratory, Campbell Scientific Ltd, oct 2012.

[114] DECC, "UK Renewable Energy Roadmap Update 2013," Department of Energy and Climate Change, Department of Energy & Climate Change 3 Whitehall Place London SW1A 2AW, Government Report, nov 2013.

[115] B. S. Ferrier, "A Double-Moment Multiple-Phase Four-Class Bulk Ice Scheme. Part I: Description," *J. Atmos. Sci.*, vol. 51, no. 2, pp. 249–280, jan 1994.

[116] G. Bowden, P. Barker, V. Shestopal, and J. Twidell, "The Weibull distribution function and wind power statistics," *Wind Eng. (ISSN 0309-524X)*, vol. 7, pp. 85–98, 1983. [Online]. Available: http://adsabs.harvard.edu/abs/1983WiEng...7...85B

[117] Cengel YA, *Heat and Mass Transfer A Practical Approach.* McGraw-Hill, 2006. [Online]. Available: http://ebooks.cambridge.org/ref/id/CBO9780511676420A021

[118] B. Harris, *Engineering Composite Materials.* IOM, 1999. [Online]. Available: https://books.google.co.uk/books/about/Engineering{_}Composite{_}Materials.html?id=9MVRAAAAMAAJ{&}pgis=1

[119] J. Summerscales and P. A. Annis, *Microstructural characterisation of fibre-reinforced composites.* Woodhead Publishing Ltd, 1998.

[120] J. M. Swift, "Simulated Hail Ice Mechanical Properties and Failure Mechanism at Quasi-Static Strain Rates," Ph.D. dissertation, University of Washington, jul 2013. [Online]. Available: https://digital.lib.washington.edu/researchworks/handle/1773/22847

[121] ASHRAE, "ASHRAE Handbook-Fundamentals," *ASHRAE Handbook-Fundamentals*, pp. 21.1–21.67, 2009.

[122] I. Rocha, S. Raijmaekers, R. Nijssen, F. van der Meer, and L. Sluys, "Hygrothermal ageing behaviour of a glass/epoxy composite used in wind turbine blades," *Compos. Struct.*, 2017. [Online]. Available: http://www.sciencedirect.com/science/article/pii/S026382231631858X

[123] Z. Tang, C. Hang, T. Suo, Y. Wang, L. Dai, Y. Zhang, and Y. Li, "Numerical and experimental investigation on hail impact on composite panels," *Int. J. Impact Eng.*, may 2016. [Online]. Available: http://www.sciencedirect.com/science/article/pii/S0734743X16303050

[124] Livermore Software Technology Corporation, *LS-DYNA Keyword User's Manual, vol. I*, 2007, vol. I, no. May.

[125] ——, *LS-DYNA Keyword User's Manual, vol. I*, 2007, vol. I, no. May.

[126] K. K. Chawla, *Composite Materials*. New York, NY: Springer New York, 2012. [Online]. Available: http://link.springer.com/10.1007/978-0-387-74365-3

[127] D. Samborsky, J. Mandell, and P. Agastra, "3-D Static Elastic Constants and Strength Properties of a Glass/Epoxy Unidirectional Laminate," Montana State University, Tech. Rep., 2012. [Online]. Available: http://www.coe.montana.edu/composites/documents/3DStaticPropertyReport.pdf

[128] S. Abrate, "Soft impacts on aerospace structures," *Prog. Aerosp. Sci.*, dec 2015. [Online]. Available: http://www.sciencedirect.com/science/article/pii/S0376042115300294

[129] LSTC Inc and DYNAmore GMBH, "LS-DYNA ® support site." [Online]. Available: http://www.dynasupport.com/